12-2018

Development of Anti-Icing Airfield Heated Pavement Systems Using Solar Energy

Joseph Daniels
University of Arkansas, Fayetteville

Development of Anti-Icing Airfield Heated Pavement Systems Using Solar Energy

A dissertation submitted in partial fulfillment
of the requirements for the degree of
Doctor of Philosophy in Engineering

by

Joseph W. Daniels, III
North Carolina A&T State University
Bachelor of Science in Civil Engineering, 2013

December 2018
University of Arkansas

This dissertation is approved for recommendation to the Graduate Council.

_____
Ernest Heymsfield, Ph.D., P.E.
Dissertation Director

_____
W. Micah Hale, Ph.D., P.E.
Committee Member

_____
R. Panneer Selvam, Ph.D., P.E.
Committee Member

_____
Halil Ceylan, Ph.D., P.E.
Committee Member

_____
Wayne Hodo, Ph.D., P.E.
Committee Member

ABSTRACT

This dissertation analyzes developing and assessing the viability of an anti-icing airfield heated pavement system using solar energy. This study includes two components, a field experimentation component and a numerical analysis component. Field experimentation investigates two systems: (1) an electrical heated pavement system with a photovoltaic energy system as its power source, and (2) a hydronic heated pavement system with a solar water-heating system as its heating source. The systems operate under an automated thermostat heating sequence for operation optimization and energy conservation. Study results found the solar systems capable of supplying enough energy to maintain pavement surface temperature above freezing and melt snow. A finite element model (FEM) extends the near-surface electrical heated pavement system analysis to assess the energy required to heat a cold region airport's airfield pavement. A benefit-cost analysis (BCA) expands the hydronic system analysis to assess the viability for implementing a solar-hydronic heated pavement system at an apron area.

ACKNOWLEDGMENTS

I am so grateful to God for giving me the strength and the stamina to conduct and document the research in this dissertation. Through this doctoral experience, my testimony is one of faith, perseverance, and thanksgiving. I started this journey without a research topic, research funding, or laboratory research experience. Yet, I set out on this journey and pursued the research herein as it mirrored my research passion and objective.

In my thanksgiving, I want to give a special thanks to my advisor Dr. Ernest Heymsfield for taking a chance on me. Dr. Heymsfield has worked with me tirelessly to improve my technical writing, develop the research methods herein, expand my network within my research field domestically and internationally, and assist in pursuing multiple research funding opportunities. Through our teamwork, we were granted three Dwight D. Eisenhower Graduate Fellowship Awards, the 2017 Airport Cooperative Research Program (ACRP) Graduate Research Award, and the 2017 Secretary of Transportation's Recognizing Aviation & Aerospace Innovation in Science and Engineering (RAISE) Award.

In my thanksgiving, I want to express my gratitude to Dr. W. Micah Hale for the endless support he has shown me throughout this program. As a teacher's assistant for the first three years of my program, I did not have funding during those summer months. Dr. Hale offered me summer research assistant positions, affording the opportunities to participate in a variety of concrete related projects, while focusing on my research and being paid in the process. His support also allowed me to attend multiple conferences and give a research presentation in the Czech Republic.

In my thanksgiving, it is with deep appreciation that I thank Mark Kuss, David Peachee, and Robert Saunders for their involvement in the laboratory and field experimentation. Likewise, I

thank the Northwest Arkansas Regional Airport operations team for offering their airport pavement deicing expertise and providing data needed to perform analyses throughout my research.

Lastly, in my thanksgiving, I give special thanks to Tiffany Williams (fiancée), Joseph W. Daniels, Jr. (father), Madelyn Daniels (mother), and Joia Daniels (sister) for their endless love, encouragement, and motivation along this journey. This doctorate is as much yours as it is mine.

DEDICATION

I dedicate this dissertation to my late grandmother, Evangeline “Van” Moore. As a child, my grandmother called me every day after school to ask what I had learned. Though annoying at the time, she instilled the importance of education and my constant pursuit of knowledge. This dissertation is submitted in her honor.

I dedicate this dissertation to the late, Megan Browning. Ms. Browning was a student of mine who displayed a strong work ethic, and was determined to find solutions to every problem placed in front of her. Her persistent approach to learning was inspiring and infectious. This dissertation is submitted in her honor.

I dedicate this dissertation to those who have lost their lives to police brutality and those who continue the fight for racial and social justice and equality. During my doctoral program, I led community efforts to fight for, and bring awareness to racial and social injustice. Engaging in these efforts from a doctoral student platform allowed me to address racial and social issues in a place and space where such topics lay dormant. This dissertation is submitted in honor and support of those who continue to seek justice and equality for all.

Lastly, I dedicate this dissertation to my fiancée, Tiffany Williams, my father, Joseph W. Daniels, Jr., my mother, Madelyn Daniels, and my sister, Joia Daniels.

TABLE OF CONTENTS

Chapter 1: Introduction 1
Dissertation Objectives 2
Dissertation Organization 3
Background 4
Problem Statement 5
Chapter 2: Literature Review 9
Problem Statement 9
State of Heated Pavement System (HPS) Research 9
State of Airfield Heated Pavement System (AHPS) Research 18
Airfield Heated Pavement / Snow and Ice Control Compatibility 21
Chapter 3: Field Experimentation Methodology 25
Overview 25
Outdoor Test Facility Design 25
Snow-Melting Heat Flux Requirement 28
Solar – Electrical Heated Pavement System Approach 28
Solar – Hydronic HeatED PAVEMENT System Approach 63
Snow Making 72
Chapter 4: Field experimentation Results and Discussion 74
Solar – Electrical Heated Pavement System Approach 74
Solar – Hydronic Heated Pavement System Approach 78
Chapter 5: Finite Element Analysis 87
Introduction 87
Methodology 87
FEM Results and Discussion 91
Summary 97
Chapter 6: Benefit Cost Analysis 98
Introduction 98
Methodology 99
Case Study: Northwest Arkansas Regional Airport 103
Chapter 7: Conclusions 113
References 116
Appendix A 124
Appendix B 137

Appendix C 145
Appendix D 149
Appendix E 155
Appendix F 160

ACRONYMS

AC – Advisory circular
AC – Alternating current
ACRP – Airport Cooperative Research Program
ACS – Automated control system
AHPS – Airfield heated pavement system
AOA – Air operations area
APS – Aircraft parking stand
ASHRAE – American Society of Heating, Refrigerating and Air-Conditioning Engineers
ASR – Alkali-silica reaction
ASROC – Annual snow removal operating cost
ASTM – American Society for Testing and Materials
BCA – Benefit-cost analysis
BCR – Benefit-cost ratio
CFHW – Carbon fiber heat wire
CL – Centerline
DAQ – Data acquisition system
DC – Direct current
DCHE – Downhole coaxial heat exchanger
DHE – Downhole heat exchanger
DSM – Des Moines International Airport
ECC – Electrically conductive concrete
EHPS – Electrical heated pavement system
ENRC – Engineering research center
FAA – Federal Aviation Administration
FEA – Finite Element Analysis
FEM – Finite element model
FFC – Fuel and Flight Crew
FPC – Flat plate collector
GSHE – Ground source heat exchanger
HHPS – Hydronic heated pavement system
HP-ETC – Heat Pipe Evacuated Tube Collector
HPS – Heated Pavement System
IR – Infrared
ISU – Iowa State University
LGA – LaGuardia Airport
MR – Modulus of rupture
NiCr-80/20 – Nickel-Chromium (Ni – 80%, Cr – 20%)
NPV – Net Present Value
NRC – National Research Council of Canada
ORD – Chicago's O'Hare International Airport
PC – Proof-of-concept
PCC – Portland cement concrete
PDP – Pavement deicing product
PEGASAS – Partnership to Enhance General Aviation Safety, Accessibility, and Sustainability

PEX – Cross-linked polyethylene
PV – Present value
PVES – Photovoltaic energy system
RPM – Revenue passenger mile
RTM – Revenue ton mile
SICP – Snow and Ice Control Plan
Solar-EHPS – Solar powered electrical heated pavement system
Solar-HHPS – Solar heated hydronic heated pavement system
SRC – Snow removal cost
SRE – Snow removal equipment
SWHS – Solar water heating system
TM# - Test Mat (number)
TPST – Target pavement surface temperature
TWSDH – Total winter season delay hour
UA – University of Arkansas
US – United States
VDC – Voltage using direct current
VLPT – Value of lost passenger time
VOT – Value of time
XNA – Northwest Arkansas Regional Airport

LIST OF PUBLISHED PAPERS

Daniels, J. and Heymsfield, E., 2018. Development of Anti-Icing Airfield Pavement using Surface-Embedded Heat Wire. International Journal of Pavement Engineering, 19(10), 1-11.

Daniels, J., Heymsfield, E., Kuss, M., and Saunders, R. "Development of Automated Electrical Heat Grid for Pavement Snowmelt," Thermal Science and Engineering Progress, submitted for review for journal publication.

Daniels, J., Heymsfield, E., and Kuss, M. "Hydronic Heated Pavement System Performance using a Solar Water Heating System with Heat Pipe Evacuated Tube Solar Collectors," Solar Energy Journal, submitted for review for journal publication.

Daniels, J. and Heymsfield, E. "Development of Anti-Icing Airfield Heated Pavement System using Solar Energy," Transportation Research Record, submitted for review for journal publication.

CHAPTER 1: INTRODUCTION

Civil aviation is a pivotal asset for global economics, domestic and international connectivity, and new global business opportunities. In the United States (U.S.), from 2014 data, the aviation industry was responsible for 5.1-percent of the U.S. economy, generating $1.6 trillion in total economic activity (FAA 2016). This accounted for 1.23-trillion revenue passenger miles (RPM) and an excess of 64 billion freight revenue ton-miles (RTM). In 2014, the Federal Aviation Administration (FAA) forecasted a 2.8-percent annual RPM growth in a 20-year analysis period. This represents an increase from 872-million air travel passengers to 1.15-billion in 2034. Freight (RTM) is also expected to increase by half by 2034 (FAA 2014c).

With the rising demand in U.S. passenger and cargo transport, the FAA, on a macro-level, is tasked with enhancing the system's infrastructure, and developing and incorporating new technology. Additionally, the FAA plans to continue innovative practices by increasing system safety, reliability, capacity, and environmental protection (FAA 2010). Pertinent to the material in this dissertation, on a micro-level, the FAA is coordinating methods to improve winter operation safety and strengthen winter operation reliability (ACRP 2015).

This dissertation investigates how to improve winter operation safety and improve winter operation reliability by developing an anti-icing heated pavement system using renewable energy for airport implementation. An electrical and hydronic heated pavement system are investigated in this study through field experimentation. The investigated systems incorporate solar energy technology suited for electrical energy generation and fluid heat exchange. The studied electrical heated pavement system incorporates near-surface electrical heat wires and a photovoltaic energy system. Near-surface electrical heating is a novel approach to concentrate heat transfer to the pavement surface and reduce energy requirements to optimize the use of solar energy. A

finite element model (FEM) is developed in this work to expand the experimental analysis of the solar near-surface electrical heated pavement system (solar-EHPS) to various ambient weather conditions in cold geographic regions in the US. The FEM validates the solar-EHPS experimental work. Additionally, the operation and economic advances of a hydronic heating pavement system incorporating modern solar water-heating technology is examined. A cost analysis investigates the benefits and limitations of the solar hydronic heated pavement system (solar-HHPS) for implementation at the local Northwest Arkansas Regional Airport (XNA).

DISSERTATION OBJECTIVES

This research dissertation analyzes the development and assesses the viability of a solar powered anti-icing airfield heated pavement system (AHPS). Two novel techniques are described in this study. The first technique couples a photovoltaic energy system with an electrical heated pavement system (EHPS) using near-surface heating elements. The second technique investigates a solar water-heating system coupled with a hydronic heated pavement system (HHPS). The goal in implementing either of these techniques is to reduce operational cost and increase the viability for AHPS implementation. Consequently, the objectives of this AHPS research project are to:

Objective #

1. Investigate the potential of a solar – electrical heated pavement system (solar-EHPS) using a near-surface electrical heat grid prototype and a photovoltaic energy system,
2. Establish a numerical model, validated through experimental results, to extend the solar-EHPS approach with the near-surface electrical heat grid prototype to U.S. cold region airports, and

3. Determine the (a) operation and (b) economic benefits of a solar – hydronic heated pavement system (solar-HHPS) considering state of the art solar water-heating technology.

These objectives are executed through:

Task #

1. laboratory and field experiments on the heated pavement system designs,
2. finite element modeling for the near-surface electrical heat grid prototype study, and
3. a benefit-cost analysis for the solar-HHPS approach using the Northwest Arkansas Regional Airport (XNA) as a case study.

The AHPS research contributions include:

Contribution #

1. an analysis of pavement heating and heating operation when heat elements are positioned near the pavement surface;
2. an analysis of pavement heating and heating operation for a solar hydronic heated pavement system;
3. determining the practicality of a solar energy power source; and
4. providing a current economic benchmark for an AHPS utilizing solar water-heating technology.

DISSERTATION ORGANIZATION

This dissertation is organized into seven chapters. Chapter 1 introduces the current state of US airport's conventional pavement deicing methods, addresses the conventional pavement deicing method limitations, and provides an overview of the advantages to using airfield heated pavement systems as a pavement deicing alternative. Chapter 2 is a literature review of heated

pavement system installations domestically and internationally at roadways, bridge decks, and airfields. Current research initiatives for airfield heated pavement systems are addressed along with the contributions made by the work herein to the current direction in AHPS research. Chapter 3 details the methodology used to perform field experiments on the two solar heated pavement approaches studied in this presented project. Chapter 4 presents the field experiment results along with discussions on these results. Chapter 3 and Chapter 4 fulfill research Objectives #1 and #3(a). Chapter 5 details the finite element model development for the solar-EHPS analysis, which extends the pavement heating analysis to U.S. airports considering their winter weather conditions. Chapter 5 fulfills research Objective #2. Chapter 6 details the benefit-cost analysis used to assess the financial viability for implementing a solar-HHPS at Northwest Arkansas Regional Airport (XNA). Chapter 6 fulfills research Objective #3(b). Chapter 7 summarizes the study's conclusions and offers recommendations for future research interests for continued study towards AHPS implementation. The appendix material provides additional testing results from the field experiments and the finite element analysis.

BACKGROUND

US airports in cold climate regions experience annual winter weather conditions that cripple the civil aviation system. Winter weather conditions inherently reduce air traffic volume resulting from flight delays and cancellations, and occasional airport closure (FAA 2008).

Snow, slush, or ice on the airfield pavement, in the air operations area (AOA), greatly intensifies safety risks for aircraft ground operations. Such winter contaminants create slippery pavement conditions in which aircraft are prone to runway veer-offs and overruns, taxiway veer-offs, and apron area delays. Wet wintry pavement conditions contributed to more than 50 accidents from 1998 to 2004 with a majority of these accidents reporting fatalities (NASA 2004). The FAA

provides guidance for airport winter safety operations to combat safety hazards and air traffic reduction (FAA 2008). Airports experiencing annual snowfall at or above 15-cm are recommended to having a snow and ice control plan (SICP) with the goal of maintaining a "no more than wet" pavement surface condition. However, it is impractical to clear the entire AOA concurrently. Thus, specific pavement areas, denoted "Priority 1", are cleared first to sustain airport operations. Priority 1 areas include in-service runways, primary taxiways, and emergency access roads (FAA 2008).

Under the SICP, airports currently use conventional pavement deicing methods employing a snow-removal equipment fleet and pavement deicing products (PDP). The snow-removal equipment fleet, consisting of sweepers, plows, and blowers, clear winter contaminants from the paved surface. An airport's snow-removal fleet is sized to meet specific snow removal time constraints at "Priority 1" airfield pavement locations (FAA 2014a). Pavement deicing products are used to melt ice and/or prevent ice-pavement bonding when necessary. Airports use FAA-approved PDPs including ethylene glycol, potassium acetate fluid, sodium acetate pellets, and sodium formate pellets (ACRP 2009, FAA 2008, Shi 2008). Deicing procedures, including snow clearance routines and chemical application rates, are specific to individual airports and weather conditions. Weather forecasting technology (i.e. Weather Support to Deicing Decision Making System) is a resource for assisting in snow and ice control preparation and accumulation prevention (FAA 2008).

PROBLEM STATEMENT

SICP limitations present a safety risk for aircraft ground operations. These limitations are exposed in various weather conditions and are caused by multiple factors. These factors include, but are not limited to, elevated winter storm intensity, storm event duration, contaminant types,

and change in climate conditions. As such, safety risks are heightened when weather conditions exceed pavement clearance and treatment capacity. Below are recent events for winter aircraft accidents and incidents at US commercial airports during wet wintry conditions.

December 25, 2017 – Boston Logan International Airport, Boston, Massachusetts (Moore 2017)

Boston Logan International Airport performed pavement-deicing activities throughout the day. The runway was shut down in the morning to perform clearance operations. JetBlue Flight 50 skidded down the runway and began to spin as the aircraft decreased in speed. The aircraft came to rest in the grass facing 180 degrees from the landing position. No injuries were reported in this incident.

December 11, 2016 – Detroit Metropolitan Airport, Detroit, Michigan (Wood 2016)

As Delta Airlines Flight 724 landed and approached its taxiway turnoff, the aircraft skidded into the grassy area between the runway and taxiway. No passengers or crewmembers were injured and the airfield remained operational with isolated emergency efforts.

December 30, 2015 – O'Hare International Airport, Chicago, Illinois (Waldroup 2015)

United Flight 1977 was unable to stop when landing on the 3,962-m runway due to snow and ice, and came to rest in the overrun area at the end of the runway. There were no reported injuries and investigation showed no damage to the aircraft. Snowfall lasted for hours during the day and throughout the evening, delaying multiple outbound and inbound flights into O'Hare Airport. This incident caused airfield closure for a few hours in order to bring the aircraft to the terminal. Nearly 100 flights were cancelled.

March 5, 2015 – LaGuardia Airport, New York, New York (Santora and McGeehan 2015)

Delta Flight 1086, carrying 132 passengers/crew members, skidded off the runway and crashed into the earthen berm, which prevented the aircraft from entering Flushing Bay. Skidding occurred almost immediately when the aircraft touched down. The crash hospitalized a few passengers and left others with minor injuries. The aircraft was severely damaged and fuel leaked for hours. Passengers stated that the runway looked covered with snow as the aircraft prepared to land. However, the airport reported the runway was deiced minutes prior to the aircraft landing. Additionally, two flights reported good braking condition prior to Delta Flight 1086's landing activity. The airport was closed for 3-hours with only one runway opening thereafter. Hundreds of flights were cancelled.

January 6, 2014 – John F. Kennedy Airport, New York, New York (Sandoval and Moore 2014)

Delta Airlines Flight 4100 slid into the grass as the pilot attempted steering the aircraft from the runway to the taxiway. The incident caused a temporary airport closure as a result, diverting eight flights. No injuries were reported. The aircraft was towed to the gate while extensive pavement deicing operation took place.

December 17, 2013 – Dane County Regional Airport, Madison, Wisconsin (Mutzabaugh 2013)

Delta Flight 385 slid off the taxiway turnoff after landing. At the time of landing, there was 50-mm of snow on the ground and light snowfall. Visibility was down to a quarter mile. This incident occurred near the primary runway. The airport was closed for an hour while the secondary runway was cleared.

From the previous examples, the conventional pavement deicing methods are susceptible to reoccurring hazardous pavement conditions between clearance and treatment operations. Additionally, these methods are time-consuming and labor intensive.

Conventional pavement deicing in the SICP is also detrimental to the airfield infrastructure. Negative impacts of using PDPs on concrete pavements include concrete surface distresses, reinforcing steel corrosion, and aircraft landing gear corrosion (Shi 2008). Additionally, chemical deicers have been found to induce/accelerate alkali-silica reaction (ASR) in airfield pavements (Joel 2005, Rangaraju 2007, Rangaraju 2007a). Sumsion and Guthrie (2013) provide a comprehensive review on deicing salt effects on concrete pavement. Snow removal equipment (SRE) also has the potential for causing pavement damage, destroying runway edge lighting, and creating slick spots by exposing black ice (Shi 2008).

Airfield heated pavement systems (AHPS) provide an alternative solution for airside snow and ice control. AHPS heat the pavement surface to melt snow (deicing) and/or to prevent snow and ice accumulation (anti-icing). AHPS advantages include the following (FAA 2011):

1. Safety improvements for aircraft ground movements, landing, and takeoff,
2. Reduction in negative impacts caused by airside PDPs, and
3. Improvements to air traffic efficiency and safety by reducing snow clearance operations.

Implementing AHPS on active airfields has been limited. Cost (capital, maintenance, and operational) and complex system design and construction have restricted AHPS implementation at US airports. However, several research projects, like the one documented herein, are being conducted to improve pavement heating efficiency and investigate system capital and operation cost viability (Anand et al. 2017, Ceylan 2015, Ziegler 2009).

CHAPTER 2: LITERATURE REVIEW

PROBLEM STATEMENT

Snow and ice on the airfield pavement greatly intensify safety risks for aircraft ground operations. These winter contaminants have contributed to over 50 aircraft accidents/incidents from 1998 to 2004 (NASA 2004). Conventional snow and ice control practices on the airfield pavement incorporate heavy equipment for snow removal and pavement deicing products for ice melting. However, these practices have resulted in detrimental effects to the airfield pavement, aircraft landing gear, aircraft engines, and the environment (Shi 2008). In addition, these procedural methods induce flight delays (Anand et al. 2017).

STATE OF HEATED PAVEMENT SYSTEM (HPS) RESEARCH

For over 70-years, heated pavement systems (HPS) have been utilized in some form for roadway and bridge deck deicing. Researchers have studied the development, construction, operation, snow-melting performance, and cost of electrical, hydronic, and electrically conductive concrete heated pavement systems. Below is a review of notable projects.

Electrical Heated Pavement Systems

Electrical heated pavement systems (EHPS) transfer electric current through in-pavement resistive cables or meshwork to generate heat for pavement snowmelt. EHPS consist of an electric heating element, an electrical distribution network, an electrical power source and a control system. The power source depends on the heat element selection. Insulated cables operate with high voltage. Uninsulated wire or meshwork operate at low voltage and high current. The control system in the EHPS uses pavement temperature and moisture sensors for automatic on/off system operation.

Between 1956 and 1968, twenty-nine (29) EHPS projects were constructed in multiple counties across England (Williamson and Hogbin 1969). The Road Research Laboratory in Berkshire, England, assessed each system's construction, performance, and capital and operation cost. A 150-W/m^2 to 200-W/m^2 heat flux was required to maintain pavement temperature above freezing. The average unit capital cost and average unit annual operating cost were \$11.15/m^2, in 1968 dollars, and \$0.36/m^2, in 1968 dollars, respectively. In comparison to roadway chemical treatment, which costs \$0.03/m^2/year, in 1968 dollars, Williamson and Hogbin (1969) found the EHPS projects were at least 30 times more expensive.

In 1961, an EHPS construction installed copper-sheathed, mineral-insulated cable on a 3-percent graded roadway approach and bridge deck in Newark, New Jersey (Henderson 1961). The system was designed for a 378-W/m^2 heat flux for the road pavement and 430-W/m^2 heat flux for the bridge deck to prevent ice and heavy snow accumulation. The estimated capital cost, not including paving or labor, was \$24/m^2, in 1961 dollars (Henderson 1961). This installation failed due to electric cable pullout during the bituminous concrete overlay process. However, in 1964, this system design was installed on two ramps and a bridge deck in Teterboro, New Jersey with improved installation methods. Adequate snow melting performance was reported between 1964 and 1970 with the designed 378-W/m^2 to 430-W/m^2 pavement heat flux. The average annual operating cost was estimated at \$4.84/m^2, in 1970 dollars (Winters 1970).

Henderson (1961) and Williamson and Hogbin (1969) concluded that the required heavy electrical power supply made EHPS cost prohibitive for large-scale application. The issue of justifying the economics stalled EHPS projects in Kentucky, Pennsylvania, Texas, and West Virginia (Zenewitz 1977). Therefore, EHPS applications are recommended at critical roadway

locations where pedestrian and vehicle operation safety are compromised in wet wintry conditions, and chemical treatment and snow removal operation is unsuccessful.

In 2006, an EHPS was selected over standard chemical deicing application at a critical road and bridge section on Interstate 84 in Ladd Canyon, Oregon (Joerger and Martinez 2006). The 6-percent grade highway section is the site for seasonal truck accidents due to wet wintry weather conditions. Insulated heat cable installation on the 798-m^2 heated bridge deck area used a rectangular serpentine configuration. Insulated heat cable on the 8,919-m^2 heated roadway area was installed in 44-mm surface grooves cut along the wheel tracks in the 3.67-m width lane. System operation was automated using pavement temperature and moisture sensors. The 2006 construction and approximate first year operation cost were $1,354,000 and $20,000, respectively. Satisfactory snow melting performance avoided highway closure during the first year operation (Joerger and Martinez 2006).

Lai et al. (2015) studied an EHPS for anti-skid and accident prevention in the tunnel portal of the Dongnanli Tunnel, in Tumen, Jilin (China). The installed insulated heat cable covered a 400-m^2 area outside the tunnel and a 400-m^2 area inside the tunnel. The insulated heat cable was configured in a continuous serpentine layout. In seasonal air temperature below -10°C, a 200-W/m^2 to 400-W/m^2 pavement heat flux was required to develop anti-icing conditions. The system activation was dependent on detecting snowfall in the weather forecast, so that the system would provide immediate snowmelt upon snowfall. During their 2010-2011 winter field experimental program, optimal snow melting surface temperature was achieved when the system activated 4 to 6 hours prior to snowfall (Lai et al. 2015).

Other EHPS research in China has investigated carbon fiber heating wire (CFHW) to replace insulated heating cables (Zhao et al. 2010, Zhao et al. 2011, Wu et al. 2015). CFHW has high

mechanical performance and high electrothermal efficiency with an approximate 35-Ω/m resistance per length (Zhao et al. 2010). Field deicing experiments were performed at Dalian University of Technology on a 2-m x 1-m x 0.25-m concrete slab. For ease of installation, the CFHW was twisted around a reinforcing meshwork 0.04-m below the finished surface (Zhao et al 2010). With this configuration, a 500-W/m^2 heat flux melted a 40-mm snow layer in 2.5-hours in -3°C air temperature. CFHW cost approximately \$1.60/m^2, which is significantly less than its insulated cable counterpart at \$54/m^2 (Yehia and Tuan 1999, Zhao et al. 2010).

Hydronic Heated Pavement Systems

Hydronic heated pavement systems (HHPS) circulate heated fluid through a pavement-embedded pipe network to transfer heat to the pavement surface for snowmelt. HHPS consist of a radiant heating grid ("hydronic grid"), a thermal distribution system, and a heat source. To optimize system performance and reduce operation cost, researchers have investigated heat sources that deliver the required pavement heat flux at low cost. Electric and oil-fired boilers are the typical heat sources for hydronic systems. However, for the last 70-years, electric and oil-fired boilers have been replaced with renewable energy as a HHPS heat source.

In 1948, the first HHPS utilizing geothermal energy was installed on a 137-m x 15-m critical roadway section in Klamath Falls, OR (Lund 2010). Geothermal energy was accessed through a 128-m geothermal well and extracted with a Downhole Heat Exchanger (DHE). The DHE connected directly to the pavement-embedded hydronic grid consisting of 19-mm wrought iron pipe spaced at 45.7-cm, embedded 7.6-cm below the surface, and configured in serpentine loops. The pavement-geothermal system circulated 50 / 50 ethylene glycol-water solution at 189.3-liter/min. The DHE supplied fluid temperature between 38°C and 54°C. The heated fluid

produced a 129.3-W/m^2 pavement heat flux. This enabled a snow free pavement during a 7.6-cm/hr snowfall in -23°C air temperature conditions (Lund 2010).

The previously discussed Klamath Falls snow-melting performance influenced the New Jersey Department of Transportation to install their own hydronic-geothermal system. In the 1969-1970 winter season, Winters (1970) conducted an experimental study in Trenton, New Jersey. This study investigated a shallow ground source heat exchanger (GSHE) as a HHPS heat source. The GSHE connected directly to multiple 3.96-m x 3.05-m hydronic pavement test slabs and multiple wrought iron pipe diameter and spacing configurations were evaluated for snow-melting performance. Pipe diameter included 19-mm, 25.4-mm, and 31.75-mm, and pipe spacing ranged from 15.24-cm to 45.72-cm. Additionally, a hydronic grid using plastic tubing was assessed. A 12.8°C average ground temperature was recorded when the winter season began. Testing using manual system activation was conducted over five snowstorms, with air temperature between -8.9°C and 1.3°C. Winters (1970) found the concrete pavement system with the 19-mm diameter wrought iron pipe embedded 50.8-mm deep and spaced 15.24-cm apart to be optimum for pavement snowmelt. However, melting time exceeded 12-hours. The system operated for 200-hours over the testing season. During the testing period, the ground temperature decreased by 7.22°C (Winters 1970).

Winters (1970) concluded that an automated control operation system should be included in the HHPS to activate pavement heating prior to snowfall. Including an automated control operation system ensures HPS activation for immediate snowmelt at the onslaught of a snowstorm, and system deactivation when snowstorm conditions end and the pavement is clear. Additionally, the study showed that higher fluid supply temperature was needed for cost and time efficient snow-melting operation. Winters (1970) recommended recharging ground heat using solar heat

collected by the pavement during summer months. Other researchers have incorporated heat pumps within the geothermal system to raise fluid supply temperature to a designed temperature in an environmentally friendly manner (Minsk 1999, Balbay and Esen 2010). Future HHPS installations should include plastic tubing to avoid corrosion and deterioration issues characteristic to metallic piping (Lund 1999). However, plastic tubing thermal conductivity is less than metallic piping (Winters 1970). Consequently, tube spacing is reduced and supply fluid temperature should be greater than 37.78°C (Winters 1970).

Winters' (1970) findings were reflected in the Klamath Falls system reconstruction project in 1998. After 48 years of operation, the geothermal well temperature dropped significantly, and the wrought iron piping within the pavement leaked due to corrosion. Constant piping repair produced an annual maintenance cost averaging $10,000, in 1998 dollars. The geothermal well was extended from 128-m to 304.8-m. The DHE was also extended to access hotter ground temperatures. The wrought iron pipe was replaced with 19-mm cross-linked polyethylene tubing. The tubing spacing was reduced from 45.72-cm to 35.56-cm to account for the temperature drop between the fluid entering and exiting the hydronic grid. An automated control system was added during reconstruction to activate and deactivate pavement heating as a function of air and pavement temperature. The system performed adequately after reconstruction. The estimated capital cost, annual maintenance cost, and annual operational cost were $430,000, $500, and $3,000, respectively, in 1998 dollars (Lund 1999).

For long-term use as a HHPS heat source, geothermal technology must safeguard against ground heat depletion caused by extensive overconsumption (Zeigler 2009). Morita and Tago (2000) addressed this issue in the Gaia Snow-Melting System project in Ninohe, Japan. The pavement heating system was implemented on a 9-percent grade, 266-m^2 roadway section. The hydronic

grid consisted of 16-mm polybutene tubing spaced 20-cm on-center and embedded 10-cm below the surface. Three downhole coaxial heat exchangers (DCHE) were installed in 8.9-cm diameter vertical boreholes, at 150.2-m depth, to extract ground heat. The DCHEs were connected to a heat pump to raise the supply fluid to the specified design temperature. The DCHE and heat pump supplied an average 176-W/m^2 pavement heat flux. An automated operation system using pavement temperature and moisture sensors activated heating immediately after snowfall. The system maintained snow-free pavement and safe vehicle operating conditions. During the summer months, solar energy heated the pavement to temperatures between 30°C and 50°C. This energy was collected and transferred directly to the DCHE, discharging the heat back into the ground. Recharging the ground heat source resulted in a consistent 17°C ground temperature at the beginning of the four winter test seasons. This system operates year round and has an average power consumption of 28-kWh/m^2/yr. The average annual operational cost in 1998 was $800 when electricity cost was $0.11/kWh (Morita and Tago 2000).

Electrically Conductive Concrete (ECC) Heated Pavement System

In the early 1990s, the National Research Council of Canada (NRC) developed an electrically conductive concrete (ECC) for roadway deicing application (Xie et al. 1995). ECC is a cement-based composite material comprised of conventional concrete ingredients, impregnated with conductive particles and fibers for electrical and mechanical property enhancement (Xie et al. 1995, Xie and Beaudoin 1995). Using electrically conductive concrete simplifies the electrical heated pavement construction process.

The conductive components of electrically conductive concrete reduce the material's electrical resistivity from a range of 6.54 x 10^5-Ω·cm - 11.40 x 10^5-Ω·cm to less that 1000-Ω·cm (the electrical resistivity threshold for adequate pavement heating for snow melting) (Tuan 2004,

Whittington et al. 1981). Consequently, the conductive particles and fibers in ECC are the heating elements in an electrical heated pavement system. A patented electrically conductive concrete mix design using carbon fibers and coke breeze produced a 28-day electrical resistivity of 14.2-Ω·cm and a 28-day compressive strength of 43-MPa (Xie et al. 1995). Using the patented mix, Xie et al. (1995) conducted a deicing experiment on a 30.5-cm x 24.1-cm x 5.1-cm ECC mat, in -5°C to -30°C ambient temperatures. A 150-W/m^2 to 855-W/m^2 power output range maintained the mat surface temperature between 2°C and 3°C.

The ECC developments for pavement deicing by the NRC influenced a conductive concrete feasibility analysis for bridge deck deicing sponsored by the Nebraska Department of Roads. Over 50 trial batches for electrical resistivity, mechanical strength, and heating performance were tested for developing an ECC bridge deck overlay (Yehia and Tuan 1998, Yehia and Tuan 1999, Yehia et al. 2000). Yehia et al. (2000) used low-carbon steel fibers with aspect ratios between 18 and 53, and steel shavings, an industrial waste product. As a result, the concrete mix with 1.5-percent steel fibers by volume and 15 to 20-percent steel shavings by volume produced electrical resistivity between 500-Ω·cm and 1000-Ω·cm with a compressive strength between 35-MPa and 40-MPa. An average 516-W/m^2 direct current (DC) power input raised a 30.5-cm x 30.5-cm x 2.5-cm ECC mat temperature from -1.1°C to 15.6°C in 30-minutes (Yehia and Tuan 1999).

A refined mix proportion study concluded that steel fibers at 1.5-percent by volume and steel shavings at 20-percent by volume met mechanical strength requirements for a bridge deck overlay (Yehia and Tuan 2002). Heat testing found that alternating current (AC) use improved the heat generation uniformity in the ECC slab. Additionally, perforated steel plates should be used as the concrete embedded electrode to enhance concrete-electrode contact. Anti-icing and

deicing experiments were performed on a 3.6-m x 1.2-m x 0.15-m ECC overlay test slab in Lincoln, Nebraska. An average 590-W/m^2 power input generated enough heat in the ECC overlay to prevent ice and snow accumulation. In five snowstorm experiments the average unit operating cost was \$0.70/m^2, in 2002 dollars. ECC overlay preheating improved melting performance, and reduced operating cost. In comparison to conventional concrete cost at \$51.30/m^3, using steel fibers and steel shavings increased concrete cost to \$270.10/m^3, in 2002 dollars (Yehia and Tuan 2002).

Carbon and graphite products were tried instead of steel shavings in the ECC mix in the Tuan and Yehia (2004) study. Tuan and Yehia (2004) developed a mix design with 1.5-percent by volume steel fibers and 25-percent by volume carbon and graphite particles. This mix design had a 400-Ω·cm electrical resistivity, a 34.5-MPa compressive strength, and 1.65°C per minute heating rate. In 2002, the steel fiber and carbon/graphite particle mix was used for a 36-m x 8.5-m x 0.102-m ECC inlay on the Roca Spur Bridge in Roca, Nebraska (Tuan and Yehia 2004). The 0.102-m ECC inlay was divided into 52 individual 4.1-m x 1.2-m slabs. The system was powered using a three-phase, 600-V, 208-A, AC power supply from grid energy. The system was equipped with a temperature-sensing unit, a power-switching unit, a current-monitoring unit, and an operating interface unit. Thermostat operation activated slab heating when the slab temperature dropped below 1.7°C and deactivated slab heating when the slab temperature rose above 12.8°C. In four snowstorms, the bridge deck maintained a snow-free condition with an average 452-W/m^2 power output. Energy consumption per snowstorm averaged 3,200-kWh, 58-kWh per slab, and cost \$260, in 2002 dollars. The total construction cost for the ECC deicing system was approximately \$195,000, in 2002 dollars. The unit cost for this system in 2002 was \$635/m^2 (Tuan and Yehia 2004).

Gains have been made to improve concrete conductivity through mix designs incorporating steel fibers, carbon fibers, nano-carbon based powders and fibers, nickel fibers and graphite products (Tuan 2004, Tang et al. 2005, Zhang et al. 2011). Steel fibers, in particular, increase concrete's thermal energy storage and absorption capacity (Chanh 2004, Htun et al. 2014). Effective use of these materials is important economically. The use of 1-percent of steel fibers in a concrete mix approximately doubles the concrete material cost (Chanh 2004). Consequently, mixing procedures are under investigation to uniformly disperse conductive materials in the concrete mix (Gopalakrishnan et al. 2017).

STATE OF AIRFIELD HEATED PAVEMENT SYSTEM (AHPS) RESEARCH

The viability for heating airfield pavements has been investigated for over 50-years. Electrical, hydronic, and electrically conductive concrete pavement heating studies have assessed snowmelt performance, cost, and economic justification for system implementation. Preliminary research concentrated on HPS runway implementation to improve safety for aircraft landing and takeoff activities while mitigating snow removal equipment use so to maintain on-time flight operations (Pravda et al. 1975).

Electrical Cable AHPS

In a 1975 FAA funded project, Pravda et al. (1975) conducted a HPS study at Chicago's O'Hare International Airport. This study compared the potential for implementing an electrical heated pavement system, a solar-heat pipe heated pavement system, and an oil-fired steam heat pipe heated pavement system for a 139,354-m^2 runway area and 5,574-m^2 ramp pavement area. The designed surface heat flux requirement at O'Hare International Airport in the 1970s was 404-W/m^2. The electrical heated pavement system design consisted of a high voltage substation, high voltage underground cables, electrical heating cables, and pavement runoff drainage trenches.

For the pavement heating system design, a single heat cable covered a 750-m^2 surface area in a serpentine configuration with 10.16-cm cable spacing positioned 76.2-mm below the surface. System activation was forecast dependent, meaning the pavement was preheated under anticipated snowfall. Results from this economic analysis are summarized in Table 1. Table 1 includes the capital, total annual, and annual operating cost for the runway area and ramp area (Pravda et al. 1975).

Table 1: Cost Breakdown of Each Pavement Heating System per Airfield Pavement Area

Pavement Location	Electrical Heated Pavement System	Solar Heated Pavement System	Steam Heated Pavement System
Capital Cost, USD in 1975 (*Capital Cost, USD in 2018*)			
Runway	8,092,000 (*37,8411,380*)	8,772,700 (*41,024,602*)	5,901,065 (*27,595,705*)
Ramp	500,440 (*2,340,254*)	696,231 (*3,255,850*)	662,200 (*3,096,708*)
Total Annual Cost, USD in 1975 (*Total Annual Cost, USD in 2018*)			
Runway	1,498,358 (*7,006,912*)	741,816 (*3,469,024*)	630,685 (*2,949,331*)
Ramp	83,296 (*389,525*)	74,333 (*347,610*)	86,112 (*402,693*)
Annual Operating Cost, USD in 1975 (*Annual Operating Cost, USD in 2018*)			
Runway	850,998 (*3,979,602*)	40,000 (*187,056*)	158,600 (*741,676*)
Ramp	43,242 (*202,216*)	20,000 (*93,528*)	33,136 (*154,957*)

Note: Values in table are directly from Pravda (1975) and converted to USD value in 2018. The cost categories are defined as follows: 1) Capital Cost – pertains to system materials, equipment, and initial expenses; 2) Annual Operating Cost – cost pertains to system operation, maintenance, materials, and labor; 3) Total Annual Cost – pertains to "Annual Operating Cost" including depreciation and interest rates.

Limited electrical AHPS studies have been conducted since the Pravda et al. (1975) study. Laboratory electrical AHPS studies in China are currently under investigation, focusing on heating and snow melting performance, and heat generation optimization (Lai et al. 2014). Lai et al. (2014) tested a 4.6-m x 4.6-m x 0.4-m outdoor airport simulated pavement with embedded carbon fiber heat wires. Testing was performed in Beijing, China during five snowstorms. Their results found that a pavement heat flux between 250-W/m^2 to 400-W/m^2 is capable of melting up to 12-mm of snow within 2 to 4-hours (Lai et al. 2014). In a literature review, this author found no electrical AHPS implemented at an active airfield.

Hydronic AHPS

The solar-heat pipe heated pavement system design, in the Pravda et al. (1975) study mentioned above, consisted of heat pipes, gravity-assisted heat-pipe flat plate collectors, an underground storage tank, and circulation pumps. As an exhaustible energy source, the solar collector area and storage tank volume were sized to meet the specified surface heat flux and the annual energy demand (Pravda et al. 1975). Results from this economic analysis are also summarized in Table 1. Pravda et al. (1975) recommended using the solar AHPS on priority pavement areas (i.e. runways, high-speed turnoffs, taxiways, aprons) at medium capacity airports located in moderate winter climate areas. The Pravda et al. recommendations were supported by (1) a lower annual operating cost in relation to the electrical and oil-fired steam system, (2) a constant annual operating cost, and (3) technological advances that would be made in solar energy systems, which would continue to improve system performance (Pravda 1975).

In 2002, Zwarycz (2002) proposed designs for a hydronic system using geothermal energy for the 150,000-m^2 runway at Goleniow Airport in Szczecin, Poland. A geothermal heat exchanger connected directly to a heat pump was designed to extract ground heat between 40°C and 60°C to use for airfield pavement deicing and airport terminal heating. The designed pavement heat flux was 200-W/m^2. The calculated annual operational cost for the hydronic system was estimated at $195,000, in 2002 dollars (Zwarycz 2002).

Electrically Conductive Concrete AHPS

In the 1990's, at Chicago's O'Hare International Airport a patented graphite modified electrically conductive asphalt pavement system was installed on an in-service taxiway (Derwin et al. 2003). A 2.5-hour pre-heat time, with an average power input of 484-W/m^2, was required to produce pavement anti-icing conditions. Installing the electrically conductive asphalt system

was estimated at \$161/m^2 with an approximate \$2,400 per hour operation cost, in 1994 dollars, to heat a 3,048-m runway.

In 2011, Heymsfield et al. (2012) developed a conductive concrete overlay for an airfield runway anti-icing system using solar energy. The mixture design contained 17.2-percent graphite powder by volume and 2.7-percent steel fiber by volume. The concrete mixture had a compressive strength of 42.4-MPa and an electrical resistivity of 396-Ω·cm. Continual energy from a photovoltaic energy system was used to supply outdoor test slabs in Fayetteville, Arkansas. Study results found that a high-energy input was required to sustain an above-freezing pavement surface temperature. Additionally, the study found a non-uniform temperature distribution at the pavement surface (Heymsfield et al. 2012).

AIRFIELD HEATED PAVEMENT / SNOW AND ICE CONTROL COMPATIBILITY

Large capital and operational costs have made AHPS for the runway cost prohibitive (Zeigler 2009). Consequently, AHPS should be implemented at strategic airside locations that will cost effectively improve aircraft and personnel safety, enhance pavement deicing efficiency, reduce winter season flight delays, and optimize snow and ice control operations (Ceylan 2015; and T. Seely, personal communication, Oct. 11, 2017). Studies in collaboration with airport operators and snow and ice control personnel suggest that an AHPS is most beneficially located in the apron area, specifically on aircraft-parking stands (APS) where snow and ice removal practices are conducted by hand, Figure 1, or with light equipment (Anand et al. 2017, Ceylan 2015, Ziegler 2009).

Figure 1: Aircraft parking stand snow removal at Northwest Arkansas Regional Airport.

The APS is a heavily foot and vehicle trafficked area with aircraft refueling operations, luggage handling, aircraft waste disposal operations, aircraft catering restocking, etc., Figure 2(a) (Anand et al. 2017). Snow and ice in this area, Figure 2(b), reduce operation speed and increase the risk of personal injury.

(a) (b)

Figure 2: Aircraft parking stand (a) with normal operation and (b) with layer of snow.

Additionally, snow and ice in the APS affect aircraft pushback operations. Slippery pavement conditions can cause traction issues for the airplane tug, in Figure 3, and increase gate delays (T. Seely, personal communication, Oct. 11, 2017). Thus, current research focuses locating the AHPS in the apron area and using the AHPS as a complement to the conventional SICP.

Figure 3: Airplane tug location in aircraft parking stand.

Electrically conductive concrete research work for the airfield apron area is currently being advanced at Iowa State University (ISU) through the FAA Air Transportation Center of Excellence Partnership to Enhance General Aviation Safety, Accessibility and Sustainability (PEGASAS) program. ISU researchers have developed a conductive concrete mix design using synthetic carbon fiber and a fiber-dispersing agent. The mix design is used to develop a HPS capable of melting 25.4-mm of snow in approximately 35-minutes (Abdualla 2016). Installation and performance testing using the mix design was conducted on an apron area at Des Moines International Airport. Initial testing maintained a "no more than wet" surface with a power density of 333-W/m^2 and operation cost of \$0.19/m^2, in 2017 dollars, utilizing grid energy (Iowa State University 2017). ISU has proposed using precast panels in the pavement construction process to ensure quality control while increasing pavement and heating performance (Abdualla 2016).

Conversely, hydronic heated pavement systems (HHPS) are the major HPS type used for airfield apron area applications (Anand et al. 2017, Ceylan 2015, Kopec 2015). A Binghamton University (New York, U.S.) research team designed a hydronic-geothermal system utilizing a horizontal closed-looped system and a geothermal heat pump (Ziegler 2009). The hydronic-geothermal system design was constructed and operated on a 372-m^2 APS at Greater

Binghamton Airport. The heated area remained clear of snow and ice accumulation during the first year of system operation. Construction and annual operation cost were $1,300,000 and $15,000, respectively, in 2015 dollars (Kopec 2015).

Internationally, two European airports have implemented hydronic-geothermal systems that are currently in use. Stockholm-Arlanda Airport, in Sweden, uses HHPS on 54 APS. Each parking stand consists of approximately 1,700-m^2 pavement area (Anand et al. 2017). Oslo Airport, in Gardermoen, Norway, uses HHPS on 35 APS, each covering approximately a 700-m^2 pavement area (Anand et al. 2017). Construction and annual operating cost for each parking stand is $325,000 and $16,500, respectively. According to the Oslo Airport's operations team, AHPS in aircraft parking stands are preferred for enhanced safety conditions and reduced gate area delays (Anand et al. 2017).

Airports are currently embracing incorporating solar energy systems to provide a large percentage of their terminal building energy needs. However, except for Heymsfield et al. (2012), no studies have explored using solar energy technology as an AHPS power source at the apron area. Hawaii's Honolulu Airport is currently installing 4,260 new solar panels in 2018 with the goal of 100-percent clean energy generation by 2045 (Frangoul 2018). Cold region airports, like Minneapolis-St. Paul International Airport, have installed solar panels in proximity to the airport's terminal building and apron area (Pickerel 2016). Airport's solar infrastructure proximity to the airfield's apron area warrants the investigation of solar powered AHPS in the apron area. Consequently, this dissertation analyzes the development and assesses the viability of incorporating a solar power AHPS for implementation at the airport apron area.

CHAPTER 3: FIELD EXPERIMENTATION METHODOLOGY

OVERVIEW

An electrical heated pavement system and hydronic heated pavement system are investigated incorporating renewable solar energy technology suited for electrical energy generation and fluid heat exchange. Field experimentation is conducted at the University of Arkansas's (UA) Engineering Research Center (ENRC) at an existing 19.8-m x 19.8-m secure outdoor testing facility. This chapter details the solar electrical heated pavement system (solar-EHPS) and solar hydronic heated pavement system (solar-HHPS) construction, instrumentation, and operation. It also outlines the experimental program during winter season testing.

OUTDOOR TEST FACILITY DESIGN

The experimental test setup for the electric heated pavement system approach and the hydronic heated pavement system approach is described in the following sections.

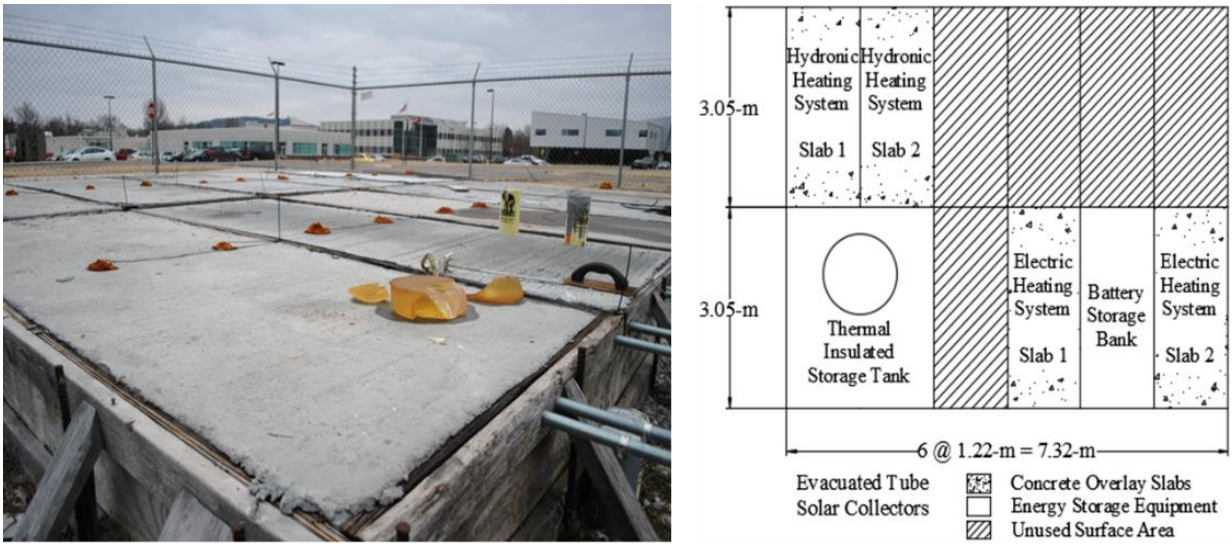

(a) (b)

Figure 4: (a) existing test platform surface and (b) test layout diagram, aerial view.

The outdoor concrete overlay test slabs lay on an existing 7.3-m x 6.1-m experimental platform from an earlier Heymsfield et al. (2012) study, Figure 4(a). Figure 4(b) shows the slab and

energy equipment layout for both heated pavement systems. The overlay for the hydronic system is 12.7-cm thick to accommodate the embedded tube concrete cover requirement (50.8-mm). The overlay for the electric system is 10.2-cm thick, Figure 5. The pavement has a 1.5-percent slope to provide for adequate surface drainage.

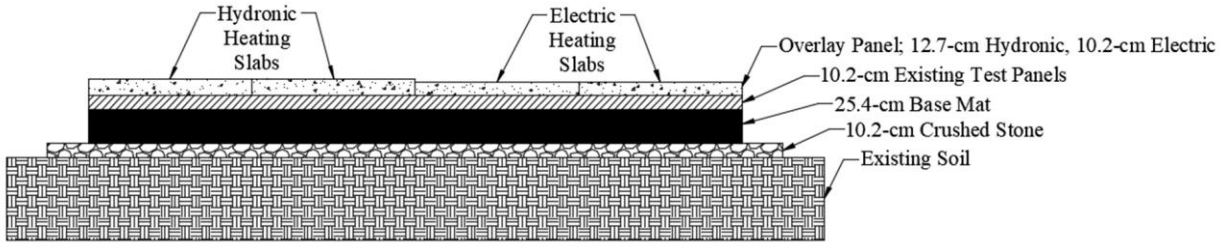

Figure 5: Experimental test setup, elevation view.

All concrete used for laboratory and field experimentation was developed using the Northwest Arkansas Regional (XNA) Airport's Runway 16/34 reconstruction mixture design. Table 2 details the reconstruction mix design.

Table 2: Northwest Arkansas Regional Airport Runway 16/34 Reconstruction Mixture Design

Materials	Type	Content	Volume (%)
Cement	Ashgrove Cement	237.3 kg/m^3	7.5
Fly Ash	Headwaters Type F	59.3 kg/m^3	2.4
Course Aggregate	APAC Limestone	1122.5 kg/m^3	43.0
Fine Aggregate	APAC Sand	741.6 kg/m^3	28.9
Water	Tap Water	121.6 kg/m^3	12.2
Air	Air	n/a	6.0
Water-Reducing Admixture	BASF: Pozzolith 700N	4.0 fl oz/cwt	n/a
Air-Entraining Admixture	BASF: MB-AE 90	3.0 fl oz/cwt	n/a

Laboratory testing was performed on XNA's reconstruction mix design to confirm airfield pavement design specification were met (ACPA 2002, FAA 2014b, Packard 1995). Table 3 details the concrete ingredients for laboratory testing. Nine trial batches were tested for slump, air content, and compressive strength, following procedures in ASTM C143, ASTM C231, and ASTM C39, respectively. Concrete slump specification for pavement is greater than 2.54-cm and less than 7.62-cm. Concrete pavement susceptible to severe conditions and chemical

deicers, with 19-mm aggregate, requires a 5-percent to 8-percent air content. Airport pavement design is based on flexural strength with a desired modulus of rupture between 4.13-MPa and 4.83-MPa. According to Packard (1995), compressive strength testing can be converted to an approximate flexural strength using Eq. 1;

$$MR = K\sqrt{f'c} \quad (1)$$

where MR is the modulus of rupture (flexural strength, MPa), K is a constant between 8 and 10, and f'c is compressive strength.

Table 3: Laboratory Mixture Design Components

Materials	Type	Specification
Cement	Ashgrove Cement Type I/II	ASTM C 150
Fly Ash	Dolet Hills Class F	ASTM C 618
Course Aggregate	Limestone (19-mm)	ASTM C 33
Fine Aggregate	Arkansas River Sand	ASTM C 33
Water	Tap Water	
Air	Air	
Water-Reducing Admixture	ADVA® Cast 575	ASTM C 494
Air-Entraining Admixture	TERAPAVE® AEA	ASTM C 260

Table 4 shows each trial mix batch. The chemical admixtures varied for each trial mix batch. Trial mix 9, in Table 5, was selected to produce test slab specimens. All three test criteria were met for trial mix 9. The increase in slump from trial mix 8 to trial mix 9 provided ease of concrete placement.

Table 4: Laboratory Trial Mix Batches

Mix	Batch Size	Cement	Fly Ash	Course	Fine	Water	AEA		HRWR	
	m^3	kg	kg	kg	kg	kg	fl oz/cwt	mL	fl oz/cwt	mL
1	0.0286	6.76	1.68	32.4	22.1	2.54	1.5	8.3	3.0	16.5
2	0.0286	6.76	1.68	32.4	22.1	2.54	1.1	6.1	3.5	19.3
3	0.0286	6.76	1.68	31.8	22.7	2.49	1.1	6.1	3.5	19.3
4	0.0286	6.76	1.68	31.7	22.2	3.08	1.0	5.5	3.3	18.2
5	0.0439	10.39	2.59	49.3	35.1	3.31	1.0	8.5	4.0	33.9
6	0.0399	9.48	2.36	44.6	31.1	4.35	1.0	7.7	4.0	30.9
7	0.0399	9.48	2.36	44.3	30.9	4.81	1.0	7.7	3.5	27.1
8	0.0399	9.48	2.36	44.6	31.4	4.04	0.8	6.2	3.7	28.6
9	0.0399	9.48	2.36	44.6	31.5	3.90	0.8	5.8	3.9	30.2

Table 5: Laboratory Trial Batch Test Results

Mix	Un. Wt. kg/m^3	f'c (28 Days) MPa	MR (conversion) MPa	Slump cm	Air Content %
1	2266.3	36.7	4.52	3.81	7.4
2	2338.7	46.4	5.09	0.00	5.0
3	2223.4	29.0	4.03	6.35	9.0
4	2311.8	38.3	4.62	4.44	7.2
5	2292.6	32.5	4.26	6.98	7.2
6	2209.3	28.9	4.02	13.3	11.0
7	2313.1	33.9	4.35	4.44	7.6
8	2304.1	36.4	4.51	5.08	6.8
9	2313.1	38.5	4.64	6.35	6.6

SNOW-MELTING HEAT FLUX REQUIREMENT

Pavement heating requirements are determined using the ASHRAE 2011 Fundamentals Handbook as specified in FAA AC 150/5370-17 (ASHRAE 2011, FAA 2011). Eq. 2 is the steady-state energy balance equation used for determining the snow melting surface heat flux (ASHRAE 2011):

$$q_o = q_s + q_m + A_r(q_h + q_e) \quad (2)$$

where, q_o is the snow-melting surface heat flux (W/m^2), q_s is the sensible heat flux (W/m^2), q_m is the latent heat flux (W/m^2), q_h is the convective and radiative heat flux for a snow-free surface (W/m^2), q_e is the evaporation heat flux (W/m^2), and A_r is the snow-free area ratio, dimensionless. Each variable in Eq. (2) is determined by empirical relationships included in Chapter 51 of ASHRAE (2011) as a function of air temperature (°C), wind speed (meters/second), dew point (°C), and rate of snowfall (cm/hr). The heating demand for the airfield pavement is designed to meet a "no more than wet" condition.

SOLAR – ELECTRICAL HEATED PAVEMENT SYSTEM APPROACH

Overview

The current state of practice for electrical-based heating systems uses grid energy. With the need to reduce operation cost to increase the viability of AHPS, Heymsfield et al. (2012) developed a

conductive concrete overlay powered by a photovoltaic energy system (PVES). Continual energy from the PVES supplied energy to outdoor conductive concrete test slabs. The study showed non-uniform heat distribution and high-energy input requirements to sustain an above-freezing ("anti-icing") pavement surface temperature. The high-energy is prohibitive for developing an anti-icing pavement system that incorporates solar energy; therefore, alternative approaches were investigated to reduce energy demands.

Figure 6: Surface heating trial with copper wire from Heymsfield et al. (2012) study.

To optimize PVES use for an AHPS, Heymsfield et al. (2012) proposed using near-surface embedded heat wires, Figure 6, to achieve the following goals: (1) reduce energy requirements by concentrating heat transfer to the pavement surface, and (2) using an anti-icing heating scheme to control energy output. Therefore, a preliminary near-surface heating grid prototype study, addressed herein, was investigated for concrete slab heating performance and the corresponding energy requirements.

Preliminary Study

Laboratory Study

A preliminary proof-of-concept study investigated an electrical near-surface pavement heating prototype to (1) optimize pavement heat transfer at the surface and (2) evaluate initial energy requirements. The prototype was evaluated through heating performance and respective energy flux. A small-scale concrete prototype was constructed and tested in a controlled temperature environment to assess optimal near-surface heat wire spacing, heating performance, and heat

distribution as a function of embedded wire depth. Outdoor prototype testing was performed on a large-scale concrete slab to analyze temperature uniformity at the slab surface considering Fayetteville, Arkansas winter conditions. Ice testing was conducted to evaluate system heating response. For power supply, voltage inputs simulated deep-cycle batteries in a storage bank connected in series for an anticipated future incorporation of a photovoltaic energy system. The results from this study aided in further electrical system development, incentivizing the use of a photovoltaic energy system as an AHPS power source.

Prototype Construction and Setup

A near-surface electrical heat wire unit was installed on four, 610-mm x 305-mm x 76-mm thick test mats, using the Northwest Arkansas Regional Airport Runway 16/34 mix design. Each test mat was cast in formwork from a single batch and left outdoors for a 7-day cure (at approximately 27°C), Figure 7(a,b).

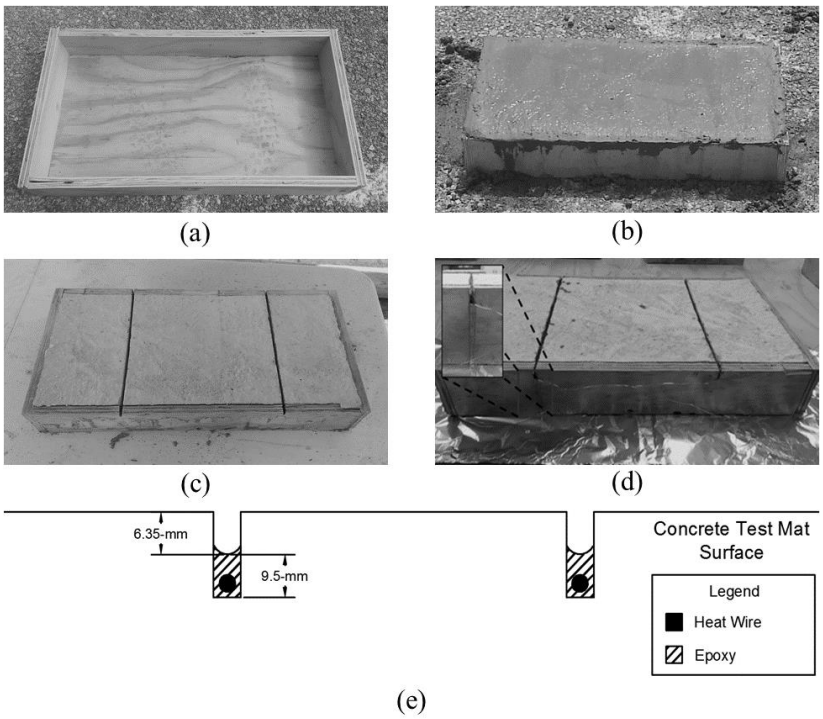

Figure 7: Construction of concrete test mats; (a) plywood formwork, (b) casting test mat, (c) grooves cut in test mat surface, (d) placement of heat wire and epoxy, (e) diagram of surface embedded heat wire.

Heat wire placement and installation takes advantage of airfield pavement grooving, which exists to provide a skid-resistant Portland cement concrete (PCC) surface. The FAA specifies pavement grooving on PCC using a plastic or saw cut grooving technique (FAA 1997). Plastic grooving is most effective, especially at large-scale construction sites, and conducted when the pavement is in its plastic state. Saw cutting is performed on hardened concrete and becomes more difficult as the concrete ages (FAA 1997). For testing purposes discussed in this dissertation, the saw cutting method was selected.

Grooves were saw cut on the test mat surface 16-mm deep and 3-mm wide, relative to FAA pavement grooving specifications, which requires a 6-mm groove depth and 6-mm groove width (FAA 1997), Figure 7(c). Using a thinner groove width than the FAA specifications improves thermal contact between the heating element and concrete. In addition, the groove depth was increased from the 6-mm FAA specified groove depth to 16-mm to provide space for the heat element and placing the sealant material.

A continuous nickel-chromium (NiCr-80/20) alloy heat resistant wire was used as the electrical heat element. NiCr-80/20 serves a variety of functions in electrical heating and was selected in this study for its rapid heating reliability, capability to heat to high temperatures, corrosion resistance, and market availability. The NiCr-80/20 gage wire used has a resistance of 2.08-Ω/m. Once the grooves were cleaned of debris, the NiCr-80/20 was placed and sealed with an epoxy resin binder, Figure 7(d). The epoxy provided a layer of corrosion protection and consistent thermal contact for the test mat-heat wire interface. The epoxy in-groove height was approximately 9.5-mm with a corresponding pavement surface to epoxy surface of 6.35-mm. The final groove depth of 6.35-mm satisfies the FAA specifications, Figure 7(e) (FAA1997).

The experiments analyzed concrete heat performance using a data acquisition system (DAQ) and Volteq adjustable direct current (DC) power supply. Type T thermocouples monitored concrete surface and internal temperature distribution. Details of their placement on/within the test mats are given in the next sections. Temperature values were recorded and saved for data processing and analysis. Heat performance tests were conducted in a 141.5-cm x 75-cm x 82.5-cm freezer chest at approximately -14°C to create a severe temperature testing environment.

Constant power was supplied to the near-surface heat wire unit. The use of DC voltage (VDC) control at 12-volt increments replicates the usage of fixed battery storage banks corresponding to future implementation of a photovoltaic energy system as a power source.

Slab Surface Temperature Distribution as a Function of Wire Spacing

This investigation assessed optimizing wire spacing through a surface temperature distribution analysis. Four wire spacing intervals were tested; 100-mm, 150-mm, 200-mm, and 300-mm on Test Mat 1 (TM1), Test Mat 2 (TM2), Test Mat 3 (TM3), and Test Mat 4 (TM4), respectively, Figure 8. The wire length on each test mat was 114.3-cm. The centerline of the groove spacing aligned with the test mat's long-dimension centerline. The power supply and embedded heat wire were connected in series.

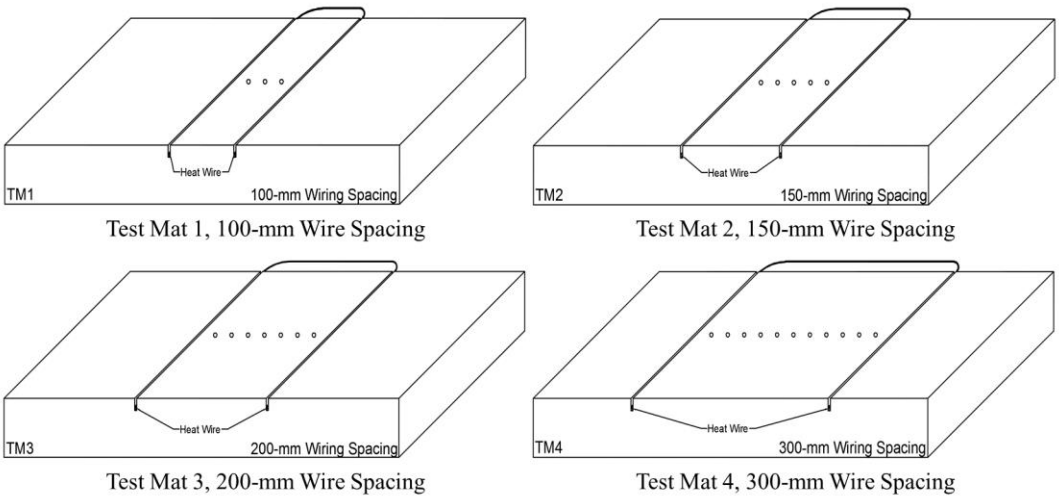

Figure 8: Concrete test mats with various wire spacing for wire interval investigation.

Testing was performed at lab-room temperature for 80-minutes. A constant 12-VDC was supplied to the near-surface NiCr-80/20 wire. Surface temperature was measured between adjacent grooves at 25-mm intervals. Figure 9 temperatures represent the temperature reading mid-distance from adjacent grooves and the averages of readings taken at 25-mm spacing intervals inward from each groove.

Figure 9 shows the surface heating time-temperature curve. Optimal wire spacing is a function of developing a uniform temperature distribution along the slab surface. Researchers (Zhao et al. 2010, Yang 2011, Lai et al. 2014) have defined slab surface uniform temperature distribution for adequate anti-icing and deicing by a transient and steady-state temperature difference no greater than 3°C. For this 80-minute heat test, the temperature difference from the hottest surface location to the coldest location is given in column 4 of Table 6. Consequently, a 100-mm to 150-mm wire spacing range is optimal, TM1 and TM2 (Figure 9(a, b)).

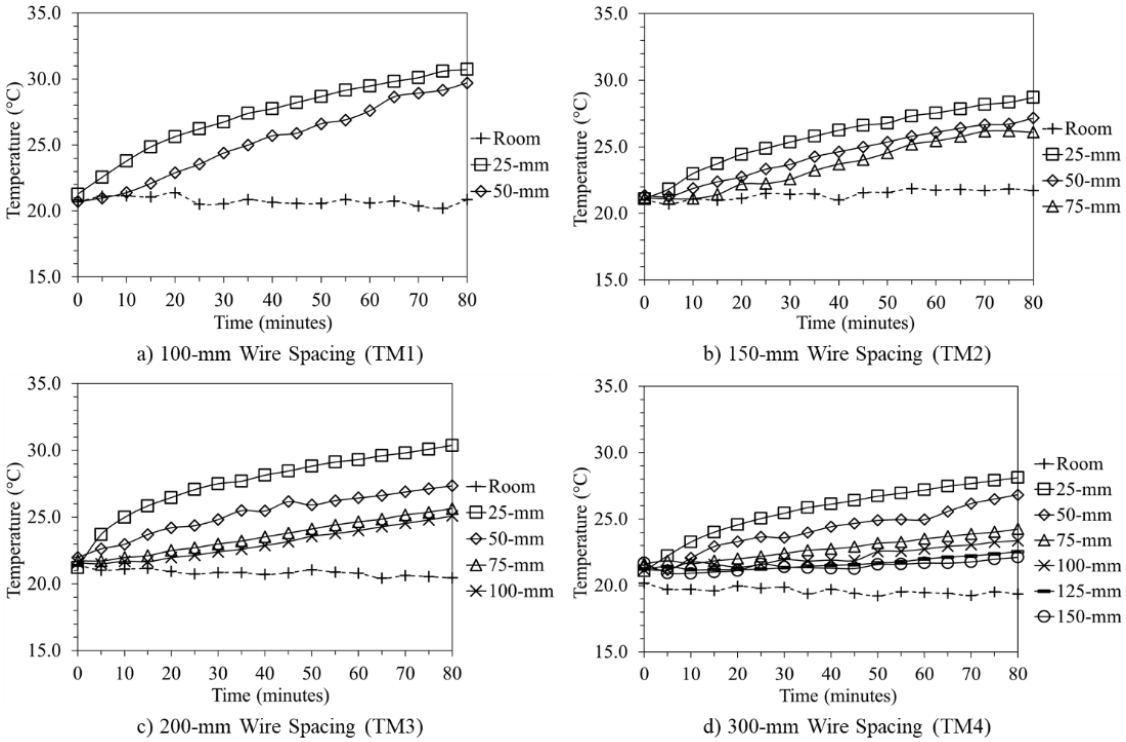

Figure 9: Comparison of surface temperature rise during 80-minute heat test for (a) 100-mm, (b) 150-mm, (c) 200-mm, and (d) 300-mm wire spacing.

As the wire spacing increased, the mid-distance temperature gradient decreased, Table 6. This behavior will result in cold spots susceptible to snow/ice striping.

Table 6: Temperature Gradients and Degree of Temperature Uniformity per Wire Spacing Interval

Concrete Test Mat	Wire Spacing (mm)	Temp. Gradient Mid-distance between wire loop (°C/80-min.)	Temperature Difference between Center Thermocouple and 25-mm Thermocouple (°C)
TM1	100	8.95	1.02
TM2	150	4.91	2.61
TM3	200	3.52	5.28
TM4	300	1.20	6.00

Heat Testing Performance

Further testing on TM1 and TM2 evaluated the heating performance of the 100-mm and 150-mm serpentine wire spacing configuration. Additional surface grooves were saw cut outside the existing grooves on TM1 and TM2 as shown in Figure 10. A continuous 187-cm length of NiCr-80/20 wire was placed in the four grooves in a serpentine 3-loop configuration. Epoxy sealed the wires using the previously discussed procedures. Figure 10 shows the thermocouple alignment on the mat surface at 25-mm intervals. Internal mat temperature distribution was measured at 25-mm, 37.5-mm, 50-mm, and 63.5-mm depths directly underneath the heat wire and in plane with the surface thermocouples, Figure 10. TM1 and TM2 were placed in the freezer chest 24-hours prior to testing to obtain a steady state temperature. The test mats, in the freezing temperature condition, were supplied with 12-VDC and 24-VDC inputs.

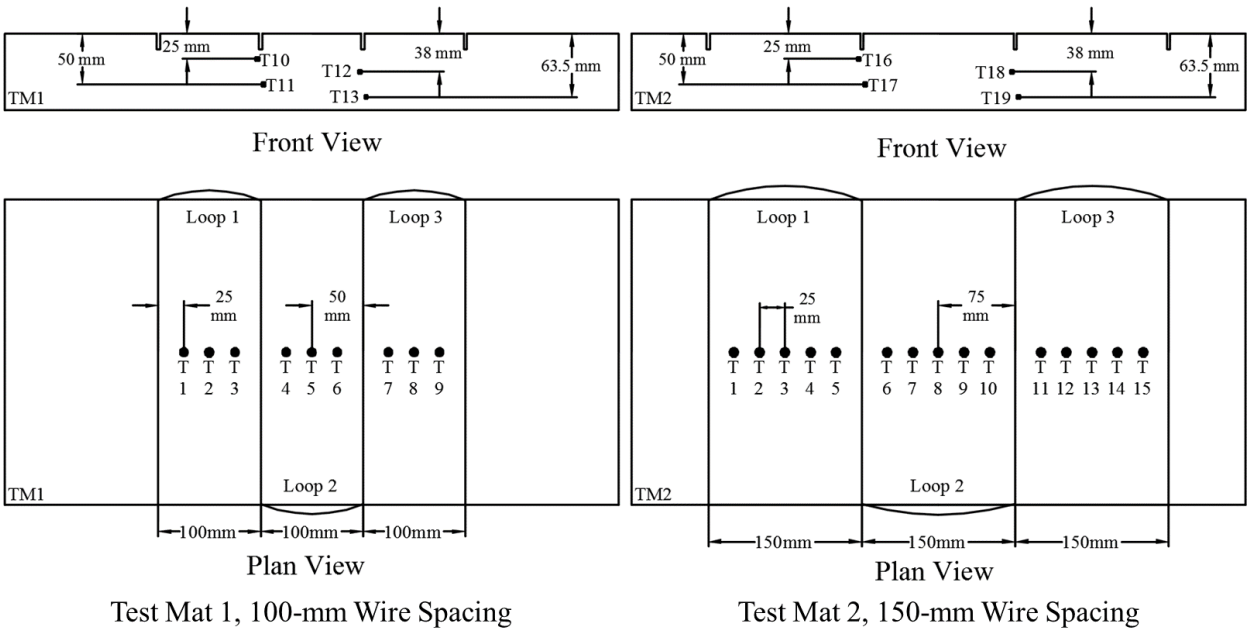

Figure 10: Concrete test mat thermocouple layout for surface and in-slab temperature distribution analysis.

Slab Temperature Distribution as a Function of Input Power

This experiment measured the behavior of surface heat distribution in controlled subfreezing temperature conditions. The freezer chest temperature oscillated as part of its cooling cycle Figure 11. The freezer lid remained closed during testing to ensure constant freezer ambient conditions.

Surface temperature curves in Figure 11 superimpose mid-loop surface temperature readings for TM1 and TM2 shown in Figure 10 *Plan View*. T2-Loop 1, T5-Loop 2, T8-Loop 3 are the mid-loop surface temperature reading locations for TM1. T3-Loop 1, T8-Loop 2, T13-Loop 3 are the mid-loop surface temperature reading locations for TM2. The initial testing surface temperature ranged between -12°C and -10°C. Uniform temperature rise between each loop was noted for both voltage inputs, Figure 11. Heating with a 12-VDC input produced an average 6.5°C and 5.3°C temperature increase for TM1 and TM2, respectively, over a 6-hour testing period.

Continued testing saw gradual heat gain though the 12-VDC voltage supply case did not adequately increase the temperature to melting (0°C).

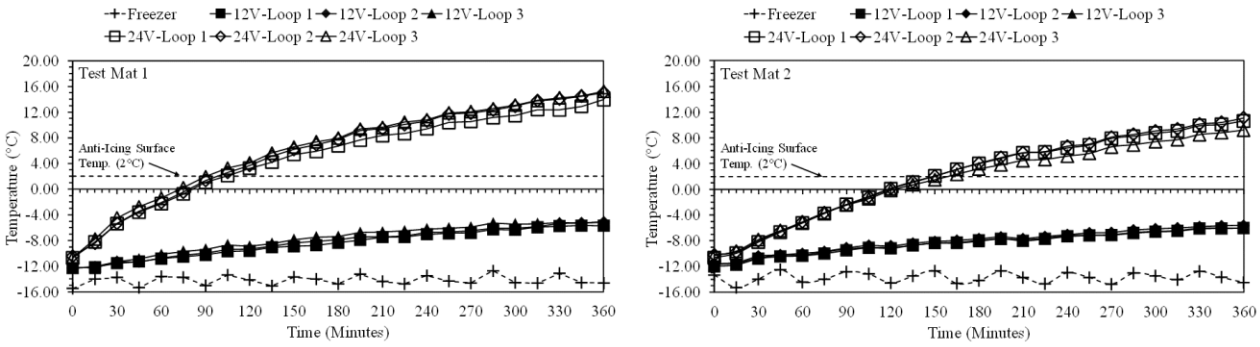

Figure 11: Surface temperature distribution during heat test on TM1 (left) and TM2 (right) in a freezing temperature environment (approximately -14°C) using 12-VDC and 24-VDC voltage input.

Heat rise with 24-VDC reached and exceeded 0°C in 80-minutes and 110-minutes for TM1 and TM2, respectively, and the anti-icing surface temperature threshold (2°C) in 95-minutes and 150 minutes for TM1 and TM2, respectively. Heating past the melting point yielded a semi-linear temperature rise at a rate of 0.054°C/minute and 0.044°C/minute for TM1 and TM2, respectively. After 6-hours of heating, with 24-VDC, the average mid-loop surface temperature rise exceeded 20°C for both test mats. The DAQ recorded continuous temperature increase for an additional 3-hours. For both voltage inputs, the temperature difference between each loop in the test mats was less than 1°C.

An internal heat rise investigation correlated the slab internal temperature rise with the surface temperature distribution. As a preliminary proof-of-concept work, thermal stress and temperature gradient effects on concrete material behavior were not analyzed. Internal temperature was measured for a depth of 25-mm to 63.5-mm at 13.5-mm intervals as shown in Figure 10 *Front View*.

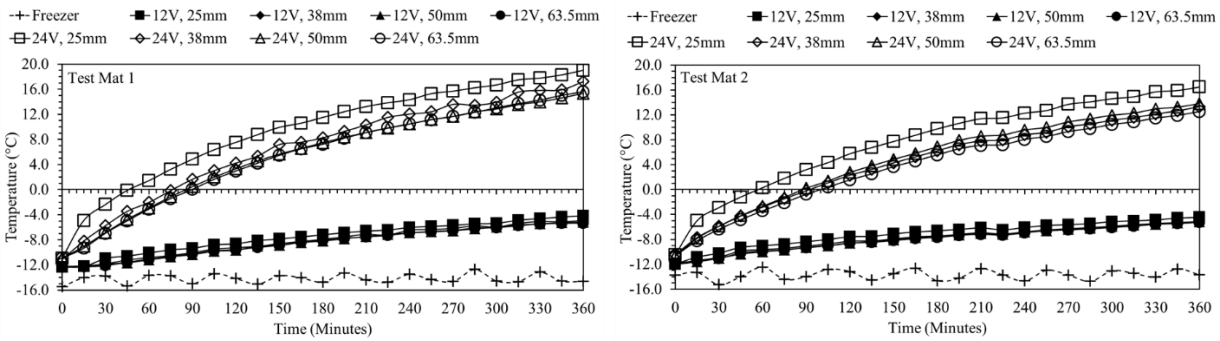

Figure 12: Internal temperature distribution during heat test on TM1 (left) and TM2 (right) in a freezing temperature environment (approximately -14°C) using 12-VDC and 24-VDC voltage inputs.

Temperature as a function of depth is shown in Figure 12. A steady, 6-hour temperature rise produced an average 6.6°C and 6.0°C increase for TM1 and TM2, respectively, with a 12-VDC input. Likewise, an average 24.0°C and 21.0°C temperature rise resulted for TM1 and TM2, respectively, with a 24-VDC input. Figure 12 shows greatest temperature rise at a 25-mm depth with the 12-VDC and 24-VDC inputs. The 24-VDC input shows a larger temperature variation between the 25-mm deep temperature reading and the temperature readings below the 38.5-mm depth. Minimal temperature variation occurred between depths greater than 38.5-mm. The test mat heating rate along the surface and internally was similar.

Slab Surface Temperature Distribution as a Function of Wire Depth

This experiment studied surface heating performance as a function of heat wire depth. Figure 13 depicts the testing configuration. Two, 450-mm NiCr-80/20 heat wires were tightly twisted, and embedded directly in the concrete. Mat 1 had a 15.875-mm wire embedment depth and Mat 2 had a 50-mm wire embedment depth. The twisted NiCr-80/20's approximate resistance was 1.04-Ω/m. Each concrete mat was insulated on all except the top surface during the heat tests to reduce side and bottom heat loss. Thermocouples measured the surface temperature distribution over the embedded wire (centerline, CL) and at 25-mm intervals perpendicular to the centerline on the surface, Figure 13.

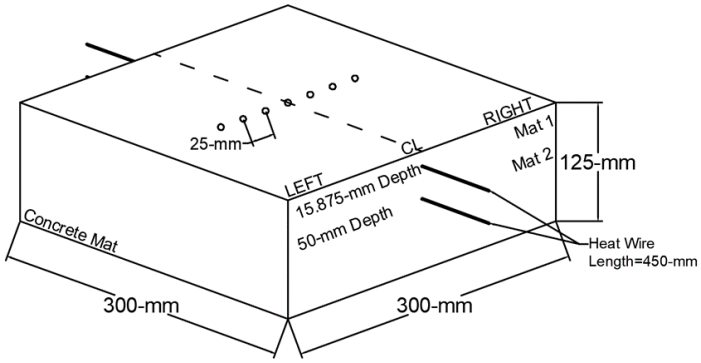

Figure 13: Test mat diagram for surface temperature distribution as a function of wire embedment depth analysis.

Heat tests were conducted at room temperature with a 27°C average initial surface temperature. Three electric current inputs were supplied to the twisted NiCr-80/20 wire for 6-hours, generating a concrete energy flux input of 372.86-W/m^2, 467.91-W/m^2, and 584.48-W/m^2. Figure 14(left) shows the surface temperature distribution at 6-hours on Mat 1 and Mat 2 for each electric current input. Temperature distribution on Mat 1 was higher than Mat 2 at all locations and electric current inputs. An increase in electric current increased the temperature at all locations while the shape of the temperature distribution curve remained consistent. Figure 14(right) shows that the heat wire/cable embedded directly in the concrete has a radial heat transfer distribution. Thus, a near-surface heat wire will exhibit a significant temperature difference across the slab surface from CL to 75-mm away from the CL. This is in contrast to the results found in Figure 9 where the distribution was uniform. It can be concluded that wire installation in a thin groove sealed with epoxy creates a composite, which changes the heat source geometry. Thus, wire installation in a thin groove sealed with epoxy promotes heat conduction in the lateral direction, Figure 14(right).

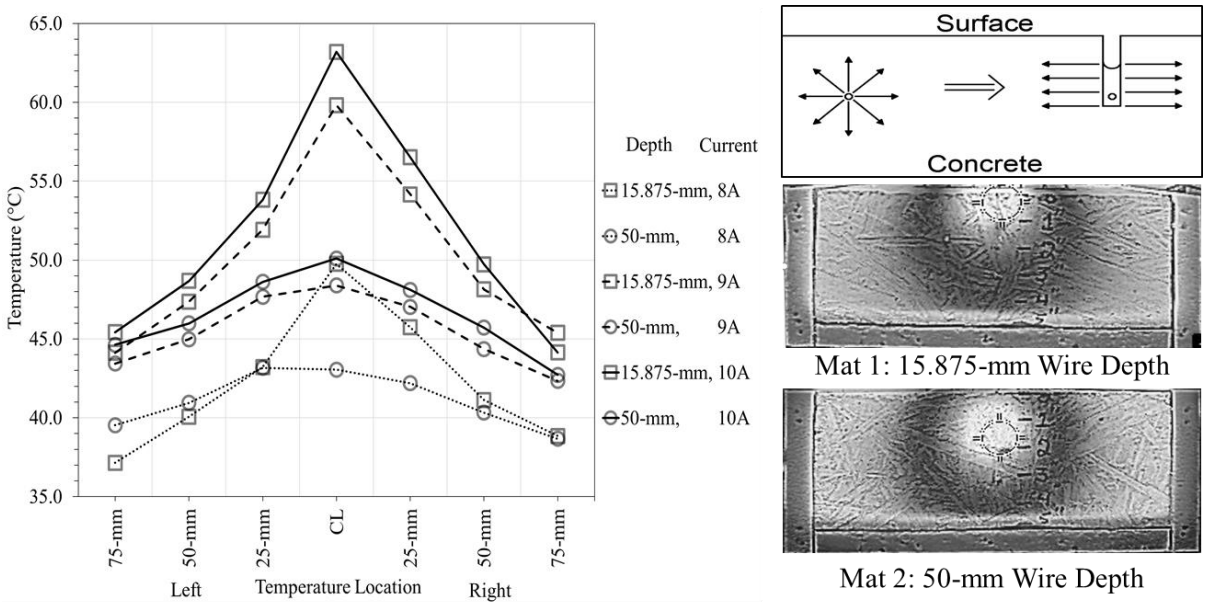

Figure 14: Surface temperature profiles (left) and infrared distribution (right) after 6-hour heating.

Field Study

Outdoor proof-of-concept testing of the prototype was conducted at the University of Arkansas's Engineering Research Center. Testing was conducted over the 2015-2016 winter season. Four, 3-m x 1.2-m x 100-mm, concrete slabs were cast using the Northwest Arkansas Regional Airport's Runway 16/34 reconstruction mix design, Figure 15.

Grooving and heat wire/epoxy placement followed the same process detailed in the earlier text section. Two near-surface heat wire configurations were considered as shown in Figure 15. Slab 1 and Slab 2 have a single serpentine loop designed to heat a 1.9-m^2 surface area. Slab 3 and Slab 4 have four individual serpentine configured sections designed to heat 0.4-m^2 surface areas. Slab 1 and Slab 3 were grooved at a 100-mm wire spacing, and Slab 2 and Slab 4 were grooved at 150-mm spacing.

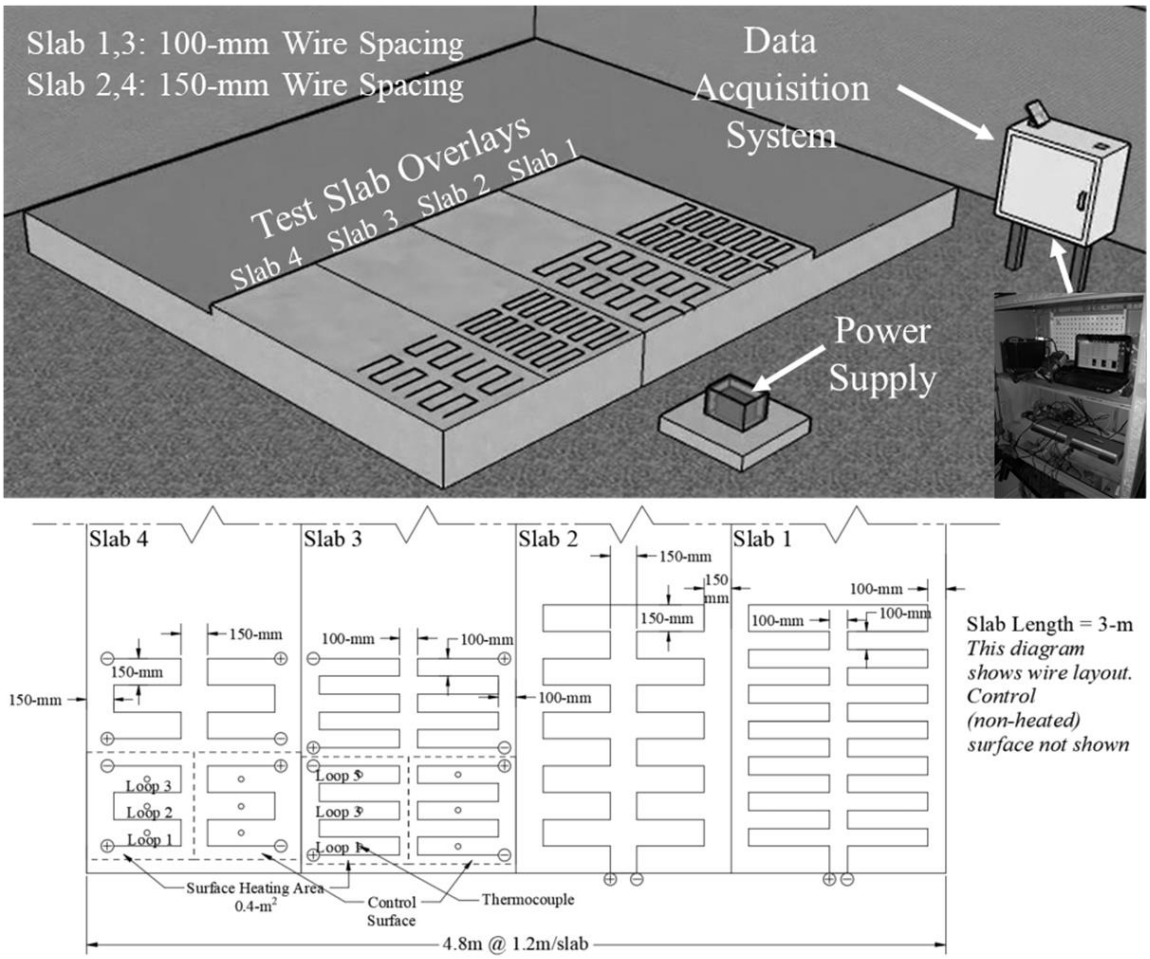

Figure 15: Heated section of outdoor concrete test slabs with surface heat wire layout.

Early tests on Slab 1 and Slab 2 showed insufficient surface heat distribution for the maximum available energy supplied. Using a single embedded wire to heat a 1.9-m^2 area produced inadequate heat generation. Consequently, only Slab 3 and Slab 4 were tested.

Thermocouple junctions were embedded at a depth of 12.7-mm into the concrete slab, mid-distance between wire loops, Figure 15. The thermocouples were placed in the "Surface Heating Area" section and in the adjacent "Control Surface" section. The DAQ measured and recorded temperature directly beneath the pavement surface while an imaging infrared (IR) thermometer gun provided on-surface thermal imaging. Two voltage inputs were considered in the field

experimental study, 24-VDC and 36-VDC, representing two and three 12-V deep-cycle batteries, respectively, in series. Power was supplied using the variable volt/amp DC power supply.

Pavement Heat Testing

Slab surface heating was assessed considering Fayetteville, Arkansas winter conditions. Slab 3 and Slab 4 testing analyzed temperature distribution uniformity in the "Surface Heating Area" at the prescribed voltage inputs, Figure 15. The adjacent non-energized "Control Surface" in Figure 15 was measured for base comparison. Testing began when air temperature fell below 0°C and at night to minimize solar radiation effects.

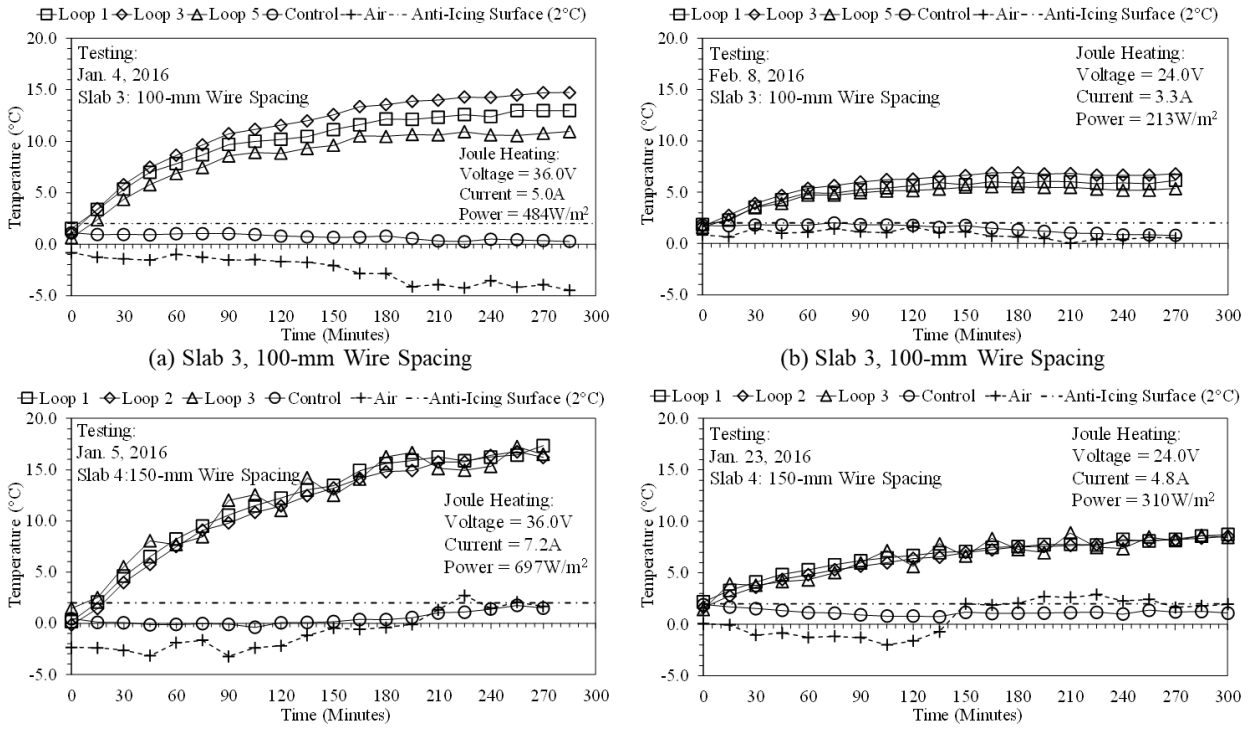

(a) Slab 3, 100-mm Wire Spacing

(b) Slab 3, 100-mm Wire Spacing

(c) Slab 4, 150-mm Wire Spacing

(d) Slab 4, 150-mm Wire Spacing

Figure 16: Time-temperature history on surface of Slab 3 (a, b) and Slab 4 (c, d) during winter season testing.

Temperature distributions on the slab surface of the heated 0.4-m^2 sections are given in Figure 16. The average surface temperature rise with a 24-VDC input was 4.21°C for Slab 3 and 6.74°C for Slab 4. With a 36-VDC input, average surface temperature rise was 11.58°C for Slab

3 and 16.96°C for Slab 4. A decrease in air temperature warranted a longer heating time to reach steady-state surface temperature even with an increase in system power input, Table 7. Though power was activated when air temperature fell below freezing, initial slab surface temperatures were above freezing as pavement temperature change lagged air temperature change. With this scheme, preheating time was not required. This heating method has the potential for limiting concrete thermal stresses, since applying heat to the slab in a subfreezing condition will induce tension stress and cracks along the pavement surface (Pravda et al. 1975). The greatest temperature rise occurred immediately following initial heat activation. Temperature rise during the first 40-minutes of heat testing rose linearly at 0.14°C/minute with 36-VDC and 0.06°C/minute with 24-VDC.

Table 7: Summary of Outdoor Prototype Heat Testing

Date	Test Slab	Weather Condtions			Surface Temperature			Heat Flux (W/m^2)	Heating Time (hour)
		Air Temp. (°C)	Wind (m/s)	Humidity (%)	Dew Point (°C)	Initial (°C)	Steady-State (°C)		
1/4/2016	3	-6.7	0	95	-8.3	1.15	12.73	484	3
1/5/2016	4	-4.4	0.45	85	-6.1	-0.1	16.86	697	4.67
1/23/2016	4	-2.8	1.8	68	-4.4	1.77	8.51	310	4.3
2/8/2016	3	-0.5	4.5	40	-10.5	1.7	5.91	213	2

Temperature rise increased with greater supplied voltage and shorter heat wire length. Since a single wire was used to heat the 0.4-m^2 section, the 150-mm wire spacing covered the Slab 4 heated area with 2.3-m of NiCr-80/20 wire while 3.5-m of NiCr-80/20 wire was used on Slab 3 with a 100-mm wire spacing. The shorter wire length, at the given supplied voltage, supplied higher amperage, resulting in greater wire heat generation and higher slab surface temperature rise.

Results indicate all power inputs in Figure 16 show a surface temperature rise that exceeds anti-icing pavement conditions. For comparison, the design pavement heat flux for Fayetteville,

Arkansas weather conditions was formulated using the steady-state energy balance, Eq. 2 (ASHRAE 2011, FAA 2011). U.S. Climate Data for Fayetteville, AR on January 4 recorded an air temperature of -6.7°C, negligible wind, 95-percent humidity, and an estimated snowfall rate of 2.54-mm/hr. Consequently, the required heat flux for this day based on the 0.4-m^2 heating area of Slab 3 is 276-W/m^2 (ASHRAE 2011). Likewise, on January 5, using the weather conditions in Table 7 and the estimated snowfall rate of 2.54-mm/hr, the Slab 4 required heat flux is 292-W/m^2. These calculated values for heat flux are 57-percent for Slab 3 and 42-percent for Slab 4 of the heat flux supplied to the slabs during the outdoor testing.

Table 8: Comparison of System Power Consumption Cost

Pavement Heating System	Electrode Embedment Depth[a] (mm)	Air Temp.[a] (°C)	Heated Surface Temp. (°C)	Power Density[a] (W/m^2)	Heat Time[a] (hour)	Energy Consumption ($kW\text{-}h/m^2$)	Energy Cost[b] ($/$m^2$)	Ref.
Carbon Fiber Heat Wire for Bridge Deck	40	-4	5	500	6	3	0.33	Zhao et al. (2010)
Carbon Fiber Grille Airport Pavement[c]	50	-1.5	3.4	350	2	0.70	0.08	Lai et al. (2014)
Carbon Fiber Tape	76	-6.7	3	127	5	0.635	0.07	Yang (2011)
Near-Surface Embedded Heat Wire	16	-4.4	16	697	4	2.8	0.31	PC[d]

Note: [a]Value was taken directly from the literature; [b]Energy cost was converted for comparison using average electricity cost in Arkansas, $0.08/kW-h according to U.S. Energy Information Administration; [c]deicing performance test, all others from heat performance tests; [d]this proof-of-concept study.

Table 8 shows the heating performance and energy cost comparison to existing electric heated pavement systems. System power density and heating test duration were taken from the literature referenced in Table 8 for cost comparison. Though this proof-of-concept (PC) system

has greater power density, the heated surface temperature as a function of heat time is significantly greater. Energy cost for each system in Table 8 is calculated using average electricity cost in Arkansas ($0.08/kWh) (USEIA 2017). The PC approach yields an energy cost in range of the developed electrical heated pavement systems referenced in Table 8.

Pavement Ice-Melting Performance

An ice melting analysis was conducted on Slab 3, 100-mm wire spacing, on January 4, 2016, and on Slab 4, 150-mm wire spacing, on January 5, 2016 and February 12, 2016. No snowstorm events occurred at the testing site during the 2015-2016 winter season to validate the anti-icing system at the UA ENRC testing facility. Consequently, crushed ice was used for testing to evaluate the system's heating/melting response. A 25-mm thick layer of crushed ice was spread evenly across the 0.4-m^2 heated and "Control Surface" sections after the heated section reached peak temperature rise. Note that even though ice was used for this testing, the melting behavior of ice is different than snow. Snow, a porous matrix of ice crystals, air, and water vapor, melts producing a liquid film interface between the snow and pavement. Heat is conducted through this interface to melt the snow. Snow melting continues until all precipitation is transformed into a liquid substrate which drains off the pavement (Liu et al. 2007). In contrast, the crushed ice, though porous, is denser and requires more time for melting as experienced in a deicing experiment conducted by Zhao et al. (2010). Therefore, the following melting performance using ice reflects an extended melt time and a corresponding slower surface temperature response.

January 4, 2016

The Slab 3 0.4-m^2 heated section was activated when air temperature dropped below 0°C. The concrete pavement was heated for 280-minutes with a power input of 484-W/m^2 developing a

consistent surface temperature between 11°C and 15°C. Wind velocity was minimal during the testing period.

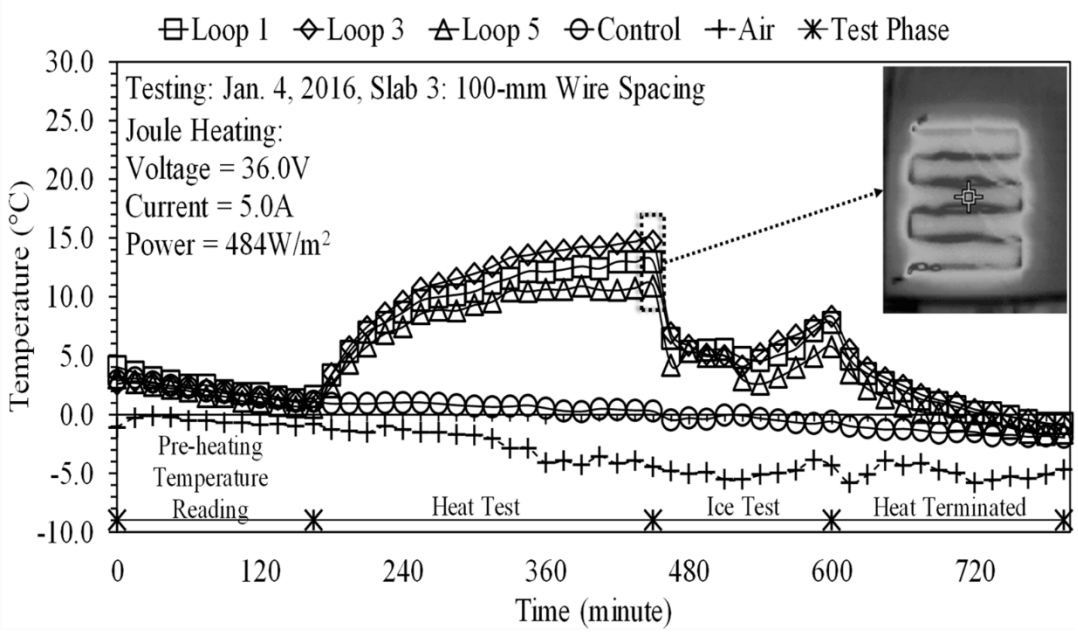

Figure 17: Time-temperature distribution for heat and ice test on Slab 3.

The time-temperature curve during the heat test in Figure 17(after 240-minutes) shows temperature variability between the loops on Slab 3, indicating temperature non-uniformity increased with time. This phenomenon may be attributed to slight inaccuracies in the temperature thermocouples used on Slab 3. Conversely, peak surface temperature rise was captured by an IR thermal gun, Figure 17(inset), and showed uniform temperature distribution at the slab surface.

A uniform layer of crushed ice was placed on Slab 3, Figure 18(left). Power input remained constant. After ice was applied to the pavement, the heated surface temperature decreased to a slab surface temperature between 3 - 5°C, Figure 17(465-minutes). The heated surface melted the ice, Figure 18(left). At 60-minutes, the ice was almost fully melted. In the melting process, a liquid film was observed between the slab and solid ice interface. The liquid film acts as an insulator sheet, decreasing heat transfer rate and increasing melting time. This highlights the

importance of drainage for heated pavement systems, which was recognized by Zeigler (2009). Once ice turned to liquid, the slab temperature rebounded on the heated section at a rate of 0.05°C/minute.

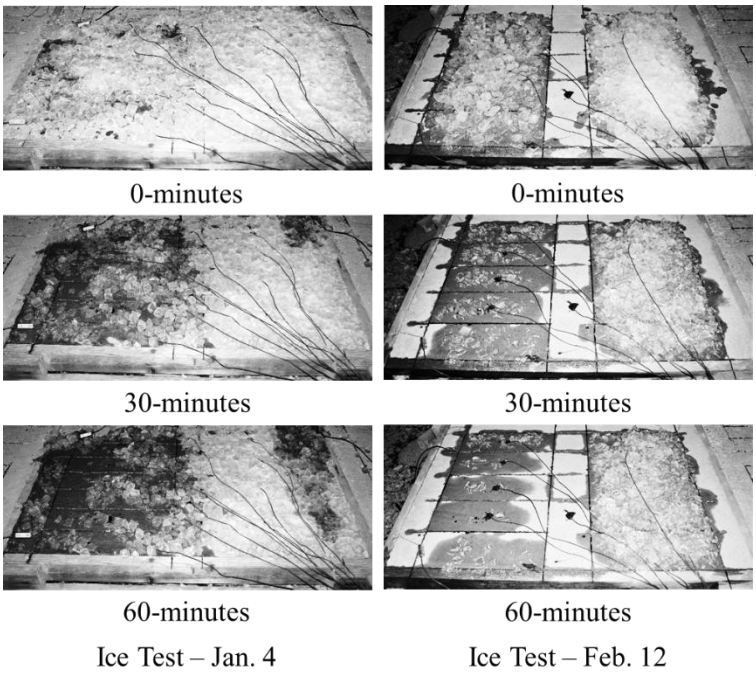

Figure 18: Melting response on Slab 3, January 4 ice test (left) and Slab 4, February 12 ice test (right).

January 5, 2016

36-VDC was supplied to Slab 4 producing an average temperature rise of 17°C with an air temperature that fluctuated between -3°C and 2.5°C, and mild winds. Steady-state temperature required 280-minutes of heating with an initial linear heat gain of 0.1375°C/minute in the first 60-minutes. The larger wire spacing resulted in improved temperature uniformity at the centerline of each loop. The aforementioned increase in current with decrease in Slab 4 wire length melted the ice at a faster rate than Slab 3.

February 12, 2016

This test began 3-hours following sunset with an initial slab surface temperature of 8.5°C. Temperatures were recorded for 3-hours prior to energizing the slab. At 5°C air temperature, the

0.4-m^2 heated section was activated with a 48-VDC input. Within 60-minutes, the DAQ recorded a linear temperature rise of 0.2°C/minute. A consistent uniform surface temperature from 28.5°C to 30°C was achieved in 280-minutes with air temperature at approximately 0°C, Figure 19. The IR image inset in Figure 19 depicts the slab surface thermal distribution just prior to placing the ice on the slab surface.

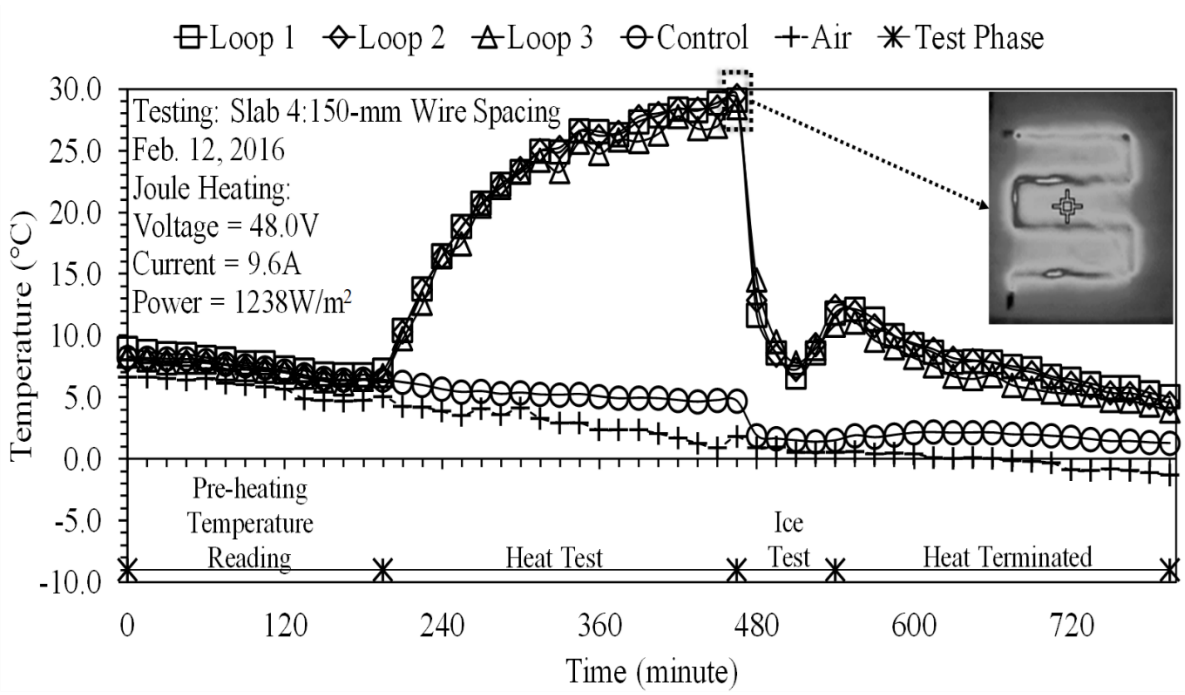

Figure 19: Time-temperature distribution for heat and ice test on Slab 4.

Figure 18(right) shows the ice melting as a function of time. After 30-minutes from the time the ice was applied, the liquid film adjacent to the embedded wire in loop 1 and loop 3 began to evaporate, Figure 18(right, 30-minutes). The remaining ice striped the center of each loop. At 60-minutes, rising surface temperature accelerated the evaporation of liquid film as the heated section returned to a dry condition. The high power input produced rapid uniform surface temperature rise suitable for pavement deicing operation. Thus, the system could be activated at the start of a snow event, however it would require a large initial power supply surge.

Preliminary Study Summary

The preliminary study addressed the proof-of-concept for pavement anti-icing using a near-surface electrical heating prototype. The prototype installation takes advantage of airfield pavement grooving which currently provides drainage and a skid-resistant PCC surface. The concept potential is based on the prototype's heating performance and power requirement. Conclusions from the results and observations from the small- and large-scale experiments include:

- The optimal wire spacing range as a function of heat element installation and uniform thermal distribution is 100-mm to 150-mm;
- TM1 (100-mm wire spacing) and TM2 (150-mm wire spacing) achieved an approximate 6°C and 20°C surface and internal temperature rise with a 12-VDC and 24-VDC input, respectively, in a 6-hour heat test in subfreezing conditions;
- A decrease in wire embedment depth showed an increase in surface temperature distribution. Likewise, the installation approach in thin surface grooves changes the traditional radial heat conduction to a more efficient lateral heat distribution across the concrete surface;
- The 213-W/m^2 to 698-W/m^2 power range showed significant pavement temperature rise with uniform heat distribution during outdoor winter testing. High power density yielded high surface temperature;
- The ice test showed adequate prototype heating unit response, melting a 25-mm layer of crushed ice in approximately 1-hour;
- Maintaining anti-icing temperatures at the pavement surface throughout the winter season will yield a reduction in energy requirements and energy cost. This, as concluded by

Heymsfield et al. (2012), would be vital in the attempt to use a photovoltaic energy system as the heating/snowmelt system power source. Thus, further development of this approach should address the following: (1) an adequate near-surface configuration to expand the heated surface area; (2) operation efficiency for energy conservation; and (3) heating efficiency to sustain anti-icing temperature and minimize thermal stresses induced in the concrete pavement.

Extended Prototype Development

Further prototype development addressed the three recommendations from the proof-of-concept study. Two approaches were assessed to energize the surface embedded heat wires: (1) an alternating heat wire heating sequence and (2) an automated heat wire thermostat heating sequence. Both approaches used surface embedded heat wires configured as a parallel circuit. Consequently, the serpentine wire configuration was replaced with a parallel wire configuration. Two, 610-mm x 305-mm x 127-mm, concrete test mats were constructed for lab testing, Figure 20. The test mats were cast in molds with a 25.4-mm styrofoam inlay, Figure 20. Near-surface wires were installed in pavement surface grooves in a parallel wire configuration. In the following text, this grid configuration will be referred to as the "prototype grid". The prototype grid installation takes advantage of surface grooves currently used on airfield pavements for drainage and skid-resistance (FAA 1997, FAA 2011). Grooves in the test mats were saw-cut by hand. Each 457.2-mm long heat wire was positioned at the bottom of the 3.175-mm (width) x 15.875-mm (depth) groove and epoxy sealed to provide corrosion resistance and thermal contact between the heat wire and concrete, Figure 20. The study used nickel-chromium alloy (NiCr-80/20) heat resistant wire for the prototype heat element. The 1-mm diameter NiCr-80/20 wire has a 1.33-Ω/m resistance per unit length.

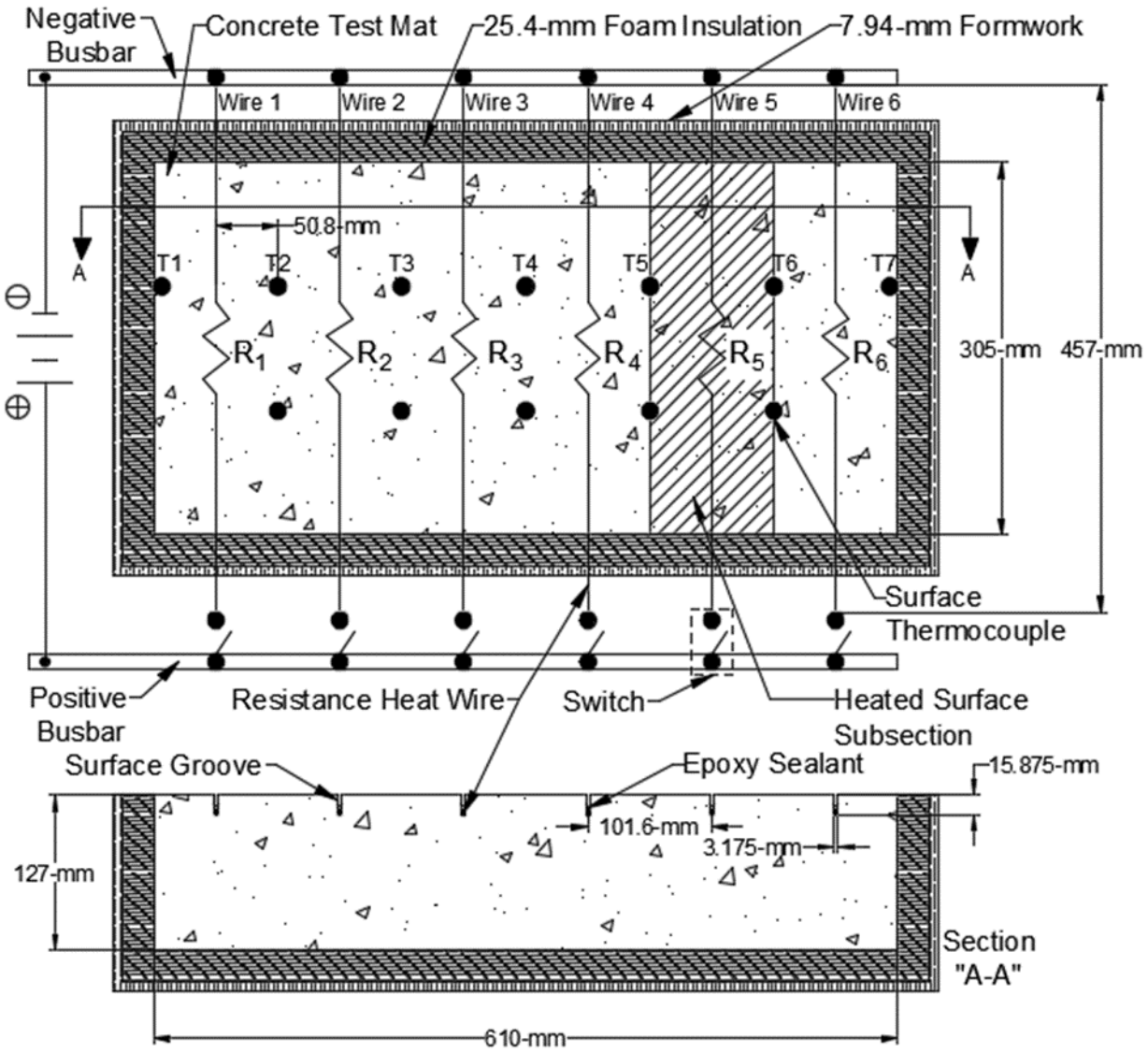

Figure 20: Laboratory prototype grid configuration on concrete test mat (TM1 shown).

In the proof-of-concept study, a parallel wire spacing range between 101.6-mm to 152.4-mm provided uniform heat distribution at the test mat surface. The heat wire-epoxy filled groove creates a composite heating medium, while the groove shape directs heat conduction laterally along the pavement surface. Extended prototype development considered two parallel wire configurations, test mat 1 (TM1) with parallel heat wires spaced at 101.6-mm and test mat 2 (TM2) with parallel wires spaced at 152.4-mm. Figure 20 depicts the electrical diagram of the prototype grid superimposed on the concrete test mat. Steel slotted flat bars serve as busbars in

the electrical circuit. Each parallel heat wire connects directly to the negative busbar and via a relay to the positive busbar. Individual surface heat wires heat their respective "Heated Surface Subsection", as identified in Figure 20. The "Manual Switchboard" in Figure 21 enabled activating current flow manually to individual embedded heat wires. Conversely, the Figure 21 "Automated Control Relay Panel" later replaced the "Manual Switchboard" to automatically activate individual embedded heat wires.

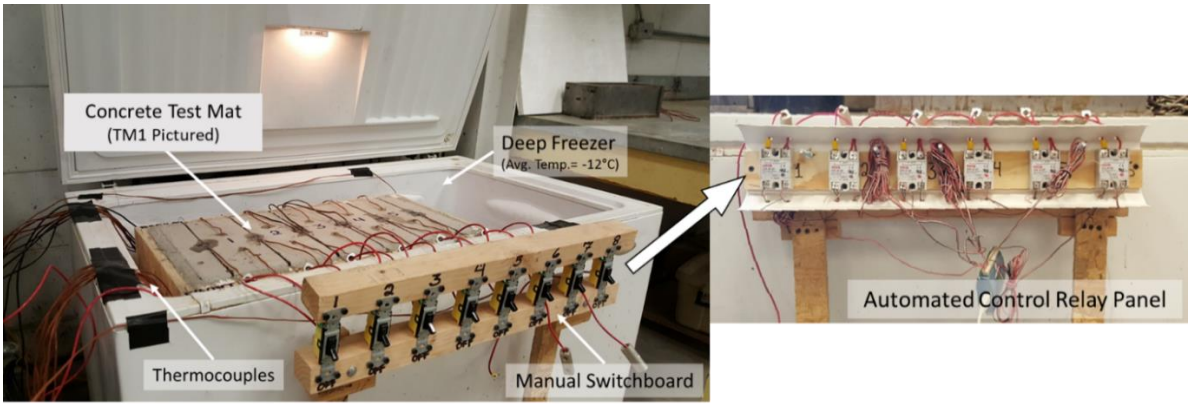

Figure 21: Laboratory testing setup.

Laboratory testing for the extended prototype development used the following equipment: data acquisition system (DAQ), variable voltage/amperage direct current (DC) power supply, programmed automated control system (ACS), switchboard, control relay panel, and freezer chest. Type T thermocouples measured surface temperature, at locations shown in Figure 20. These thermocouple positions provided temperature records to measure the uniformity of the temperature along the pavement surface. Thermocouples labeled T1 through T7, in Figure 20, measured temperatures for on/off response of the heat wires in the automated thermostat heating sequence.

Preliminary heat testing was conducted on the surface embedded heat wire to investigate the wire's heat-current behavior. An infrared thermometer gun was used to measure a single 1.0-mm diameter, 457.2-mm long NiCr-80/20 wire after a 5-minute heating period, Figure 22. The

voltage corresponding to the input current is also shown. Linear temperature rise occurred at current above 4-amps. Voltages measured from the power supply, which corresponded with the amperage in Figure 22, were later used as constant power supply inputs to investigate the test mat heating performance using the alternating heating sequence and automated thermostat heating sequence.

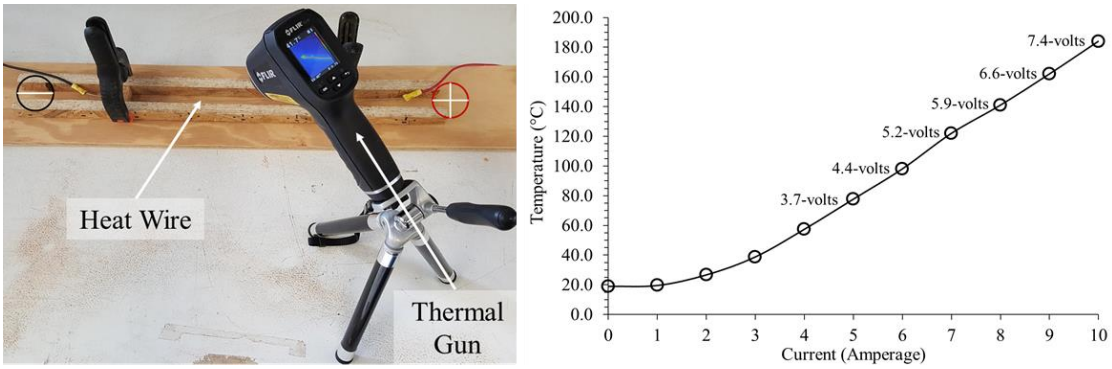

Figure 22: Heat wire temperature as a function of current input.

Prior to test mat heat testing, the designated current flows, 5-amp, 6-amp, 7-amp, 8-amp, 9-amp, and 10-amp, were produced on a single wire using a voltage input from the power supply ("power supply voltage input") set at 3.7-V, 4.4-V, 5.2-V, 5.9-V, 6.6-V, and 7.4-V, respectively. As the number of active wires increased, the total current increased but not linearly with respect to the number of wires. The current increase was less than expected due to energy losses in the wires connecting the power supply to the system. Therefore, for consistency during testing, voltage input from the power supply was held constant at 3.7-V, 4.4-V, 5.2-V, 5.9-V, 6.6-V, and 7.4-V. A clamp meter was used to measure the voltage at the busbar and current at each connection wire, Figure 21.

Slab Surface Temperature Distribution using the Fully Activated System

A full heating sequence on the prototype grid was initially tested to benchmark the test mat heating performance and energy consumption. Testing on TM1 and TM2 occurred in the freezer chest. Power was supplied to the test mat after the test mat reached constant temperature (-

12°C). Six heat tests were performed on both mats using 3.7-V, 4.4-V, 5.2-V, 5.9-V, 6.6-V, and 7.4-V voltage input. Each test was conducted over a 6-hour test period.

Studies show that the pavement surface anti-icing temperature threshold is 2°C (Tuan and Yehia 2004, Zhao et al. 2011, Lei et al. 2015). Therefore, the heating rate was recorded from initial subfreezing temperature (-12°C) to the pavement anti-icing temperature threshold (2°C). Figure 23 shows the average surface-temperature rise per voltage input. Power supply voltage input above 5.9-V heated test mats TM1 and TM2 above the 2°C anti-icing threshold.

Voltage was measured between the power supply's positive terminal and the positive busbar. Voltage drop existed on both test mats, but slightly greater on TM1's prototype grid. As a result of the voltage drop, 5.9-V, 6.6-V, and 7.4-V power supply voltage input measured 4.7-V, 5.2-V, and 5.9-V for TM1 and 5.0-V, 5.6-V, and 6.3-V for TM2, respectively. Consequently, more current flowed through each TM2 prototype grid wire resulting in greater heat generation than TM1.

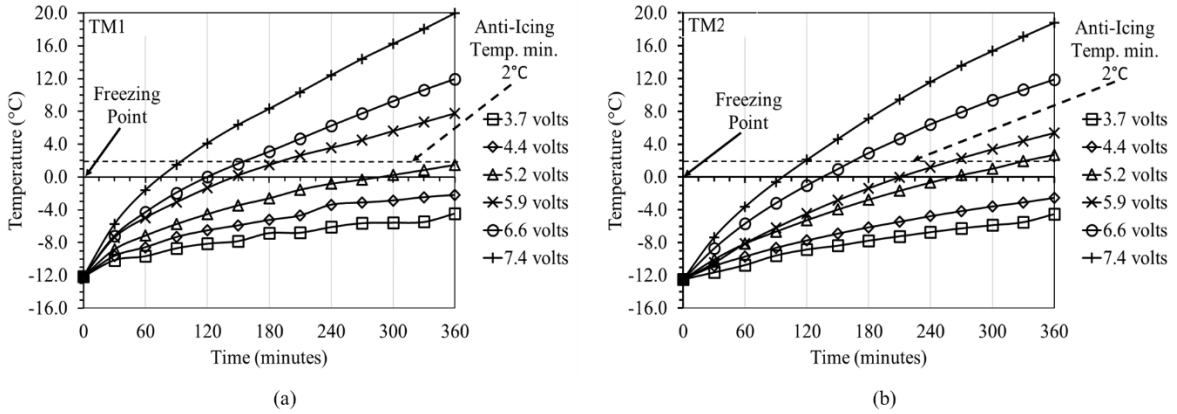

Figure 23: Time-temperature history for full heating sequence on (a) TM1 and (b) TM2.

A linear temperature growth pattern was observed during heating above the 2°C anti-icing threshold. In Figure 23(a), the TM1, anti-icing threshold temperature (2°C) was reached in 185-minutes with 5.9-V (4.7-V measured, 829-W/m^2), 155-minutes with 6.6-V (5.2-V measured, 1,029-W/m^2), and 95-minutes with 7.4-V (5.9-V measured, 1,307-W/m^2). In Figure 23(b), the

TM2, anti-icing temperature was reached in 240-minutes with 5.9-V (5.0-V measured, 667-W/m^2), 155-minutes with 6.6-V (5.6-V measured, 865-W/m^2), and 120-minutes with 7.4-V (6.3-V measured, 1,057-W/m^2). These same three power supply voltage inputs (5.9-V, 6.6-V, 7.4-V) were used to evaluate the alternating heating sequence approach discussed in the next section.

Slab Surface Temperature Distribution using Alternating Heating Sequence

Heating pavement in an alternating fashion was studied in the Roca Spur Bridge heated pavement project (Tuan 2004). Roca Spur Bridge is located outside of Lincoln, Nebraska. Slabs along the bridge length were numbered, and the odd number slabs were heated for a 30-minute period followed by the even number slabs heated for 30-minutes. This process was repeated for several hours. This heating process was incorporated manually into the discussed prototype grid system. Wires were numbered 1-6 on TM1, as shown in Figure 20, and 1-4 on TM2. For TM1, the odd wire group included wires 1, 3, and 5. The TM1 even wire group included wires 2, 4, and 6. For TM2, the odd wire group included wires 1 and 3. The TM2 even wire group included wires 2 and 4. Each heat test activated the odd wire group for the first 30-minutes followed by heating the even wire group for 30-minutes. This alternating heating process continued for a 6-hour test period.

As previously mentioned, voltage drop occurred, but was less in this experiment since fewer wires were activated at any one time. The 5.9-V, 6.6-V, and 7.4-V power supply voltage input had actual measurements of 5.2-V, 5.8-V, and 6.5-V for TM1 and 5.4-V, 6.1-V, and 6.8-V for TM2, respectively.

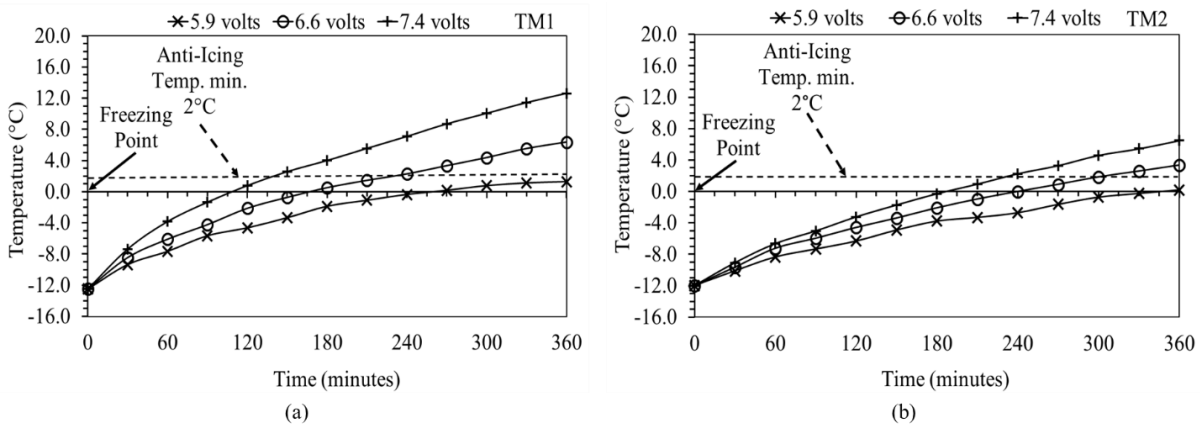

Figure 24: Time-temperature history for alternating heating sequence on (a) TM1 and (b) TM2.

The average surface-temperature rise as a function of the power supply voltage input is shown in Figure 24. As shown in Figure 24, the 5.9-V power supply voltage input did not reach the anti-icing threshold (2°C) during the test period. TM1 reached the anti-icing threshold in 235-minutes with 6.6-V power supply voltage input, and 142-minutes with 7.4-V power supply voltage input. TM2 reached the anti-icing threshold in 300-minutes with 6.6-V power supply voltage input, and 230-minutes with 7.4-V power supply voltage input.

Power, preheat time, and energy consumption comparing the full heating sequence and alternating heating sequence for TM1 and TM2 are given in Table 9. Power and energy consumption were calculated using the actual voltage measurement, which corresponds with the Table 9 power supply voltage input. Using the alternating sequence reduces the power by one-third as compared with the full heating sequence approach. However, the extended preheat time to reach the anti-icing condition using the alternating sequence produced greater energy consumption in comparison to the full heating sequence approach, Table 9. Consequently, the alternating heating sequence does not offer energy savings over the full heating sequence approach.

Table 9: Comparison of Prototype Grid Energy Consumption with a Full Heating Sequence and Alternating Heating Sequence

Heating Sequence		Power (Watts)[a]			Heat Up Time to 2°C (hours)[b]			Energy Consumption (kWh)[c]		
		5.9 volts	6.6 volts	7.4 volts	5.9 volts	6.6 volts	7.4 volts	5.9 volts	6.6 volts	7.4 volts
Full	TM1	154.0	191.3	242.8	3.1	2.6	1.6	0.4747	0.4941	0.3845
	TM2	124.0	160.8	196.3	4.0	2.6	1.8	0.4960	0.4155	0.3599
Alternating	TM1	105.1	133.4	166.4	-	3.9	2.4	-	0.5225	0.3938
	TM2	79.6	99.8	124.8	-	5.0	3.8	-	0.4990	0.4786

(a) Power calculated using the measured voltage that corresponds with the set voltage input, and the measured current

(b) Test mat preheat time to anti-icing temperature threshold for tests corresponding with the set voltage input

(c) Energy consumption for heating to anti-icing temperature threshold for tests corresponding with the set voltage input

(-) Pavement temperature did not reach the anti-icing threshold temperature in the 6-hour heat test.

Slab Surface Temperature Distribution using an Automated Thermostat Heating Sequence

This experiment assessed an automated control system capable of maintaining the test mat surface at a set temperature. For example, for TM1 the automated system used thermocouples T1-T7 in Figure 20 to switch power on/off to individual wires within the prototype grid. Specifically, the average temperature between thermocouples T1 and T2 controls current flow to Wire 1, the average temperature of T2 and T3 controls current flow to Wire 2, and so forth. When the average temperature of the "Heated Surface Subsection" in Figure 20 is above a set temperature, no current flows through the respective heat wire. Conversely, when the average temperature of the "Heated Surface Subsection" is below the set temperature, current is supplied to the wire to generate heat until the set temperature is reached.

Testing used 5.9-V, 6.6-V, and 7.4-V input settings on the volt/amp power supply. With voltage drop, these voltages translated to 4.7-V, 5.2-V, and 5.9-V input for the TM1 tests, and 5.0-V, 5.6-V, and 6.3-V input for the TM2 tests. Preheating time was similar to that found in the base case experiment. The set temperature is 2°C, the pavement anti-icing temperature threshold. Heat tests with 6.6-V power supply voltage input are given in Figure 25. The time-temperature profile shows surface temperature rise followed by a temperature hovering around the anti-icing

threshold. After 165-minutes for TM1 and 195-minutes for TM2, power supplied to the system changes as individual heat wires cycle on and off. Figure 25(a) and (b) insets are an expanded view of the pavement temperature during the last 60-minutes of the heat test. The average surface temperature oscillates about the 2°C set temperature for both test mats. Future set temperatures should consider measured temperature variability in order to produce a more uniform temperature distribution along the pavement surface.

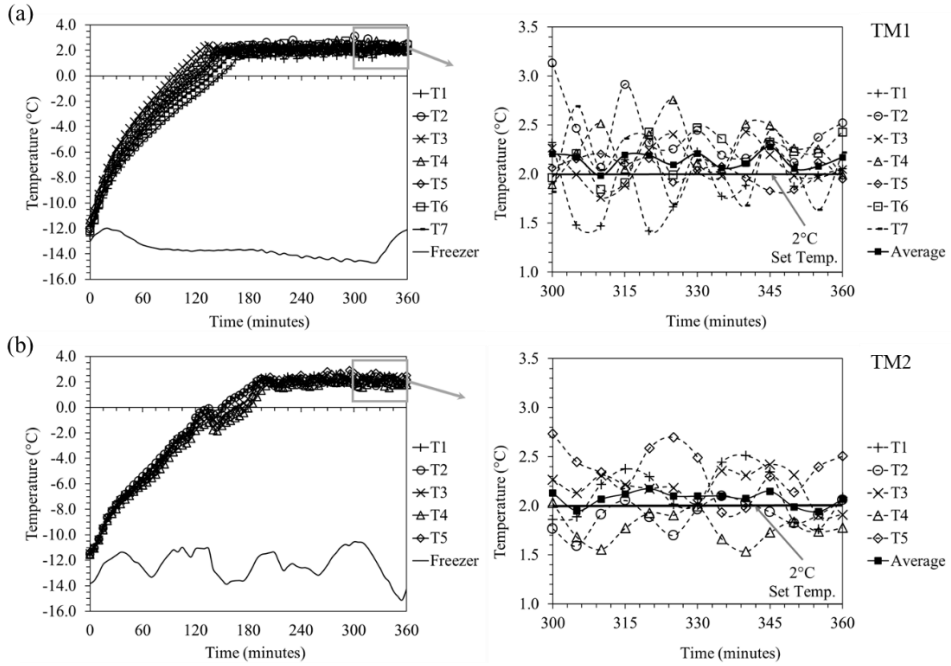

Figure 25: Time-temperature history and section profile for thermostat heating sequence on (a) TM1 and (b) TM2.

Figure 25(a, left) shows non-uniform temperature rise across the test mat surface. As a result, individual subsection heat tests were conducted. A 5.9-V power supply voltage input was supplied to each prototype grid wire individually. These tests compared temperature rise over 6-hours and the heat rate for the first 60-minutes. Temperature rise in each subsection varied no more than 2°C and therefore within temperature uniformity, Figure 26 (Zhao et al. 2011). Heating rate per surface subsection within the first 60-minutes is shown in Figure 26. The heat rate is within a 10-percent difference. Therefore, the heating inconsistency can be attributed to

the slight difference in current flow through each wire within the prototype grid and/or concrete property inhomogeneity.

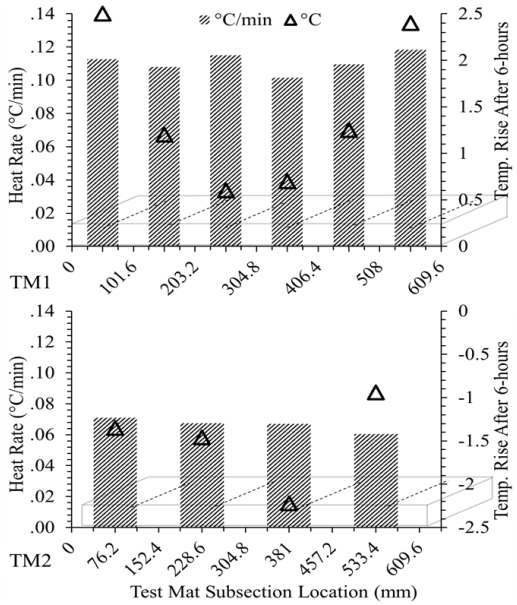

Figure 26: Uniform heat rate investigation per surface subsection.

Outdoor Testing Experimental Program

The preliminary study results discussed above were used to direct the large-scale prototype grid design, installation, instrumentation, and operation for field experimentation. Figure 27 shows a schematic of the solar-EHPS using a large-scale prototype grid.

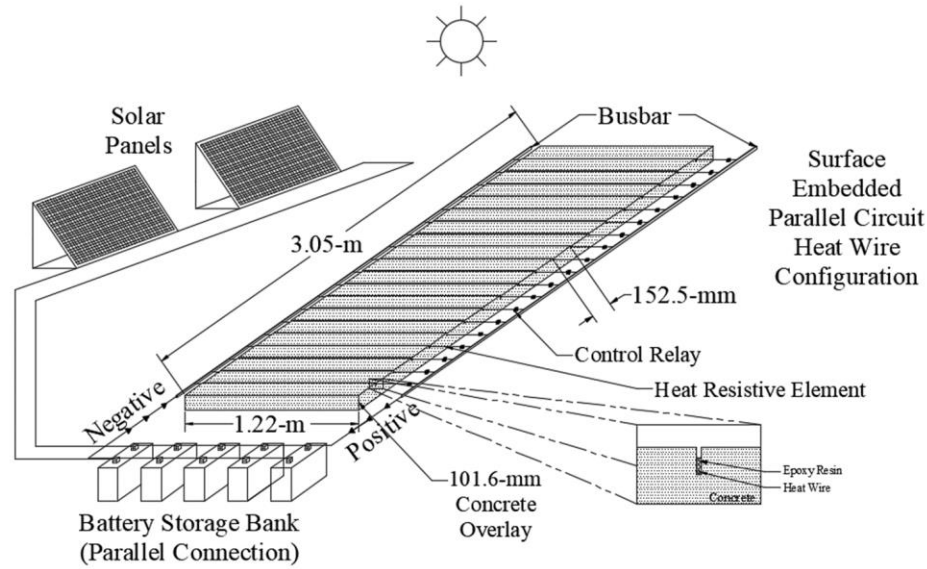

Figure 27: Schematic of electrical heating system configuration.

Construction took place at the outdoor testing facility at the UA ENRC. Two, 3.05-m x 1.22-m x 0.1-m thick concrete test slabs were cast using the XNA Runway 16/34 reconstruction concrete mix design. Transverse surface grooves on the large-scale test slab were saw cut by hand after a 24-hour cure. Groove spacing for Slab 1 and Slab 2 were 152.4-mm and 101.6-mm, respectively. Figure 28 shows the concrete installation and groove cutting process. The grooves were cleaned of debris before heat wire installation.

Figure 28: Electrical system concrete slab construction.

Nineteen (19), 1-mm diameter NiCr-80/20 wires were installed on Slab 1. Sixteen (16), 1-mm diameter NiCr-80/20 wires were installed on Slab 2. The wire installation process is shown in Figure 29. Epoxy was poured into the surface grooves by hand.

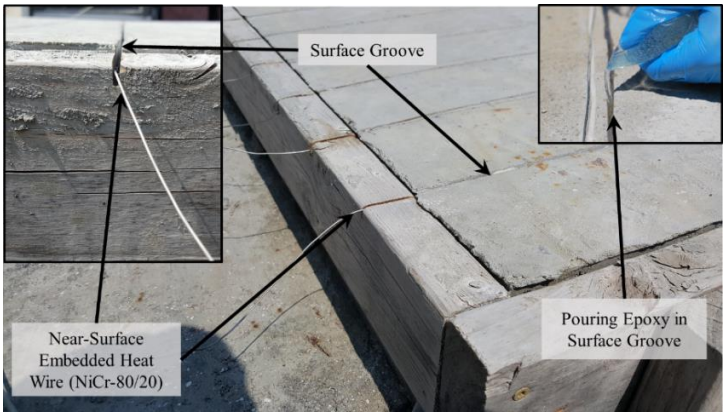

Figure 29: Heat wire and epoxy installation in surface grooves.

The prototype grid assembly included connecting the groove-embedded NiCr-80/20 wires to a control relay panel and steel plate busbar, Figure 30. Each wire was 1.8-m long, with a resistance of 2.4-Ω.

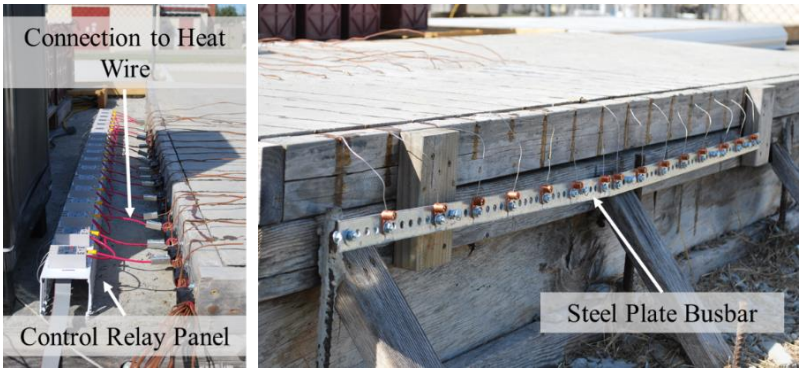

Figure 30: Parallel system assembly.

Figure 31 shows the full test slab configuration. Individual wires heat their respective surface subsection. For Slab 1, the subsection is 152.4-mm wide and 1.22-m across. For Slab 2, the subsection is 101.6-mm wide and 1.22-m across. As an example, "Heated Surface Subsection 1" is highlighted in Figure 31. The data acquisition system (DAQ) and automated control system (ACS) were located adjacent to the large-scale test slabs and battery storage banks. Thermocouple positions on the large-scale test slabs are consistent with the locations used for the extended prototype development laboratory experiment test mats. Type T thermocouples connect to the DAQ/ACS to monitor/record slab temperature data and signal on/off heating operation.

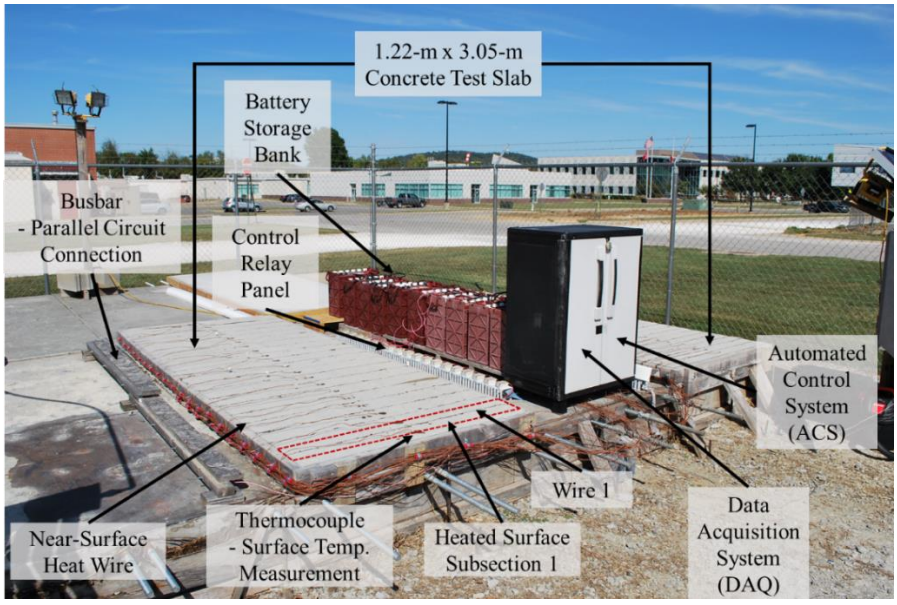

Figure 31: Large-scale test site configuration.

Automated Control System Design

Surface wires were activated using the automated thermostat heating sequence approach. This approach optimizes energy delivery to the pavement slab. The process maintains an above-freezing slab surface; therefore, energy surge and its accompanying time demand to promote a pavement anti-icing condition are eliminated. When the subsection temperature indicates a below target temperature value, the control relay corresponding to that subsection actuates for current flow and heat generation. This type of heating, "zone heating", is recommended for operation efficiency (Joerger and Martinez 2006, FAA 2011). As concluded in the previously presented laboratory study, the alternating energy supply sequence did not yield energy savings and therefore was not analyzed during the full-scale test.

Figure 32 details the automated programmed system design for an anti-icing operation scheme. At system activation, the operator sets a target pavement surface temperature (TPST). This is a manually set value determined by the operator. Between 2°C and 5°C is recommended for the anti-icing set temperature, where the actual set value is dependent on a site's ambient climate conditions (Zhao et al. 2011). The heating process is shown in Figure 32 for the "Heated Surface Subsection 1", shown in Figure 31. For Subsection 1, Wire 1 (n=1), the thermocouples adjacent to "Wire 1" on Figure 32 are T1 and T2. The average of these two temperatures is the "Avg. Heated Surface Subsection Temperature". If the average temperature is greater than TPST, the control relay is set open. Consequently, no current flows to Wire 1 and no heat is generated. If the average temperature is less than TPST, the control relay actuates and current flows through Wire 1 for heat generation. This program iterates at a 1-minute time step.

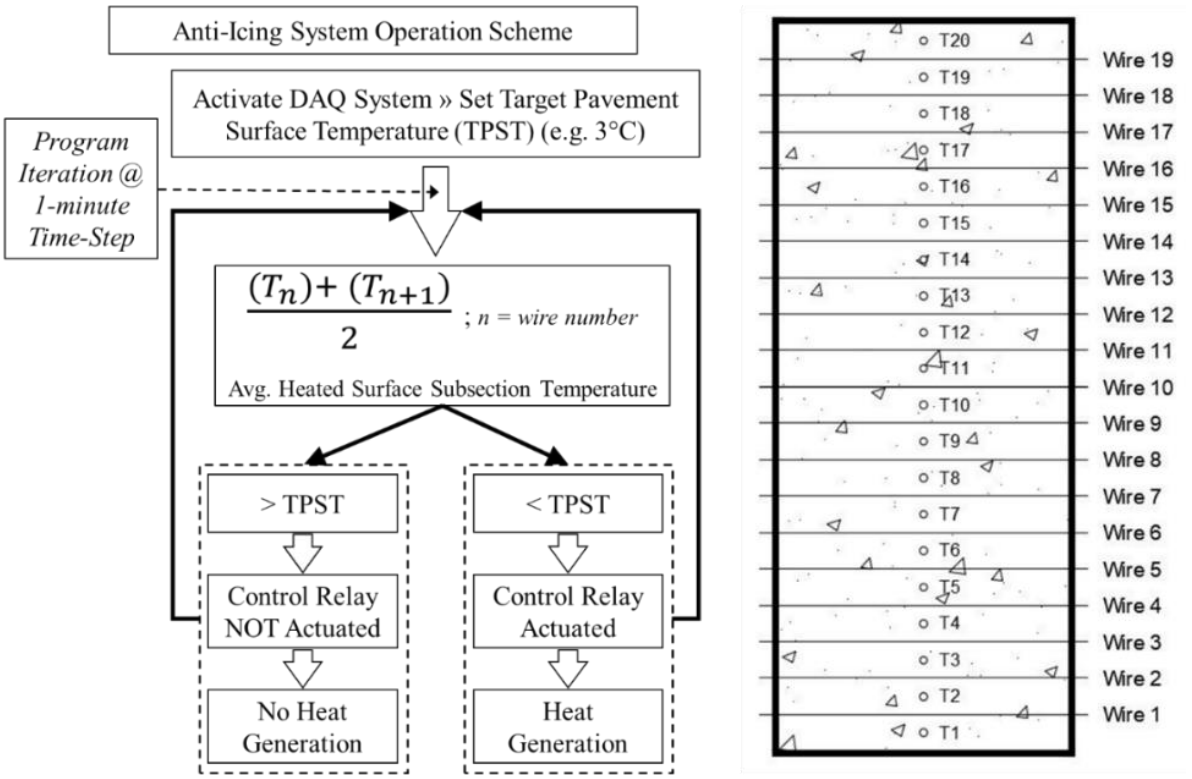

Figure 32: Automated programmed thermostat system design.

Photovoltaic Energy System

The battery storage bank, in Figure 33, is a component of the off-grid photovoltaic energy system (PVES) used in this study. The PVES is used as the power source for the large-scale test slabs. Each test slab has its own battery bank. The battery storage bank includes five, 12-V 6-cell flooded lead-acid deep cycle batteries connected in parallel. The parallel connection increases the battery amp-hour rating from 205 amp-hours at 20-hours to 1,025 amp-hours at 20-hours. The battery bank is charged using one 200-W solar panel array. The PVES includes a solar charge controller to regulate the recharge and prevent voltage overload, Figure 33. A voltage data logger was included with the DAQ to evaluate the battery bank's energy use and recharge during heating and anti-icing operation.

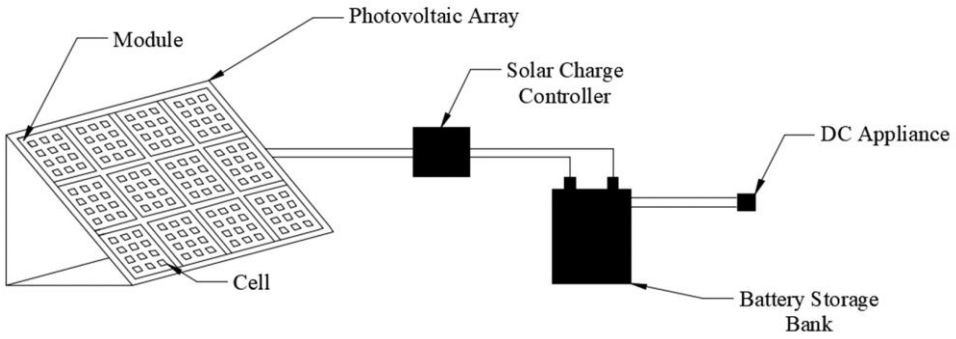

Figure 33: Photovoltaic array and battery storage system.

Performance Analysis

Field testing was used to assess the heating/snow-melting performance and energy consumption of the large-scale electrical pavement heating system. In order to optimize energy usage, pavement heating operation for the presented approach maintains the pavement surface at a constant above-freezing surface temperature to prevent winter contaminant accumulation. This prototype grid and corresponding solar energy system were used to conduct the following experiments: (1) the operation performance of the prototype grid during ambient winter weather conditions; (2) the energy performance of the PVES during prototype grid operation; and (3) the anti-icing performance of the prototype grid during a snow event. Results from the performance analysis of the large-scale electrical pavement heating system are presented in Chapter 4.

SOLAR – HYDRONIC HEATED PAVEMENT SYSTEM APPROACH

Overview

In the 1975 FAA funded project, Pravda et al. (1975) conducted a pavement heating system study investigating a solar heat-pipe HPS for implementation at an airport runway and ramp. The study recommended that for low and constant annual operating system cost, solar heat-pipe HPS use should target priority pavement areas (i.e. apron). The Pravda et al. (1975) study used gravity-assisted heat-pipe flat-plate collectors (FPC) to collect and transfer heat to a storage reservoir for pavement heating. Technological advancements in solar energy collectors

prompted revisiting this study by the author to investigate incorporating new advanced solar equipment.

A heat-pipe evacuated tube collector (HP-ETC) is investigated herein to meet the energy demand of a HHPS for maintaining an above-freezing (anti-icing) pavement temperature. A HP-ETC absorbs solar radiation (direct and diffuse) in vacuum-sealed tubes that contain copper heat pipes. Liquid within the heat pipe vaporizes to transfer heat to the copper manifold header pipe. After heat transfer, the vapor cools within the heat pipe, liquefies, and returns to the base of the heat pipe where the heat cycle is repeated. The evacuated tube's internal vacuum reduces convection and conduction losses. Additionally, the tube's cylindrical geometry enables solar radiation absorption within a wide incident angle range. Consequently, a HP-ETC can operate in cold weather and for long time periods during sunlight hours (Alghoul et al. 2005, Ayompe and Duffy 2013, Hang et al. 2012, Kalogiru 2009, Mazarron et al. 2016).

The methods to incorporate a HP-ETC and a solar water heating system (SWHS) with a HHPS are detailed in the following text section.

Outdoor Testing Experimental Program

Construction, instrumentation, and operation of the solar-hydronic heated pavement system approach took place at the outdoor testing facility at the UA ENRC (36°02'31.08"N 94°10'12.22"W). Figure 34(a) shows the experimental setup connecting two systems, a SWHS and a HHPS, directly to the fluid storage tank. An energy performance analysis assessed the HP-ETC solar energy collection and efficiency. Heat and anti-icing tests were performed on two, 3.05-m x 1.22-m x 0.13-m overlay test panels, "Slab 1" and "Slab 2", Figure 34(a). A data acquisition system (DAQ) monitored and recorded tank, collector, and concrete slab surface temperatures. A programmed automated control system (ACS) used the recorded temperatures

to operate the SWHS and HHPS. Ambient climate data were taken from the Drake Field weather station, 4.8-km from the test facility.

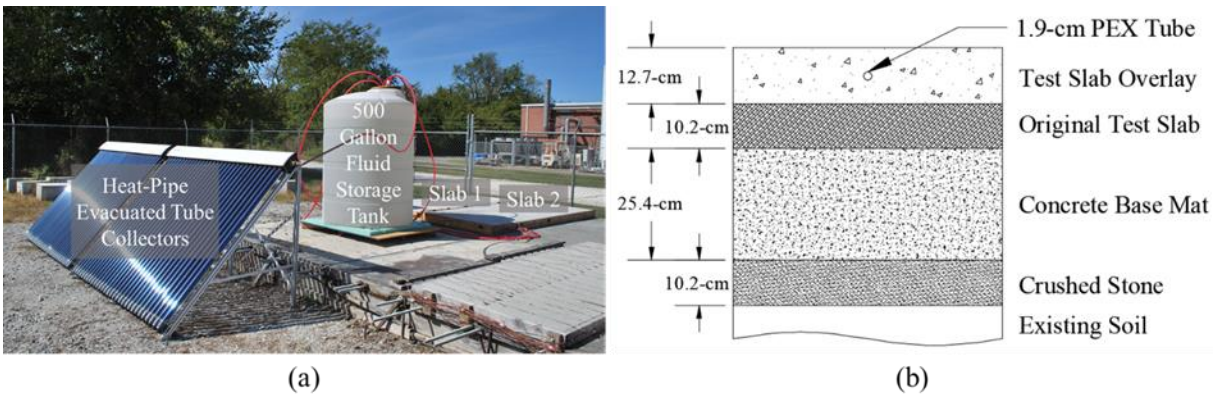

Figure 34: (a) Experimental setup and (b) testing platform cross-section view.

Thermal Storage System

An 1890-L (500-gallon) polyethylene vertical fluid storage tank, in Figure 35, stored the system's working fluid. The working fluid was a 20-percent by volume ethylene glycol-water solution to prevent freezing in the Fayetteville, Arkansas winter climate conditions. The tank was located between the HP-ETCs and heated pavement slabs. The tank was positioned on a 1.22-m x 1.22-m x 0.1-m high-density polyurethane foam board for tank bottom insulation, Figure 35. The exposed tank surface was insulated using a 15.2-cm thick wall insulation. Plastic stretch wrap enclosed the insulation to prevent moisture intrusion, Figure 35. Insulation was added to the tank lid bottom to reduce thermal loss. Supply and return tubing connected the solar water heating and hydronic heated pavement systems. Access holes were drilled into the tank lid to provide access for the supply and return tubing.

Figure 35: Filling and insulating the aboveground storage tank.

Figure 36 shows the initial tank heating test using the HP-ETCs before the tank insulation was installed and after the tank insulation was installed. The storage tank fluid temperature fluctuated between heat gain during sunlight hours and heat loss during the non-sunlight hours. After tank insulation, heat loss from the storage tank was reduced significantly.

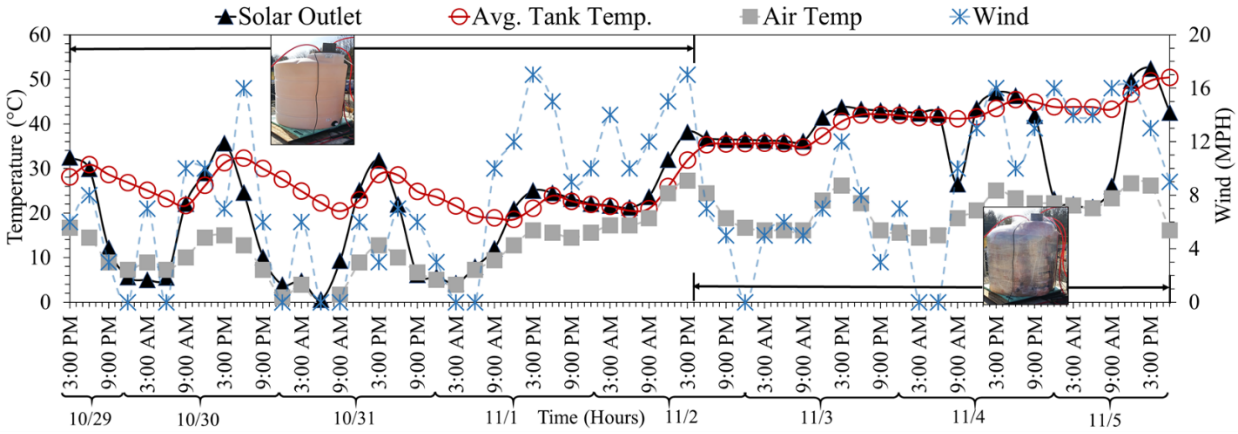

Figure 36: Storage tank fluid temperature before and after tank insulation from Oct. 29, 2017 to Nov. 5, 2017.

19-mm cross-linked polyethylene (PEX) tubing was used for the supply and return tubing. All exposed tubing was wrapped with 19-mm thick foam pipe insulation. A vertical rod within the storage tank supported thermocouples to measure temperature at various tank depths, Figure 38. Type T thermocouples were positioned along the rod to record temperature at 189-L (50-gallon) intervals from the tank bottom.

Solar Water Heating System with Heat-Pipe Evacuated Tube Collector

The solar water heating system (SWHS) collects solar energy in two, HP-ETCs, in-series, Figure 37(a,b). The SWHS is configured to transfer thermal energy to the working fluid, and transport the thermal energy to the thermally insulated storage tank. The HP-ETC used in this study is commercially available. Each HP-ETC includes 30 vacuum-sealed tubes. Each HP-ETC has a 4.901-m^2 total area and a 2.791-m^2 aperture area. The HP-ETCs were installed at the test facility in a south-facing direction, with a 45° tilt angle.

Figure 37: HP-ETC (a) placement, (b) connection, and (c) outlet temperature measuring location.

Figure 38 is a schematic diagram showing the fluid flow path between the HP-ETC and the storage tank, and the storage tank and the test pavement slab. The working fluid circulates from the tank bottom, where the fluid is cool, to the HP-ETC manifold using a submersible pump. The electric pump is rated at 124.3-watts (0.167 HP). The fluid warms as it passes through the HP-ETC manifold. The heated working fluid then returns to the storage tank at mid-level. A temperature probe was attached to the HP-ETC manifold outlet, Figure 37(c), to measure fluid temperature exiting the HP-ETC's manifold ($T_{c,o}$), Figure 38. The temperature probe is connected to a DAQ to record temperature variation continually at this location within the SWHS circuit.

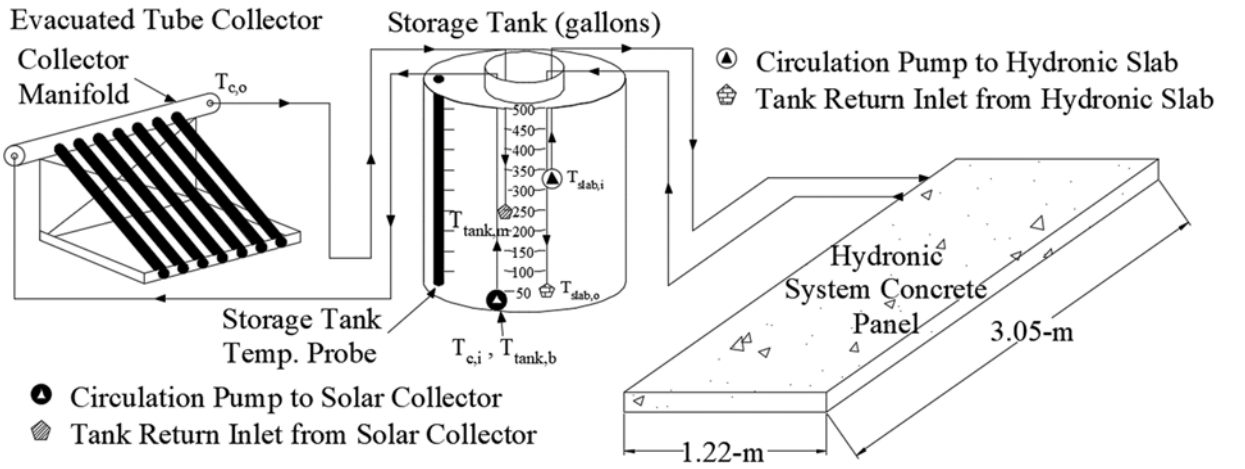

Figure 38: Schematic diagram of solar water-glycol heating subsystem (left) and hydronic heated pavement subsystem (right).

The SWHS operation is temperature-controlled. The SWHS was activated when the HP-ETC outlet temperature was greater than the fluid temperature in the middle third of the storage tank. This approach eliminated reverse heat transfer and minimized the pump's electrical energy demand. Figure 39 describes this process using an operation scheme diagram, Figure 39(a) and a visual temperature-monitoring platform, Figure 39(b). The "Tank Temp." in Figure 39(a) is the average temperature within the middle third of the tank, between 946-L and 1514-L (250-gallons and 400-gallons). This temperature is the average of the temperatures highlighted in the tank temperature column, Figure 39(b). The "Solar Panel Temp." is the HP-ETC outlet temperature ($T_{c,o}$). When "Tank Temp." is less than "Solar Panel Temp.", the submersible pump is activated to circulate the working fluid to increase the temperature of the storage tank fluid. Conversely, when "Tank Temp." is greater than "Solar Panel Temp.", no fluid circulates through the HP-ETCs. Temperature difference between the HP-ETC outlet and storage tank is reviewed at 1-minute time intervals. The SWHS operates during sunlight hours and is dependent on weather and sky conditions.

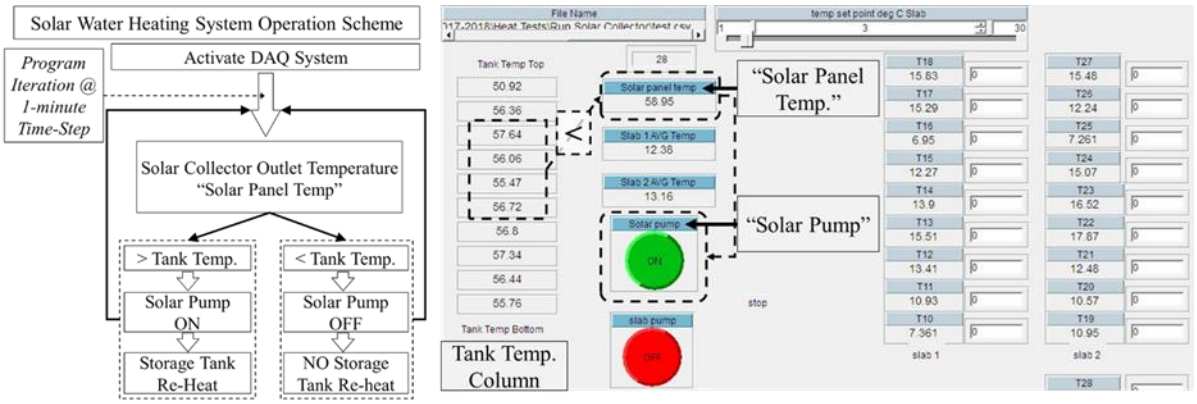

Figure 39: SWHS (a) operation scheme and (b) visual temperature-monitoring platform.

Hydronic Heated Pavement System

The hydronic heated pavement system (HHPS) transports thermal energy from the storage tank to the concrete test slabs for pavement heating. Slab 1 and Slab 2, in Figure 40, correspond to Slab 1 and Slab 2 in Figure 34(a). The concrete embedded hydronic grid consists of 19-mm PEX tubing configured in a reverse-return layout, Figure 40. The reverse-return layout provides equal heat distribution across the concrete surface (Wirsbo 2003). The PEX is spaced 22.8-cm on-center and embedded within the pavement slab 5-cm below the pavement surface.

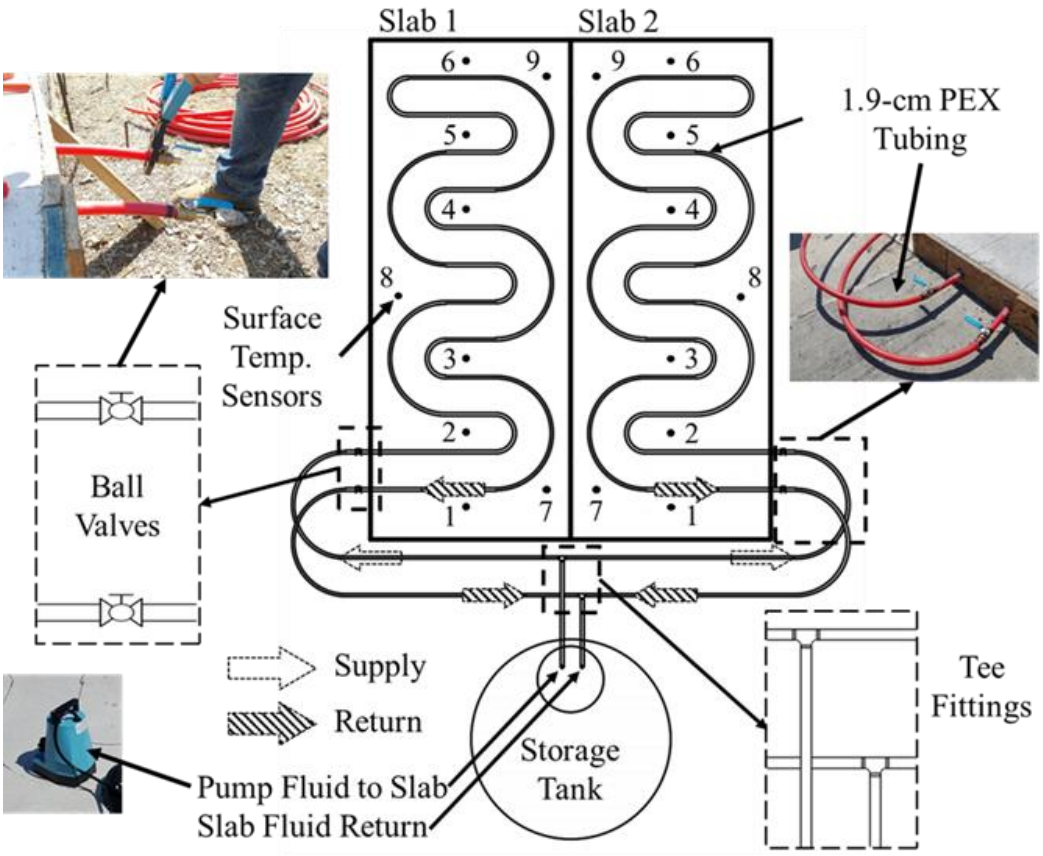

Figure 40: Schematic diagram of hydronic heated pavement subsystem.

The schematic diagram in Figure 40 details the hydronic grid connection and fluid flow. "Tee Fittings" connect the supply/return tubing from each slab to the supply/return tubing from the storage tank. Ball valves are located where the tubing exits the concrete for manual fluid flow control to each slab. A submersible pump in the storage tank circulates hot working fluid through each slab's hydronic tube grid. The pump is suspended in the storage tank from the supply PEX tubing between the 1135-L (300-gallon) and 1325-L (350-gallon) tank height, Figure 38. The average of the 1135-L (300-gallon) and 1325-L (350-gallon) tank fluid temperatures is used for the concrete slab inlet temperature ($T_{slab,i}$), Figure 38. Cooled fluid returning from the slab is discharged to the storage tank bottom ($T_{slab,o}$). $T_{slab,o}$ is represented by the 189-L (50-gallon) tank temperature reading, Figure 38.

An automated thermostat heating approach is used to maintain anti-icing slab surface temperature, and optimize electrical energy required for system operation. Type T thermocouples, connected to the DAQ, monitored and recorded slab surface temperature. Surface temperature sensors 2, 3, 4, and 5, in Figure 40, are mid-distant between the 22.8-cm spaced embedded tubing. Surface temperature sensors 1, 7, 8, and 9 are 11.4-cm from the tubing toward the slab edge. The ACS used these surface temperature readings to signal "on/off" heating operation.

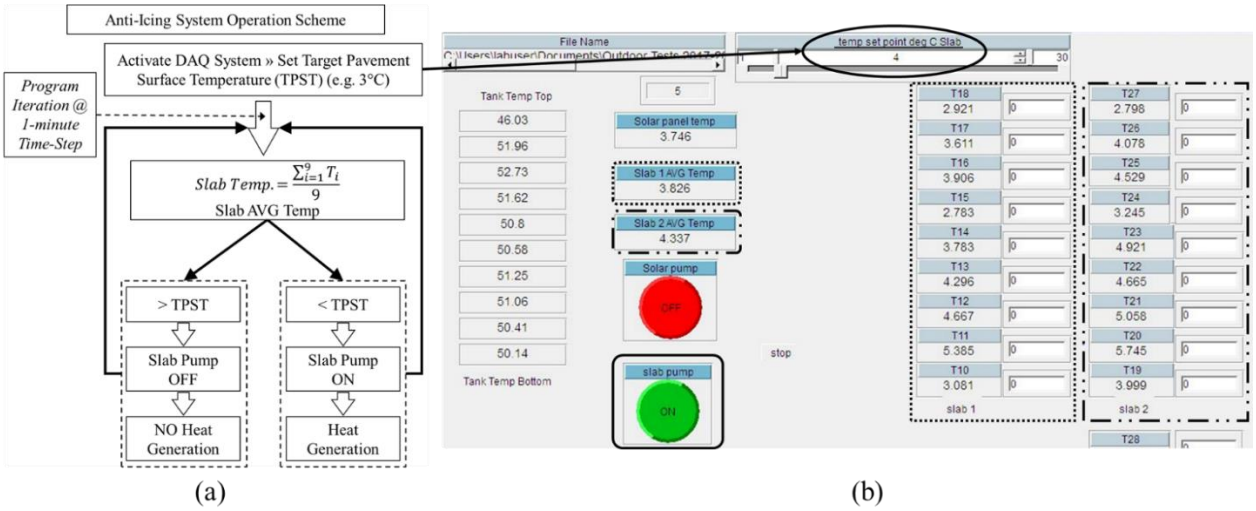

Figure 41: Hydronic heated pavement system's (a) operation scheme and (b) visual temperature-monitoring platform.

Figure 41 details the HHPS operation using the anti-icing operation scheme diagram, Figure 41(a) and the visual temperature-monitoring platform, Figure 41(b). Prior to activation, a target pavement surface temperature (TPST) is user-set. Researchers recommend a TPST from 2°C to 5°C to ensure anti-icing pavement conditions (Zhao et al. 2011). The nine thermocouple readings on each slab are averaged and indicated in Figure 41(b) as "Slab 1 AVG Temp" and "Slab 2 AVG Temp". If the "Slab (slab #) AVG Temp" for both slabs are greater than TPST, no fluid circulates through the hydronic grids, and the "Slab Pump" icon on the platform monitor remains "OFF". Conversely, if either slab has a "Slab (slab #) AVG Temp" less than TPST, the

pump circulates hot working fluid through the hydronic grid. The "Slab Pump" icon on the platform monitor reads "ON" during this flow sequence. Average slab temperatures are monitored at a 1-minute time interval.

Heat tests were performed during the time period when the slab surface temperature fell below the set TPST. Anti-icing tests were performed during man-made snow events at the testing facility. Results from the heat tests and anti-icing tests are included in Chapter 4.

Performance Analysis

Test cycles for both systems (SWHS and HHPS) were conducted over a 24-hour period. The SWHS testing period covered one full calendar day from 12:00 AM to 11:59 PM. Conversely, the HHPS testing period was conducted over a span of two consecutive calendar days starting and ending at 12:00 PM (noon). Electric grid energy powered the two submersible pumps included in the operating system. Energy consumption for each system operation was dependent on pump activation time.

SNOW MAKING

No natural snow events occurred during the 2017-2018 winter season. Consequently, a snowmaking machine was used to create wet snow for testing purposes, Figure 42. Manmade snow is produced by thermodynamically altering a pressurized mist. Consequently, snow production required adequate outdoor snowmaking air temperature and relative humidity. The snowmaking machine used in this work was capable of producing 17-mm of snow per hour with 74-m^2 ground coverage. Surveillance cameras at the test site captured real-time anti-icing operation performance during the snowmaking process.

Figure 42: Manmade snow with a snowmaking machine.

CHAPTER 4: FIELD EXPERIMENTATION RESULTS AND DISCUSSION

SOLAR – ELECTRICAL HEATED PAVEMENT SYSTEM APPROACH

System Operation Performance

Winter season testing was performed on solar-EHPS Slab 1. Initial outdoor tests were conducted over three days during a cold weekend in October 2017. The system was activated at 7:00PM on October 27, 2017 following sunset, with air temperature around 5°C and 3-meters per second (mps) wind speed. The TPST was set to 3°C. Figure 43 shows the average pavement surface temperature profile over the 3-day test period. The superimposed air temperature and wind speed are taken from the Drake Field weather station, 4.8-km from the testing facility (Weather Company 2018). The pavement surface temperature rose above the air temperature during sunlight hours and clear weather conditions. At night, the heating system ensured that the average pavement surface temperature was maintained at TPST during below-freezing air temperature and mild wind conditions. Heat tests during two nights, in below-freezing temperatures, validated the system's capability to sustain anti-icing temperature conditions.

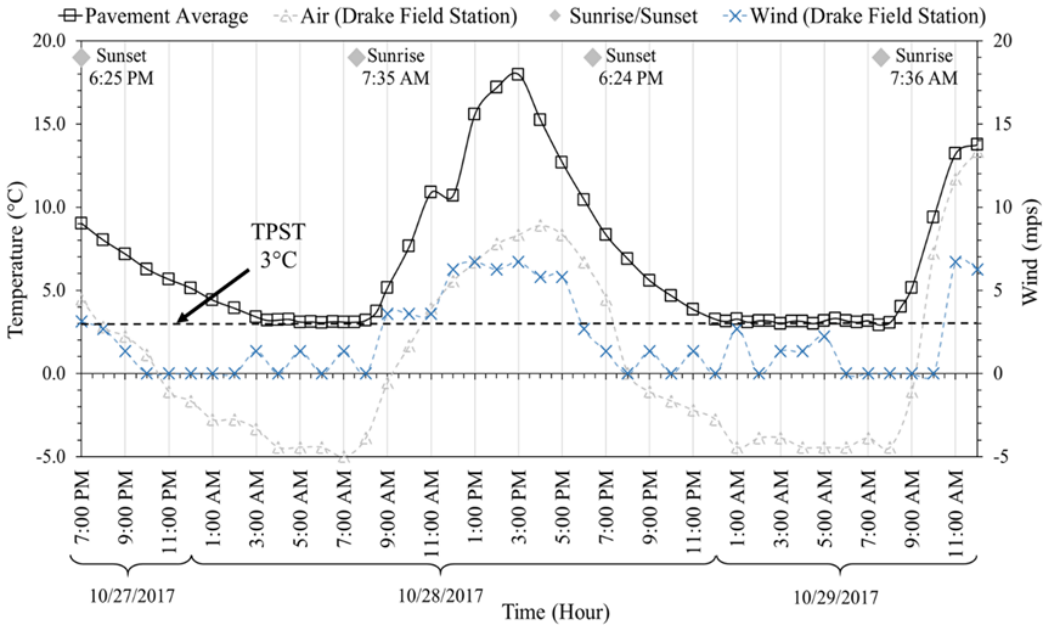

Figure 43: Electrical prototype grid system heating performance in subfreezing weather conditions.

System Energy Performance with PVES

Figure 44 shows the battery bank voltage curve in relation to the time-temperature profile of a heat test conducted between April 7, 2018 and April 8, 2018. Each "Sub" curve represents a "Heated Surface Subsection" on the test slab, Figure 31. When the prototype grid is activated, the voltage discharge remains relatively constant (6:00PM – 12:00AM) then decreases rapidly as the battery energy is depleted (3:30AM – 5:00AM). The voltage data were converted into power to equate the energy consumption during the prototype grid operating test cycle. Energy consumption during the 8.4-hour (11:35PM – 8:00AM) heating period was 2.1-kWh.

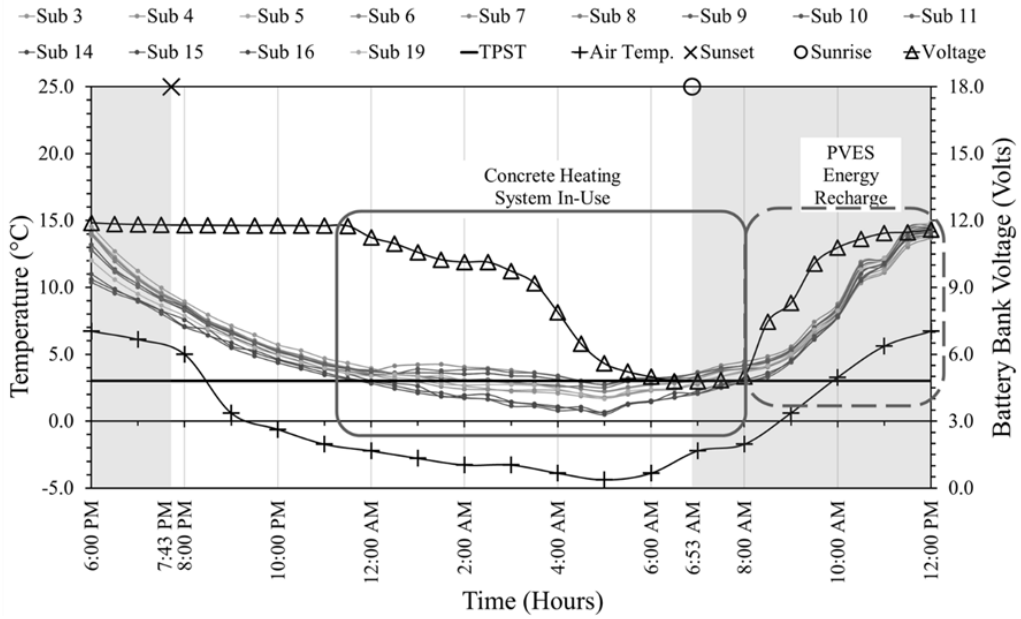

Figure 44: Outdoor heat test assessing energy consumption during prototype grid system operation.

The voltage discharge during system activation affects heat generation in the individual heat wires of the grid. As the voltage decreases, the rate of heat generation decreases quickly.

At sunrise, Figure 44 (6:53AM), prototype grid subsections were below TPST and pulled energy from the battery bank. After sunrise, radiant heat began warming the concrete surface while the solar array collected solar energy and transferred energy to the battery storage bank and the prototype grid. Before all the heated surface subsections reached TPST, the pavement was

heated through the combined effect of direct solar radiant energy and heat generated in the prototype grid. Once the slab surface reached TPST, Figure 44 (8:00AM), the battery bank began its recharging cycle with electric DC energy from the 200-W solar panel with no discharge. Battery recharging continued during daylight until sunset.

System Snow Melting Performance

An anti-icing experiment was conducted on December 7, 2017 to evaluate the prototype grid melting performance during a snow event. Wet snow was created using a snowmaking machine. The heating system was activated at 1:00AM on December 7, 2017 with a 3°C TPST, -4.4°C air temperature, and calm wind conditions. Figure 45 shows a temperature-time history curve of the prototype grid's heating/anti-icing performance considering transient outdoor weather conditions. Each "Sub" curve represents a "Heated Surface Subsection", Figure 31, on the test slab. The slab maintained an above freezing temperature for 3.5-hours prior to snowfall at 4:37AM. Snowfall began at 4:37AM, causing the surface temperature to drop below the TPST, but still remaining above 0°C. The snow continued until the end of the testing period at 11:00AM.

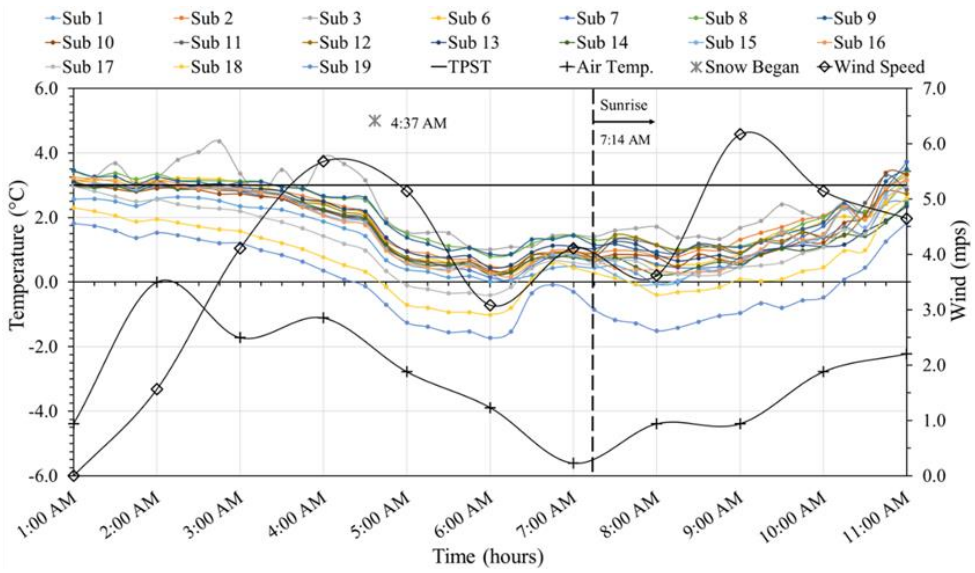

Figure 45: Test slab time-temperature profile for anti-icing performance (December 7, 2017).

A surveillance camera captured the slab snow melting process. Figure 46 shows the snapshot images at one-hour intervals during the 6-hour snow event. After the first hour (5:37 AM), a significant portion of the slab surface was wet with light snow accumulation near the slab edge. Prior to sunrise, the slab remained above freezing even with decreasing air temperature. After 7:37AM, sunrise, the slab temperature rebounded, with accompanying snow melting and draining. After a short period of time, snow began to accumulate over the majority of the slab surface due to discharged batteries caused by the energy demand over the long testing period. As the battery bank charge became depleted, current flow and corresponding heat generation through each heat wire dropped rapidly. The battery bank remained depleted during the early sunlight hours. After the batteries began recharging, energy was transmitted to the slab to maintain an above freezing slab surface temperature, Figure 45.

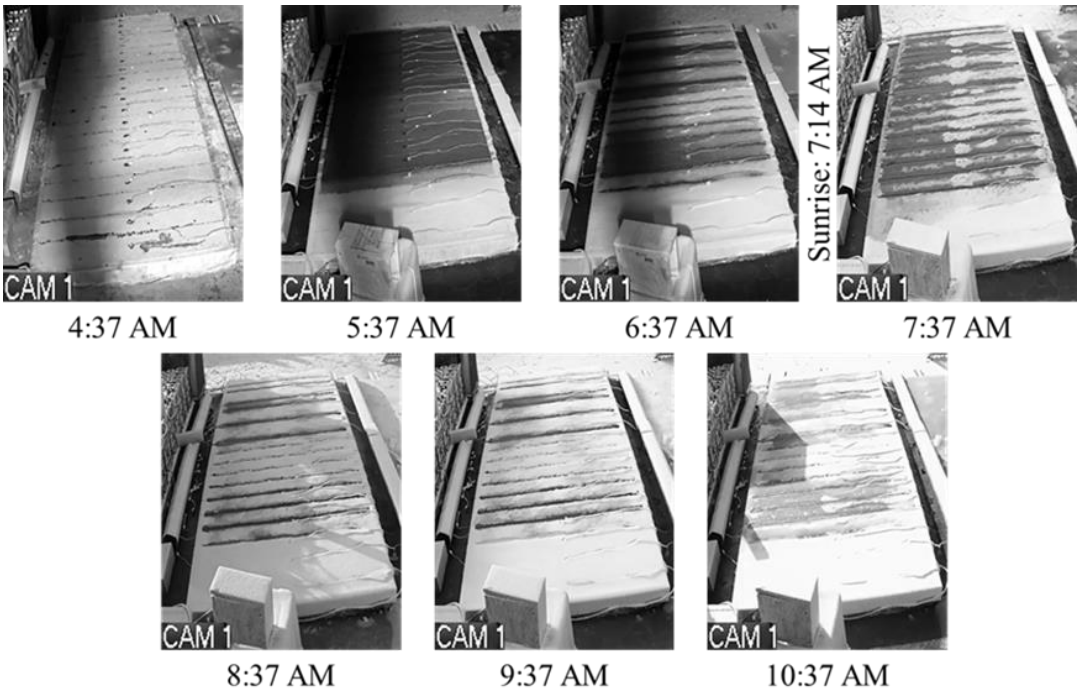

Figure 46: Prototype grid melting response during manmade snowfall.

SOLAR – HYDRONIC HEATED PAVEMENT SYSTEM APPROACH

Pavement Heat Test Operation Performance

Twenty-five (25) hydronic pavement heating test cycles were conducted over the 2017-2018 winter season. Table 10 summarizes the data collected for each test cycle with a 3°C pre-set TPST. The Table 10 "System Operation" column is the time between the slab pump's initial activation and final deactivation within the 24-hour test cycle. The pavement heating performance, tank temperature drop, and energy consumption are evaluated considering the air temperature and wind speed experienced during each test cycle's system operation.

Table 10: Hydronic Pavement Heating Test Cycles with 3°C TPST

Test Cycle* Date	System Operation (hr)	Air Temp. (°C) / Wind (m/s)			Avg. Slab	Tank Temp. (°C)			Energy Consumed	
		Low	Avg.	High	Temp. (°C)	Initial	Final	ΔT	Pump ON (hr)	kWh
12/6 - 12/7	11.0	-5.6 / 0.0	-2.0 / 2.6	3.3 / 5.7	2.9	65.2	50.3	14.9	6.2	0.77
12/9 - 12/10	14.1	-6.1 / 0.0	-3.3 / 1.8	5.6 / 4.6	3.2	43.2	37.5	5.7	2.6	0.32
12/10 - 12/11	9.4	-3.3 / 0.0	-1.1 / 1.5	1.1 / 3.1	3.2	46.7	40.7	6.0	1.3	0.16
12/12 - 12/13	11.5	-4.4 / 0.0	-0.8 / 2.2	5.6 / 5.7	3.3	54.9	47.2	7.7	1.2	0.14
12/13 - 12/14	3.8	-2.2 / 0.0	-0.5 / 0.8	3.3 / 2.6	3.6	51.8	49.4	2.4	0.4	0.05
12/14 - 12/15	9.5	-4.4 / 0.0	-2.5 / 1.1	-0.6 / 3.1	3.5	51.2	45.3	5.9	1.3	0.16
12/25 - 12/26	15.0	-6.1 / 0.0	-1.6 / 1.7	1.1 / 4.1	3.0	30.2	23.4	6.8	6.2	0.77
12/26 - 12/27	12.5	-8.9 / 2.6	-7.2 / 3.2	-5.0 / 4.1	1.4	27.9	20.9	7.0	12.2	1.51
1/13 - 1/14	16.7	-6.7 / 0.0	-3.1 / 1.1	0.0 / 3.1	3.1	47.3	33.7	13.7	4.4	0.55
1/14 - 1/15	18.0	-2.2 / 0.0	0.0 / 3.7	2.2 / 6.2	3.2	37.3	28.6	8.7	2.9	0.36
1/18 - 1/19	15.3	-1.1 / 0.0	0.6 / 4.0	5.6 / 7.2	2.5	31.2	21.4	9.8	12.1	1.51
1/22 - 1/23	5.4	-2.2 / 0.0	-0.3 / 2.9	1.7 / 6.2	3.1	40.8	37.4	3.4	1.2	0.15
1/23 - 1/24	12.6	-7.2 / 0.0	-4.5 / 0.8	0.0 / 2.1	3.1	46.1	33.4	12.8	4.0	0.49
1/24 - 1/25	9.8	-3.9 / 0.0	0.0 / 2.0	5.6 / 4.7	3.2	46.2	38.3	7.9	1.7	0.21
1/27 - 1/28	9.8	-6.1 / 0.0	-4.3 / 0.0	-1.1 / 0.0	3.2	56.1	45.8	10.3	2.2	0.28
1/28 - 1/29	9.3	-2.8 / 0.0	-1.3 / 2.1	1.1 / 4.6	3.3	53.9	47.6	6.2	1.2	0.15
2/1 - 2/2	12.7	-6.7 / 0.0	-3.8 / 2.1	0.6 / 4.1	3.2	55.0	44.3	10.6	3.3	0.41
2/2 - 2/3	7.2	-2.8 / 0.0	-1.2 / 0.8	0.6 / 3.1	3.3	53.8	46.4	7.4	1.2	0.15
2/11 - 2/12	10.4	-6.7 / 0.0	-5.4 / 2.9	-5.0 / 4.6	2.0	21.6	17.3	4.3	9.6	1.20
2/17 - 2/18	10.2	-3.9 / 0.0	-1.9 / 0.3	0.6 / 1.6	3.1	34.8	28.0	6.8	1.8	0.22
2/25 - 2/26	4.9	-0.6 / 0.0	0.1 / 0.9	0.6 / 2.6	3.1	34.9	33.3	1.6	0.3	0.03
3/1 - 3/2	5.2	-2.8 / 0.0	-2.1 / 0.0	-1.1 / 0.0	3.2	42.3	41.5	0.8	0.3	0.03
3/12 - 3/13	7.5	-5.0 / 0.0	-3.7 / 0.0	-2.2 / 0.0	3.3	67.8	59.6	8.2	1.0	0.12
3/13 - 3/14	5.9	-5.0 / 0.0	-3.6 / 0.7	-1.7 / 1.6	3.3	69.8	60.3	9.5	0.8	0.10
3/20 - 3/21	2.2	-3.3 / 0.0	-2 / 1.8	-1.1 / 3.1	3.3	74.0	73.1	0.9	0.1	0.05

*Test cycles span two consecutive days. Test labelling is represented as follows: month/day – month/day.

Figure 47 shows the pavement heating performance for the December 9-10, 2017 test cycle. The shaded section represents non-sunlight hours during the test cycle. Air temperature and wind

speed are superimposed on the Figure 47 temperature plot. The hydronic heated pavement system (HHPS) operation began at 5:44 PM. The pavement heating cycle lasted 14.1-hours. At startup, the pump was activated for 2-minutes followed by pump inactivity for 80-minutes. As the air temperature decreased, the pump activation time increased with shorter deactivation periods to maintain TPST. Figure 47 shows this on/off heating cycle behavior with the Slab 1 and Slab 2 temperature curves oscillating about the TPST throughout the 14.1-hour heated pavement system operation. During the 14.1-hour operation period, the HHPS pump operated for 2.6 hours using 0.32-kWh of electric energy. During the test period, the SWHS was inactive and the storage tank temperature dropped by 5.7°C. Temperature within the storage tank was depth independent.

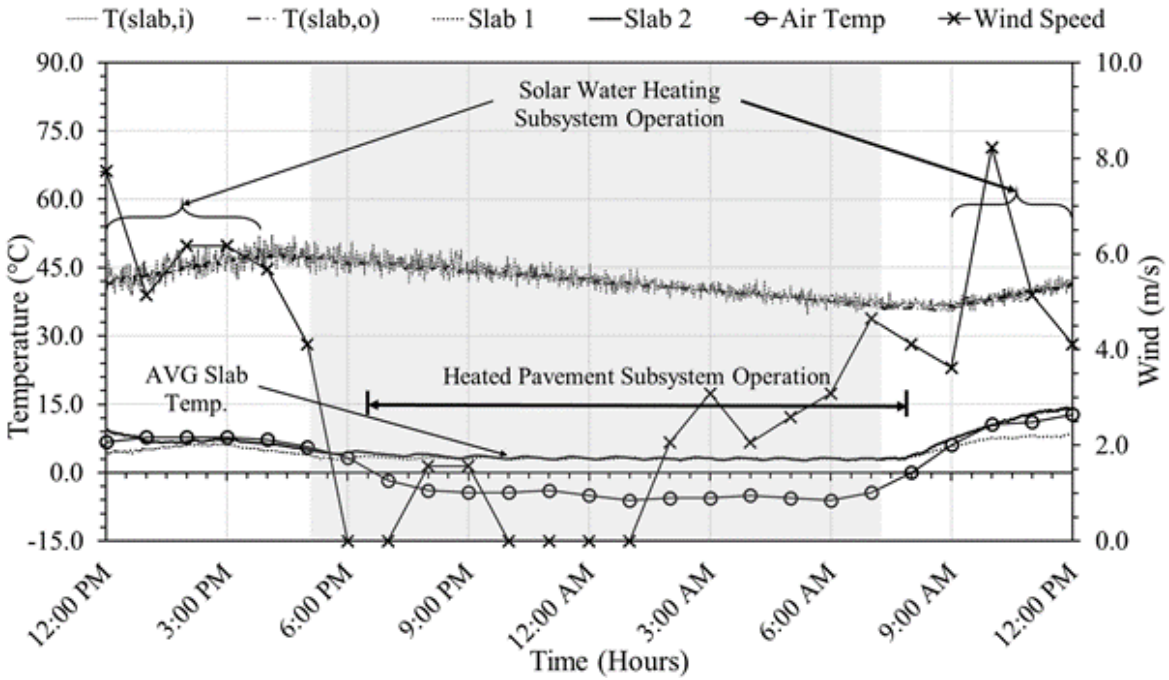

Figure 47: Hydronic pavement heating performance during December 9-10, 2017 test cycle.

Pavement Anti-icing Test Performance

An anti-icing experiment was conducted on December 7, 2017, during the December 6-7, 2017 heat test cycle. The HHPS was activated at 9:49 PM on December 6 to maintain a 3°C pavement surface temperature.

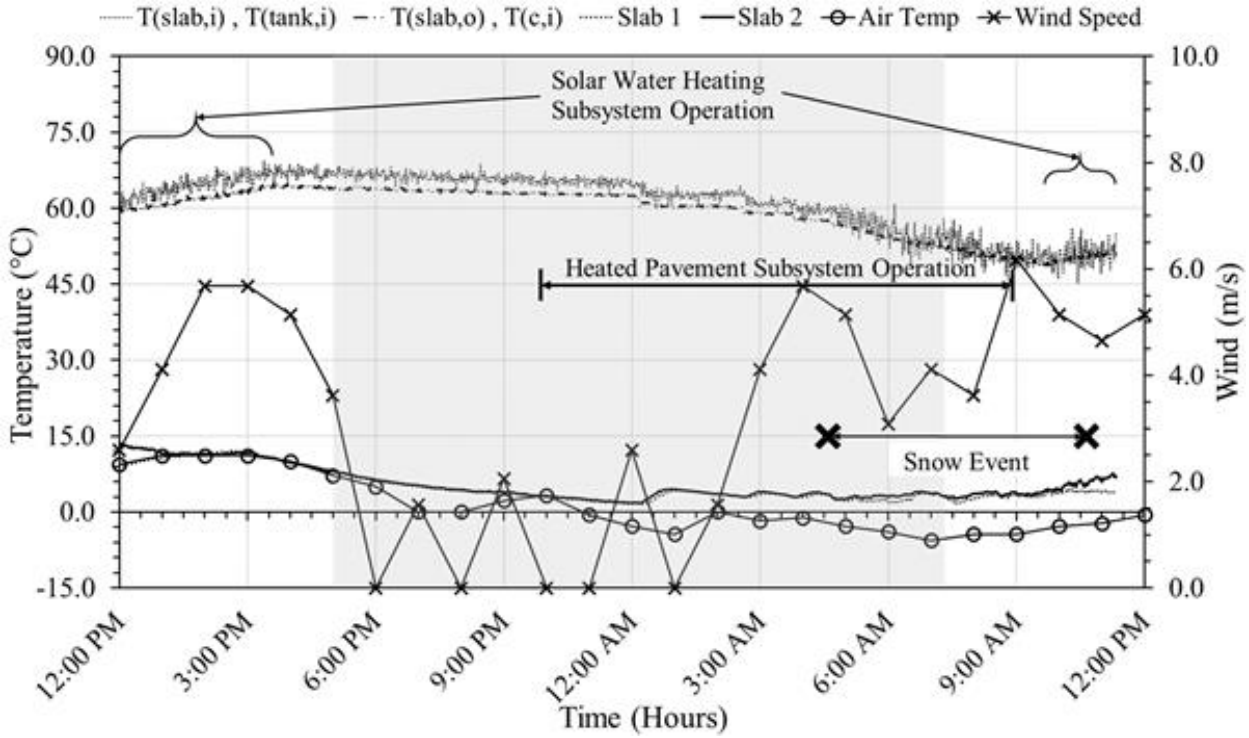

Figure 48: Hydronic pavement anti-icing performance during December 6-7, 2017 test cycle.

Snowfall, using a snowmaking machine, began at 4:37 AM on December 7, Figure 49. At that time, the storage tank fluid temperature was 60°C, Figure 48. Figure 49 shows one-hour interval snapshot images during the 6-hour snow event. No snow accumulated on Slab 1 or Slab 2 during the first hour, Figure 49. At 6:37 AM, snow began to accumulate along the pavement edges. Additional snow accumulated along the slab edges for the test duration. An infrared image taken at 8:53 AM with a thermal imaging infrared camera showed above freezing surface temperature in the snow-free area, Figure 49.

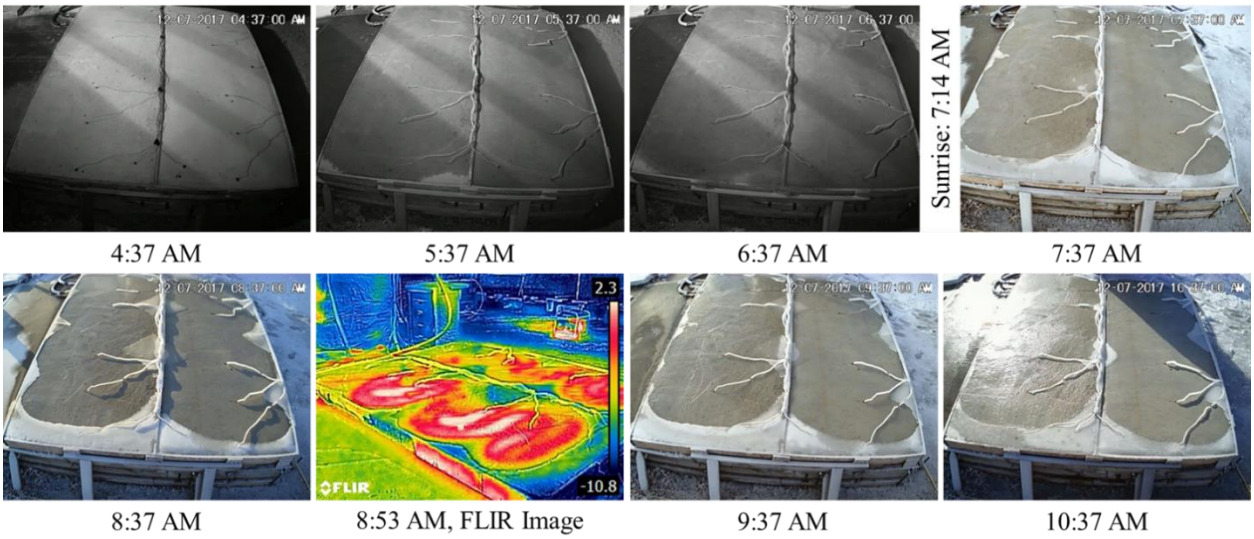

Figure 49: Hydronic pavement melting response during December 7, 2017 manmade snowfall.

Continuous pavement heating was required to maintain anti-icing surface conditions. As a result, the HHPS operated for 4.13-hours using 0.51-kWh of electrical energy. During the test period, the storage tank fluid temperature dropped from 60°C to 49.4°C.

Figure 50 shows snow accumulation on the HP-ETC's glass tubes the next morning. Snow/ice buildup on each tube reduces the HP-ETC efficiency. Since vacuum-sealed tubes do not transfer internal heat to the outer glass layer, snow and ice melting for the evacuated tubes depend on ambient temperature and solar radiation. This melting process can be time consuming and will affect the HP-ETC efficiency following snowfall.

Figure 50: Snowfall impact on HP-ETC.

Solar Water Heating System Energy Performance

Figure 51 shows the SWHS tank heating performance for the December 10, 2017 tank-heating test cycle. The test was conducted under clear sky conditions with 9.77-daylight hours. The shaded region to the left represents non-sunlight hours before sunrise (7:16 AM). The shaded region to the right represents non-sunlight hours after sunset (5:02 PM). The HP-ETC began collecting solar radiation after sunrise. Tank fluid heating was initiated when the HP-ETC outlet temperature ($T_{c,o}$) spiked at 8:50 AM, Figure 51. The air temperature and wind speed are superimposed on Figure 51. During the time the solar pump was activated, 7.43-hours, the storage tank fluid temperature increased 11.5°C.

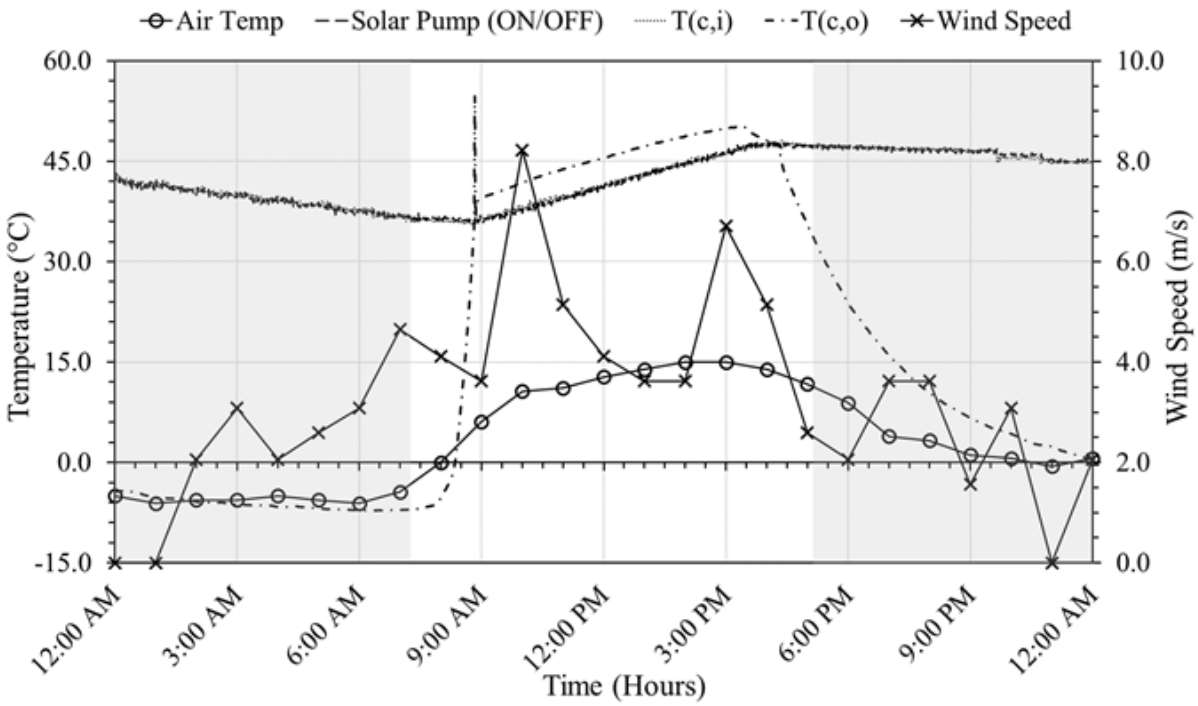

Figure 51: Storage tank heating performance on December 10, 2017

A SWHS energy performance analysis was conducted considering the following temperatures: working fluid temperature entering the HP-ETC manifold ($T_{c,i}$), working fluid temperature exiting the HP-ETC manifold ($T_{c,o}$), working fluid temperature entering the tank ($T_{tank,m}$), and working fluid temperature exiting the tank for heating ($T_{tank,b}$). Figure 38 shows these

temperature reading locations. The energy performance analysis evaluates the useable solar energy collected by the HP-ETC and its impact on the storage tank fluid temperature. The power collected by the HP-ETC is calculated using Eq. 3 at 1-minute intervals, where ṁ is the mass flow rate and C_p is the fluid's specific heat capacity (Kalagirou 2009, Ayompe and Duffy 2013).

$$Q_c = \dot{m} C_p (T_{c,o} - T_{c,i}) \quad (3)$$

Working fluid density and specific heat capacity are temperature sensitive and change as temperature increases. However, to simplify the calculations, each experiment assumed a constant mass flow rate (ṁ) and a working fluid specific heat capacity (C_p) that corresponded with the initial tank bottom temperature ($T_{(tank,b\_initial)}$). Table 11 is a summary of the computed values to calculate the HP-ETC total energy collected per experiment, multiplying the power by the duration of the tank-heating test cycle.

Table 11: Energy Performance Analysis Parameters

Experiment Date	Initial Tank Temp. $T_{(tank,b\_initial)}$	Solar Pump "ON" (hr)	ṁ (kg/s)	C_p (J/kg·°C)	$T_{c,i}$ (°C)	$T_{c,o}$ (°C)	Q_c (MJ)
12/6/2017 (c)	53.1	6.7	0.199	3,895.0	59.8	63.1	62.0
12/10/2017 (c)	35.5	7.4	0.200	3,855.2	42.2	45.8	74.4
12/13/2017 (c)	45.2	7.0	0.200	3,877.2	50.7	53.4	52.4
12/14/2017 (i)	48.5	4.8	0.199	3,884.5	50.1	51.6	20.1
12/26/2017 (c)	22.5	6.8	0.201	3,825.7	28.1	31.4	62.4
1/1/2018 (c)	14.3	6.6	0.202	3,807.1	21	24.6	65.2
1/2/2018 (o)	17.2	2.5	0.202	3,813.7	18.8	19.4	4.2
1/3/2018 (c)	12.8	7.2	0.202	3,803.7	19.7	23.5	75.6
1/14/2018 (o)	31.7	5.5	0.201	3,846.6	34.5	35.8	19.7
1/17/2018 (c)	11.2	7.3	0.202	3,800.0	18.1	22.2	82.7
1/23/2018 (i)	36.4	5.6	0.200	3,857.2	40.8	43.3	39.1
1/24/2018 (c)	33.5	7.4	0.201	3,850.5	39.7	42.9	65.5
1/28/2018 (c)	44.6	7.3	0.200	3,875.7	50.5	53.9	69.1
2/2/2018 (c)	42.2	7.3	0.200	3,870.4	48.7	52.2	71.5
3/13/2018 (c)	57.7	7.8	0.198	3,906.0	62.9	66.8	84.5

Note: (c), (i), (o) in the "Experiment Date" column indicate a clear, intermediate, or overcast weather condition, respectively.

Figure 52 and Figure 53 show the HP-ETC power time history curve for January 3, 2018 (clear sky conditions) and January 2, 2018 (overcast sky conditions). Fluid temperature entering and

exiting the HP-ETC manifold and the air temperature during the respective heating cycles are superimposed on the Figure 52 and Figure 53 plots. The shaded regions represent non-sunlight hours. The manifold temperature difference, $T_{c,o} - T_{c,i}$, is directly proportional to the power collected by the HP-ETC. In clear sky conditions, Figure 52, the manifold temperature difference was relatively constant, indicating a relatively constant power collection on the HP-ETC surface at each time interval.

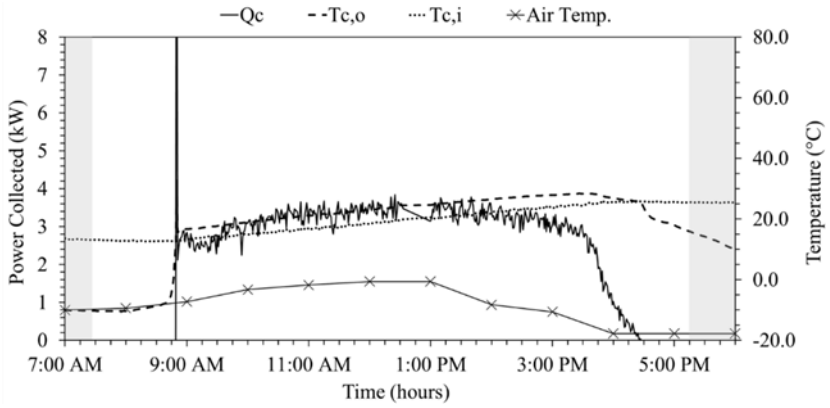

Figure 52: HP-ETC power curve during the January 3, 2018 tank-heating test cycle, clear sky conditions.

Conversely, the manifold temperature difference in overcast sky conditions, Figure 53, fluctuated under the transient weather conditions. Thus, the area under the power collected curve, Q_c, is the total energy collected by the HP-ETC for the tank-heating test cycle.

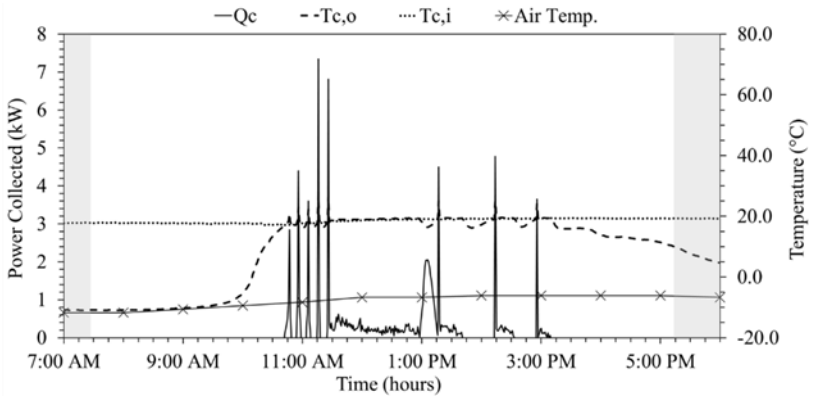

Figure 53: HP-ETC power curve during the January 2, 2018 tank-heating test cycle, overcast sky conditions.

Figure 54 shows the storage tank fluid temperature rise and tank-heating test cycle duration. During clear sky conditions, the two HP-ETC panels in series collected energy at an average daily power of 2.7-kW. For these conditions, the collected energy delivered heat to the storage tank fluid for an average 11.3°C temperature rise over an average 7.16-hour tank-heating operation time.

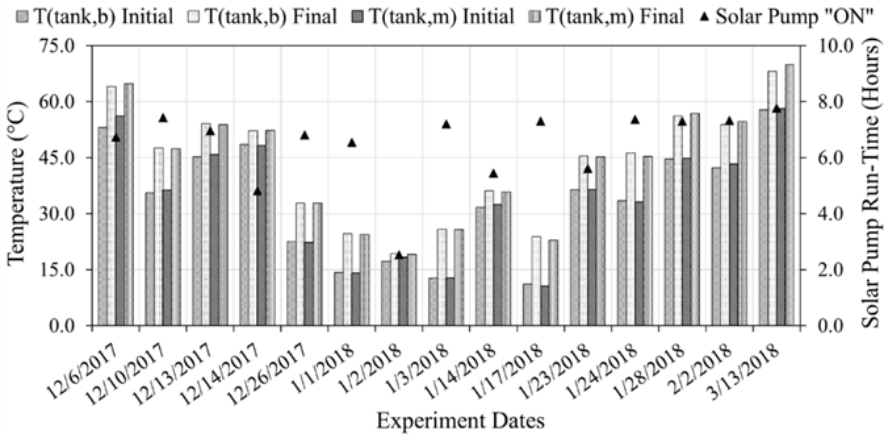

Figure 54: Storage tank fluid temperature rise using HP-ETCs.

Field Experimentation Summary

Solar-EHPS

The anti-icing scheme used for the large-scale solar-EHPS utilizes the automated thermostat heating sequence. Energy was continually supplied to the outdoor test slab to ensure an above-freezing pavement temperature in below-freezing ambient conditions. This energy protocol was used to eliminate needing a power surge for snow/ice removal. Heat operation is by zone and is surface temperature-dependent. Preliminary testing conducted on the 1.22-m x 3.05-m concrete test slab validated the approach and showed a sustained temperature above a set anti-icing temperature in freezing air temperature and mild wind conditions. The battery storage bank supplied enough energy to maintain the TPST for 3.5-hours and above 0°C for the test duration. Proper battery bank sizing capacity is required for developing a relatively constant slab temperature for the entire test duration. Testing showed that battery energy depletion

compromised proper heat generation, and that this resulted in some snow-accumulation on the pavement surface. However, increasing the battery bank size is costly. Therefore, advances in electrical energy storage technology are warranted in order to improve the attractiveness of using a PVES within an electrical AHPS.

Solar-HHPS

For the solar-HHPS, results showed that the SWHS with HP-ETCs provided adequate thermal energy to maintain concrete surface temperatures above freezing. In -5.4°C air temperature, the test slabs maintained an average 2.0°C surface temperature using heated fluid from a storage tank with an initial 21.6°C storage tank fluid temperature. The low initial storage tank fluid temperature required longer pump operation periods, but the storage tank fluid temperature drop was minimal. An anti-icing test was performed during a pavement heating test cycle. The pavement maintained a snow-free surface during a 6-hour manmade snowfall in subfreezing ambient conditions. Continuous HHPS operation was required resulting in the storage tank fluid temperature decreasing by 11.6°C. The presented solar water heating system consisting of two in-series HP-ETCs raised the storage tank temperature 11.5°C during winter daylight hours and clear sky conditions. In clear sky conditions, the HP-ETC collected an average daily power of 2.7-kW. The maximum storage tank fluid temperature recorded during the study period was 74.0°C. Future research should record on-site solar irradiance in order to calculate the HP-ETC efficiency. This calculation will aid in optimizing the SWHS configuration. A HHPS for the airport apron area coupled with a SWHS has the potential to maintain anti-icing pavement conditions during airfield winter operation. Additionally, the SWHS proximity to the airport terminal has the potential for providing year-round economic benefits for terminal building heating and cooling.

CHAPTER 5: FINITE ELEMENT ANALYSIS

INTRODUCTION

The solar-EHPS's near-surface prototype grid approach is site specific to the weather and light conditions of Fayetteville, Arkansas. Thus, a finite element model (FEM) was developed to extend the experimental prototype grid analysis to U.S. commercial airports in other climatically cold regions, which include the Upper Midwest region, the Ohio Valley region, and the Northeast region (NOAA 2017b). The discussed finite element analysis (FEA) examines weather-specific pavement heating requirements and pavement heat distribution. COMSOL Multi-Physics software was used to build the two-dimensional, heat transfer, time-dependent numerical model (COMSOL 2018).

METHODOLOGY

The FEM development and analysis were conducted in four phases as shown in Figure 55. Phase details are provided in the next text sections.

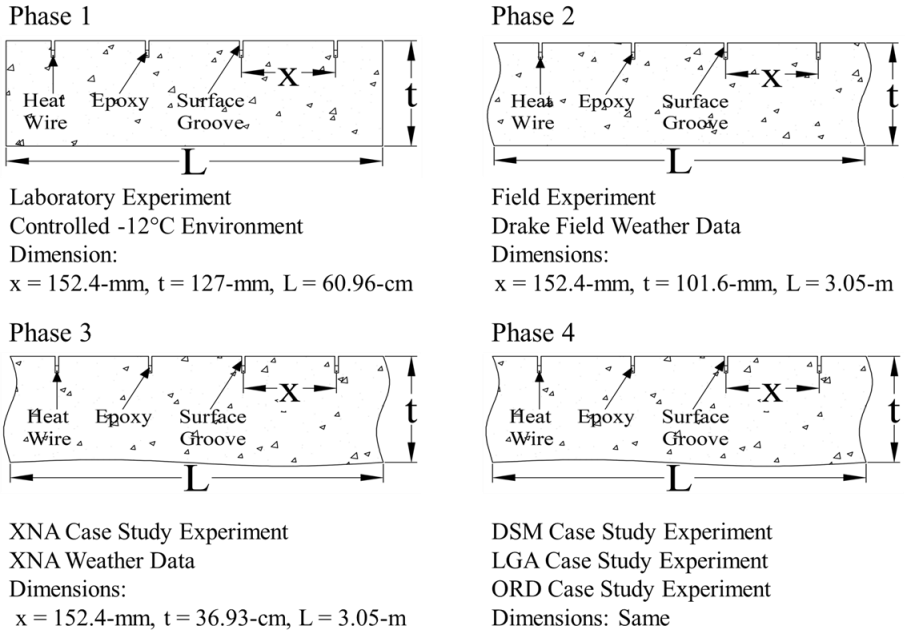

Figure 55: Finite element model development and analysis phases. The airport codes DSM, LGA, and ORD, represent Des Moines International Airport, LaGuardia Airport, and O'Hare International Airport, respectively.

Phase 1: FEM Calibration

The FEM was created and calibrated in Phase 1. The model geometry used the cross-section dimensions of Test Mat 2 (TM2), from the "Slab Surface Temperature Distribution using the Fully Activated System" section discussed in Chapter 3. Model calibration used the surface heat distribution test conducted in the freezer chest with 9-amp current supply to each near-surface embedded heat wire. Material properties, boundary conditions, and heat loads were adjusted for model verification.

Phase 2: FEM Validation

In Phase 2, the calibrated FEM simulated the solar-EHPS Slab 1 heating considering Fayetteville, Arkansas weather conditions. An ASHRAE climate data tool in COMSOL can incorporate time-dependent weather conditions to the model as a function of date, time, and weather station. Thus, air temperature, wind speed, and relative humidity taken from the Drake Field weather station are applied to the model and change automatically within the time-dependent simulation. This same process is followed in Phase 3 and Phase 4. The model geometry was adjusted to meet the solar-EHPS Slab 1 cross-section dimensions. Results from the solar-EHPS field experimentation validated the FEM.

Phase 3: XNA Study

In Phase 3, the validated solar-EHPS Slab 1 model was used to simulate pavement heating under Northwest Arkansas Regional Airport (XNA) weather conditions. The XNA weather station was selected in the ASHRAE climate data tool. The model geometry was adjusted to meet XNA pavement design thickness.

Pavement Design Thickness using FAARFIELD

FAA's FAARFIELD airport pavement design computer program was used to generate the pavement design thickness for this study (FAA 2009). The design was for a rigid pavement with

a 20-year design life. FAARFIELD required data for aircraft categories that depart from XNA, annual aircraft departure statistics from XNA, and annual aircraft operation growth rate.

Table 12: XNA Aircraft Departure Statistics

Number of Departures per Week (5/31/2018-6/6/2018)			
A319-100 STD	**A320-100**	**B717 HGW**	**B737-800**
4	3	6	4
Hawker-800XP	**D-30**	**Citation-X**	**Falcon-2000**
1	3	2	3
RegionalJet-200	**RegionalJet-700**	**EMB-175std**	**ERJ-135**
34	36	49	2
ERJ-145 ER	**EMB-170 STD**	**MD83**	**MD90-30 ER**
43	87	16	6
Number of Departures per Year			
A319-100 STD	**A320-100**	**B717 HGW**	**B737-800**
208	156	312	208
Hawker-800XP	**D-30**	**Citation-X**	**Falcon-2000**
52	156	104	156
RegionalJet-200	**RegionalJet-700**	**EMB-175 STD**	**ERJ-135**
1768	1872	2548	104
ERJ-145 ER	**EMB-170 STD**	**MD83**	**MD90-30 ER**
2236	4524	832	312

*Note: Bold text are the category aircraft that depart from XNA.

Table 12 shows the 16 aircraft categories that depart from XNA. A modified data collection determined the number of aircraft category departures at XNA in one week using FlightExplorer.com (Flight Explorer 2018). The annual departure statistics per aircraft category were estimated by multiplying the one week data by 52. According to the 2016 FAA Forecast, the annual flight growth rate is 2.8-percent (FAA 2016). These data were loaded into the FAARFIELD program for design. Figure 56 shows the generated XNA pavement design thickness used for the FEM model geometry discussed in this study.

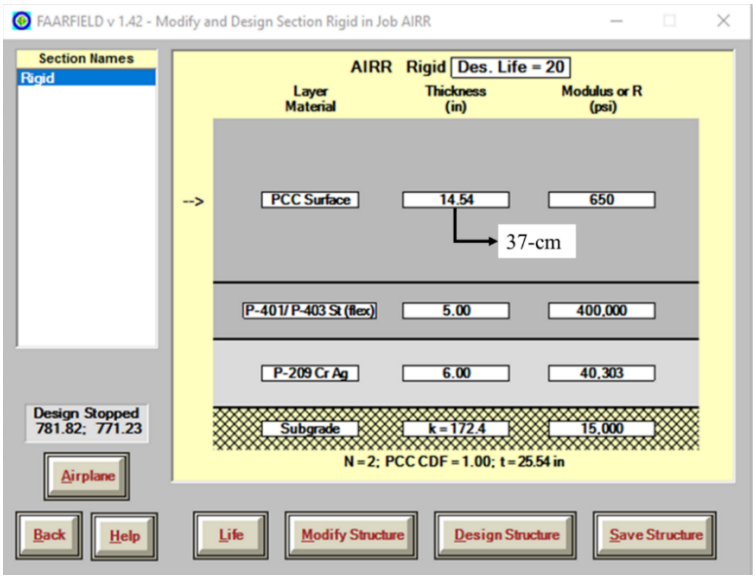

Figure 56: FAARFIELD's XNA pavement design thickness profile.

Phase 4: Cold Region Airport Study

In Phase 4, the validated solar-EHPS Slab 1 model from Phase 3 was used to perform simulations to assess the pavement surface heating requirements at U.S. commercial airports representing airports in cold region areas throughout the nation. Des Moines International Airport (DSM) was selected to represent the Upper Midwest region. Chicago's O'Hare International Airport (ORD) was selected to represent the Ohio Valley region. LaGuardia Airport (LGA) was selected to represent the Northeast region. Figure 57 shows the airport locations. Four simulations were performed for each airport's analysis considering the winter weather conditions in November, December, January, and February.

Figure 57: Climatically consistent regions map with airport locations (NOAA 2017b).

For each airport's respective analysis, the airport's weather station was selected in COMSOL's ASHRAE climate data tool. As stated in "Phase 2: FEM Validation", the climate data tool applies recorded weather conditions to the pavement heating simulation from a specific weather station for a selected date and time. The date and time selected in each airport's respective COMSOL analysis considers the airport's 10-year average winter weather conditions in November, December, January, and February. The date within November 2017, December 2017, January 2018, and February 2018, which best reflects their respective 10-year monthly averages for air temperature, dew point, wind speed, and relative humidity was chosen. The 10-year winter weather statistics for DSM, ORD, and LGA were obtained from NOAA (2017a).

FEM RESULTS AND DISCUSSION

Phase 1: FEM Calibration

The preliminary FEM model was developed to analyze the laboratory heat testing of the near-surface electrical prototype grid. Figure 58 shows the two-dimensional concrete test mat cross-section. The surface grooves have a 3.175-mm width, 15.875-mm depth, and are spaced 152.4-mm apart. The heat wire depth is 14.41-mm and the epoxy height in the groove is 9.65-mm. A natural convection boundary condition was used for the FEM along the concrete surface and an insulation boundary condition was applied to the concrete cross-section sides and bottom. A heat generation load was applied to each heat wire as a function of current supply. Heat transfer simulation analyzed temperature at the surface node mid-distant between adjacent grooves.

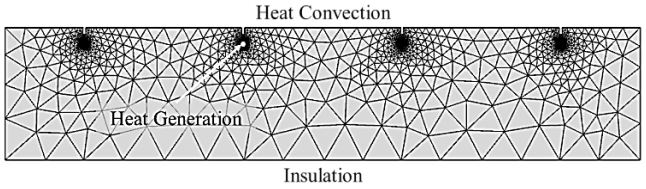

Figure 58: Laboratory test mat 2 (TM2) FEM cross-section.

Figure 59 compares the calculated FEM average surface temperature rise to the average surface temperature rise of the experimental slab. The FEM curve underestimates the experimental curve. However, the average surface temperatures converge with time.

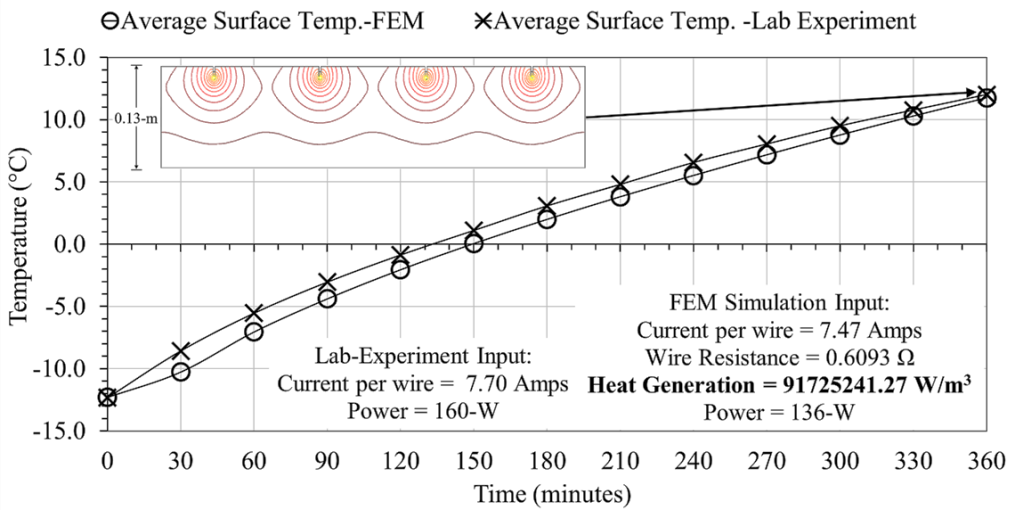

Figure 59: FEM and lab test mat surface temperature distribution comparison.

The Figure 59(inset) is an isothermal contour image showing the cross-section heat distribution as a function of depth. Table 13 shows the material properties for the heat transfer analysis. These properties were assumed to remain constant during the FEM analysis.

Table 13: FEM Material Properties

Material Properties			
Material	Density	Thermal Conductivity	Heat Capacity
	kg/m^3	W/m·°C	J/kg·°C
Concrete	2313.1	1.6	1036.0
NiChrome Heat Wire	8420.0	11.3	460.0
Epoxy	1025.7	1.0	1000.0

Phase 2: FEM Validation

The Phase 2 FEM validation used the solar-EHPS Slab 1 heat test results from the December 7, 2017 heating and snow melting experiment. Only a section of the solar-EHPS Slab 1 was considered in order to simplify the evaluation, Figure 60.

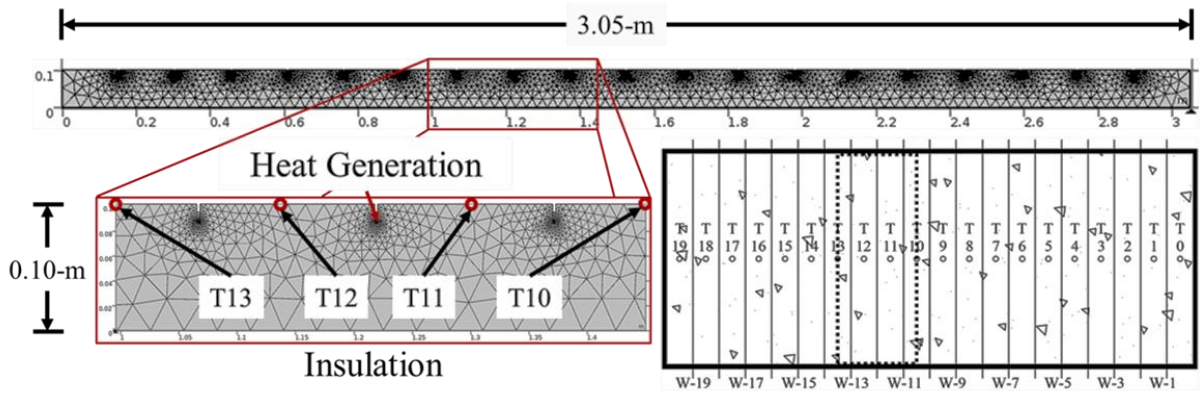

Figure 60: Solar-EHPS Slab 1 cross-section (top), evaluated cross-section (bottom left), and surface diagram (bottom right).

Figure 61 compares the calculated FEM average surface temperature rise to the average surface temperature rise of the field test slab. A conservative FEM simulation was used for comparison by assuming the wire heat generation in the FEM model to be constant in contrast to the actual gradual heat generation reduction caused by energy usage from the battery storage bank. The Figure 61(inset) is an isothermal contour image showing a segment of the cross-section heat distribution as a function of depth. The cross-section heat distribution in the Figure 61(inset) creates a saddle-shape between the embedded heat wires. Conversely, the cross-section in Figure 59(inset) shows a radial heat distribution around the embedded heat wire. This change in temperature distribution is due to wind effects and transient ambient conditions applied to the FEM.

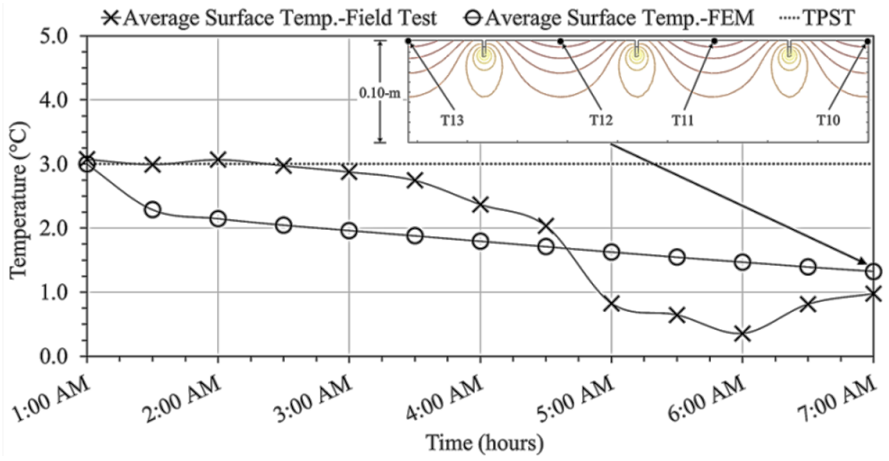

Figure 61: FEM and solar-EHPS Slab 1 surface temperature distribution comparison.

Phase 3: XNA Study

Heat transfer simulations were performed on the FEM model considering XNA weather conditions. A sensitivity analysis was conducted on the wire current supply to determine the heat generation rate required to maintain the concrete surface temperature at a 3°C TPST. Figure 62 compares the concrete surface temperature under a heating simulation and a non-heating simulation scenario using ambient conditions on December 23, 2017 from 12AM to 6AM. The surface temperature measurements are taken at the surface node equidistant between each wire/groove. The initial concrete temperature was set to 3°C since the solar-EHPS is designed to activate when surface temperature falls below the TPST. Figure 62 shows the temperature drop due to ambient conditions followed by the temperature gain to attain TPST during the 6-hour simulation. The heat generation per wire is given in Figure 62.

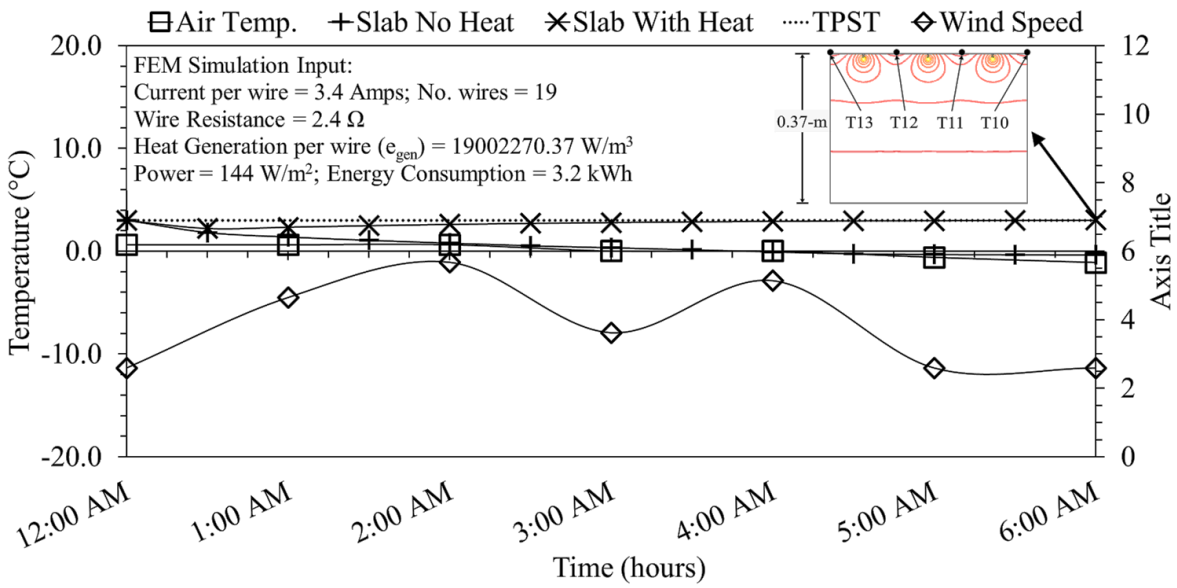

Figure 62: FEM heat testing simulation for XNA pavement.

The Figure 62(inset) is an isothermal contour image showing a segment of the cross-section heat distribution as a function of depth. The contour shape shows temperature variability at the surface, which creates a saddle shape between adjacent heat wires. Marginal temperature variability is identified at increased depths.

Phase 4: Cold Region Airport Study

Heat transfer simulations were performed on the solar-EHPS Slab 1 model under DSM, ORD, and LGA weather conditions. Figure 63, Figure 64, and Figure 65 compares the concrete surface temperature under a non-heating simulation, a heating simulation, and a pre-heating to a 3°C TPST simulation scenario using ambient conditions on January 17, 2018 for DSM, January 15, 2018 for ORD, and January 15, 2018 for LGA. Simulations performed under each airport's weather condition for November 2017, December 2017, and February 2018 are in Appendix E. Time-related air temperature and wind speed on the dates used in each simulation are superimposed on Figure 63, Figure 64, and Figure 65.

Table 14: Airport Snowfall Statistics and Average January Weather Statistics

Selected Airport Code	DSM	ORD	LGA
Snowfall Hours per Winter Season (hours)	105	100.5	50.6
Snowfall Amount per Winter Season (cm)	71	75	53
Winter Days with Snowfall (days)	21	23.1	9.2
Snowfall Duration per Day (hours/day)	5	4.35	5.5
January Avg. Air Temperature (°C)	-5	-5	0.56
January Avg. Dew Point (°C)	-10	-8.33	-7.22
January Avg. Wind Speed (m/s)	4.9	4.9	5.3
January Avg. Relative Humidity (%)	69	72	58

Table 14 includes the annual snowfall data, and the 10-year average January weather statistics for DSM, ORD, and LGA. The simulated heating duration was based on the snowfall duration per day plus two-hours accounting for pavement preheating time, Table 14. Each analysis for all three simulations began at 12:00 AM with the initial model temperature at 0°C. Under the heating simulation, a sensitivity analysis was conducted on the wire current supply to determine the heat generation rate and heat flux required to achieve the concrete surface at 3°C TPST. Under the pre-heating simulation, a sensitivity analysis was conducted on the wire current supply to determine the heat generation rate and heat flux required for the two-hour surface pre-heating from 0°C to 3°C TPST.

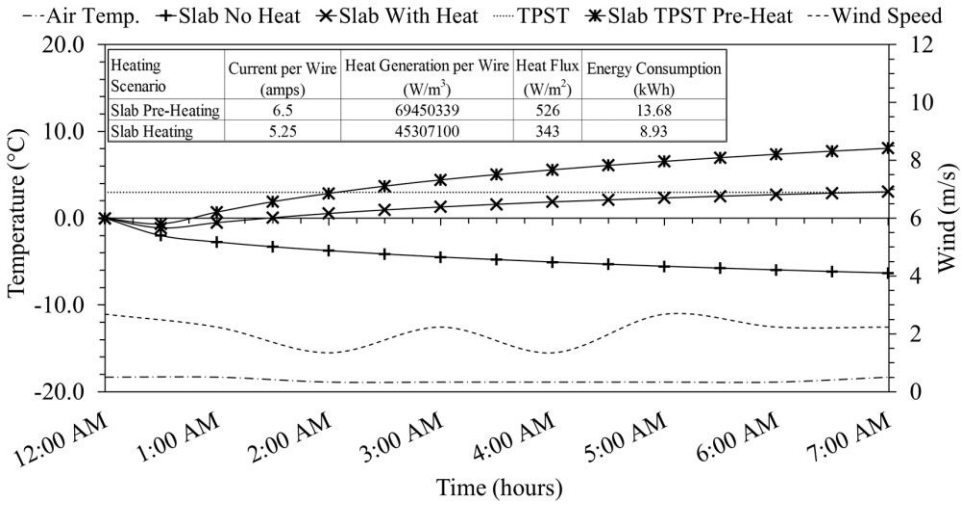

Heating Scenario	Current per Wire (amps)	Heat Generation per Wire (W/m^3)	Heat Flux (W/m^2)	Energy Consumption (kWh)
Slab Pre-Heating	6.5	69450339	526	13.68
Slab Heating	5.25	45307100	343	8.93

Figure 63: FEM heat testing simulation for DSM pavement on January 17, 2018.

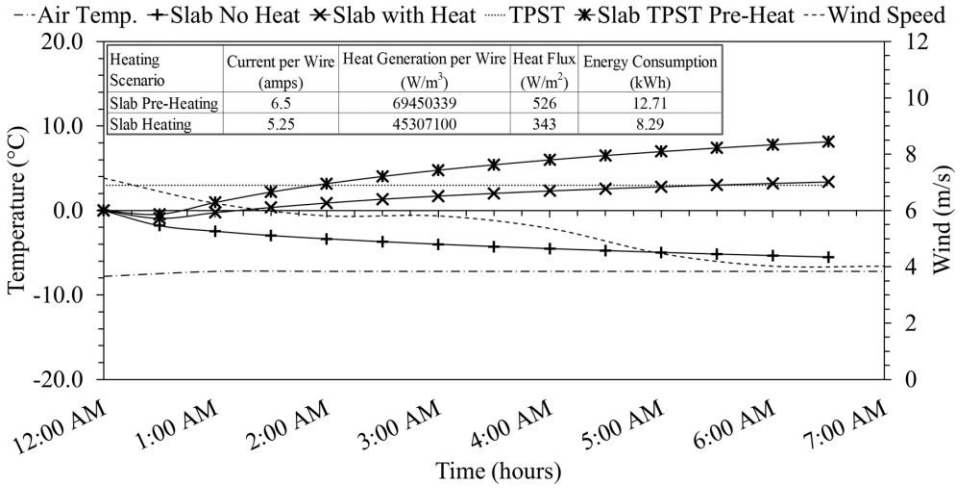

Heating Scenario	Current per Wire (amps)	Heat Generation per Wire (W/m^3)	Heat Flux (W/m^2)	Energy Consumption (kWh)
Slab Pre-Heating	6.5	69450339	526	12.71
Slab Heating	5.25	45307100	343	8.29

Figure 64: FEM heat testing simulation for ORD pavement on January 15, 2018.

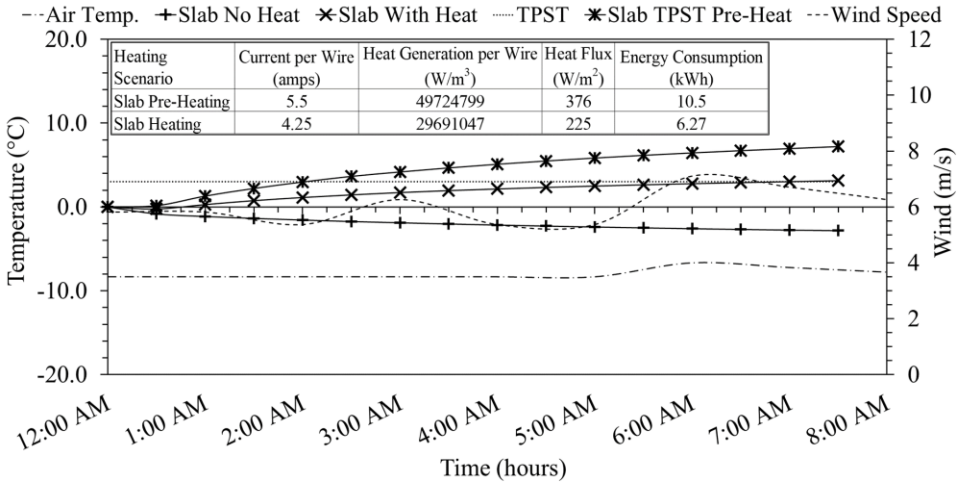

Heating Scenario	Current per Wire (amps)	Heat Generation per Wire (W/m^3)	Heat Flux (W/m^2)	Energy Consumption (kWh)
Slab Pre-Heating	5.5	49724799	376	10.5
Slab Heating	4.25	29691047	225	6.27

Figure 65: FEM heat testing simulation for LGA pavement on January 15, 2018.

Figure 63, Figure 64, and Figure 65 show the temperature time history, wind time history, and power requirement for each simulation scenario. The pavement pre-heating and pavement heating simulations indicate the upper and lower heat flux boundaries, respectively, to achieve and maintain anti-icing conditions when the pavement heating system activates at a 0°C pavement surface temperature.

SUMMARY

The finite element model extended the solar-EHPS's near-surface prototype grid approach to analyze pavement-heating requirements at XNA and airports representing the Upper Midwest, Ohio Valley, and Northeast climatic regions. The pavement heating performance and their respective heat flux are indicative of their ambient weather conditions and a constant energy supply to the near-surface embedded heat wires. Pre-heating the pavement requires a greater heat flux, whereas maintaining the pavement at TPST requires a reduced heat flux, but a continuous energy supply. To be coupled with a photovoltaic energy system, the energy storage sizing must have the capacity to deliver the heat flux required for the duration of a storm before the battery storage bank becomes energy depleted.

Additionally, a high heat flux for pavement pre-heating will induce higher thermal stresses at the concrete surface, causing durability issues. Future prototype grid development should evaluate the thermal stresses produced by near-surface heating and multiple cyclic heating cycles.

CHAPTER 6: BENEFIT COST ANALYSIS

INTRODUCTION

A benefit-cost analysis (BCA) extended the solar-hydronic heated pavement system (solar-HHPS) analysis to justify, economically, the system's implementation potential at the Northwest Arkansas Regional Airport (XNA) apron area. The Federal Aviation Administration (FAA) specifies using a BCA to evaluate airport alternative projects (FAA 1999). Figure 66(a) shows the FAA's BCA process. In 2017, Anand et al. (2017) developed a BCA spreadsheet tool to evaluate airfield heated pavement systems (AHPS) as a pavement snow and ice control alternative. The tool follows the FAA BCA guidance. The Anand et al. (2017) AHPS BCA spreadsheet tool evaluates the theoretical energy and financial viability of a conventional HHPS for airfield implementation. Conventional HHPSs use electric or oil-fired boilers as the working fluid heat source.

The AHPS BCA tool was previously validated through multiple case studies. These case studies assessed the energy and financial viability of a conventional HHPS at the apron area of three commercial airports and two general aviation airports (Anand et al. 2017). Anand et al. (2017) concluded that the AHPS BCA tool is suitable in an airport's investigation to install and operate any type of HPS at a specified air operations area (AOA) given "airport-specific data." Consequently, the BCA discussed in this dissertation was conducted using the AHPS BCA spreadsheet tool and followed the analysis process shown in Figure 66(b).

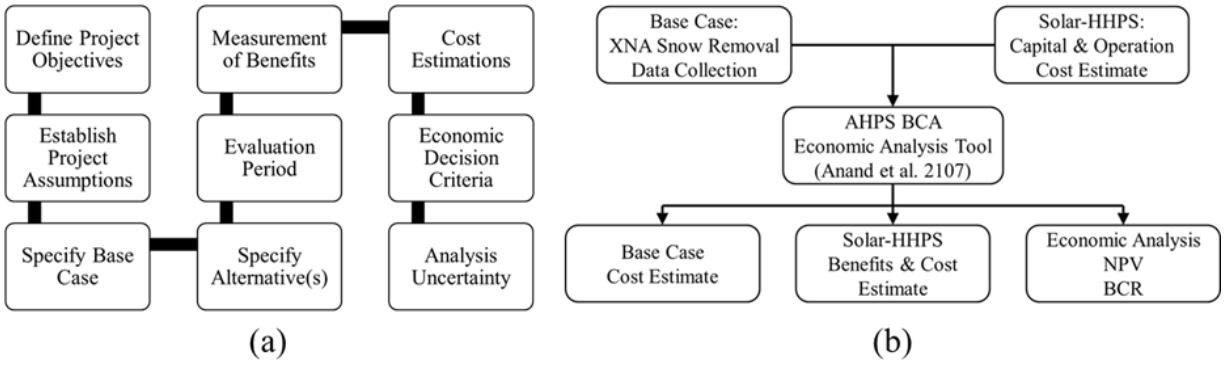

Figure 66: Benefit-cost analysis flow diagram

METHODOLOGY

The procedures outlined in Anand et al. (2017) were followed to execute the BCA for the solar-HHPS approach. The spreadsheet tool was modified to estimate the solar-HHPS cost using cost data from the field experimentation setup and operation described in this dissertation. The sections below detail each procedure shown in Figure 66(b).

Base Case –Snow Removal/Airport Data Collection

Cold region airports use the conventional pavement deicing method, with snow removal equipment (SRE) and pavement deicing products (PDPs), to remove snow and ice from the AOA. However, the SRE fleet size and PDP application rate is a function of AOA size and weather conditions. Therefore, data collection investigating an airport's snow removal operation should include the:

- AOA size,
- sum of SRE and SRE cost,
- SRE fuel capacity and usage rate, and airport fuel cost,
- PDP type, average PDP application rate, and unit cost of PDP,
- total number of snow removal personnel and labor cost, and
- the snow removal routine described in the airport's snow and ice control plan (SICP).

Data collection are best attained through direct or indirect correspondence with the airport's operations management staff. Additional airport-specific data that are required for the spreadsheet tool include:

- the projected growth in airport activity (FAA 1999),
- the future changes in airport facilities and capacity (FAA 1999),
- the airport's winter climate history (NOAA 2017a), and
- flight operation statistics.

This additional data collection is best attained through online data sources. To monetize the heated pavement system benefits, flight statistics are required.

Alternative – Solar-HHPS Field Experimentation Data Collection

The solar-HHPS valuation assesses the hydronic heated pavement system (HHPS) and solar water-heating system (SWHS) separately, and is based on the field experimentation equipment cost and operation cost. The HHPS equipment include cross-linked polyethylene tubing (PEX), Portland cement concrete, working fluid, storage tank, and a fluid circulation pump. The SWHS equipment include solar water-heating collectors, supply and return tubing, and a fluid circulation pump. The operation cost was determined based on the pavement heating and storage tank fluid heating test cycles from the 2017-2018 winter field experimentation.

Base Case – Cost Estimation

Snow removal cost estimates include the initial SRE procurement and the annual operation cost consisting of SRE fuel and maintenance cost, PDP cost, and snow removal personnel labor cost. SRE maintenance cost is assumed 1-percecnt of the SRE purchase cost (Anand et al. 2017). Initial cost and annual snow removal operating cost (ASROC) estimates are calculated in the AHPS BCA spreadsheet tool using Eq. 5 and Eq. 6, respectively (Anand et al. 2017). A

pavement area ratio converts the cost corresponding to the total AOA to the cost of the AOA location under investigation (i.e. apron area).

$$\text{Initial Cost} = SRE\ Purchase\ Cost \times \frac{Apron\ Area}{Total\ AOA} \quad (5)$$

$$\text{ASROC} = (\sum Fuel + PDP + Labor + SRE\ Maintenance) \times \frac{Apron\ Area}{Total\ AOA} \quad (6)$$

Airport snow removal operation cost is a function of winter weather, and varies annually. For simplicity, the operation cost for the 2017-2018 winter season is the assumed annual snow removal operation cost.

Alternative – Solar-HHPS Cost Estimation

New construction is required for a solar-HHPS implementation. Solar-HHPS cost estimates include a capital and operation cost. Capital cost equals the equipment cost. Construction labor cost is not included in this analysis. The operation cost consists of energy requirements to circulate the working fluid through the HHPS and the SWHS. Maintenance is assumed 1-percent of the combined HHPS and SWHS capital cost.

Alternative – Solar-HHPS Benefit Estimation

Apron area HHPS offer benefits including the reduction in passenger loss time (Passenger Benefit), reduction in aircraft fuel and flight crew time waste (Airline Benefit), and enhancement in safety for aircraft-parking stand (APS) staff (Staff Safety Benefit) (FAA 1999). Airport-specific data are required to monetize each benefit in the AHPS BCA spreadsheet tool. The passenger benefit's monetized estimate is calculated using the value of lost passenger time (VLPT) cost formula, Eq. 7, and the total winter season delay hour (TWSDH) formula, Eq. 10. The airline benefit's monetized estimate is calculated using the fuel and flight crew (FFC) cost formula, Eq. 8, and the TWSDH formula, Eq. 10. The staff safety benefit's monetized estimate is calculated using the injury cost formula, Eq. 9.

VLPT Cost = $Total\ Aircraft\ Seats \times Pass.Load\ Factor \times$ **Total Winter Season Delay Hours** (**TWSDH**) $\times$ [($Leisure\ Passengers$ (%) $\times$ **Value of Time for Leisure**) + ($Business\ Passengers$ (%) $\times$ **Value of Time for Business**)] (7)

FFC Cost = **Total Winter Season Delay Hrs** (**TWSDH**) $\times$ **Airline Delay Cost** (Air, Ground, Gate) (8)

Injury Cost = **Injury Type**(minor, moderate, serious)(%) $\times$ **VSL** $\times$ **VSL Fraction for injury type** $\times$ **incident rate** $\times$ $No.full\ time\ employees$ (9)

TWSDH = $Winter\ Season\ Operations \times$ **Snow Related Delays** (%) $\times$ $Flight\ Operation\ Growth\ Rate \times Avg.Duration\ of\ One\ Delay\ (hours)$ (10)

Airport-specific data variables in Eq. 7 through Eq. 10 are in italics. Variables in Eq. 7 through Eq. 10 using the Anand et al. (2017) study values are in bold. The Guidebook for Airport Winter Operations was used as a reference for the passenger delay costs and the airline delay costs (ACRP 2015), and the Bureau of Labor Statistics was used as a reference for the cost of personnel injury (BLS 2016). The "Snow Related Delays" variable uses an expert assumption addressed by Anand et al. (2017).

Economic Analysis Framework

Net present value (NPV) and benefit-cost ratio (BCR) are used to evaluate the viability of the solar-HHPS pavement deicing alternative. NPV, Eq. 11 (FAA 1999), compares the present value of the solar-HHPS benefits to the present value of the solar-HHPS cost. A positive NPV indicates a potential investment alternative.

$$\text{NPV} = \sum_{t=0}^{k} \frac{B_t}{(1+r)^t} + \sum_{t=0}^{k} \frac{C_t}{(1+r)^t}, \quad (11)$$

where B_t is the future annual benefits in constant dollars (positive value), C_t is the future annual cost in constant dollars (negative value), r is the annual real discount rate, k is the analysis period, and t is the index from 0 to k representing the year under consideration.

BCR, Eq. 12 (Anand et al. 2017, FAA 1999), is the ratio of the present value (PV) of solar-HHPS benefits to the present value (PV) of solar-HHPS cost. A BCR greater than or equal to 1 indicates a potential investment alternative.

$$\text{BCR} = \frac{PV\ of\ (Solar{-}HHPS\ Benefits)}{PV\ of\ (Solar{-}HHPS\ Cost)} \tag{12}$$

Both the NPV and BCR approaches should be considered in order to offset deficiencies in the two approaches (FAA 1999). The analysis period for airport projects is 20-years. The real discount rate for airport projects is 7-percent (FAA 1999).

CASE STUDY: NORTHWEST ARKANSAS REGIONAL AIRPORT

The following text sections summarize existing conditions at XNA and the economic analysis results for implementing the solar-HHPS at the XNA apron area. XNA data collection targeted information specific to its future growth projections and activities, its winter weather conditions, and its current snow removal operations. Data gathering used online databases cited in the following sections, and through surveys and discussions with XNA's operations management team. The survey questions and responses are provided in Appendix F. Set input parameters in the AHPS BCA tool (the bold variables in Eq. 7 through Eq. 10) were verified to ensure their validity. A field experimentation program tested the solar-HHPS approach in winter weather conditions similar to that experienced at XNA. Modifications to the AHPS BCA spreadsheet tool accepted these factors and used field experimental results for the solar-HHPS initial and operation cost estimations.

Base Case: XNA Snow Removal Operation

XNA is a public, small hub airport with commercial and general aviation operations, Figure 67. XNA services four mainline airlines. 46,740 total operations and 725,284 total enplanements were recorded in 2017 (Airport Traffic Statistics 2018). According to the FAA Terminal Area

Forecast, which projects aviation activities at US airports, XNA is projected to see a 2-percent airport operations growth rate for the next 20-years (TAF 2018). Additionally, the annual total enplanement is estimated to increase to 1.3-million by 2038 (Rosa 2017, TAF 2018).

Figure 67: XNA aerial view (Google Earth).

These projections prompted XNA airport expansion projects estimating $223,287,000 over the next 20-years (Rosa 2017). One major project includes a new terminal concourse, highlighted in Figure 68, adding 8-gates/APS to the 82,312-m^2 apron area. The concrete pavement in the apron area is currently deteriorating due to alkali-silica reaction issues observed shortly after the airfield was constructed in 1997 (Richards 2018). Consequently, the terminal project and necessary pavement reconstruction is an advantageous scenario to investigate the financial viability for implementing a solar-HHPS within the apron area.

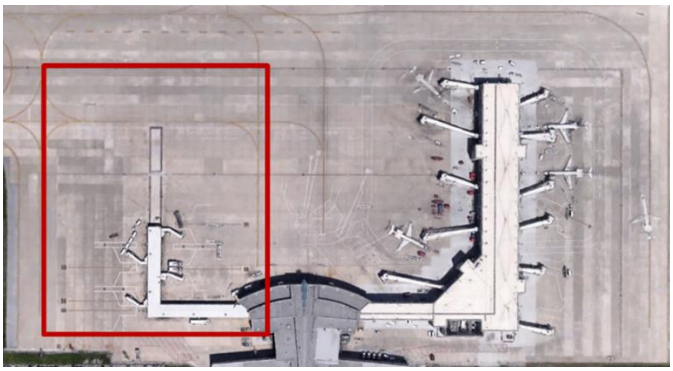
Figure 68: XNA apron area aerial view.

Table 15 lists the cost breakdown for the XNA snow removal operation by calculating the initial and annual operation cost. The initial cost consists of the SRE purchase cost. XNA received a FAA grant for new SRE procurement. Two plow trucks/chemical spreaders (Figure 69a), two multi-tasking vehicles (Figure 69b), and two snow blowers (Figure 69c) were purchased for $3,141,266. The new SRE cost is added to the existing SRE purchase cost ($664,510). The sum of the new SRE cost and existing SRE cost is the estimated initial snow removal equipment cost ($3,805,776).

Table 15: XNA Conventional Pavement Deicing Cost Breakdown

Cost of XNA Current Snow and Ice Control Method			
Item	Quantity	Unit Price ($)	Total Cost ($)
Initial Cost			
Snow Removal Equipment (SRE)	11	varies	$ 3,805,776.00
Operation Cost			
Chemical - Potassium Acetate/Propylene Glycol Blend (liters)	50089	1.76	$ 88,156.64
Chemical - Sodium Formate/Acetate Blend (kg)	47008	1.8	$ 84,614.40
Labor - Snow and Ice Control Personnel	8	25/hr	$ 32,000.00
Fuel - Snow Removal Equipment	11	32.4	$ 57,024.00
Maintenance			
Annual SRE maintenance cost (1%)	-	-	$ 38,057.76
Total Cost for Apron Area			
Capital	$		736,564.86
Operation and Maintenance	$		58,362.67

The operation cost consists of the PDP cost, SRE fuel cost, SRE maintenance cost, and labor cost. XNA uses a sodium formate/acetate blend solid deicer for pavement deicing (Figure 69d) and a potassium acetate/propylene glycol blend liquid deicer for anti-icing treatment (Figure 69e). Table 15 shows the total PDP cost for the 2017-2018 winter season based on data supplied to the author by XNA's operation managers.

Figure 69: XNA snow removal equipment and pavement treatment chemical; (a) plow truck/chemical spreader, (b) multi-tasking vehicle, (c) snow blower, (d) sodium formate/acetate pellet deicier, (e) potassium acetate/propylene glycol liquid deicer.

SRE fuel cost calculations required the following assumptions; (1) each SRE vehicle operates for 12-hours on one tank of fuel, (2) each SRE vehicle has the same fuel capacity, (3) XNA performs 50 snow removal/pavement treatment operations per year, and (4) each snow removal/pavement treatment operation has a 3.2-hour duration (the average HHPS operation time from the field experiment). The SRE fuel price was $0.66/liter ($2.50/gallon). The total cost of fueling the entire XNA fleet is the sum of the SRE fuel capacity multiplied by the XNA fuel price. Thus, the SRE hourly fuel cost is the quotient of the total fleet fueling cost divided by the product of 12-hours and eleven total SRE. Multiplying the hourly SRE fuel cost by the assumed total snow removal duration time gives the annual SRE fuel cost given in Table 15. Labor cost calculations required the following assumptions; (1) XNA performs 50 annual snow removal/pavement treatment operations, and (2) each operation has a 3.2-hour duration (the average HHPS operation time from the field experiment). The annual snow removal labor cost is the product of the number of snow removal operators, the hourly labor wage, and the assumed total snow removal duration time, Table 15.

Alternative: Solar-HHPS Pavement Anti-icing Operation

Table 16 details the solar-HHPS capital and operation cost. For the HHPS, a unit cost per square meter was calculated by dividing the equipment cost by the experimental "Test Slab Area". Similarly, for the SWHS, a unit cost per liter was calculated by dividing the equipment cost by the experimental heated fluid storage "Tank Capacity". The scale up conversion metric maintained the test slab area – fluid storage tank capacity relationship. Thus, the capital cost estimate was conducted as follows. The apron surface area is multiplied by the HHPS unit cost. The storage tank capacity is scaled to maintain the slab area – tank capacity relationship. Lastly, the scaled tank capacity is multiplied by the SWHS unit cost. The capital cost for the HHPS and SWHS on the full apron area is $28,118,817 and $35,270,385, respectively. Maintenance cost is assumed as 1-percent of the combined capital cost.

Table 16: Solar-HHPS Cost Breakdown

Capital Cost Breakdown for Field Experimentation					
Hydronic Heated Pavement Subsystem (HHPS)			Solar Water-Heating Subsystem (SWHS)		
Test Slab Area	7.43	m^2	Tank Capacity	1892.7	liters
Item	Quantity	Unit Price ($/$m^2$)	Item	Quantity	Unit Price ($/liter)
Concrete	-	322.92	Solar Collector	2	0.95
PEX (meter)	24.22	5.24	Storage Tank	1	0.24
Pump	1	13.45	Insulation	2	0.03
-	-	-	Pump	1	0.05
-	-	-	20%Glycol-Water	-	0.41
Total		$ 341.61	Total		$ 1.68
Operation Cost Breakdown for Field Experimentation					
Hydronic Heated Pavement Subsystem (HHPS)			Solar Water-Heating Subsystem (SWHS)		
Operation Time	3.2	hour	Operation Time	7.03	hour
Pump Power	124.3	Watts	Pump Power	124.3	Watts
Energy Consumption	0.39776	kWh	Energy Consumption	0.873829	kWh
Electricity Cost (Avg)	$ 0.07	USD/kWh	Electricity Cost (Avg)	$ 0.07	USD/kWh
Operation Cost	$ 0.03		Operation Cost	$ 0.06	
Operation Unit Price	$ 0.0039	USD/m^2	Operation Unit Price	$ 0.000034	USD/liter

HHPS and SWHS operation cost is a function of the average pump activation time derived from the field experimentation previously discussed in this dissertation. As mentioned prior, it is assumed that 50 pavement snow removal operations are performed at XNA over a single winter

season. Thus, the total estimated operation time is 160-hours based on the HHPS operation time. The operation costs for HHPS and SWHS on the full apron area are $16,129 and $35,450, respectively.

Table 17: Monetized Benefit Input Parameters

REDUCED LOST PASSENGER TIME		
Item	Quantity	
Flight Operations Growth Rate (TAF 2018)	*2.00%*	
Weather Related Delays (Anand et al. 2017)	**2.00%**	
No. of Aircraft Seats (Appendix E)	*105*	
Load Factor (BTS 2018)	*67.42%*	
Passengers Traveling for Leisure (Appendix E)	*35.00%*	
Passengers Traveling for Business (Appendix E)	*65.00%*	
VOT for Leisure (ACRP 2015, Anand et al. 2017)	**36.10**	
VOT for Business (ACRP 2015, Anand et al. 2017)	**63.20**	
REDUCED CREW TIME AND FUEL WASTAGE		
Variable Aircraft Direct Operating Costs		
Mid air (ACRP 2015, Anand et al. 2017)	**4456**	**($/hr)**
Ground (ACRP 2015, Anand et al. 2017)	**2148**	**($/hr)**
Gate (ACRP 2015, Anand et al. 2017)	**1443**	**($/hr)**
Assuming All Delays Equal; Combined Value (Anand et al. 2017)	**2682**	**($/hr)**
REDUCED COST DUE TO INJURIES		
Incidence Rates are Calculated per 10,000 Workers	Type of Injury (%)	Fraction of VSL
Classified bruises, sprains, and tears; Minor (BLS 2016)	**60%**	**0.0030**
Classified fractures; Moderate (BLS 2016)	**25%**	**0.0470**
Classified multiple traumatic; Serious (BLS 2016)	**15%**	**0.1050**
Value of Statistical Life (VSL), (2014) (BLS 2016)	**9600000**	
XNA Full-Time Employees	*50*	

Table 17 lists the input variables for the monetized benefit estimates. The values in bold are estimates held constant from the original AHPS BCA spreadsheet tool. Anand et al. (2107) uses an average hourly cost for the "Reduced Crew Time and Fuel Wastage" benefit estimate. The values in italics are airport-specific data from online databases and a survey completed by the XNA operations managers.

Table 18 shows the individual and total benefit estimation for the 20-year analysis period. The Year 1 winter aircraft operations are the total operations recorded from December 2017 to March 2018. The winter operations are estimated to grow annually by 2-percent. The delayed operations related to snow and ice are 2-percent of the winter aircraft operations, Table 18. The

total winter season delay hours (TWSDH) is determined assuming that the average duration of one delayed operation is 60-min. The Passenger Benefit and Airline Benefit increase are proportional to the increase in winter operations. The safety benefit estimate remains constant as the number of XNA full-time employees remain constant.

Table 18: Benefit Estimation Breakdown for 20-Year Analysis Period

Year	Winter Operations	Delayed Operations	TWSDH	Value of Lost Time (Passenger Benefit)	Fuel/Flight Crew Cost (Airline Benefit)	Injury Cost (Safety Benefit)	Total Benefit
1	13795	276	276	$1,049,120.39	$740,055.77	$5,344.32	$1,794,520.48
2	14071	281	281	$1,070,102.80	$754,856.88	$5,344.32	$1,830,304.00
3	14352	287	287	$1,091,504.85	$769,954.02	$5,344.32	$1,866,803.19
4	14639	293	293	$1,113,334.95	$785,353.10	$5,344.32	$1,904,032.37
5	14932	299	299	$1,135,601.65	$801,060.16	$5,344.32	$1,942,006.13
6	15231	305	305	$1,158,313.68	$817,081.37	$5,344.32	$1,980,739.37
7	15535	311	311	$1,181,479.96	$833,422.99	$5,344.32	$2,020,247.27
8	15846	317	317	$1,205,109.56	$850,091.45	$5,344.32	$2,060,545.33
9	16163	323	323	$1,229,211.75	$867,093.28	$5,344.32	$2,101,649.35
10	16486	330	330	$1,253,795.98	$884,435.15	$5,344.32	$2,143,575.45
11	16816	336	336	$1,278,871.90	$902,123.85	$5,344.32	$2,186,340.07
12	17152	343	343	$1,304,449.34	$920,166.33	$5,344.32	$2,229,959.99
13	17495	350	350	$1,330,538.33	$938,569.65	$5,344.32	$2,274,452.30
14	17845	357	357	$1,357,149.09	$957,341.05	$5,344.32	$2,319,834.46
15	18202	364	364	$1,384,292.07	$976,487.87	$5,344.32	$2,366,124.26
16	18566	371	371	$1,411,977.92	$996,017.62	$5,344.32	$2,413,339.86
17	18938	379	379	$1,440,217.47	$1,015,937.98	$5,344.32	$2,461,499.77
18	19316	386	386	$1,469,021.82	$1,036,256.74	$5,344.32	$2,510,622.88
19	19703	394	394	$1,498,402.26	$1,056,981.87	$5,344.32	$2,560,728.45
20	20097	402	402	$1,528,370.31	$1,078,121.51	$5,344.32	$2,611,836.13

Economic Analysis: Solar-HHPS Benefit Cost Comparison

The present values for the solar-HHPS cost and benefits, and the XNA snow removal cost were calculated in the AHPS BCA spreadsheet tool with a 20-year analysis period and 7-percent real discount rate. Table 19 summarizes the economic analysis results for the solar-HHPS pavement deicing alternative.

Table 19: Economic Analysis Summary

Cost Parameters	Solar-HHPS
Analysis Period	20
Capital Cost	$ 63,389,201.76
Operation and Maintenance (O&M) cost (annual)	$ 768,536.62
Benefits (annual)	$ 1,794,520.48
Economic Analysis of Monetary Benefits and Costs for the Entire Analysis Period	
Present Value of Costs	$ (71,531,089.71)
Present Value of Benefits	$ 22,099,373.82
Net Present Value	$ (49,431,715.89)
Present Value of Cost (Base Case)	$ 1,354,859.80
Benefit Cost Ratio	0.309
Incremental Benefit Cost Ratio	0.315

Figure 70 compares the annual solar-HHPS benefits to the annual solar-HHPS cost. The benefit estimates are positive values and the cost estimates are negative values. Figure 70 indicates that the solar-HHPS equivalent annual capital cost makes the use of a solar-HHPS for the full apron area cost prohibitive. The solar-HHPS capital cost is directly proportional to the heated pavement area. Consequently, a reduction in the heated pavement area within the apron area can increase the solar-HHPS viability. This is evaluated in a sensitivity analysis.

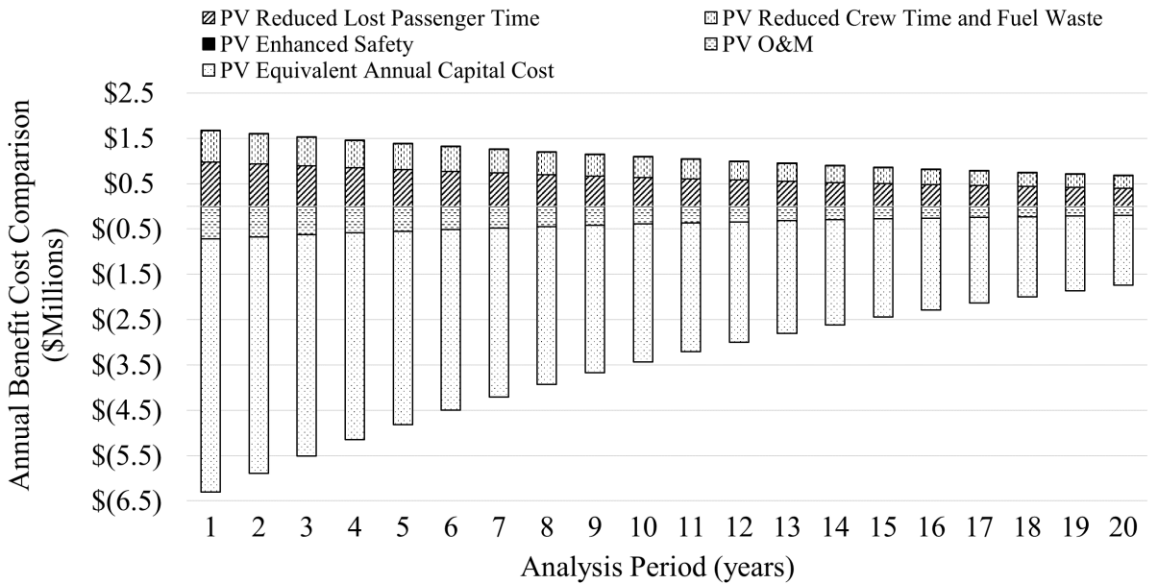

Figure 70: Net present value benefit and cost comparison for the 20-year analysis period.

Sensitivity Analysis

A sensitivity analysis was performed to evaluate the solar-HHPS alternative as a function of the heated pavement area and the estimated snow-related flight delay time. The initial analysis evaluated the solar-HHPS for the entire apron area considering a 30-min flight delay time (Figure 71, "Apron A") and a 60-min flight delay time (Figure 71, "Apron B"). Both of these cases show a BCR less than 1. However, the monetized benefits directly correspond to the APS area. Therefore, the solar-HHPS BCR was reevaluated for a 1264-m^2 parking stand at 4, 8, and 16 gates, Figure 71. Figure 71 compares the NPV of the XNA snow removal cost (SRC) for the apron area, the NPV of the solar-HHPS cost per APS, and the NPV of the solar-HHPS benefit per APS. Additionally, an incremental BCR is calculated for Figure 71 dividing the NPV of solar-HHPS benefits by the value of the NPV of the solar-HHPS cost minus the NPV of the XNA-SRC (Anand et al. 2017). The four-gate case represents each of the four mainline commercial airlines using XNA having a single APS supported by a solar-HHPS. The eight-gate case represents each APS at an XNA concourse supported by a solar-HHPS. Lastly, the sixteen-gate case allows each active APS to be supported by a solar-HHPS. These analyses considered a 30-min flight delay time and a 60-min flight delay time, Figure 71. Figure 71 shows that a reduction in the heated pavement area improves the solar-HHPS viability. Conversely, reducing the estimated snow-related flight delay time decreases the solar-HHPS viability, Figure 71.

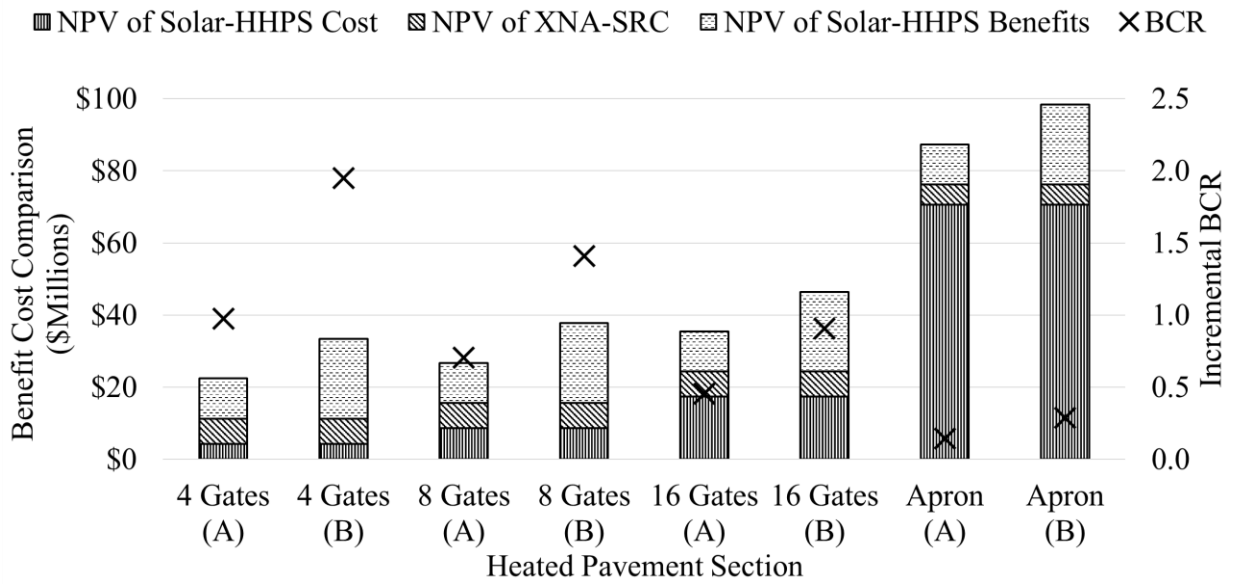

Figure 71: Benefit-cost comparison for the solar-HHPS sensitivity analysis where (A) represents a 30-min flight delay time, and (B) represents a 60-min flight delay time.

The benefit cost ratio and net present value imply that the solar-HHPS is viable for the four-gate/APS case and the eight-gate/APS case with a 60-min flight delay time assumption considering Northwest Arkansas Regional Airport ambient conditions. However, reevaluating the solar-HHPS with the solar water heating system configured to support year-round terminal building heating and cooling will greatly improve its financial viability.

CHAPTER 7: CONCLUSIONS

Snow and ice on the airfield pavement greatly intensify safety risks to aircraft ground operations. Airfield heated pavement systems (AHPS) are being researched to maintain a "no more than wet" pavement condition for safe aircraft ground movement. AHPS installation for runway snowmelt is cost prohibitive. Consequently, AHPS implementation should be in strategic locations to (1) complement the airport's conventional pavement deicing method, (2) improve aircraft and personnel safety measures, and (3) improve aircraft operations efficiency. Therefore, AHPS at aircraft-parking stands (APS) is suggested.

This study analyzed the development and assessed the viability of two solar powered anti-icing AHPSs. A large-scale solar electrical heated pavement system (solar-EHPS) and a solar hydronic heated pavement system (solar-HHPS) were built and evaluated by the author to investigate each system's suitability for pavement heating and pavement snow melting. Electric energy was generated using a photovoltaic energy system (PVES) and thermal energy was collected in a solar water-heating system (SWHS). Field experimentation was performed at an outdoor testing facility at the University of Arkansas's Engineering Research Center, in Fayetteville, Arkansas.

A near-surface heat wire grid prototype was developed for the solar-EHPS to concentrate heat transfer to the concrete pavement surface. The wire grid was placed near surface to reduce the electric energy demand placed on the PVES. During experiments, the solar-EHPS maintained the concrete pavement surface temperature above-freezing in sub-freezing ambient conditions. However, continuous operation during the heating and snow melting experiment depleted energy from the PVES's battery storage bank resulting in reduced near-surface wire heat generation.

This energy reduction affects the system's snow melting performance during extended snowfall durations.

The solar-EHPS laboratory and field experiment results validated a finite element model (FEM) developed to evaluate airport pavement heating at Des Moines International Airport (upper Midwest climatic region), Chicago's O'Hare International Airport (the Ohio Valley climatic region), and LaGuardia Airport (the Northeast climatic region). Based on the FEM analysis, a high pavement heat flux is required for pavement pre-heating and the climate determined pavement heat flux calculated using ASHRAE (2011), is required to maintain the surface temperature at a target pavement surface temperature (TPST). The weakness in the solar-EHPS approach is the PVES energy storage. However, future advances in electric energy storage technology will increase the solar-EHPS's viability and attractiveness. Further testing on the near-surface heat wire grid should consider thermal stresses caused by the cyclic thermal loading due to heating at the concrete surface.

The solar-HHPS experiments evaluated the pavement heating performance using fluid heated with heat-pipe evacuated tube collectors (HP-ETC). The solar-HHPS maintained an above-freezing pavement surface temperature and an anti-icing pavement condition during heating and snow melting experiments. The designed automated system optimized the solar-HHPS operation, conserving energy required to operate the circulation pumps. Further testing should (1) incorporate a flow meter and regulator for the hydronic heated pavement system and the solar water-heating system to optimize fluid flow for thermal distribution and thermal collection, respectively, and (2) use a pyranometer at the test facility to measure daily solar radiation to calculate the HP-ETC efficiency.

A benefit-cost analysis investigated the economic justification for installing a solar-HHPS at the Northwest Arkansas Regional Airport's apron area. The conservative benefits and cost estimations show potential viability for a solar-HHPS at aircraft parking stands in moderate climate conditions. Monetizing an airport's year-round use of a solar water-heating system considering terminal building heating and cooling will greatly improve the solar-HHPS implementation viability.

REFERENCES

Abdualla, H., Halil, C., Kim, S., Gopalakrishnan, K., Taylor, P., & Turkan, Y. (2016). System Requirements for Electrically Conductive Concrete Heated Pavements. *Transportation Research Record*, TRB Paper 16-4176.

Airport Cooperative Research Program (ACRP). (2009). Deicing Practices, Fact Sheet. *Transportation Research Board*.

Airport Cooperative Research Program (ACRP). (2015). A Guidebook for Airport Winter Operations. *Transportation Research Board*, ACRP Report 123.

Airport Traffic Statistics. 2018. *Northwest Arkansas Regional Airport Enplanement Statistics 1998-2018*. Retrieved from the Fly XNA website: http://www.flyxna.com/about-us/air-traffic-statistics/

Alghoul, M., Sulaiman, M., Azmi, B., & Wahab, M. (2005). Review of materials for solar thermal collectors. *Anti-Corrosion Methods and Materials*, 52(4), 199-206.

American Concrete Pavement Association (ACPA). (2002). Concrete Pavement for General-Aviation, Business and Commuter Aircraft. *IS202.03P*

American Society of Heating, Refrigeration, and Air-Conditioning Engineers (ASHRAE). (2011). *2011 ASHRAE Handbook: Chapter 51: Snow Melting and Freeze Protection*. Washington, D.C.

Anand, P., Nahvi, A., Ceylan, H., Pyrialakou, V.D., Gkritza, K., Gopalakrishnan, K., Kim, S., & Taylor, P.C. (2017). Energy and financial viability of hydronic heated pavement systems. *Federal Aviation Administration*, Report No. DOT/FAA/TC-17/47, final.

ASTM C39, Standard Test Method for Compressive Strength Cylinder Concrete Specimen.

ASTM C143, Standard Test Method for Slump of Hydraulic-Cement Concrete.

ASTM C231, Standard Test Method for Air Content of Freshly Mixed Concrete by the Pressure Method.

Ayompe, L., & Duffy, A. (2013). Thermal performance of a solar water heating system with heat pipe evacuated tube collector using data from a field trial. *Solar Energy*, 90, 17-28.

Balbay, A., & Esen, M. (2010). Experimental investigation of using ground source heat pump system for snow melting on pavements and bridge decks. *Scientific Research and Essays*, 5(24), 3955-3966.

Bureau of Labor Statistics (BLS). 2016. *Nonfatal Occupational Injuries and Illnesses Requiring Days Away From Work*. Retrieved from the U.S. Department of Labor Bureau of Labor Statistics website: https://www.bls.gov/news.release/archives/osh2_11102016.pdf

Bureau of Transportation Statistics (BTS). 2018. *Load Factor*. Retrieved from the U.S. Department of Transportation Bureau of Transportation Statistics website: https://www.transtats.bts.gov/Data_Elements.aspx?Data=5

Chanh, N.V. (2004). Steel Fiber Reinforced Concrete. Retrieved from online website: https://s3.amazonaws.com/academia.edu.documents/35870139/Steel_Fiber_Reinforced_Concrete.pdf?AWSAccessKeyId=AKIAIWOWYYGZ2Y53UL3A&Expires=1535565896&Signature=74rcpNr%2BzJdnAXM0mIG9qfr93Rc%3D&response-content-disposition=inline%3B%20filename%3DSteel_Fiber_Reinforced_Concrete.pdf

Ceylan, H. (2015). FAA PEGASAS COE Project 1: Heated Airport Pavements. *Present at FAA PEGASAS COE 3rd Annual Meeting*, Purdue University, Indiana.

COMSOL. (2018). *COMSOL Multiphysics: Heat Transfer*. Retrieved from COMSOL Mulitphysics® Software website: https://www.comsol.com/comsol-multiphysics

Derwin, D., Booth, P., Zaleski, P., Marsey, W., & Flood, W. (2003). Snowfree® heated pavement system to eliminate icy runways. *SAE Technical Paper*, Series No. 2003-01-2145, final.

Federal Aviation Administration (FAA). (1997). Measurement, Construction, and Maintenance of Skid-Resistant Airport Pavement Surfaces. *Advisory Circular 150/5320-12C*.

Federal Aviation Administration (FAA). (1999). Airport Benefit-Cost Analysis Guidance.

Federal Aviation Administration (FAA). (2008). Airport Winter Safety and Operation. *Advisory Circular 150/5200-30C*.

Federal Aviation Administration (FAA). (2010). *Destination 2025*. Retrieved from the Federal Aviation Administration website: https://www.faa.gov/about/plans_reports/media/Destination2025.pdf

Federal Aviation Administration (FAA). (2011). Airside Use of Heated Pavement Systems. *Advisory Circular 150/5370-17*.

Federal Aviation Administration (FAA). (2014a). Airport Snow and Ice Equipment. *Advisory Circular 150/5220-20*.

Federal Aviation Administration (FAA). (2014b). Standards for Specifying Construction of Airports. *Advisory Circular 150/5370-10G*.

Federal Aviation Administration (FAA). (2014c). *Press Release – FAA Forecast Sees Continued, Steady Growth in Air Travel*. Washington, DC. Retrieved Fro, The Federal Aviation Administration website: https://www.faa.gov/news/press_releases/news_story.cfm?newsId=15935

Federal Aviation Administration (FAA). (2016). *The Economic Impact of Civil Aviation on the U.S. Economy*. Retrieved from the Federal Aviation Administration website: https://www.faa.gov/air_traffic/publications/media/2016-economic-impact-report_FINAL.pdf

Flight Explorer. 2018. *Free Flight Tracking*. Retrieved from the Flight Explorer website: http://travel.flightexplorer.com/

Frangoul, A. (2018). *Honolulu airport is about to get thousands of new solar panels*. Retrieved from the CNBC Online website: https://www.cnbc.com/2018/07/25/honolulu-airport-is-about-to-get-thousands-of-solar-panels.html

Gopalakrishnan, K., Ceylan, H., Kim, S., Yang, S., & Abdualla, H. (2017). Electrically Conductive Mortar Characterization for Self-Heating Airfield Concrete Pavement Mix Design. *International Journal of Pavement Research and Technology*, 8(5), 315-324.

Hang, Y., Qu, M., & Zhao, F. (2012). Economic and environmental life cycle analysis of solar hot water systems in the United States. *Energy and Buildings*, 45, 181-188.

Henderson, D.J. (1961). Experimental Roadway Heating Project on a Bridge Approach. *Highway Research Board,* Highway Research Record No. 14.

Heymsfield, E., Osweiler, A., Selvam, R. P., & Kuss, M. (2012). Implementing conductive concrete with renewable energy to develop anti-icing airfield runways. *Federal Aviation Administration*, Report No. DOT/FAA/TC-13/8, final.

Htun, N.N., Sukchai, S., & Hemavibool, S. (2014). Properties of Concrete Material for Thermal Energy Storage. *International Conference and Utility Exhibition 2014 on Green Energy for Sustainable Development*, Thailand.

Iowa State University. (2017*). Heated pavement technology tested at Des Moines International Airport*. Retrieved from the Iowa State University Science Daily Online website: https://www.sciencedaily.com/releases/2017/03/170328120831.htm

Joel, R.N. (2005). Accelerated Alkali-Silica Reactivity in Portland cement concrete Pavements Exposed to Deicing Chemicals. *Federal Aviation Administration*, Engineering Brief No. 70.

Joerger, M., Martinez, F., 2006. Electric Heating of I-84 in Ladd Canyon, Oregon. *Federal Highway Administration*, Project No. FHWA-OR-RD-06-16, SPR 304-461, final.

Kalogirou, S. (2009). *Solar Energy Engineering: Processes and Systems*. London, Elsevier.

Kopec, C. (2015). Geothermal radiant heating for airfield pavements. *McFarland Johnson, Binghamton University*, Report.

Lai, Y., Liu Y., & Ma, D. (2014). Automatically melting snow on airport cement concrete pavement with carbon fiber grille. *Cold Regions Science and Technology*, 103, 57-62.

Lai, J., Qiu, J., Chen, J., Fan, J., & Wang, K. (2015). New Technology and Experimental Study on Snow-Melting Heated Pavement System in Tunnel Portal. *Advances in Materials Science and Engineering*, 2015, 1-11.

Liu, X., Rees, S.J., & Spitler, J.D. (2007). Modeling snow melting on heated pavement surfaces. Part I: Model development. *Applied Thermal Engineering*, 27, 1115-1124.

Lund, J. (1999). Reconstruction of a Pavement Geothermal Deicing System. *Geo-Heat Center Bulletin*, 14-17.

Lund, J. (2010). *Pavement snow melting*. Retrieved from the Geo-Heat Center website: https://www.oit.edu/docs/default-source/geoheat-center-documents/publications/snow-melting/tp108.pdf?sfvrsn=2

Mazarron, F., Porras-Prieto, C., Garcia, J., & Benavente, R. (2016). Feasibility of active solar water heating systems with evacuated tube collector at different operational water temperatures. *Energy Conversion and Management*, 113, 16-26.

Minsk, L.D. (1999). Heated Bridge Deck Technology. *Federal Highway Administration*, Report No. FHWA-RD-99-158, final.

Moore, J. (2017). *JetBlue Plane Slides Off Icy Runway at Boston Airport After Flying in for Christmas*. Retrieved from the Newsweek Online website: http://www.newsweek.com/jetblue-plane-slides-icy-runway-boston-airport-after-flying-christmas-758956

Morita, K., & Tago, M. (2000). Operational Characteristics of the Gaia Snow-Melting System in Ninohe, Iwate, Japan. *Geo-Heat Center Bulletin*, 5-11.

Mutzabaugh, B. (2013). *Delta 737 slides off taxiway at snowy Madison Airport*. Retrieved from the USA Today Online website: https://www.usatoday.com/story/todayinthesky/2013/12/17/delta-737-slides-off-taxiway-at-snowy-madison-airport/4051211/

National Aeronautics and Space Administration (NASA). (2004). *Research Aims to Prevent Accidents on Hazardous Runways.* Retrieved from the National Aeronautics and Space Administration website: https://www.nasa.gov/centers/langley/news/factsheets/WinterRunway.html

National Oceanic Atmospheric Administration (NOAA). (2017a). *Data Tools: 1981-2010*. Retrieved from the National Oceanic Atmospheric Administration website: https://www.ncdc.noaa.gov/cdo-web/datatools/normals

National Oceanic Atmospheric Administration (NOAA) (2017b). *Data Tools: 1981-2010*. Retrieved from the National Oceanic Atmospheric Administration website: https://www.ncdc.noaa.gov/monitoring-references/maps/us-climate-regions.php

Packard, R.G. (1995). Design of Concrete Airport Pavement. *Portland Cement Association*, EB050.03P.

Pickerel, K. (2016). *7 cool solar installations at U.S. airports*. Retrieved from the Solar Power World Online website: https://www.solarpowerworldonline.com/2016/03/7-cool-solar-installations-at-u-s-airports/

Pravda, M., Trimmer, D., & Wolf, D. (1975). Heating Systems for Airport Pavement Snow, Slush, and Ice Control. *Federal Aviation Administration*, Project No. FAA-RD-75-139, DOT-FA74WA-3421, Final.

Rangaraju, P.R. (2007). Influence of Airfield Pavement Deicing and Anti-icing Chemicals on Durability of Concrete. *Presented for FAA Worldwide Airport Technology Transfer Conference*, Atlantic City, New Jersey.

Rangaraju, P.R. (2007a). Mitigation of ASR in Presence of Pavement Deicing Chemicals. *Airport Concrete Pavement Technology Program*, Report IPRF-01-G-002-04-8.

Richards, J. (2018). *Northwest Arkansas Regional Airport Overcomes Perplexing Runways Issues Caused by Alkali-Silica Reaction*. Retrieved from the Airport Improvement Magazine Online website: https://airportimprovement.com/article/northwest-arkansas-regional-overcomes-perplexing-runway-issues-caused-alkali-silica-reaction

Rosa, J.D. (2017). *XNA board members seek financial model for $60 million in terminal projects*. Retrieved from the Talk Business & Politics Online website: https://talkbusiness.net/2017/08/xna-board-members-seek-financial-model-for-60-million-in-terminal-projects/

Sandoval, E., & Moore, T. (2014). *JFK airport reopens after plane skids off runway, causes closure*. Retrieved from the New York Daily News Online website: http://www.nydailynews.com/news/national/airplane-skids-jfk-runway-article-1.1566762. [Accessed 2 January 2018].

Santora, M., & McGeehan, P. (2015). *Plane avoids disaster as it skids off a runway at La Guardia Airport*. Retrieved from the New York Times Online website: https://www.nytimes.com/2015/03/06/nyregion/delta-plane-skids-off-the-runway-at-la-guardia-airport.html

Shi, X. (2008). Impact of airport pavement deicing products on aircraft and airfield infrastructure. *Airport Cooperative Research Program*, ACRP Synthesis 6, 25-28.

Sumsion, E.S., & Guthrie, W.S. (2013). Physical and Chemical Effects of Deicers on Concrete Pavement: Literature Review. *Utah Department of Transformation*, Report No. UT-13.09, final.

Tang, Z., Li, Z., Qian, J., & Wang, K. (2005). Experimental Study on Deicing Performance of Carbon Fiber Conductive Concrete. *Material Science Technology*, 21(1), 113-117.

Terminal Area Forecast (TAF). 2018. *National Aviation Forecast 2017*. Retrieved from the Terminal Area Forecast website: https://taf.faa.gov/

Tuan, C.Y., & Yehia, S. (2004). Evaluation of electrically conductive concrete containing carbon products for deicing. *ACI Materials Journal,* 101(4), 287-293.

Tuan, C., 2004. Conductive Concrete for Bridge Deck Deicing and Anti-icing. *Nebraska Department of Roads*, Report No. SPR-PL-1(037)P512, final.

U.S. Energy Information Administration. (2017). *State Electricity Profiles*. Retrieved from the U.S. Department of Energy website: https://www.eia.gov/electricity/state/

Waldroup, R. (2015). *United Airlines flight slides past gate at O'Hare*. Retrieved from the Chicago5 New Online website: https://www.nbcchicago.com/news/local/Plane-Skids-Off-Runway-Into-Grassy-Area-at-OHare-363819961.html

Weather Underground. (2018). *Weather History*. Retrieved from the Weather Underground website: https://www.wunderground.com/history/airport/KFYV/2018/2/7/DailyHistory.html?cm_ven=localwx_history

Whittington, H., McCarter, W., & Forde, M.C. (1981). The Conduction of Electricity through Concrete. *Magazine of Concrete Research,* 33(114), 48-60.

Wigstrand, I. (2010). *The ATES project – a sustainable solution for Stockholm-Arlanda Airport*. Retrieved Online: https://intraweb.stockton.edu/eyos/energy_studies/content/docs/effstock09/Session_6_3_ATES_Applications/55.pdf

Williamson, P.J., & Hogbin, L.E. (1969). Electrical Road Heating. *Road Research Laboratory*, Report LR 303.

Winters, F. (1970). Pavement Heating. *Snow Removal and Ice Control Research*, (115) 129-145.

Wirsbo, (2003). *Snow and Ice Melting Design Manual*. Retrieved From the Uponor Wirsbo Website: https://www.uponor-usa.com/commercial-radiant-floor-heating-and-cooling/snow-and-ice-melting.aspx

Wood, D. (2016). *Delta plane skids off taxiway into snow at Detroit Airport*. Retrieved from the Fox New Travel Online website: http://www.foxnews.com/travel/2016/12/12/delta-plane-skids-off-taxiway-into-snow-at-detroit-airport.html

Wu, J., Yang, F., & Liu, J. (2015). Carbon Fiber Heating Wire for Pavement Deicing. *Journal of Testing and Evaluation*, 43(3), 574-581.

Xie, P., Gu, P., & Beaudoin, J.J. (1995). *Conductive concrete cement-based compositions*. U.S. Patent 5447564.

Xie, P., & Beaudoin, J.J. (1995). Electrically conductive concrete and its application in deicing. *Advances in Concrete Technology*, SP-154, 399-417.

Yang, T. (2011). Experimental study on an electrical deicing technology utilizing carbon fiber tape. *University of Alaska Anchorage*, Thesis.

Yehia, S., & Tuan, C. (1998). Bridge Deck Deicing. *Transportation Concrete Proceedings*, 51-57.

Yehia, S., & Tuan, C. (1999). Conductive concrete overlay for bridge deck deicing. *ACI Materials Journal*, 96(3), 382-390.

Yehia, S., Tuan, C., Ferdon, D., & Chen, B. (2000). Conductive Concrete Overlay for Bridge Deck Deicing: Mixture Proportioning, Optimization, and Properties. *ACI Materials Journal*, 97(2), 172-181.

Yehia, S., & Tuan, C. (2002). Thin Conductive Concrete Overlay for Bridge Deck Deicing and Anti-icing. *Transportation Research Record*, Paper No. 00-0117, 45-53.

Zenewitz, J. (1977). Survey of Alternatives to the Use of Chlorides for Highway Deicing. *Federal Highway Administration*, Report No. FHWA-RD-77-52.

Zhang, K., Baoguo, H., & Xun, Y. (2011). Nickel Particle Based Electrical Resistance Heating Cementitious Composites. *Cold Regions Science and Technology*, 69, 64-69.

Zhao, H., Wang S., Wu, Z., & Che, G. (2010). Concrete slab installed with carbon fiber heating wire for bridge deck deicing. *ASCE Journal of Transportation Engineering*, 136(6), 500-509.

Zhao, H., Wu, Z., Wang S., Zheng, J., & Che, G. (2011). Concrete pavement deicing with carbon fiber heating wires. *Cold Regions Science and Technology*, 65, 413-420.

Ziegler, W. (2009). Radiant Heating of Airport Aprons. *Airport Operations and Maintenance Challenge*, Binghamton, N.Y.

Zwarycz, K. (2002). Snow melting and heating systems based on geothermal heat pumps at Goleniow Airport, Poland. *Geothermal Training Programme, The United Nations University*, 21, 431-464.

APPENDIX A

The material in this appendix include data figures for the hydronic pavement heating test cycles.

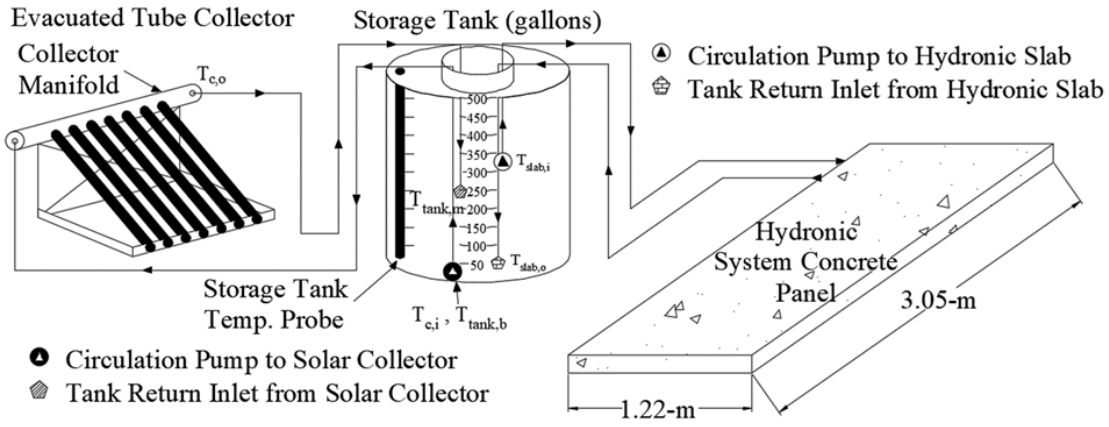

Figure 72: Schematic diagram of solar water-glycol heating subsystem (left) and hydronic heated pavement subsystem (right).

Table 20: Hydronic Pavement Heating Test Cycle with 3°C TPST

Test Cycle* Date	System Operation (hr)	Air Temp. (°C) / Wind (m/s)			Avg. Slab	Tank Temp. (°C)			Energy Consumed	
		Low	Avg.	High	Temp. (°C)	Initial	Final	ΔT	Pump ON (hr)	kWh
12/6 - 12/7	11.0	-5.6 / 0.0	-2.0 / 2.6	3.3 / 5.7	2.9	65.2	50.3	14.9	6.2	0.77
12/9 - 12/10	14.1	-6.1 / 0.0	-3.3 / 1.8	5.6 / 4.6	3.2	43.2	37.5	5.7	2.6	0.32
12/10 - 12/11	9.4	-3.3 / 0.0	-1.1 / 1.5	1.1 / 3.1	3.2	46.7	40.7	6.0	1.3	0.16
12/12 - 12/13	11.5	-4.4 / 0.0	-0.8 / 2.2	5.6 / 5.7	3.3	54.9	47.2	7.7	1.2	0.14
12/13 - 12/14	3.8	-2.2 / 0.0	-0.5 / 0.8	3.3 / 2.6	3.6	51.8	49.4	2.4	0.4	0.05
12/14 - 12/15	9.5	-4.4 / 0.0	-2.5 / 1.1	-0.6 / 3.1	3.5	51.2	45.3	5.9	1.3	0.16
12/25 - 12/26	15.0	-6.1 / 0.0	-1.6 / 1.7	1.1 / 4.1	3.0	30.2	23.4	6.8	6.2	0.77
12/26 - 12/27	12.5	-8.9 / 2.6	-7.2 / 3.2	-5.0 / 4.1	1.4	27.9	20.9	7.0	12.2	1.51
1/13 - 1/14	16.7	-6.7 / 0.0	-3.1 / 1.1	0.0 / 3.1	3.1	47.3	33.7	13.7	4.4	0.55
1/14 - 1/15	18.0	-2.2 / 0.0	0.0 / 3.7	2.2 / 6.2	3.2	37.3	28.6	8.7	2.9	0.36
1/18 - 1/19	15.3	-1.1 / 0.0	0.6 / 4.0	5.6 / 7.2	2.5	31.2	21.4	9.8	12.1	1.51
1/22 - 1/23	5.4	-2.2 / 0.0	-0.3 / 2.9	1.7 / 6.2	3.1	40.8	37.4	3.4	1.2	0.15
1/23 - 1/24	12.6	-7.2 / 0.0	-4.5 / 0.8	0.0 / 2.1	3.1	46.1	33.4	12.8	4.0	0.49
1/24 - 1/25	9.8	-3.9 / 0.0	0.0 / 2.0	5.6 / 4.7	3.2	46.2	38.3	7.9	1.7	0.21
1/27 - 1/28	9.8	-6.1 / 0.0	-4.3 / 0.0	-1.1 / 0.0	3.2	56.1	45.8	10.3	2.2	0.28
1/28 - 1/29	9.3	-2.8 / 0.0	-1.3 / 2.1	1.1 / 4.6	3.3	53.9	47.6	6.2	1.2	0.15
2/1 - 2/2	12.7	-6.7 / 0.0	-3.8 / 2.1	0.6 / 4.1	3.2	55.0	44.3	10.6	3.3	0.41
2/2 - 2/3	7.2	-2.8 / 0.0	-1.2 / 0.8	0.6 / 3.1	3.3	53.8	46.4	7.4	1.2	0.15
2/11 - 2/12	10.4	-6.7 / 0.0	-5.4 / 2.9	-5.0 / 4.6	2.0	21.6	17.3	4.3	9.6	1.20
2/17 - 2/18	10.2	-3.9 / 0.0	-1.9 / 0.3	0.6 / 1.6	3.1	34.8	28.0	6.8	1.8	0.22
2/25 - 2/26	4.9	-0.6 / 0.0	0.1 / 0.9	0.6 / 2.6	3.1	34.9	33.3	1.6	0.3	0.03
3/1 - 3/2	5.2	-2.8 / 0.0	-2.1 / 0.0	-1.1 / 0.0	3.2	42.3	41.5	0.8	0.3	0.03
3/12 - 3/13	7.5	-5.0 / 0.0	-3.7 / 0.0	-2.2 / 0.0	3.3	67.8	59.6	8.2	1.0	0.12
3/13 - 3/14	5.9	-5.0 / 0.0	-3.6 / 0.7	-1.7 / 1.6	3.3	69.8	60.3	9.5	0.8	0.10
3/20 - 3/21	2.2	-3.3 / 0.0	-2 / 1.8	-1.1 / 3.1	3.3	74.0	73.1	0.9	0.1	0.05

*Test cycles span two consecutive days. Test labelling is represented as follows: month/day – month/day.

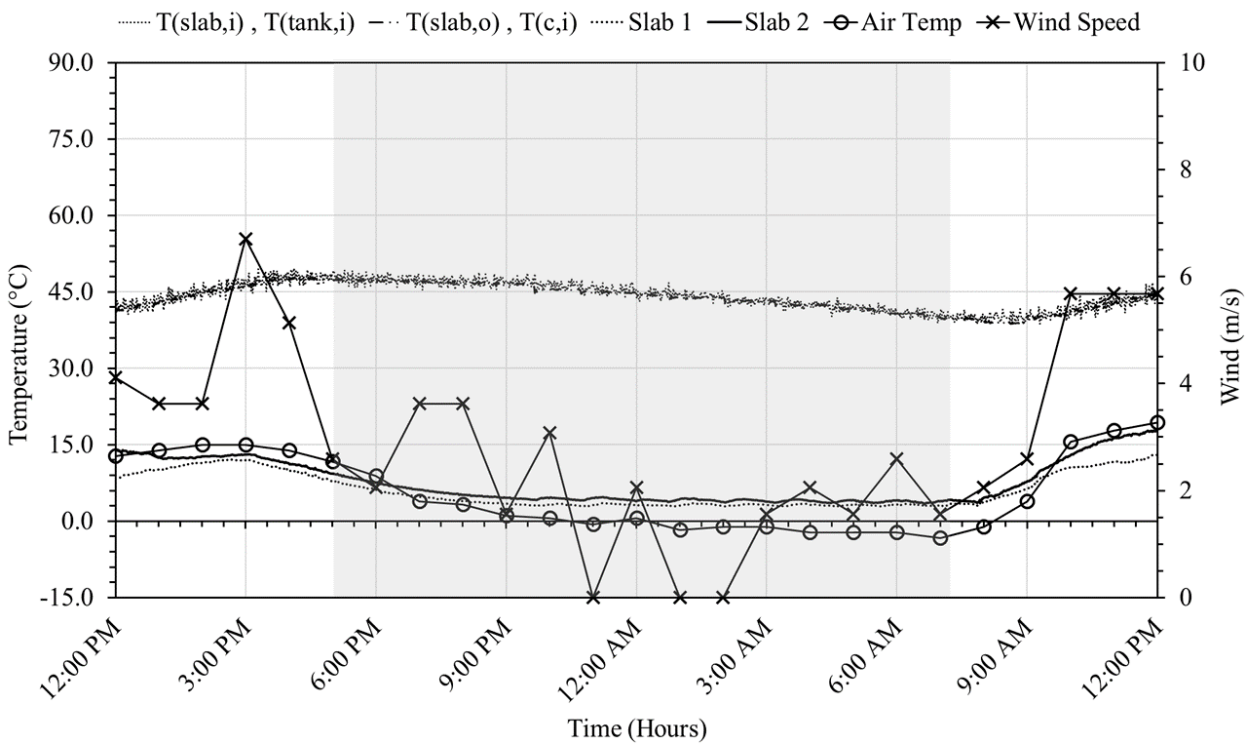

Figure 73: Hydronic pavement heating performance during December 10-11, 2017 test cycle.

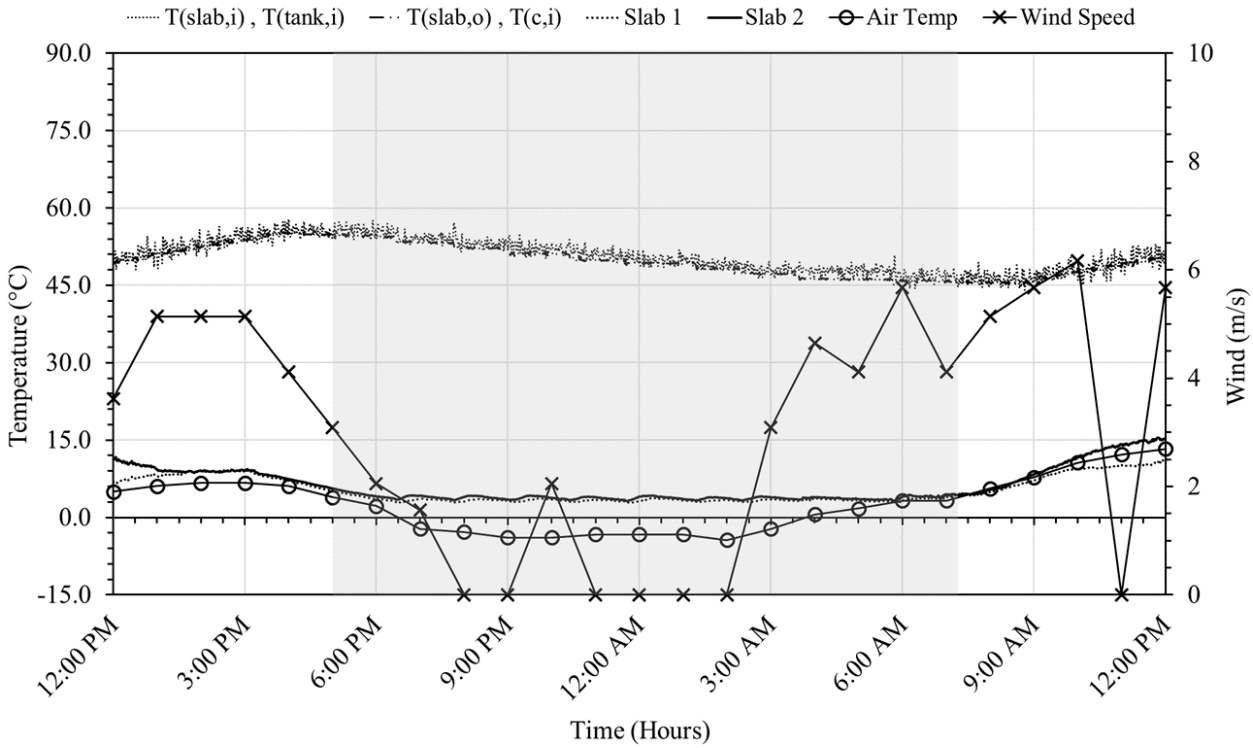

Figure 74: Hydronic pavement heating performance during December 12-13, 2017 test cycle.

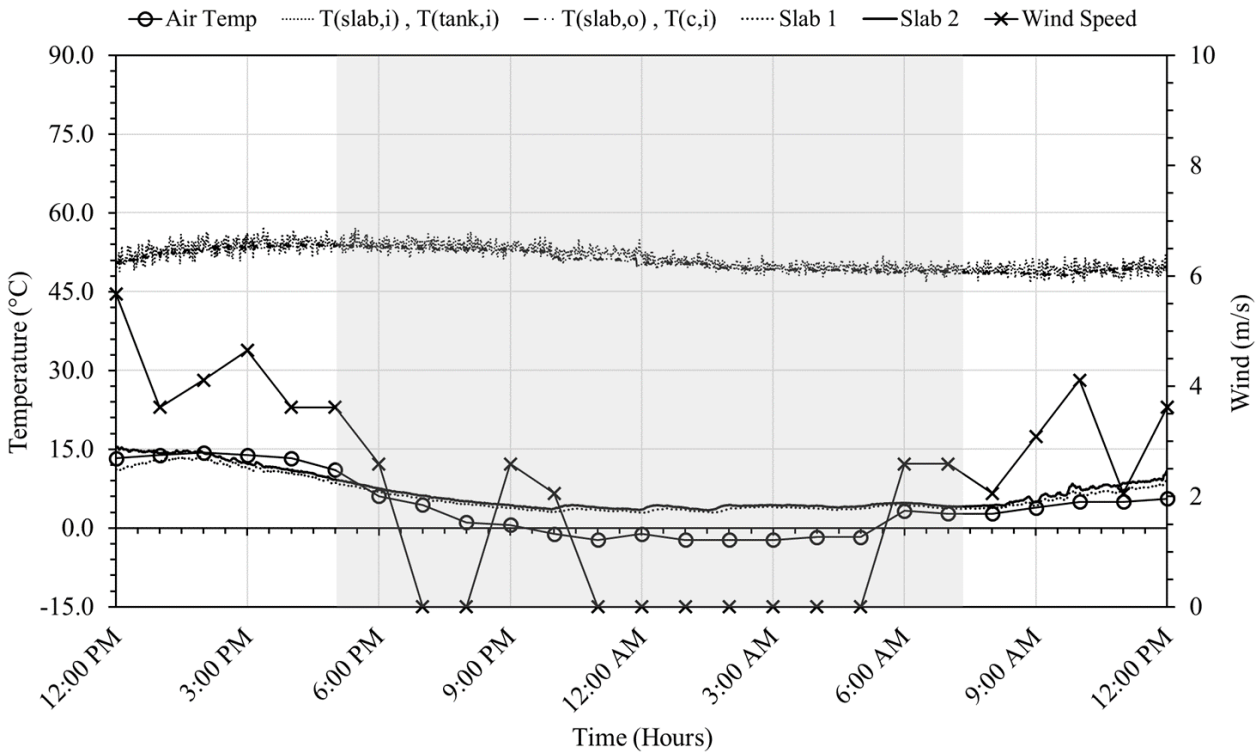

Figure 75: Hydronic pavement heating performance during December 13-14, 2017 test cycle.

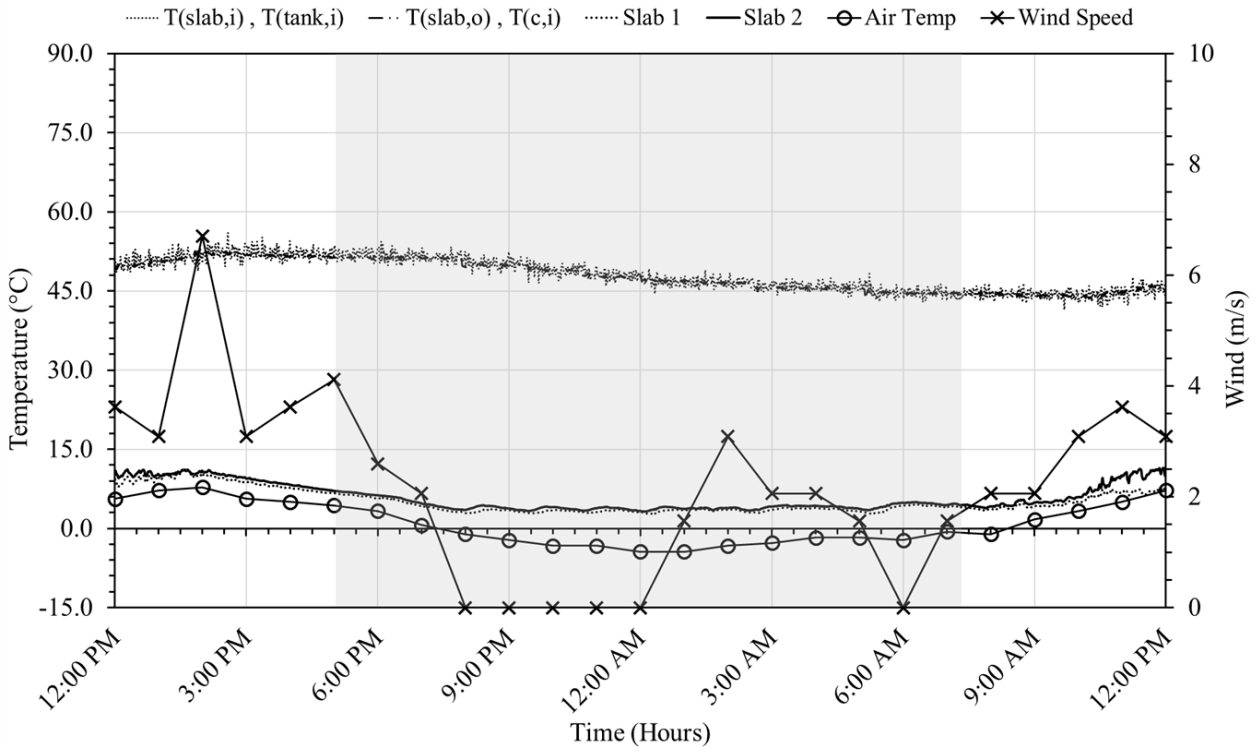

Figure 76: Hydronic pavement heating performance during December 14-15, 2017 test cycle.

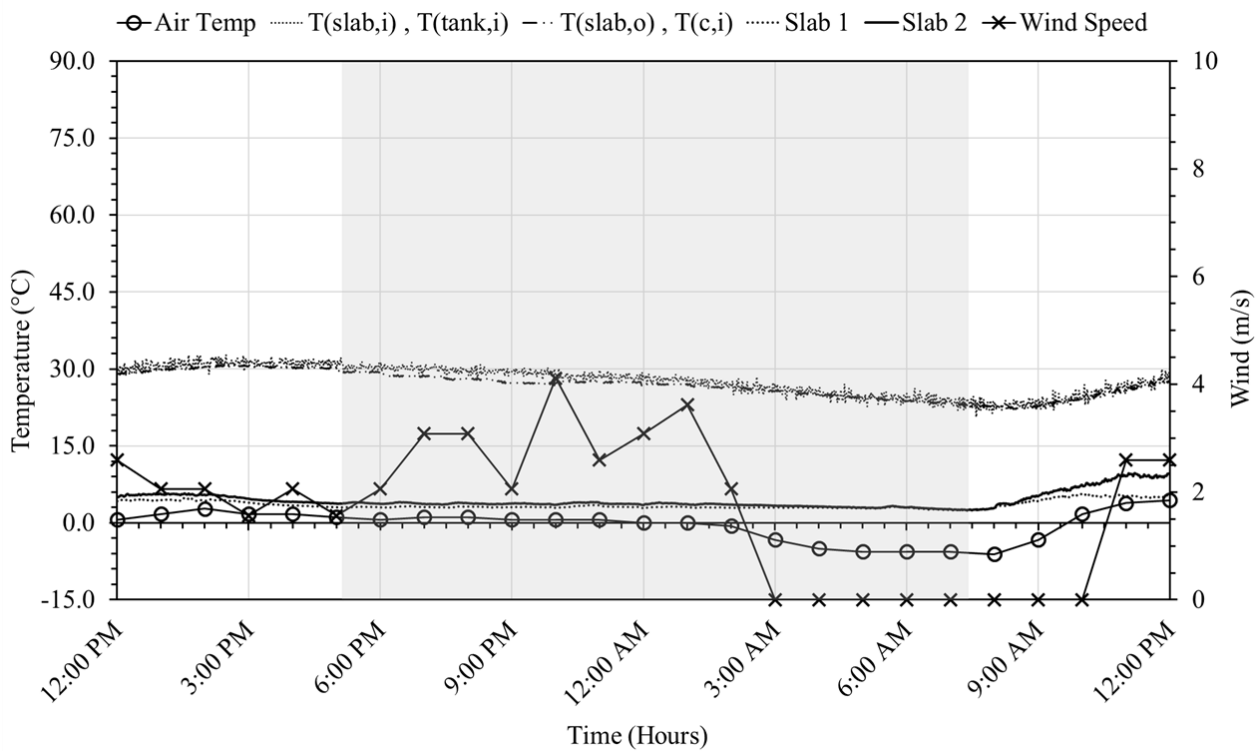

Figure 77: Hydronic pavement heating performance during December 25-26, 2017 test cycle.

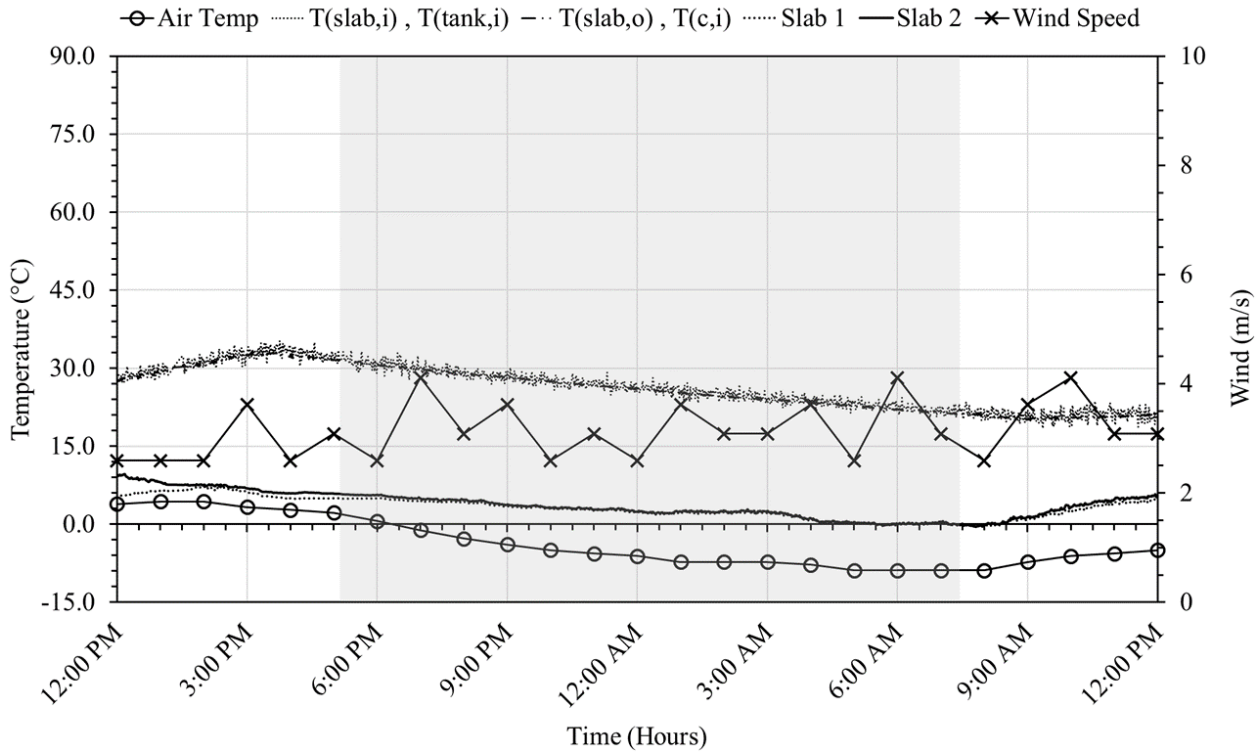

Figure 78: Hydronic pavement heating performance during December 26-27, 2017 test cycle.

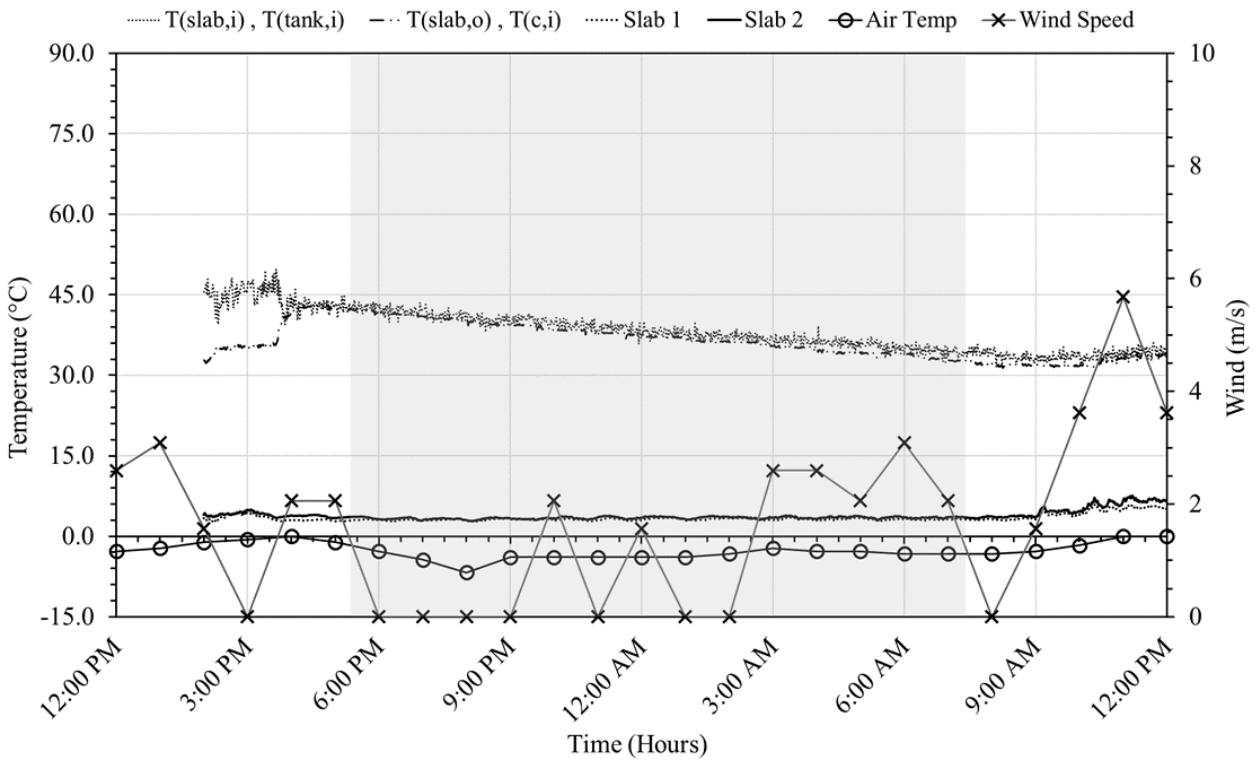

Figure 79: Hydronic pavement heating performance during January 13-14, 2018 test cycle.

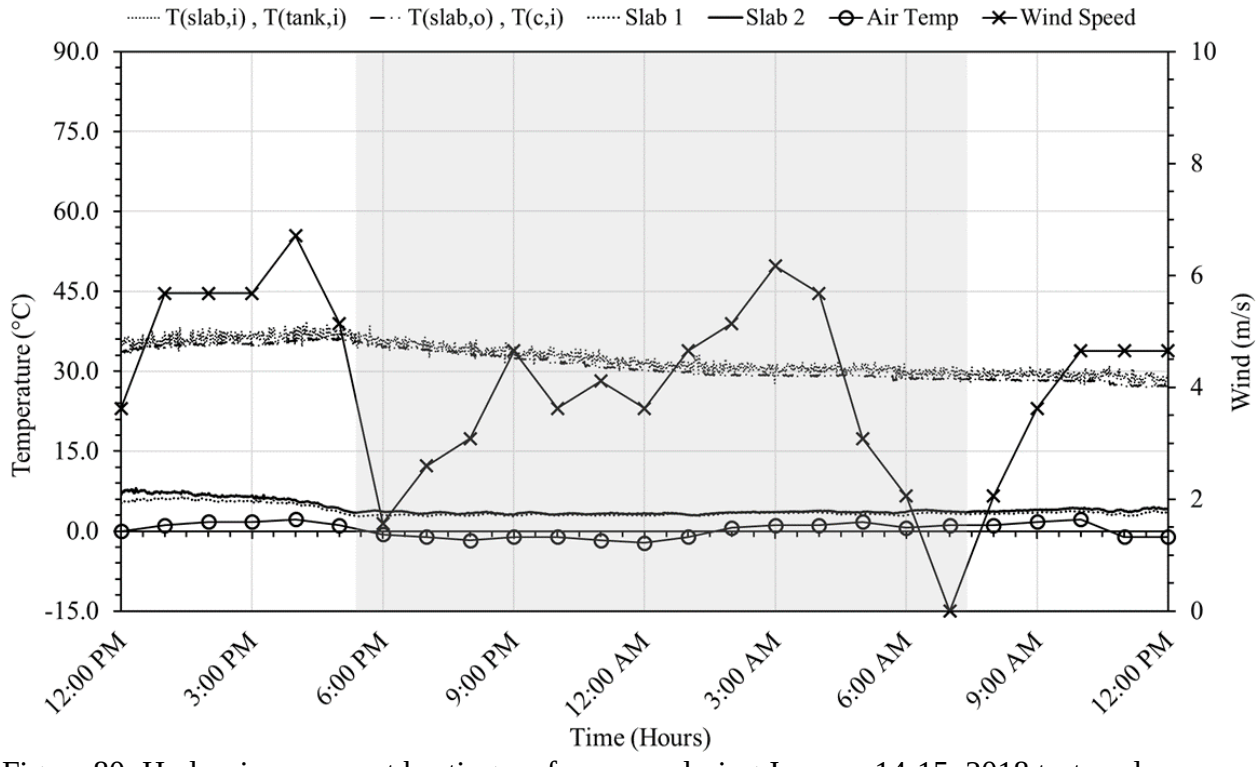

Figure 80: Hydronic pavement heating performance during January 14-15, 2018 test cycle.

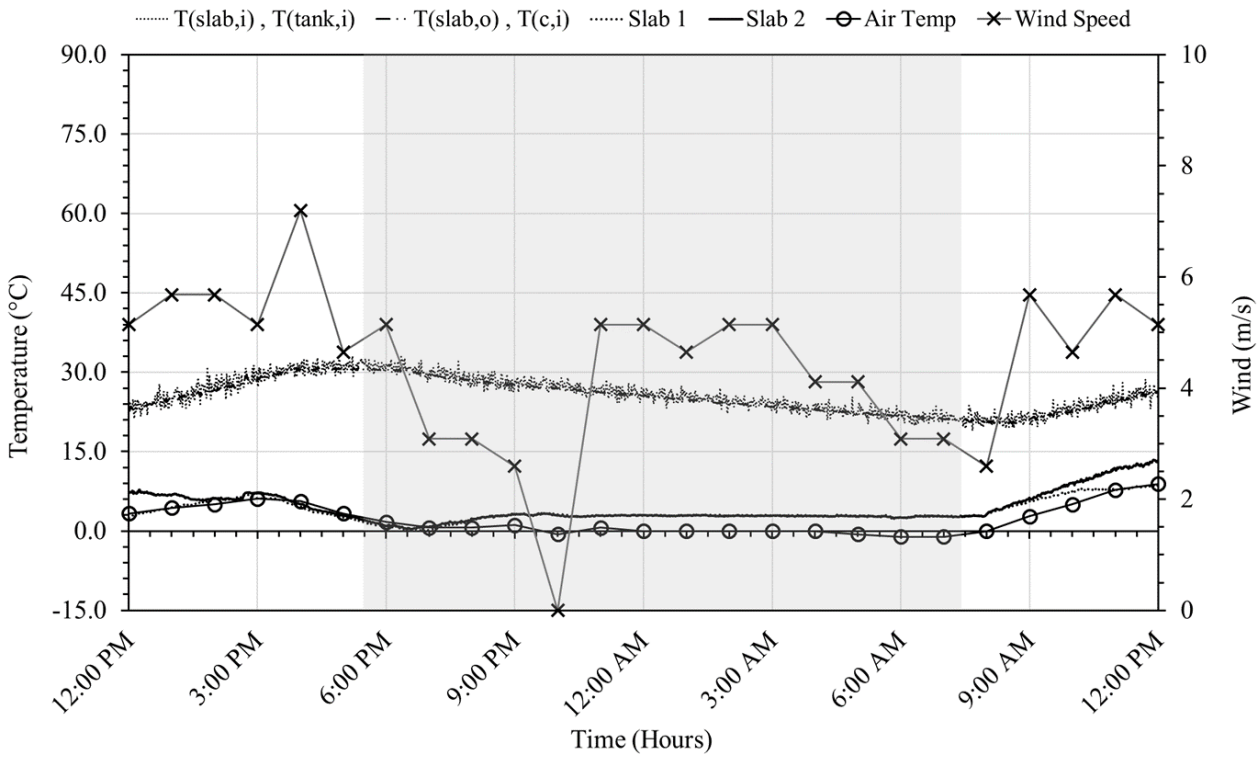

Figure 81: Hydronic pavement heating performance during January 18-19, 2018 test cycle.

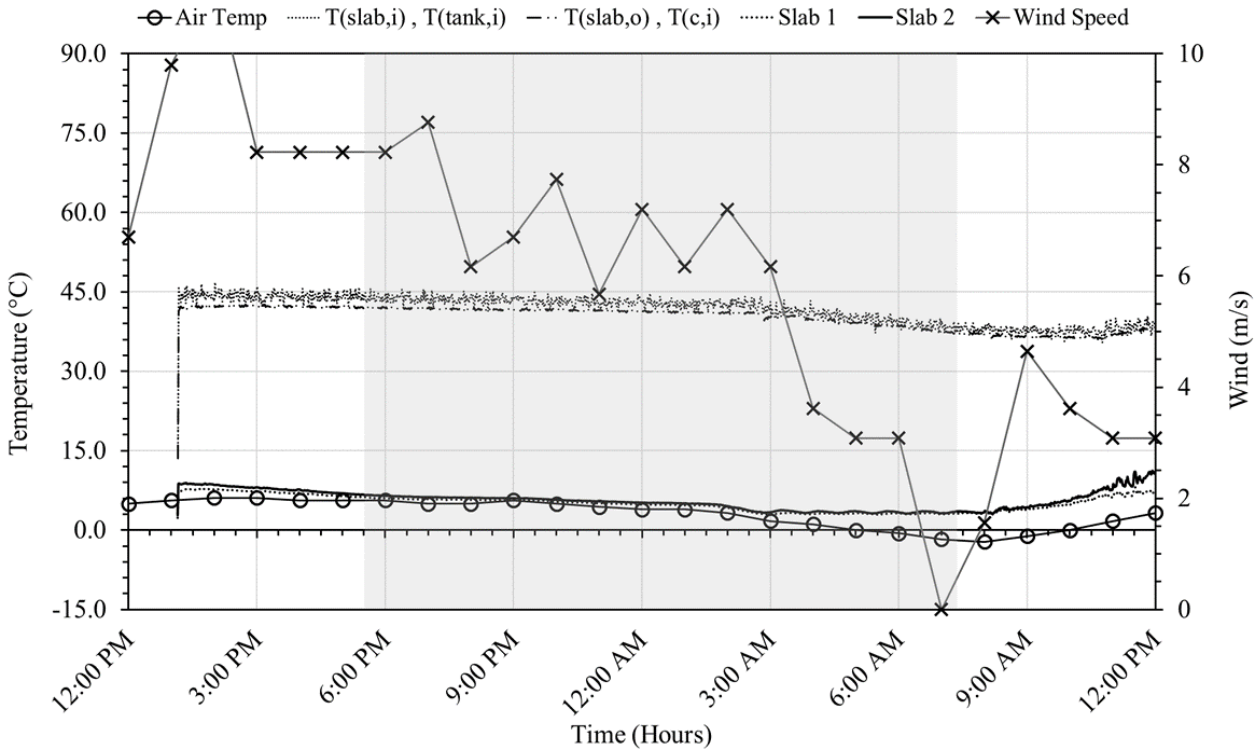

Figure 82: Hydronic pavement heating performance during January 22-23, 2018 test cycle.

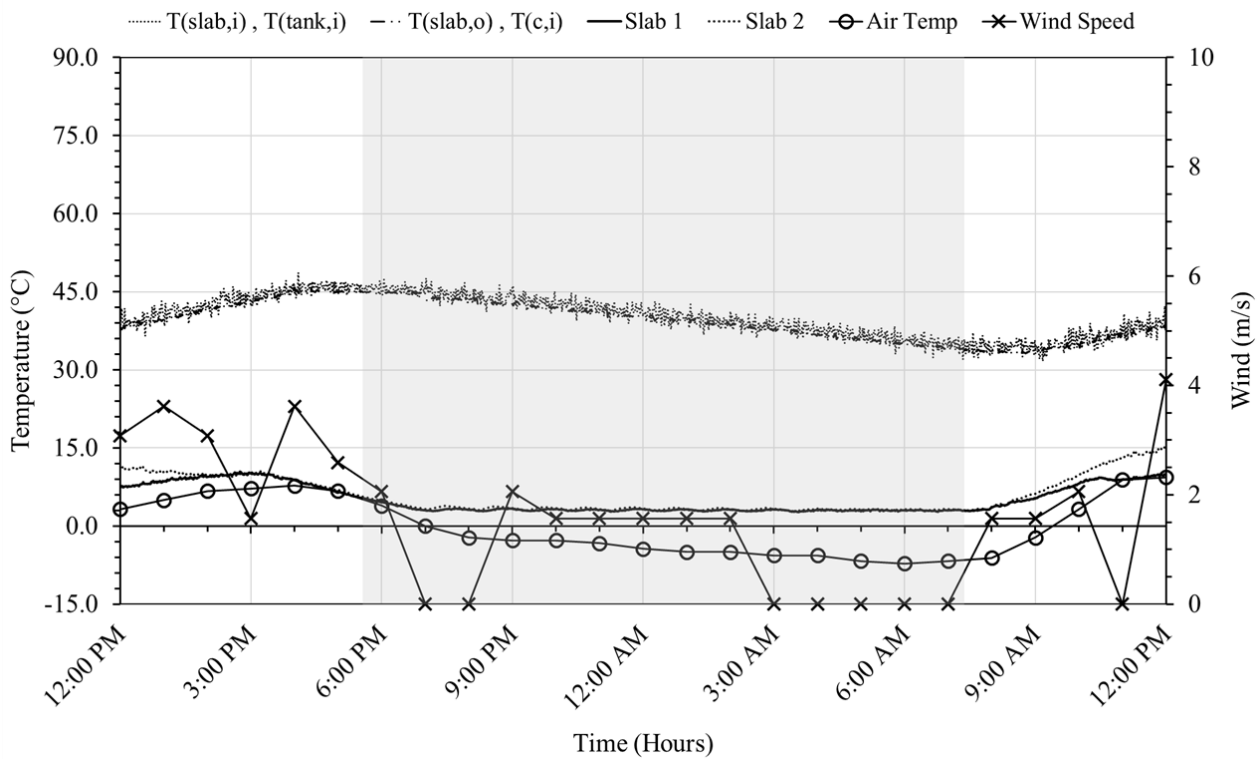

Figure 83: Hydronic pavement heating performance during January 23-24, 2018 test cycle.

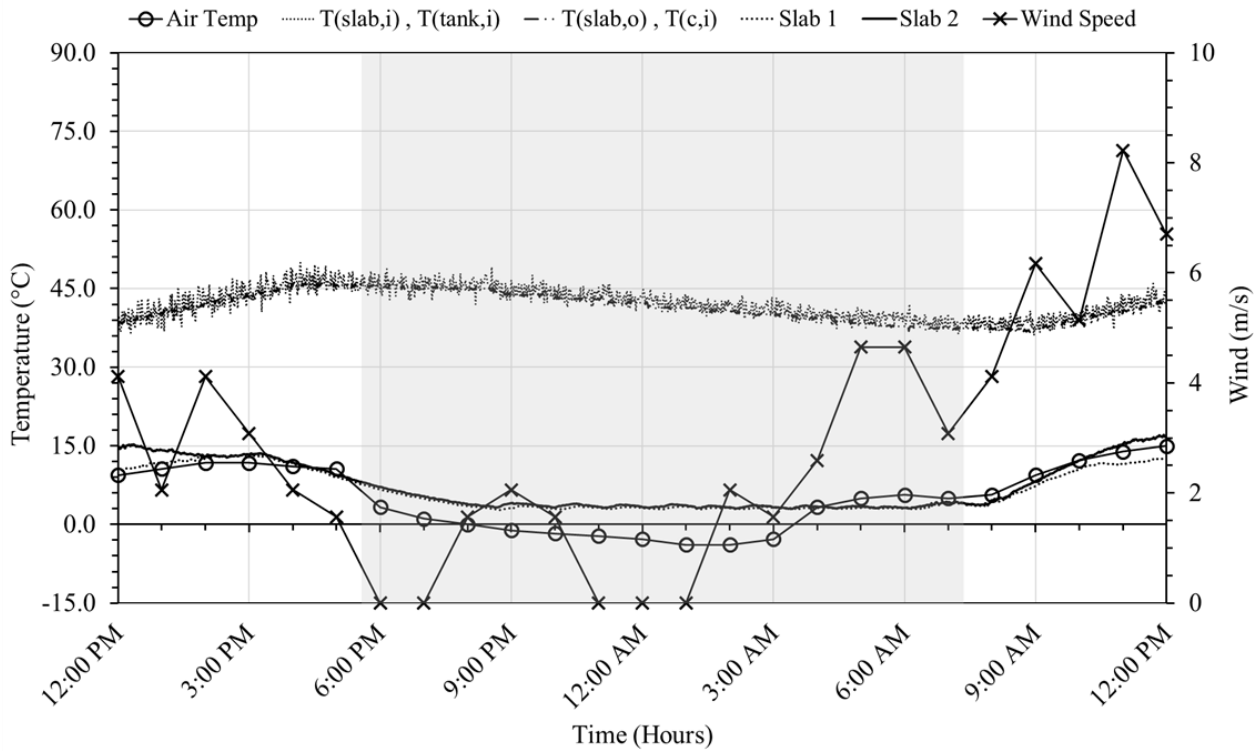

Figure 84: Hydronic pavement heating performance during January 24-25, 2018 test cycle.

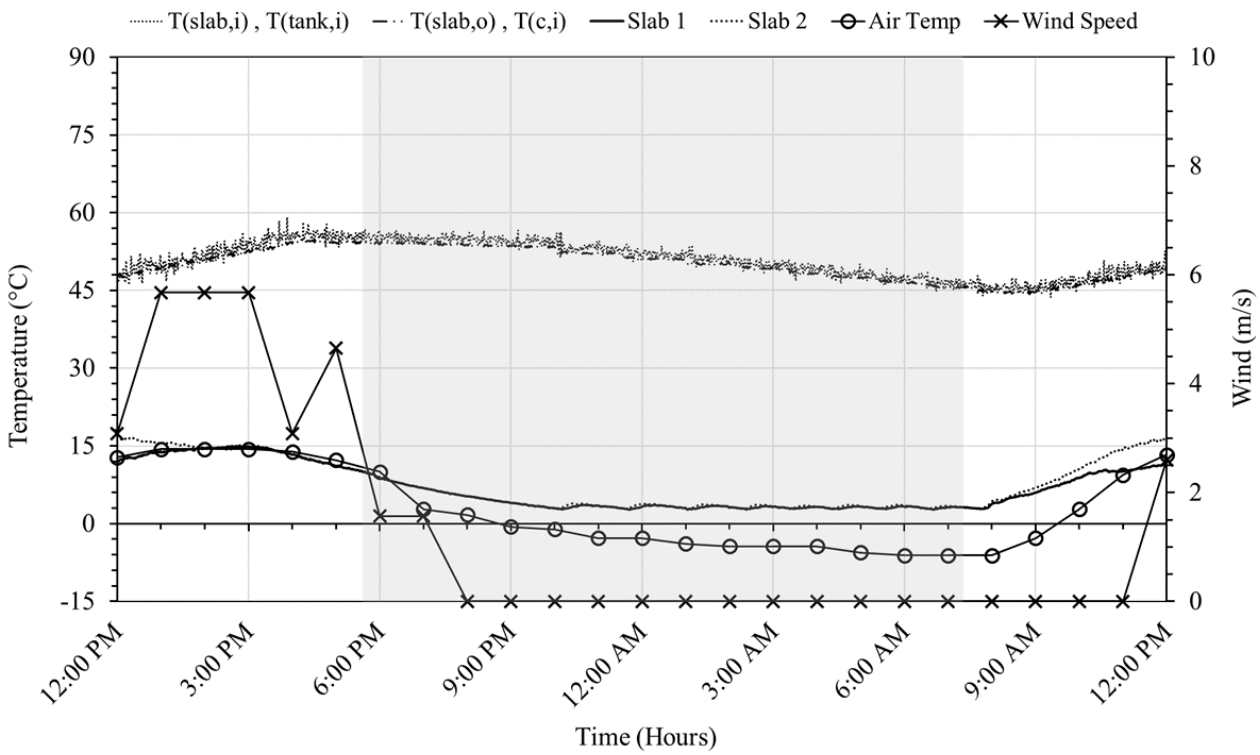

Figure 85: Hydronic pavement heating performance during January 27-28, 2018 test cycle.

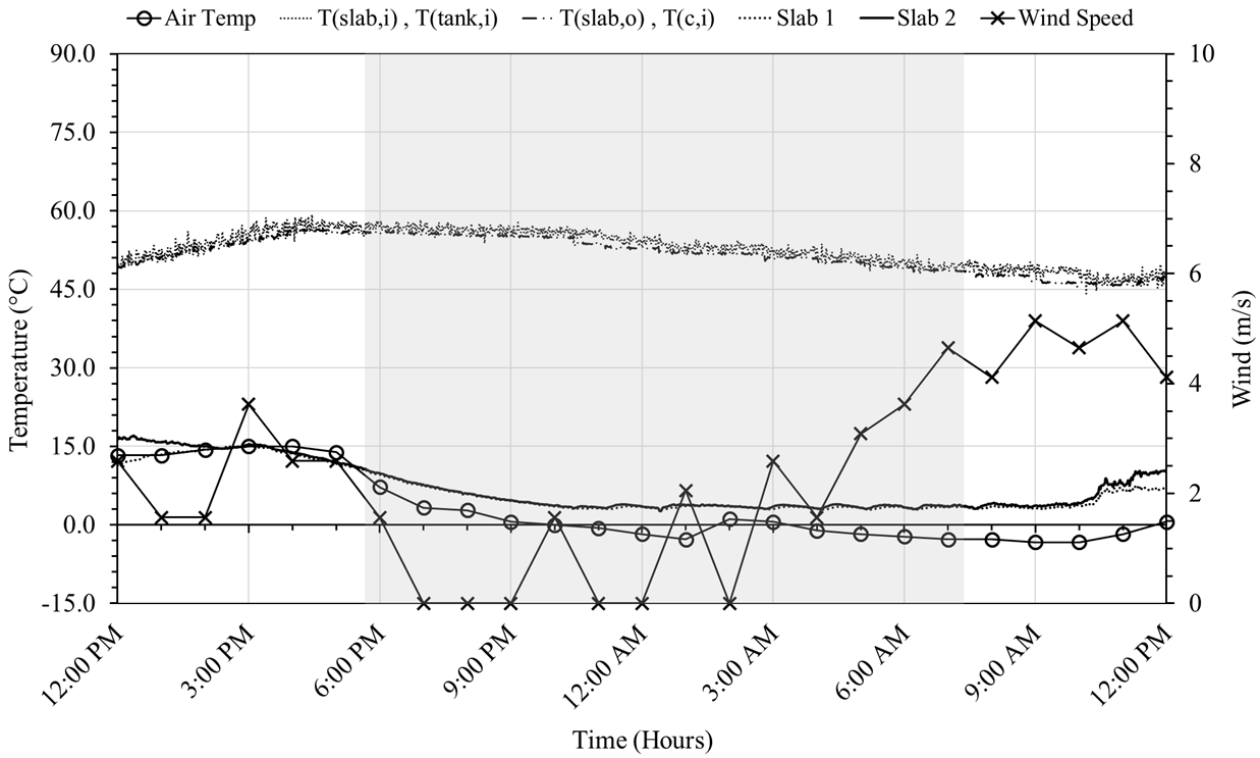

Figure 86: Hydronic pavement heating performance during January 28-29, 2018 test cycle.

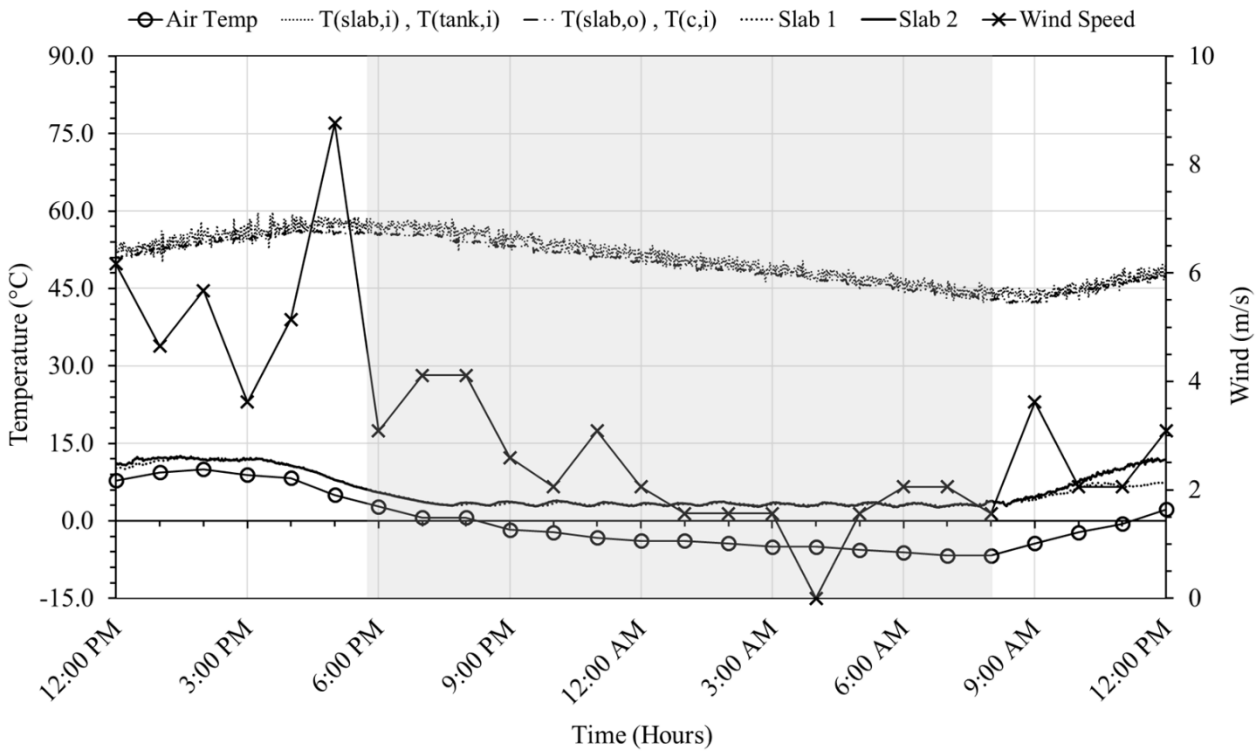

Figure 87: Hydronic pavement heating performance during February 1-2, 2018 test cycle.

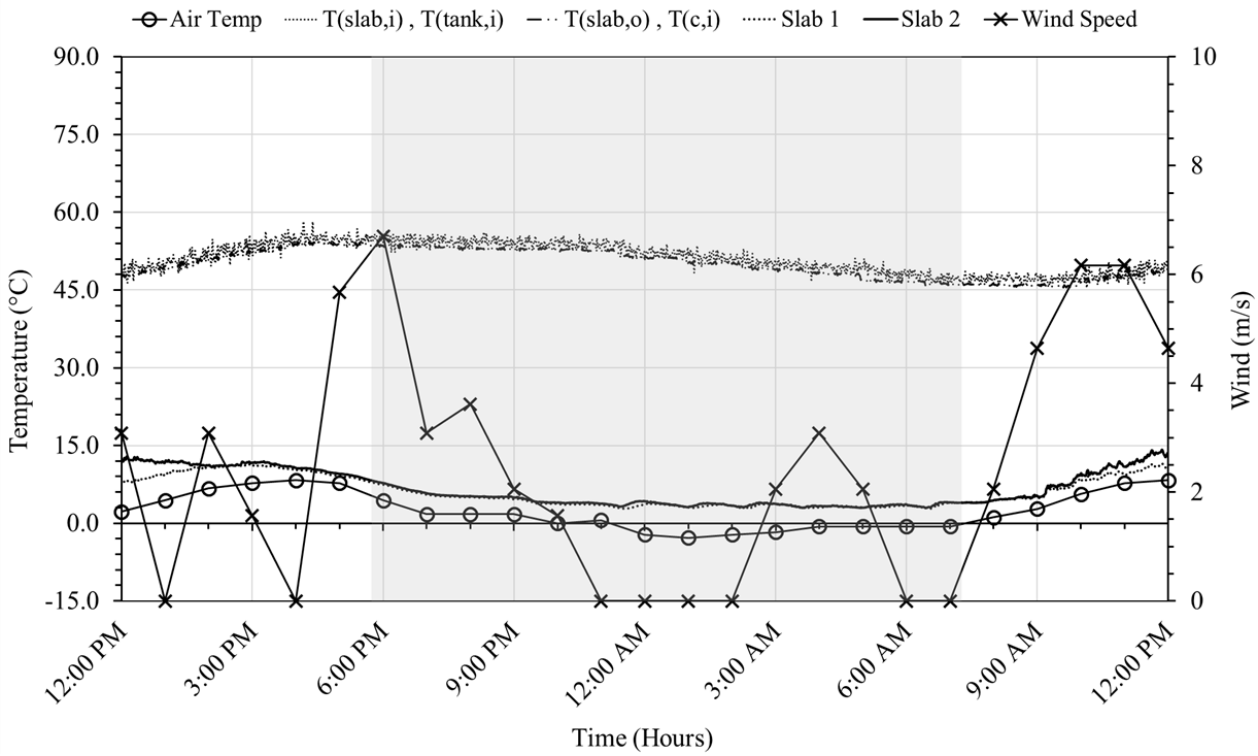

Figure 88: Hydronic pavement heating performance during February 2-3, 2018 test cycle.

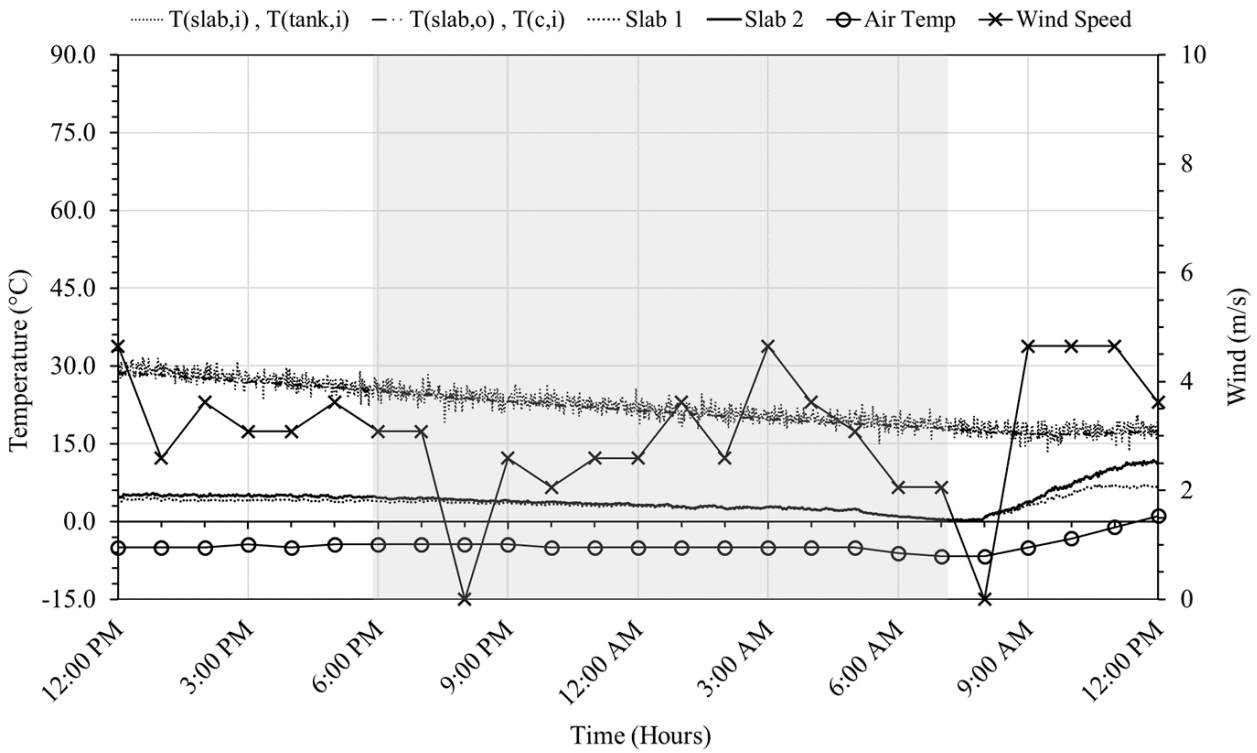

Figure 89: Hydronic pavement heating performance during February 11-12, 2018 test cycle.

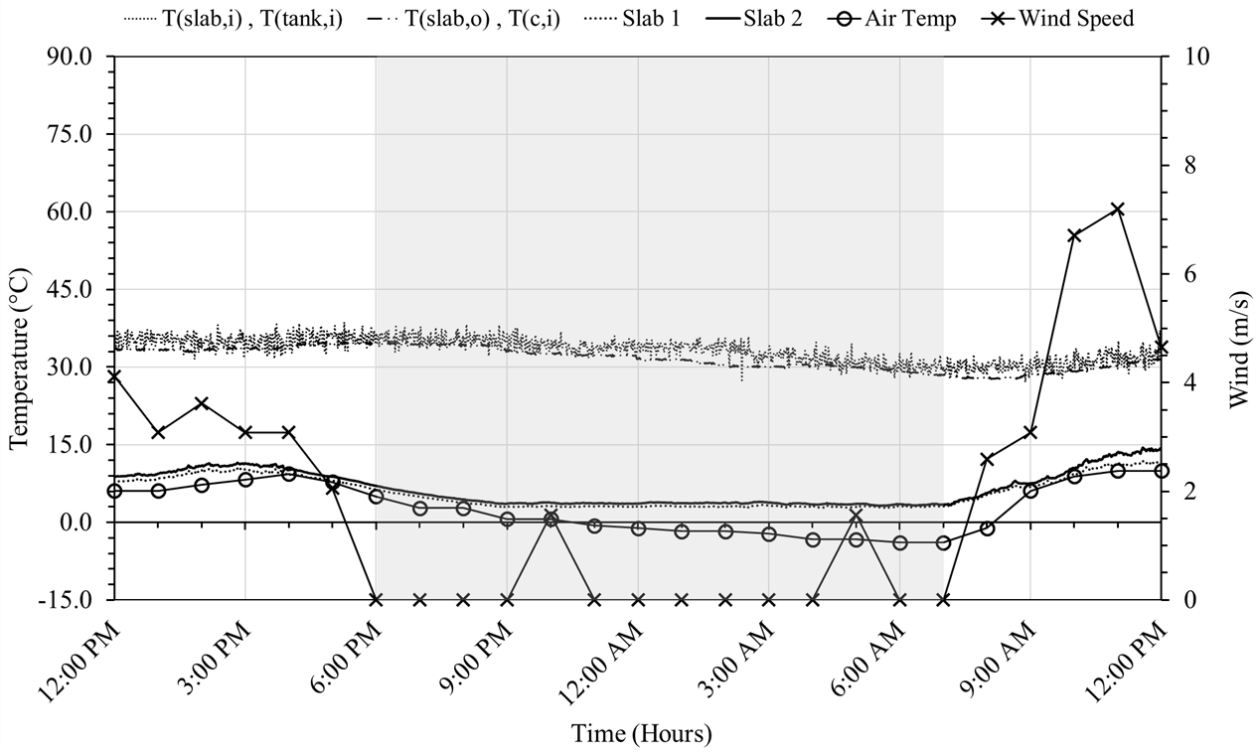

Figure 90: Hydronic pavement heating performance during February 17-18, 2018 test cycle.

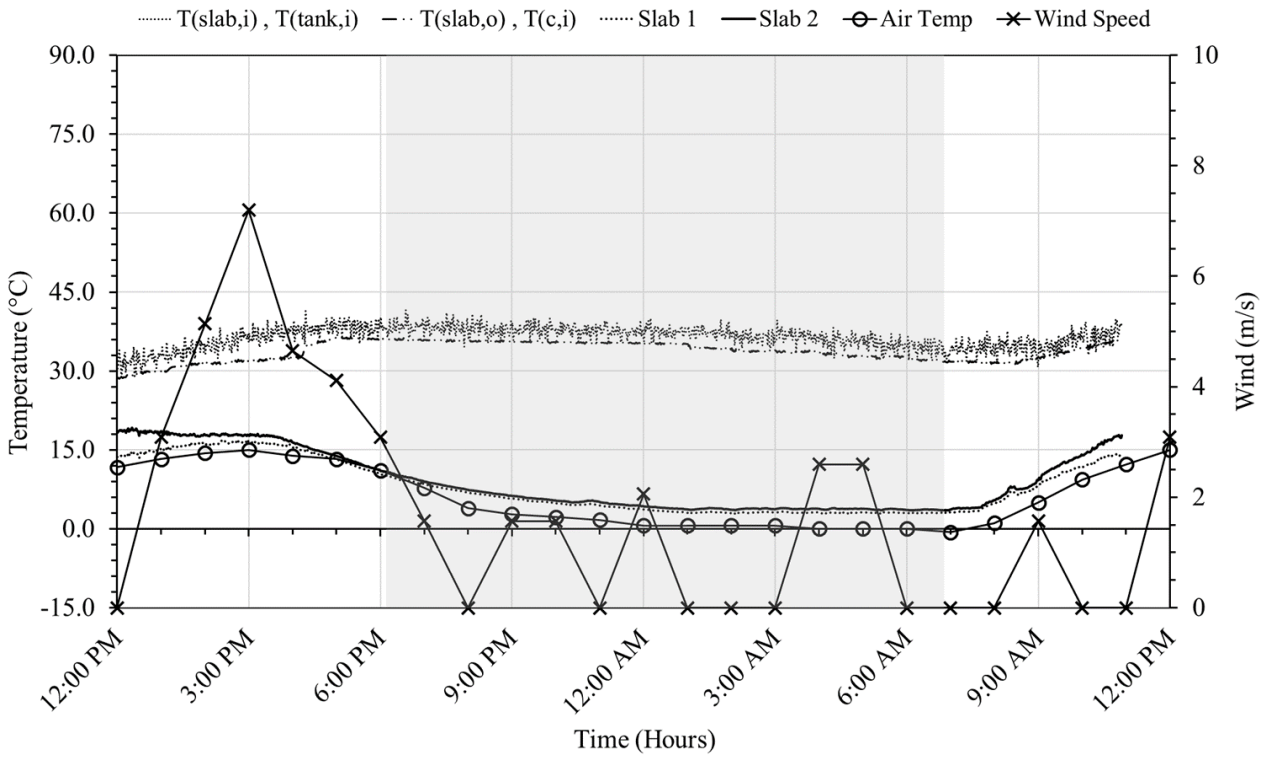

Figure 91: Hydronic pavement heating performance during February 25-26, 2018 test cycle.

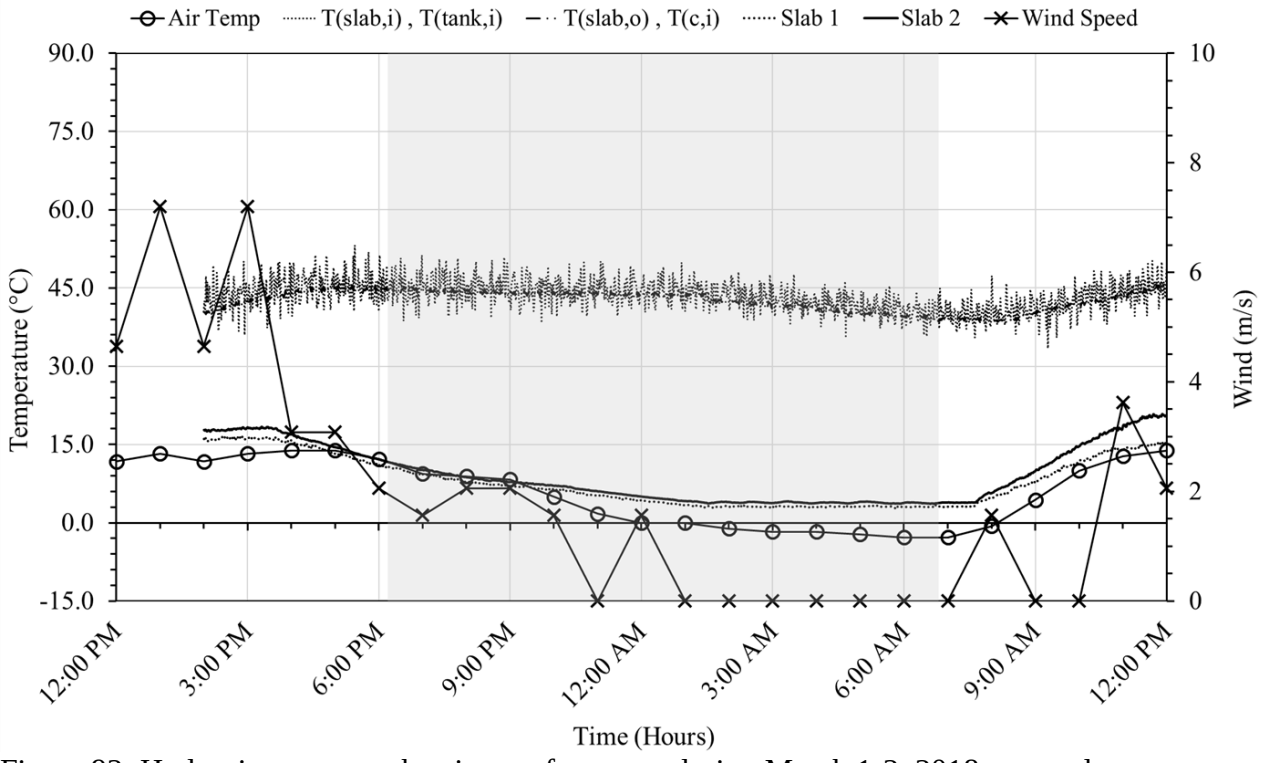

Figure 92: Hydronic pavement heating performance during March 1-2, 2018 test cycle.

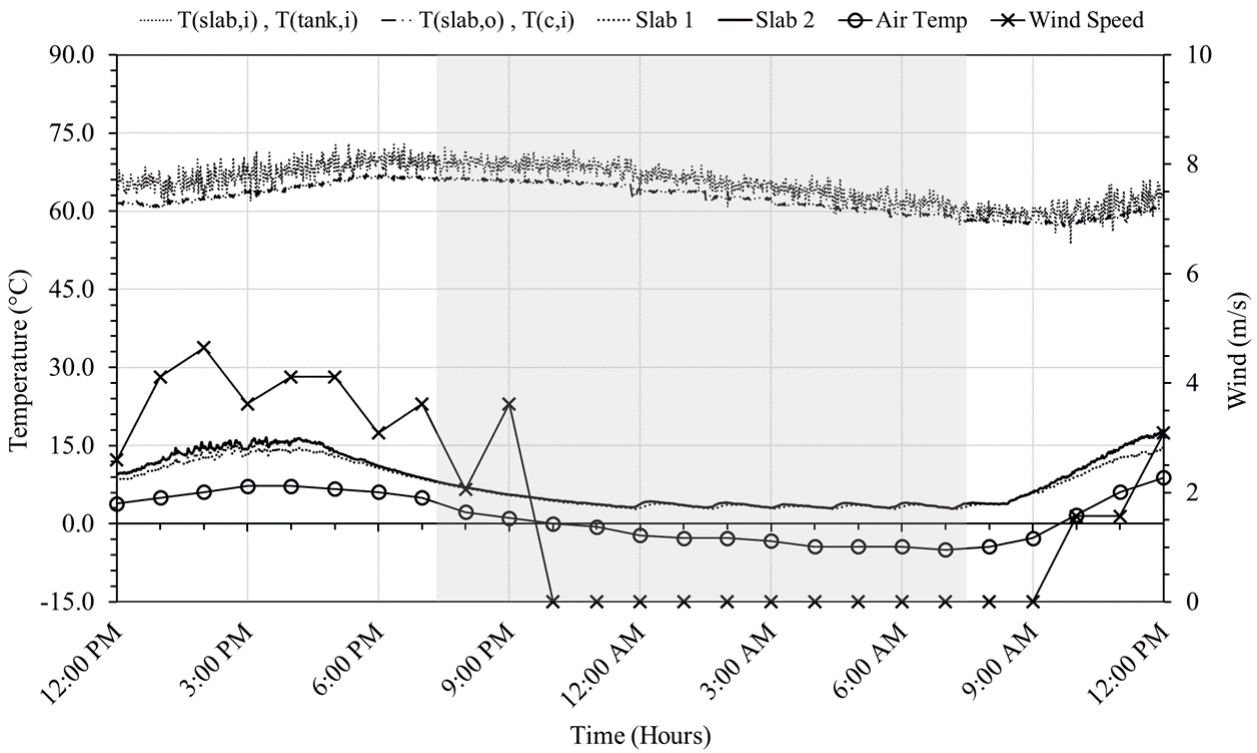

Figure 93: Hydronic pavement heating performance during March 12-13, 2018 test cycle.

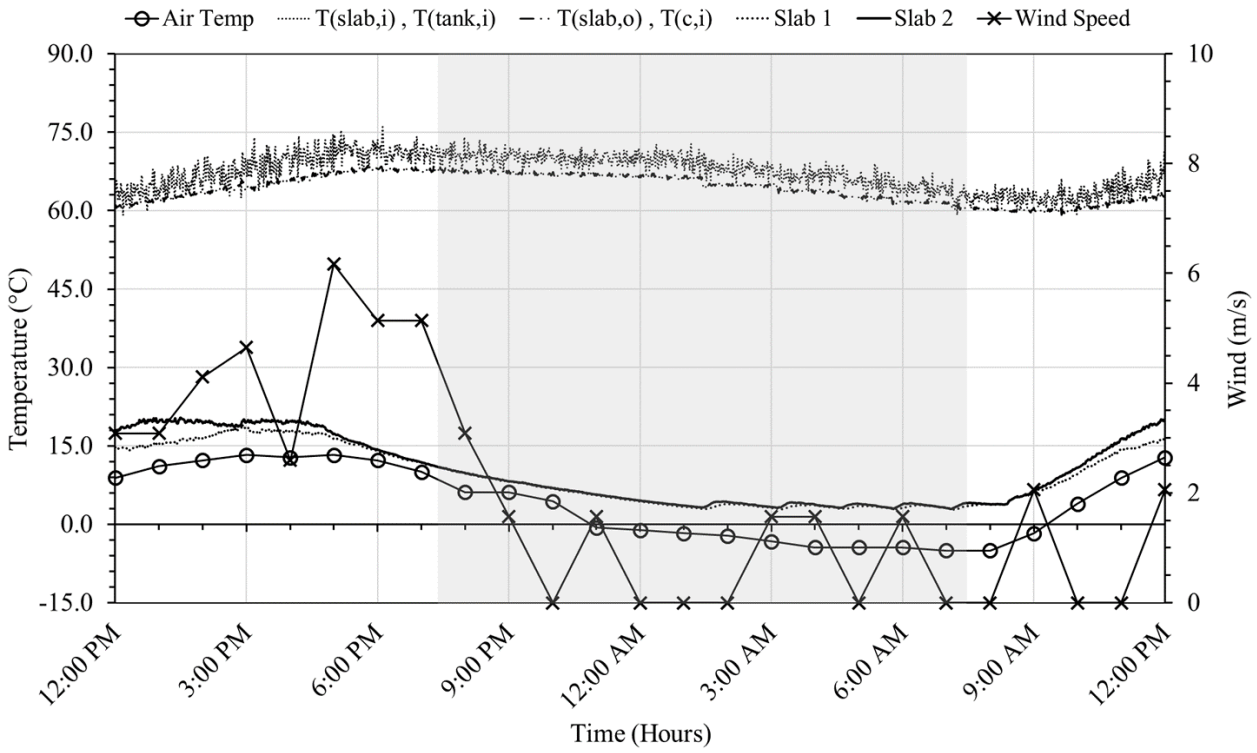

Figure 94: Hydronic pavement heating performance during March 13-14, 2018 test cycle.

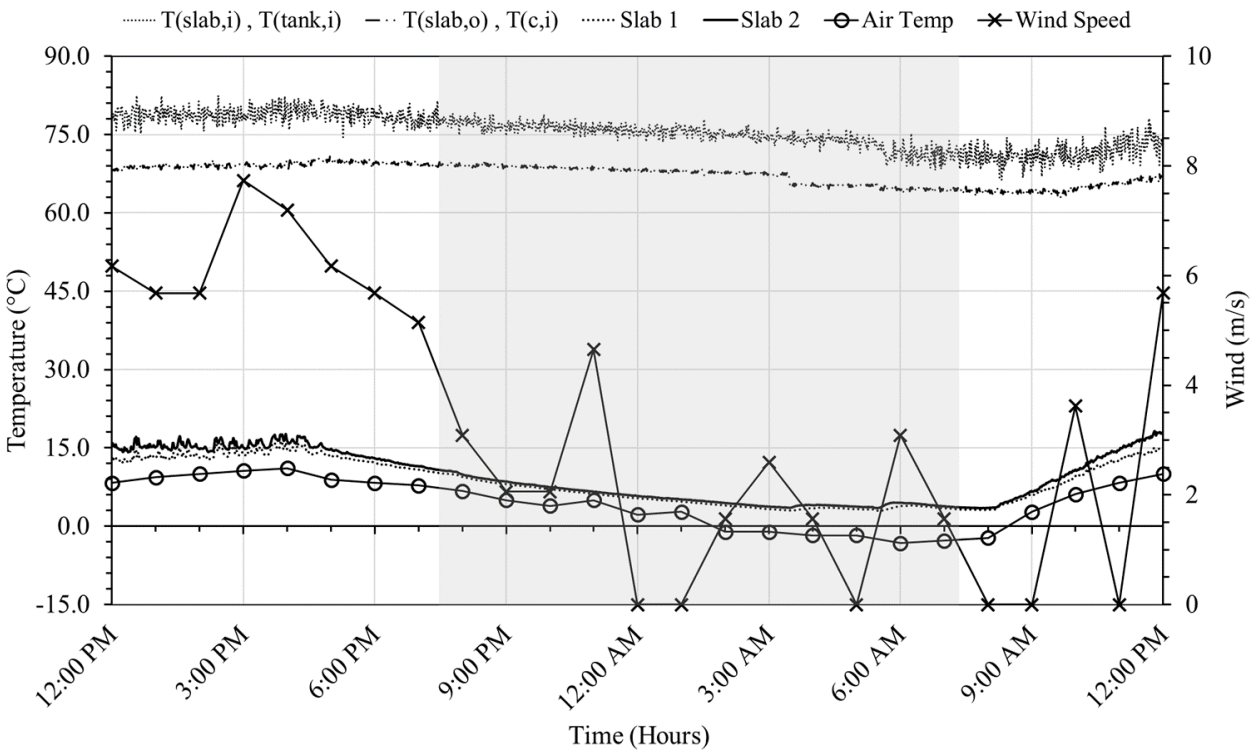

Figure 95: Hydronic pavement heating performance during March 20-21, 2018 test cycle.

APPENDIX B

The material in this appendix include data figures for the storage tank heating test cycles.

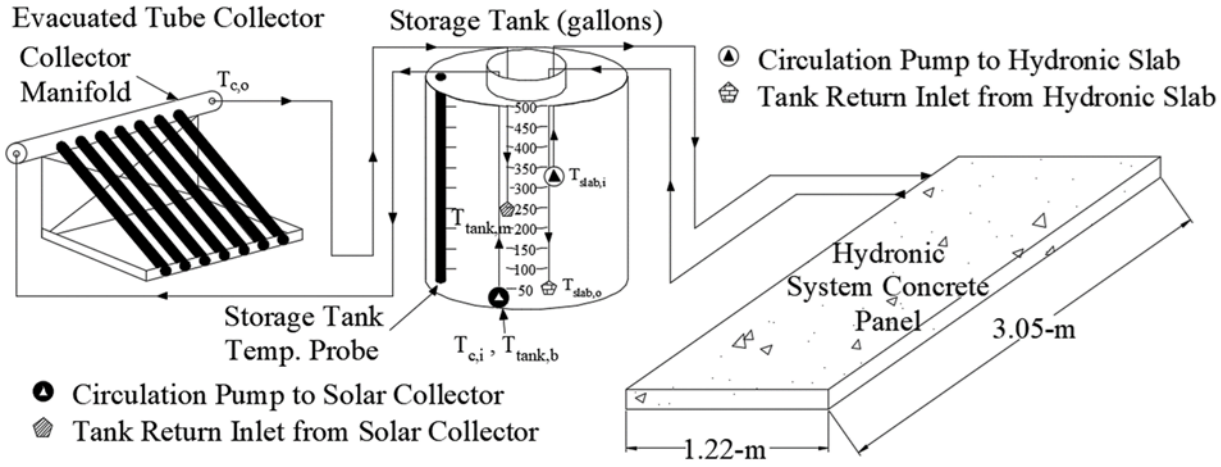

Figure 96: Schematic diagram of solar water-glycol heating subsystem (left) and hydronic heated pavement subsystem (right).

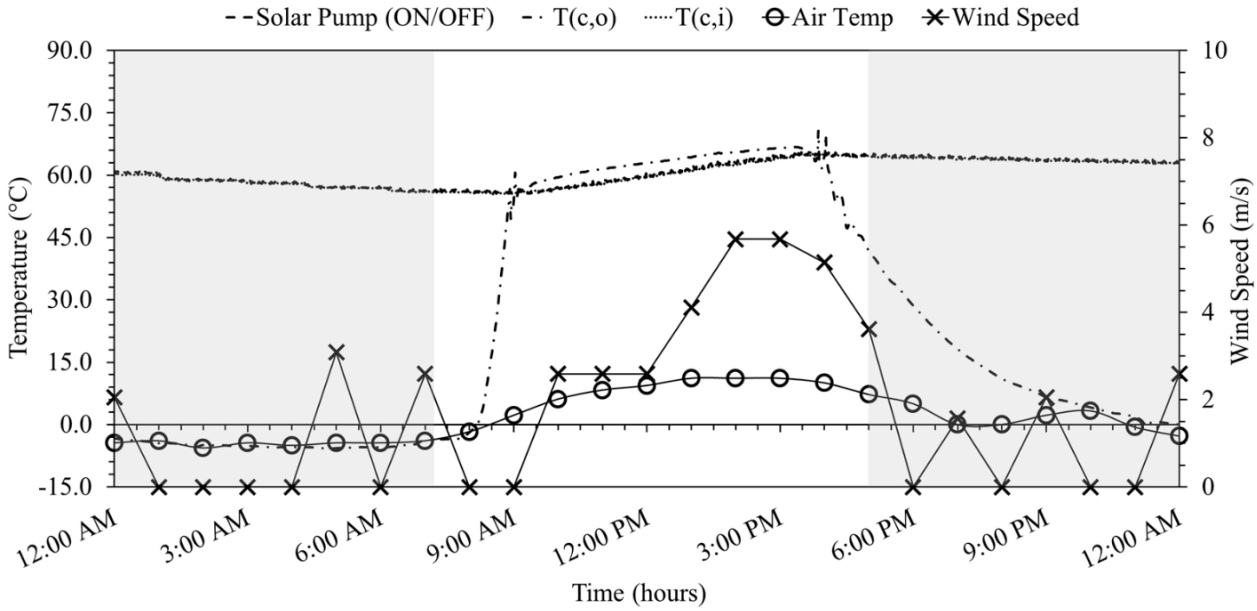

Figure 97: Storage tank heating performance on December 6, 2017.

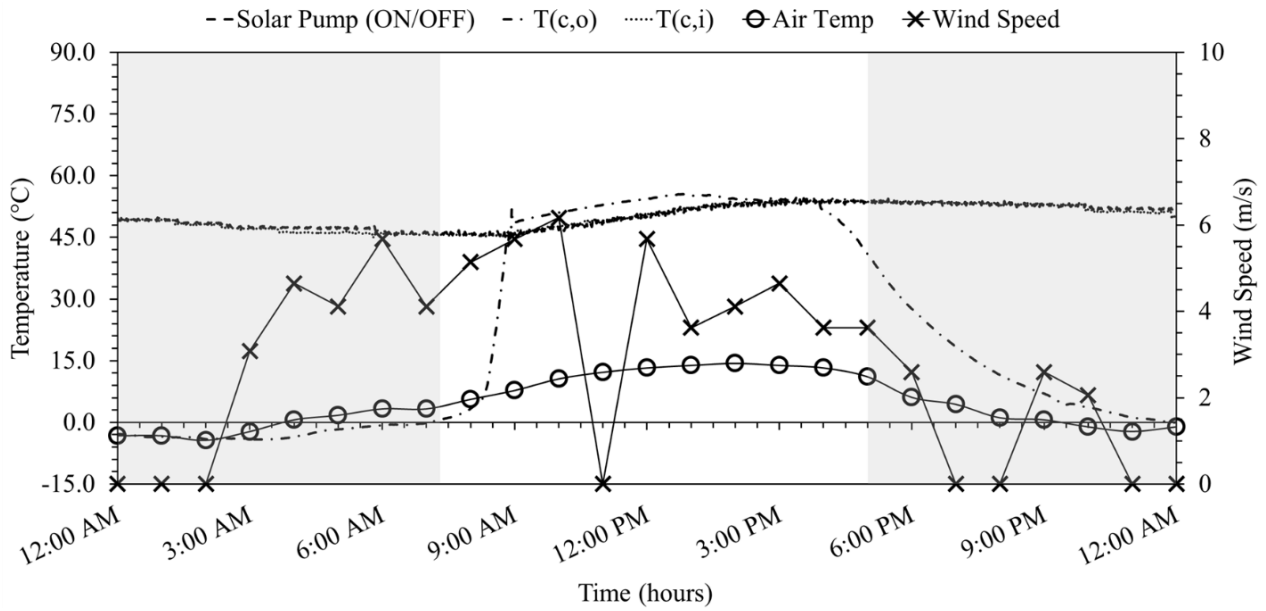

Figure 98: Storage tank heating performance on December 13, 2017.

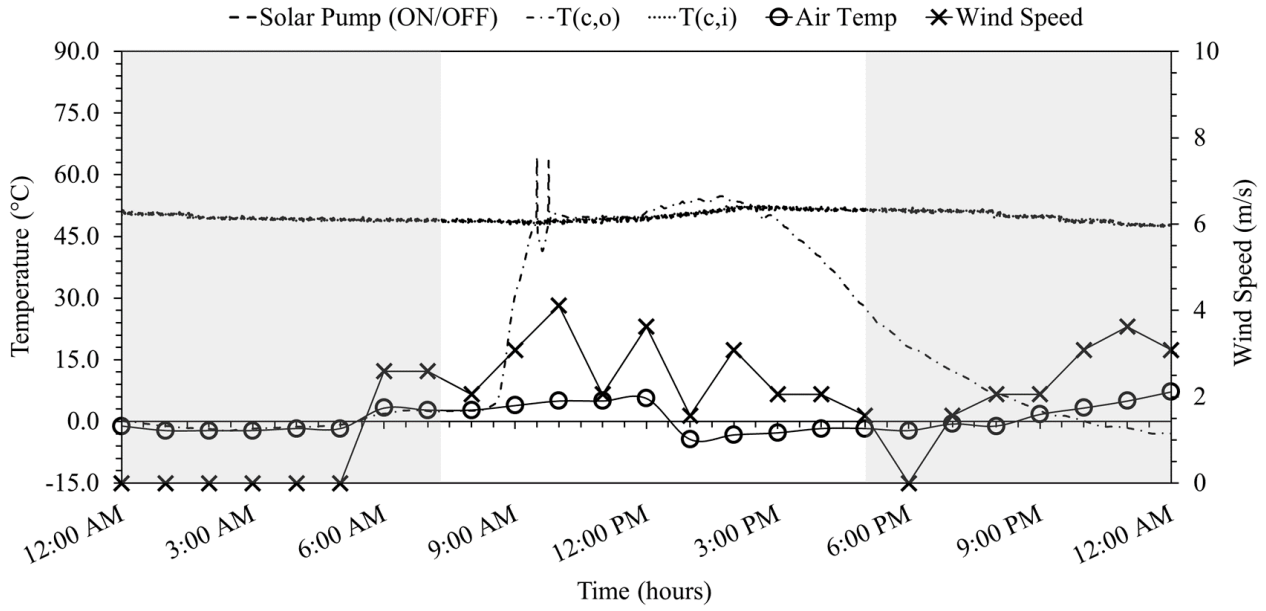

Figure 99: Storage tank heating performance on December 14, 2017.

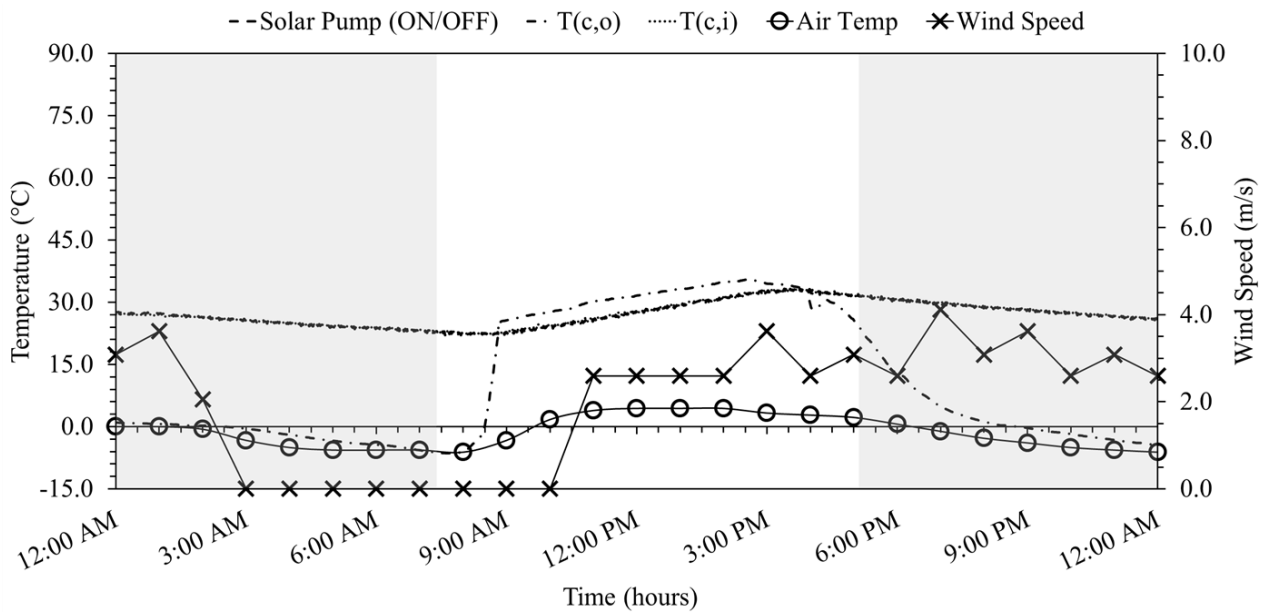

Figure 100: Storage tank heating performance on December 26, 2017.

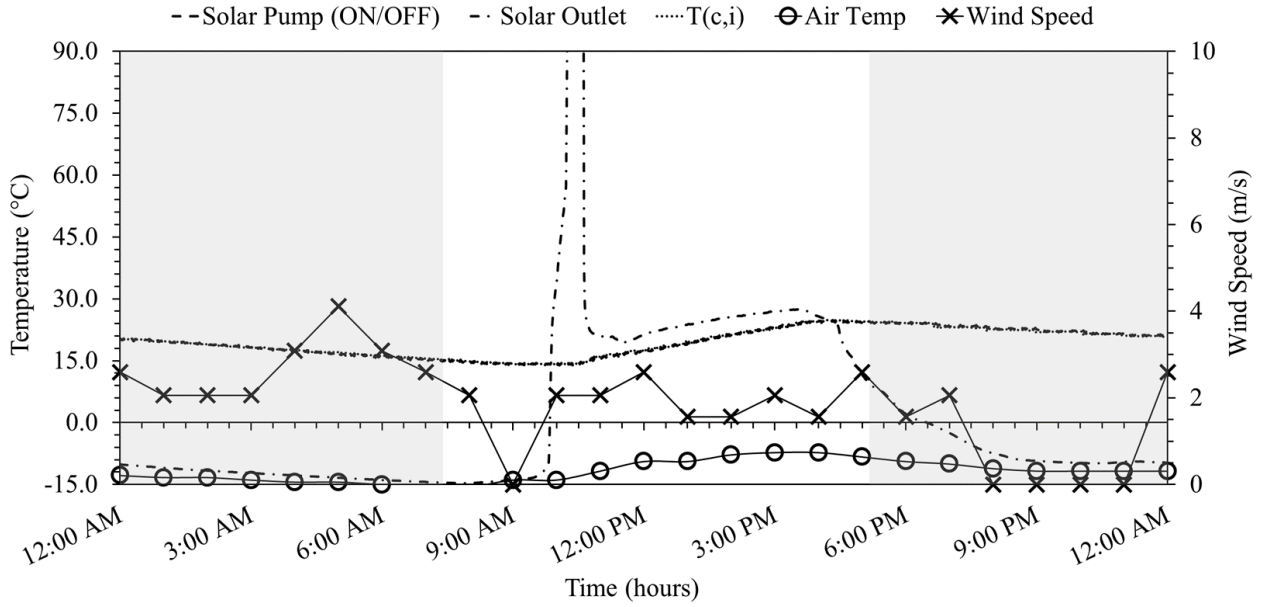

Figure 101: Storage tank heating performance on January 1, 2018.

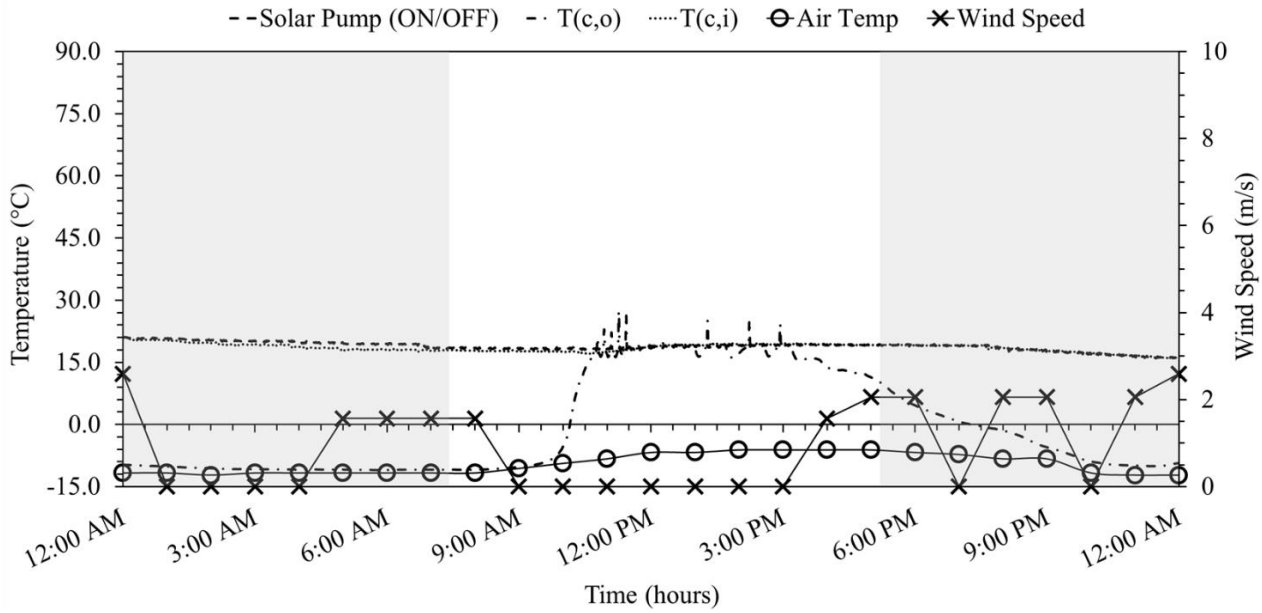

Figure 102: Storage tank heating performance on January 2, 2018.

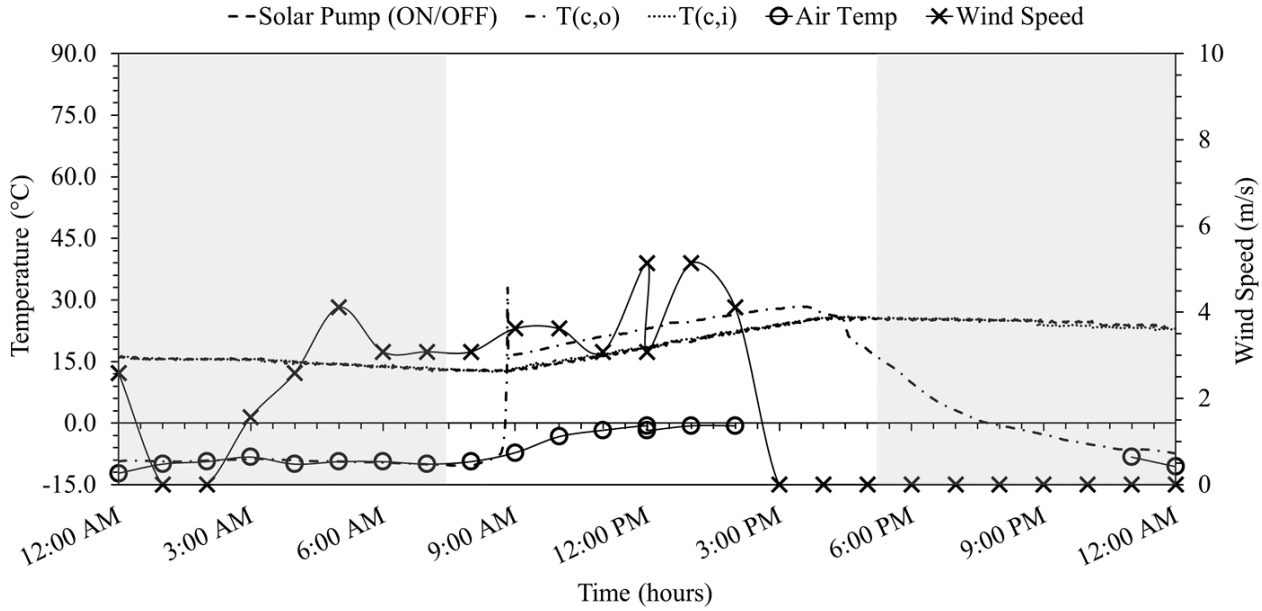

Figure 103: Storage tank heating performance on January 3, 2018.

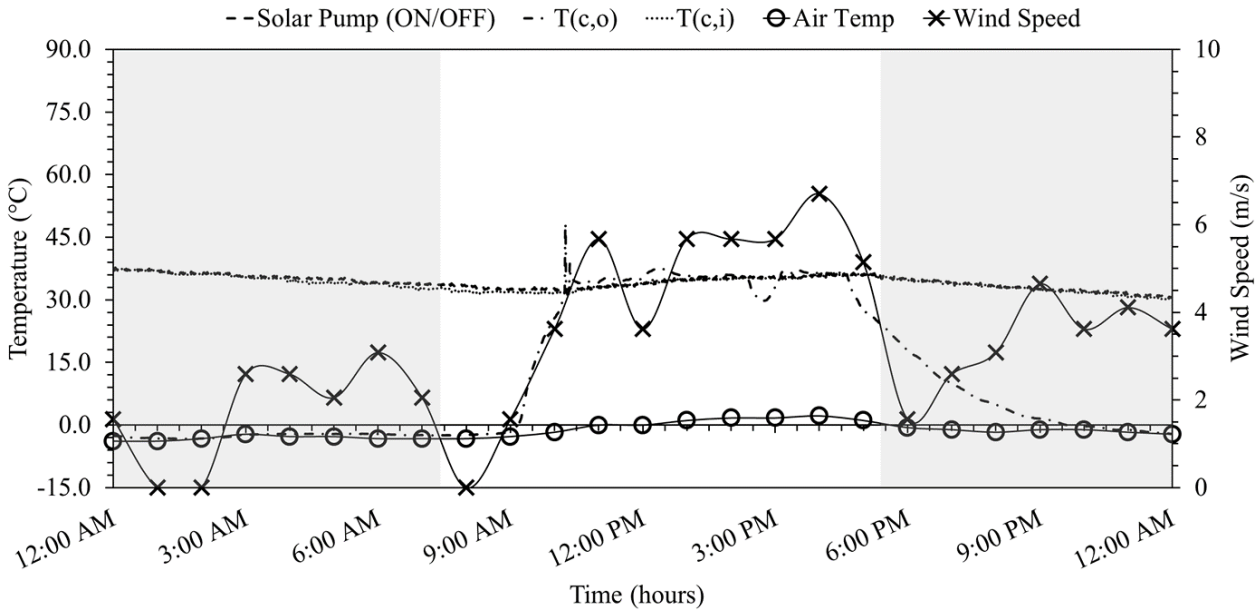

Figure 104: Storage tank heating performance on January 14, 2018.

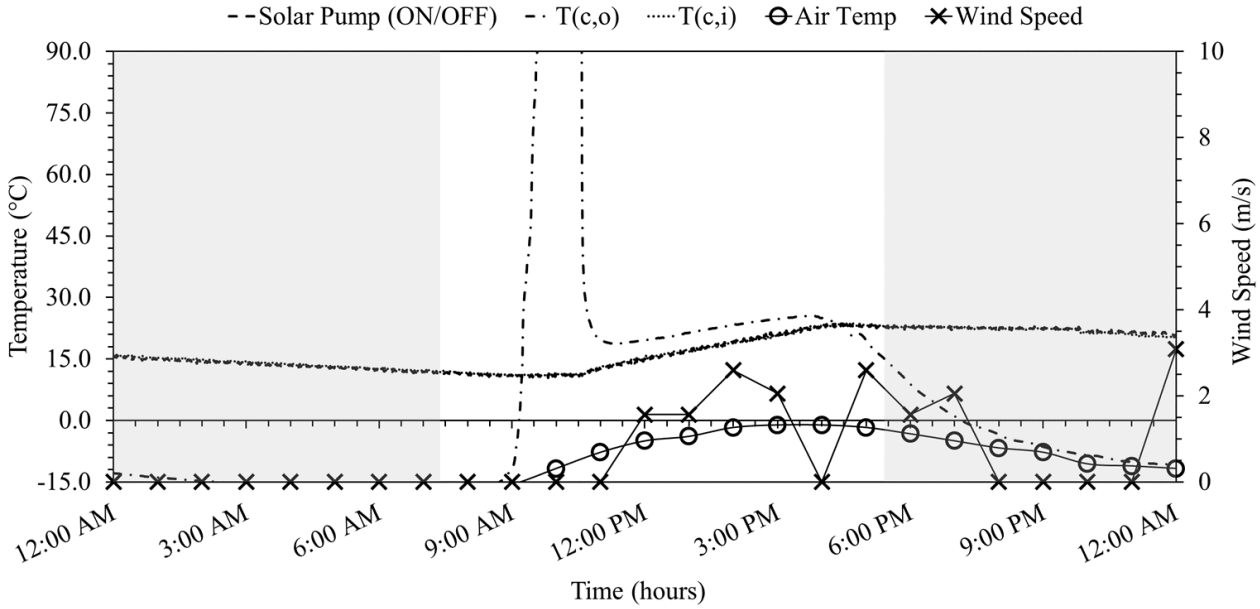

Figure 105: Storage tank heating performance on January 17, 2018.

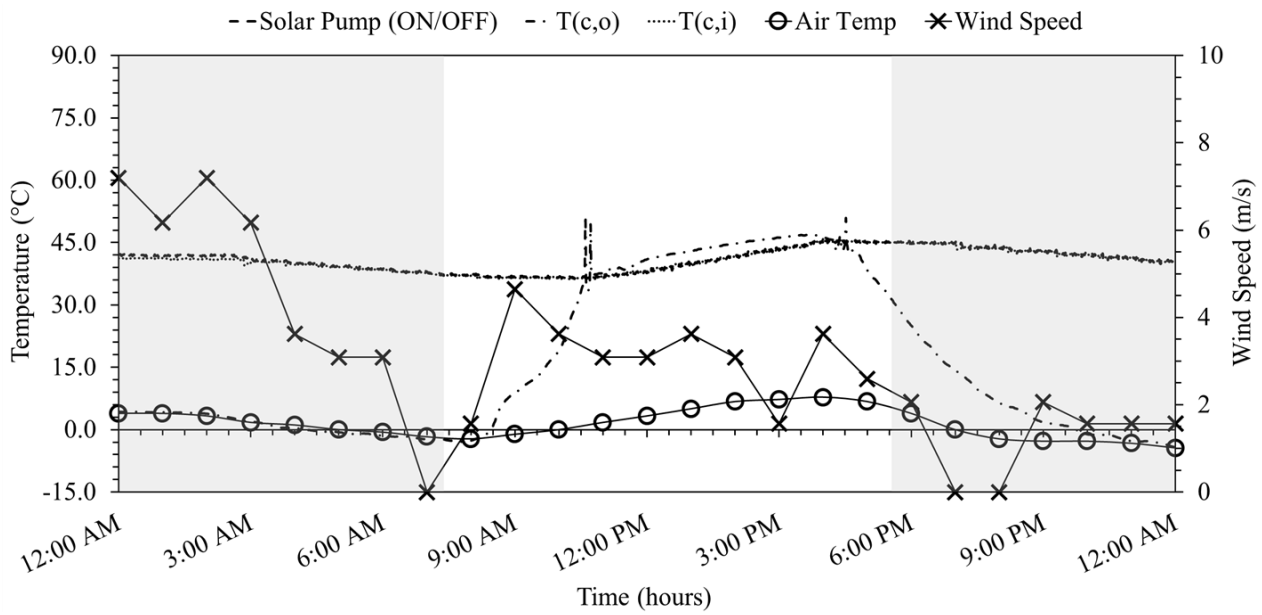

Figure 106: Storage tank heating performance on January 23, 2018.

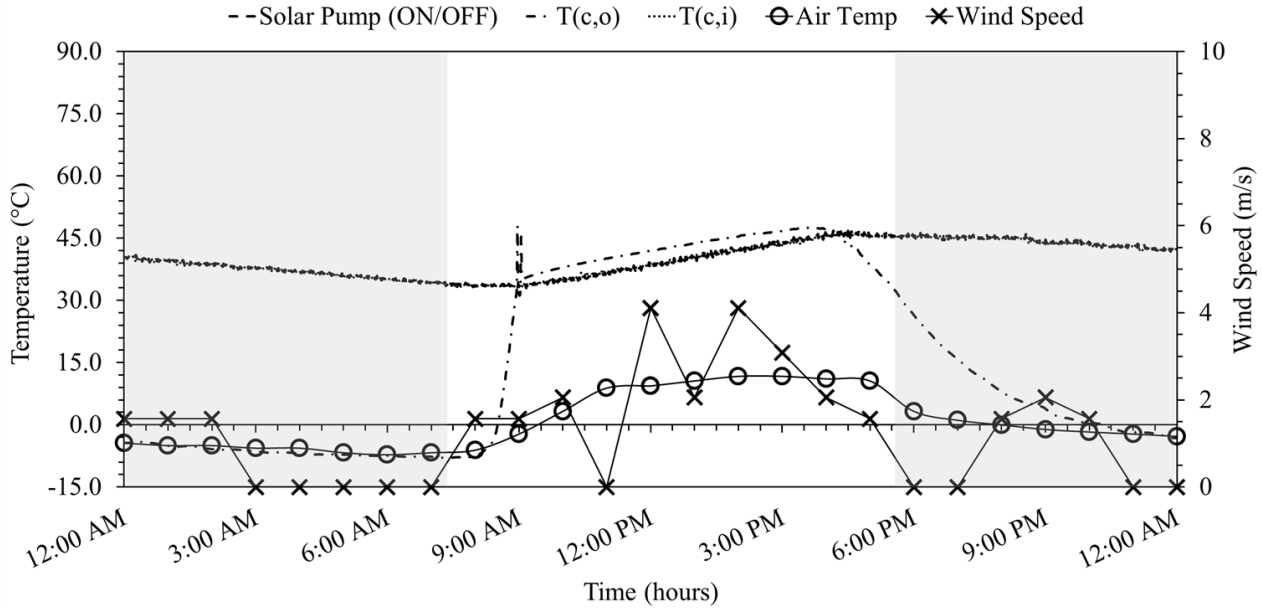

Figure 107: Storage tank heating performance on January 24, 2018.

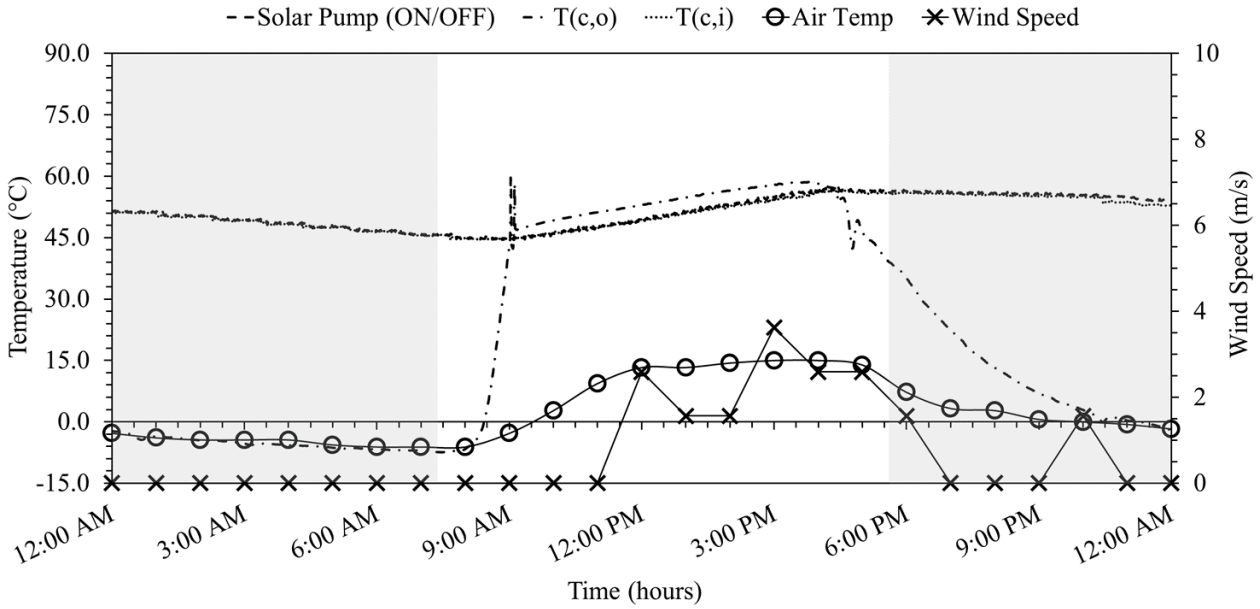

Figure 108: Storage tank heating performance on January 28, 2018.

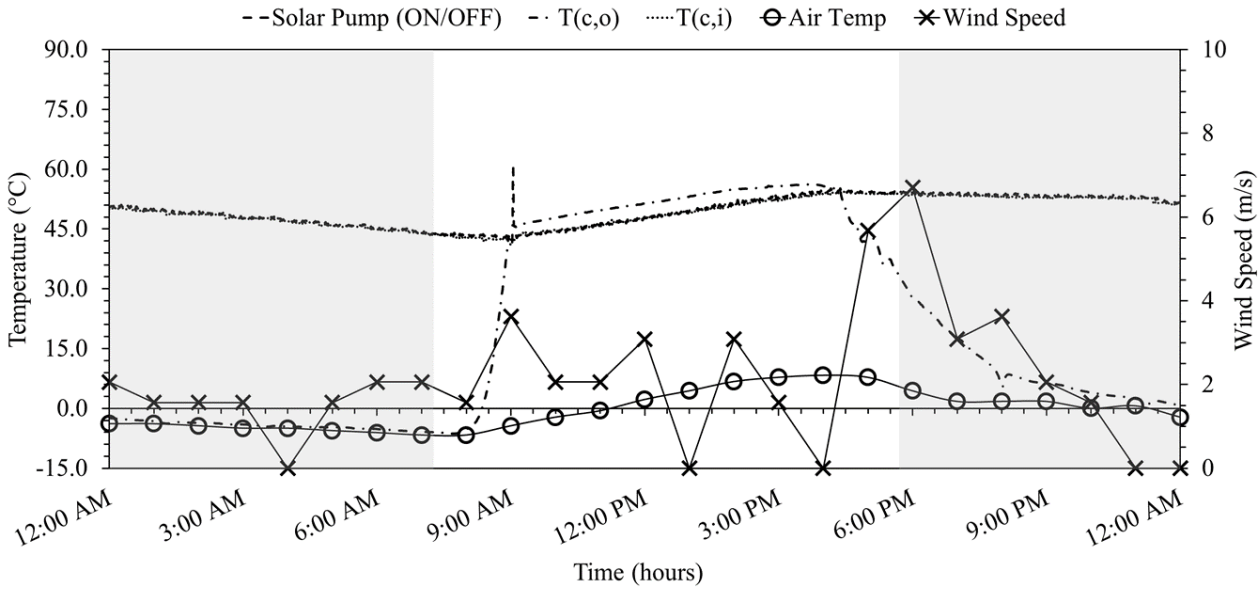

Figure 109: Storage tank heating performance on February 2, 2018.

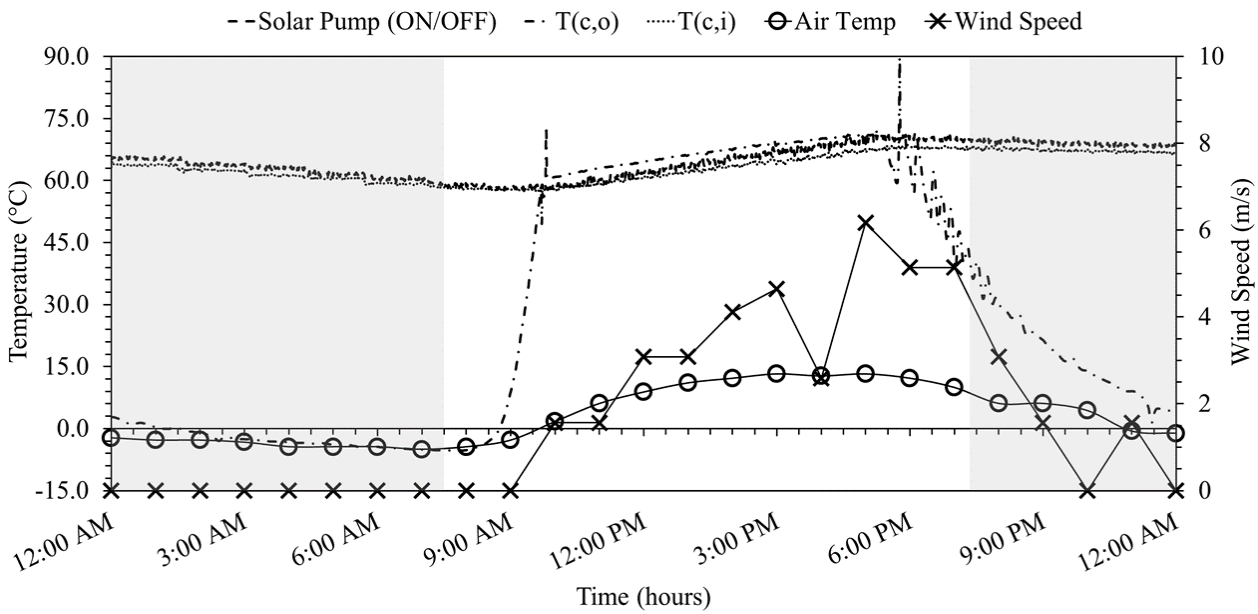

Figure 110: Storage tank heating performance on March 13, 2018.

APPENDIX C

The material in this appendix include snowmaking and snow-melting images and data figures for the hydronic pavement heating/anti-icing test cycles.

Figure 111: Snowmaking machine positioning for anti-icing tests.

DECEMBER 7-8, 2017

Figure 112: Anti-icing test image during December 7-8, 2017 test cycle.

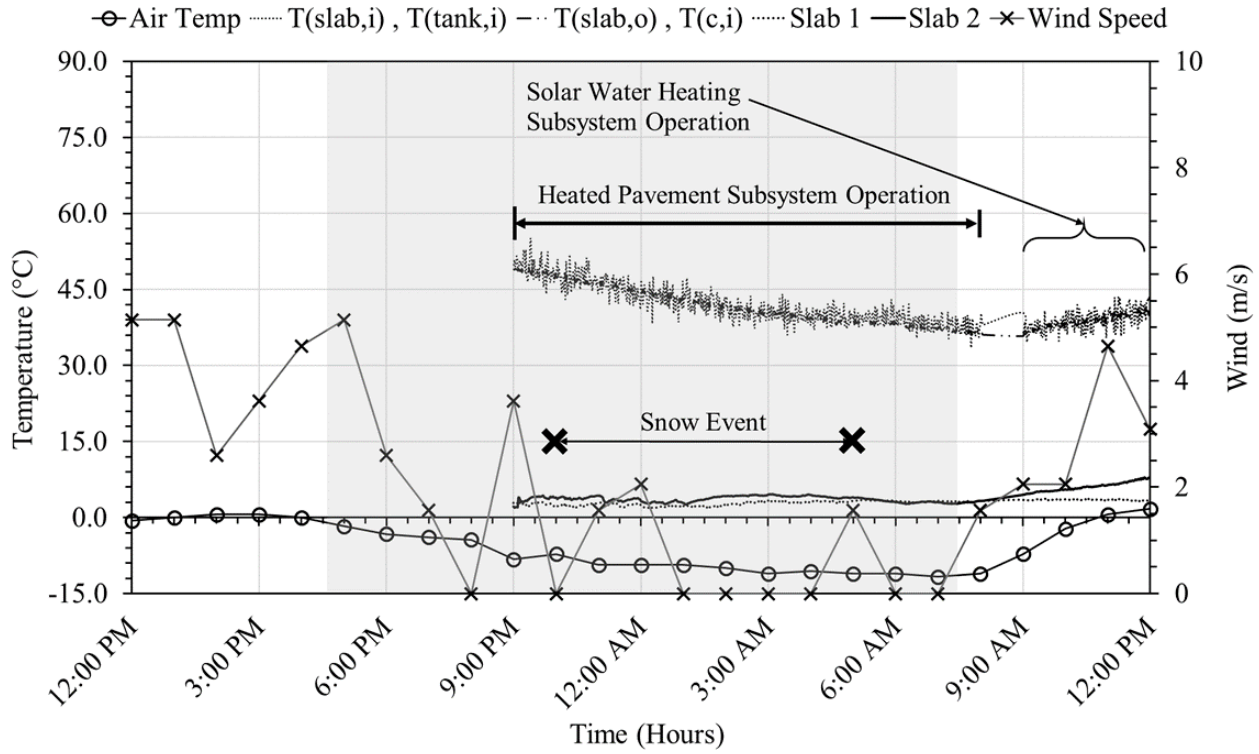

Figure 113: Hydronic pavement anti-icing performance during December 7-8, 2017 test cycle.

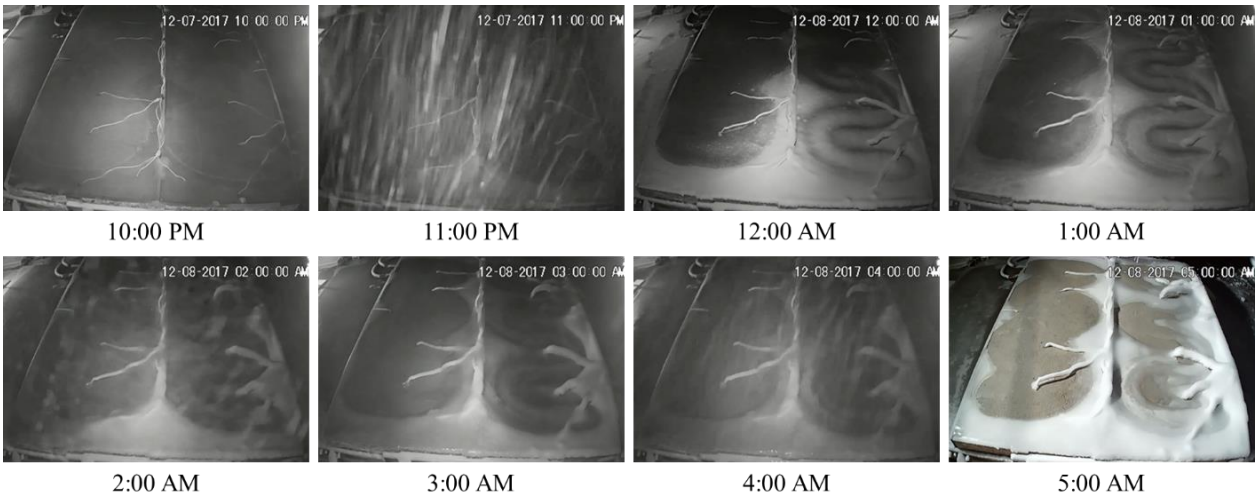

Figure 114: Hydronic pavement melting response during Dec. 7-8, 2017 manmade snowfall.

DECEMBER 22-23, 2017

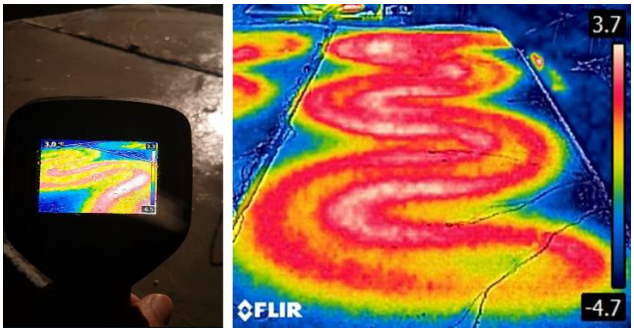

Figure 115: Anti-icing test image during December 22-23, 2017 test cycle.

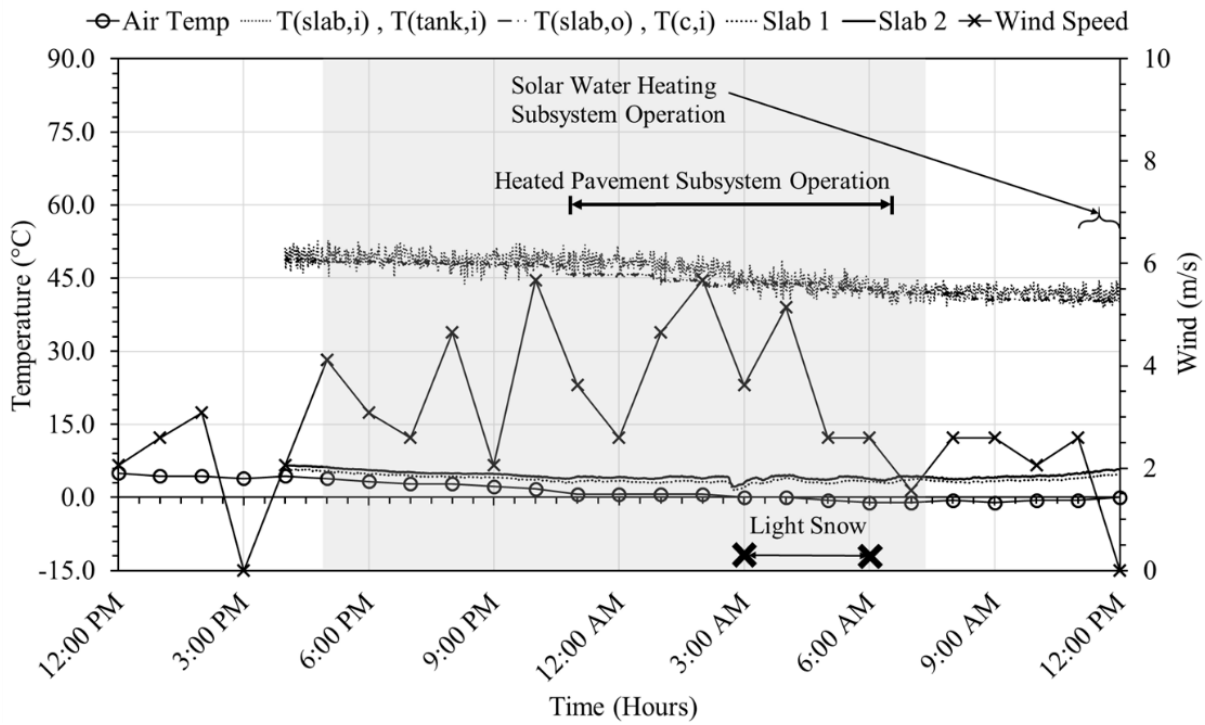

Figure 116: Hydronic pavement anti-icing performance during December 22-23, 2017 test cycle.

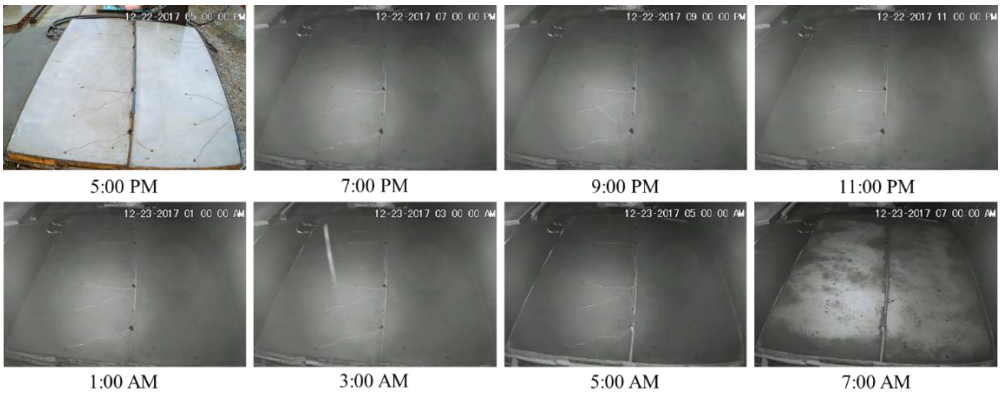

Figure 117: Hydronic pavement melting response during Dec. 22-23, 2017 manmade snowfall.

DECEMBER 24-25, 2017

Figure 118: Anti-icing test image during December 24-25, 2017 test cycle.

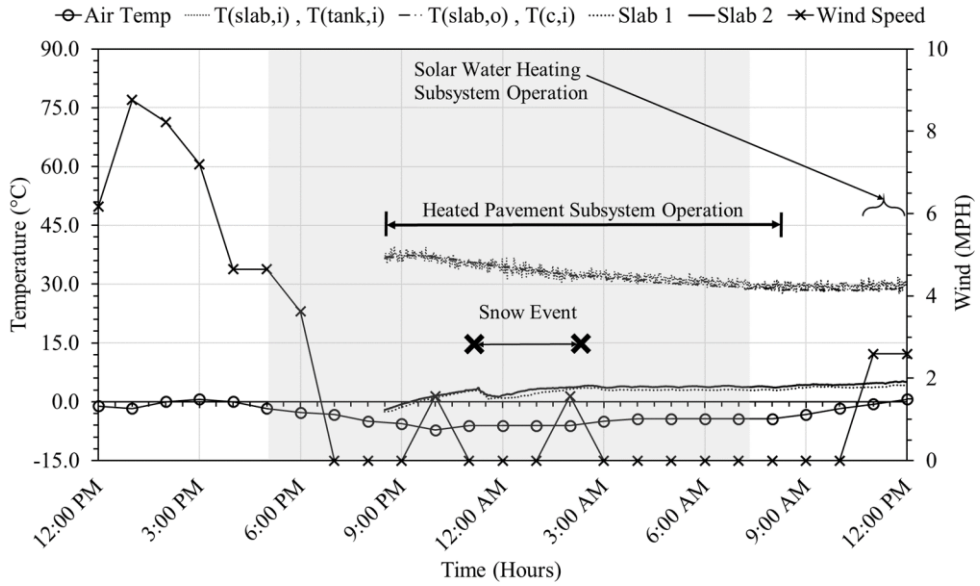

Figure 119: Hydronic pavement anti-icing performance during December 24-25, 2017 test cycle.

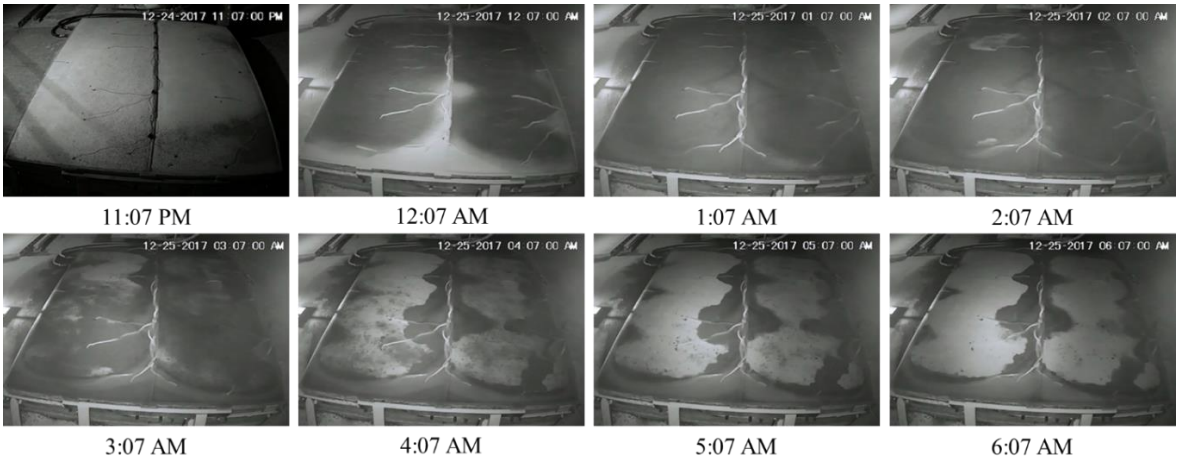

Figure 120: Hydronic pavement melting response during Dec. 24-25, 2017 manmade snowfall.

APPENDIX D

The material in this appendix include data figures for the energy performance analyses.

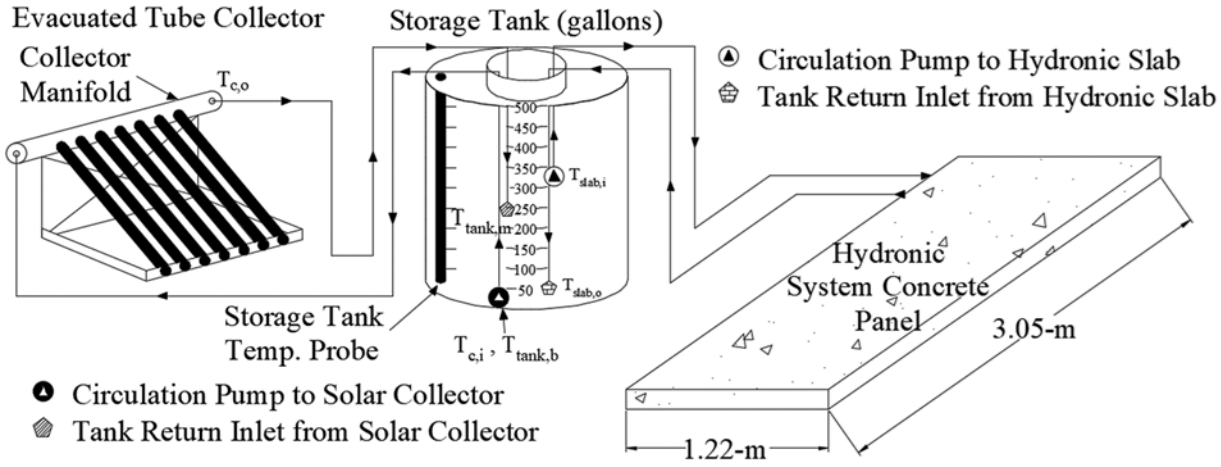

Figure 121: Schematic diagram of solar water-glycol heating subsystem (left) and hydronic heated pavement subsystem (right).

Table 21: Energy Performance Analysis Parameters

Experiment Date	Initial Tank Temp. $T_{(tank,b\_initial)}$	Solar Pump "ON" (hr)	$\dot{m}$ (kg/s)	C_p (J/kg·°C)	$T_{c,i}$ (°C)	$T_{c,o}$ (°C)	Q_c (MJ)
12/6/2017 (c)	53.1	6.7	0.199	3,895.0	59.8	63.1	62.0
12/10/2017 (c)	35.5	7.4	0.200	3,855.2	42.2	45.8	74.4
12/13/2017 (c)	45.2	7.0	0.200	3,877.2	50.7	53.4	52.4
12/14/2017 (i)	48.5	4.8	0.199	3,884.5	50.1	51.6	20.1
12/26/2017 (c)	22.5	6.8	0.201	3,825.7	28.1	31.4	62.4
1/1/2018 (c)	14.3	6.6	0.202	3,807.1	21	24.6	65.2
1/2/2018 (o)	17.2	2.5	0.202	3,813.7	18.8	19.4	4.2
1/3/2018 (c)	12.8	7.2	0.202	3,803.7	19.7	23.5	75.6
1/14/2018 (o)	31.7	5.5	0.201	3,846.6	34.5	35.8	19.7
1/17/2018 (c)	11.2	7.3	0.202	3,800.0	18.1	22.2	82.7
1/23/2018 (i)	36.4	5.6	0.200	3,857.2	40.8	43.3	39.1
1/24/2018 (c)	33.5	7.4	0.201	3,850.5	39.7	42.9	65.5
1/28/2018 (c)	44.6	7.3	0.200	3,875.7	50.5	53.9	69.1
2/2/2018 (c)	42.2	7.3	0.200	3,870.4	48.7	52.2	71.5
3/13/2018 (c)	57.7	7.8	0.198	3,906.0	62.9	66.8	84.5

Note: (c), (i), (o) in the "Experiment Date" column indicate a clear, intermediate, or overcast weather condition, respectively.

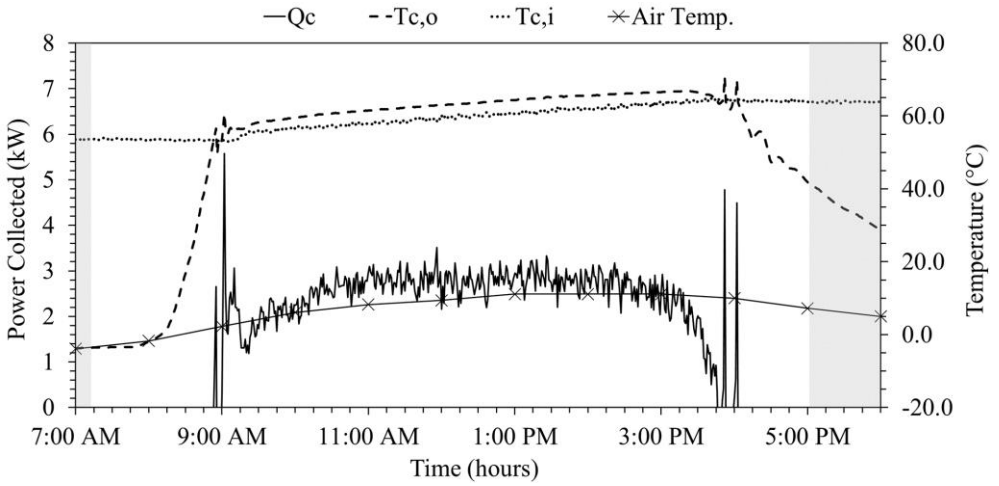

Figure 122: HP-ETC power curve during the December 6, 2017 tank-heating test cycle.

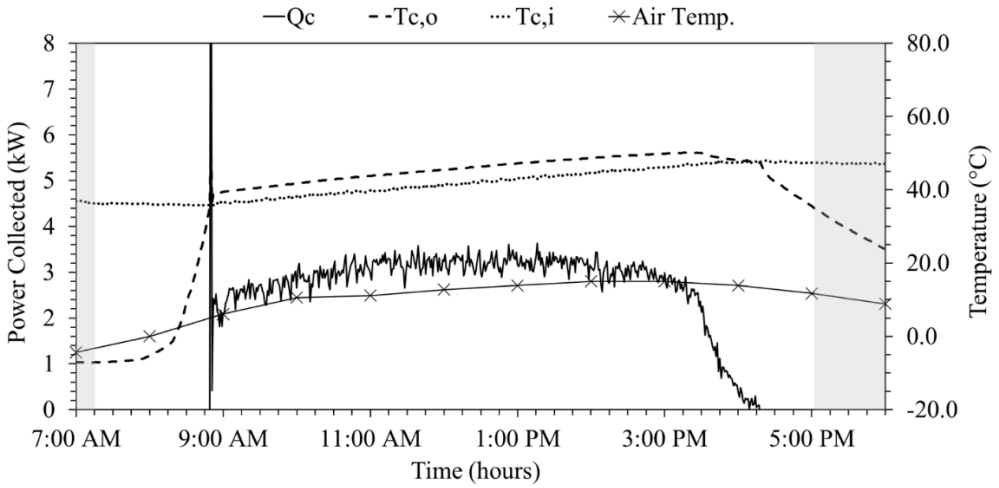

Figure 123: HP-ETC power curve during the December 6, 2017 tank-heating test cycle.

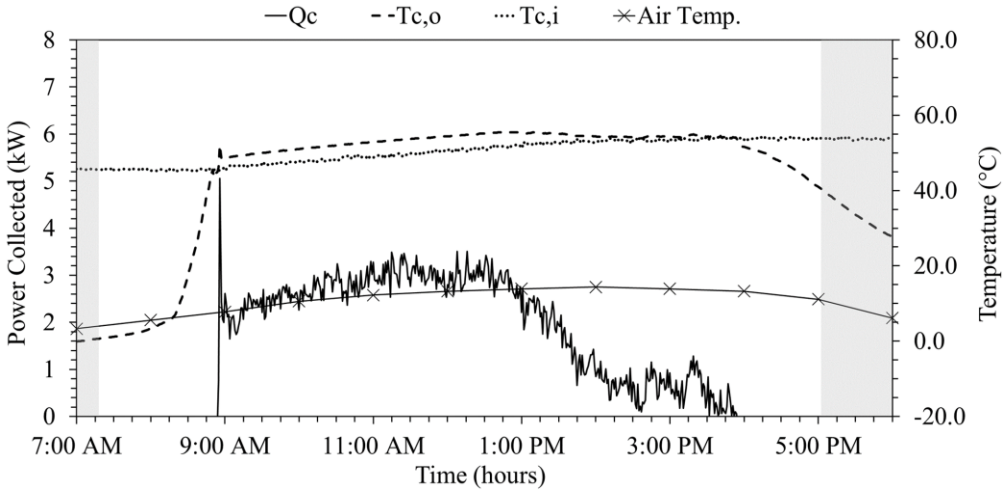

Figure 124: HP-ETC power curve during the December 6, 2017 tank-heating test cycle.

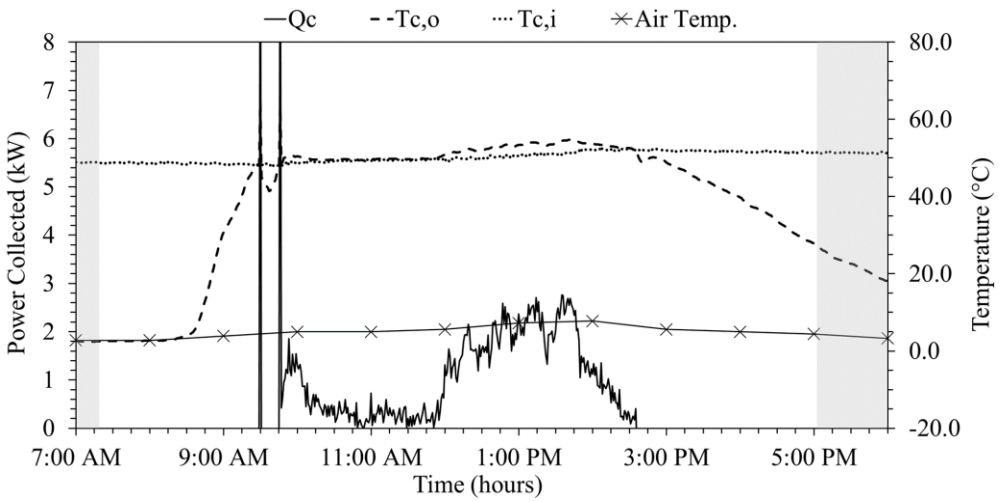

Figure 125: HP-ETC power curve during the December 6, 2017 tank-heating test cycle.

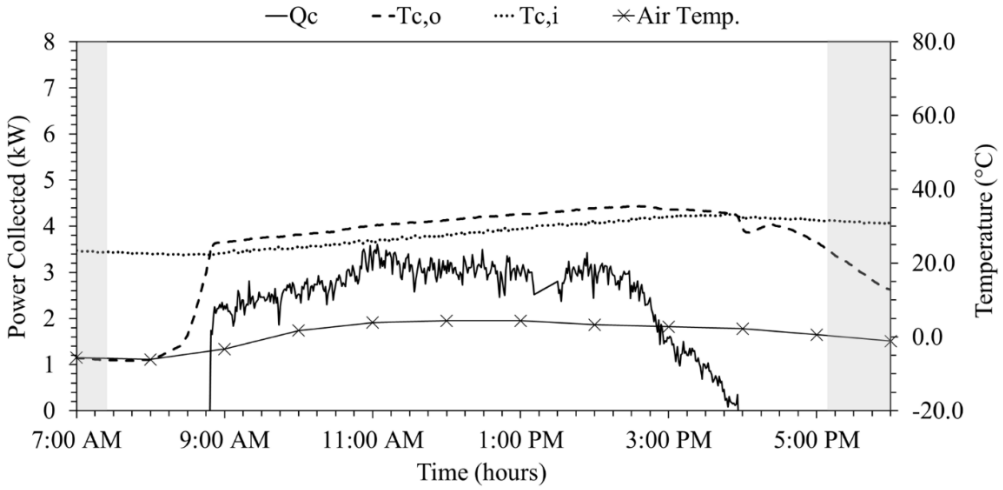

Figure 126: HP-ETC power curve during the December 6, 2017 tank-heating test cycle.

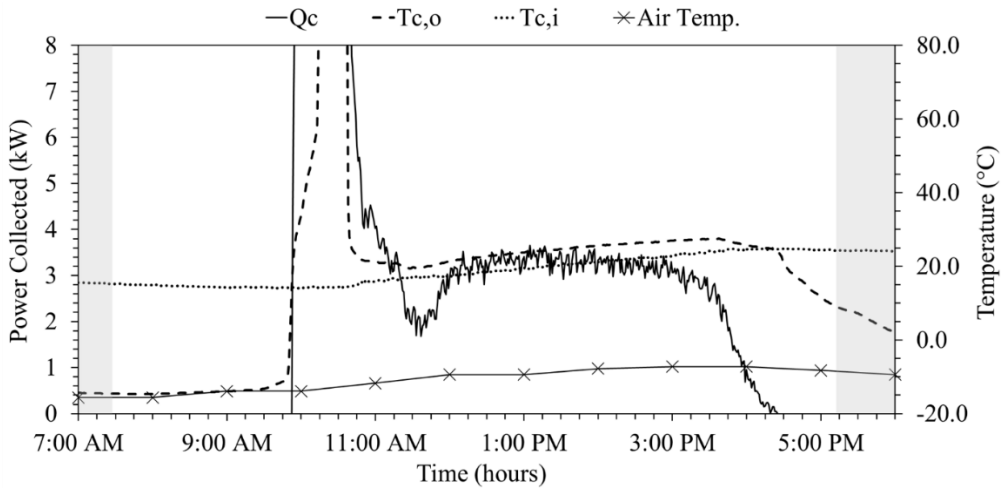

Figure 127: HP-ETC power curve during the January 1, 2018 tank-heating test cycle.

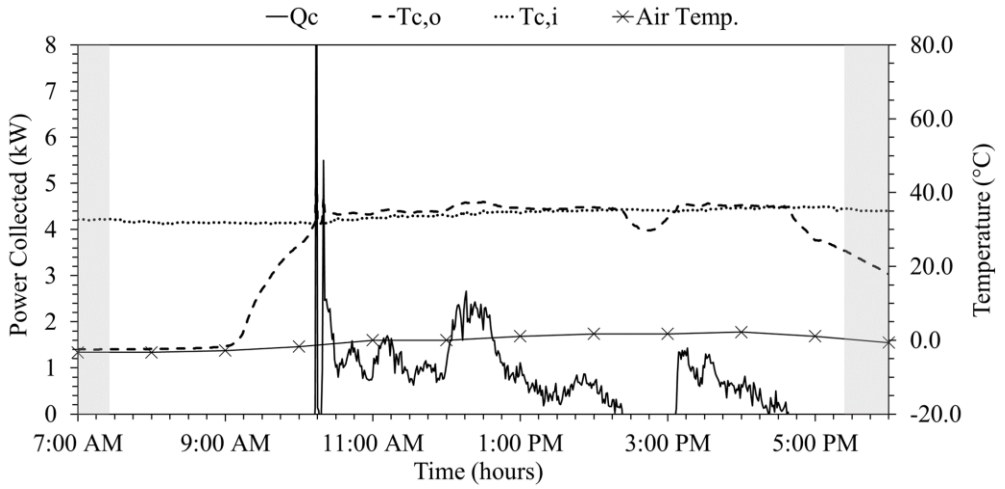

Figure 128: HP-ETC power curve during the January 14, 2018 tank-heating test cycle.

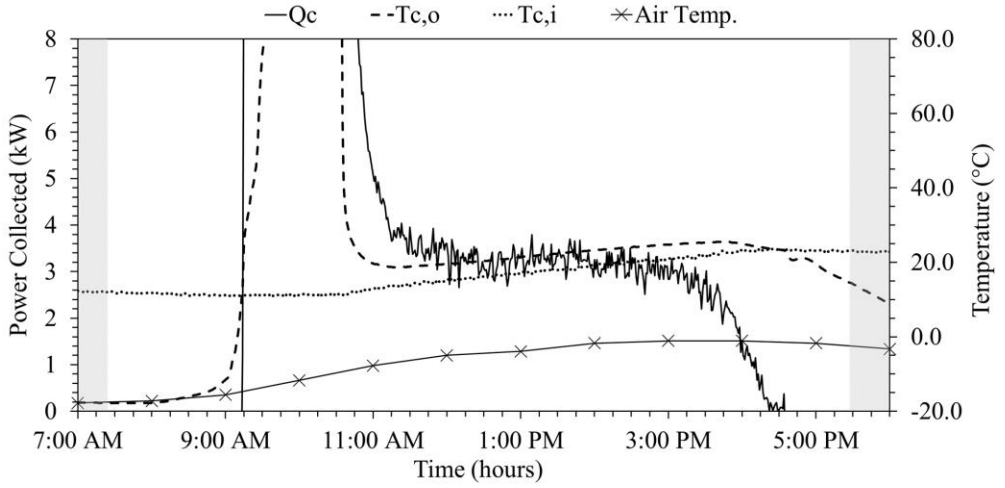

Figure 129: HP-ETC power curve during the January 17, 2018 tank-heating test cycle.

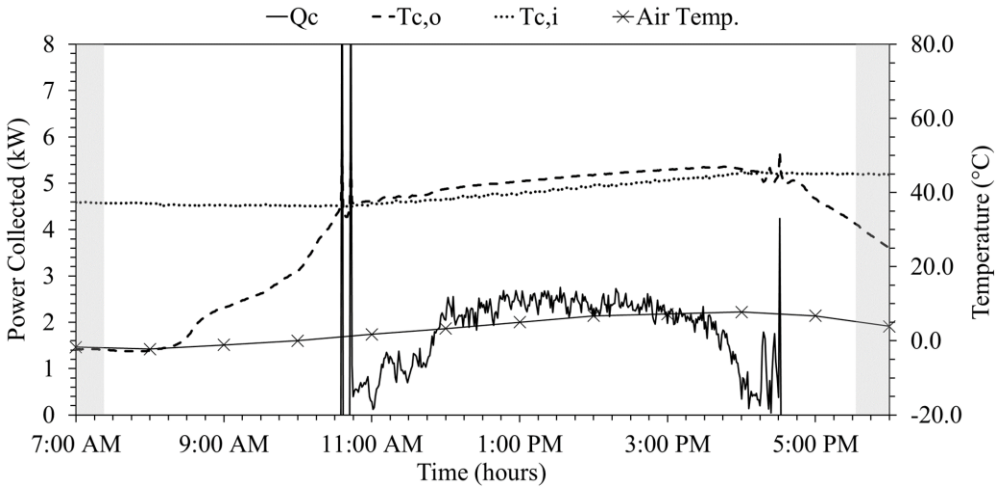

Figure 130: HP-ETC power curve during the January 23, 2018 tank-heating test cycle.

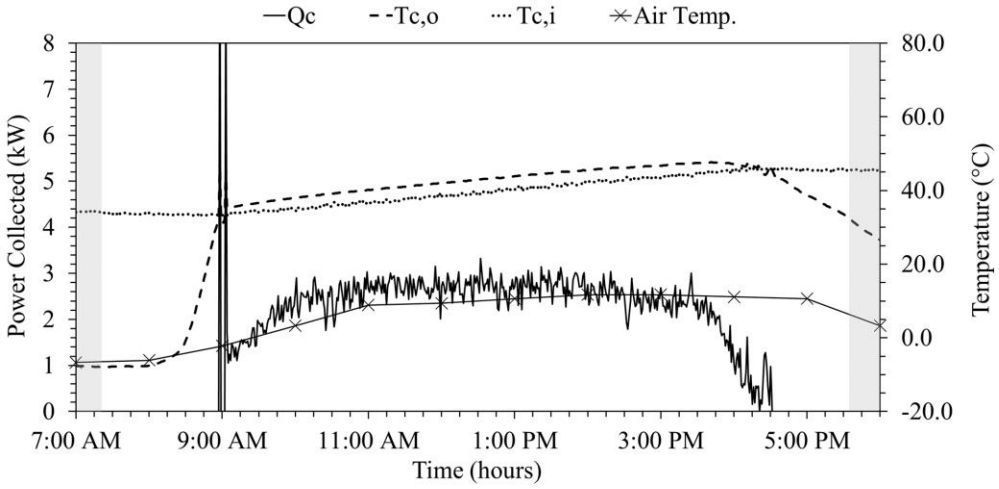

Figure 131: HP-ETC power curve during the January 24, 2018 tank-heating test cycle.

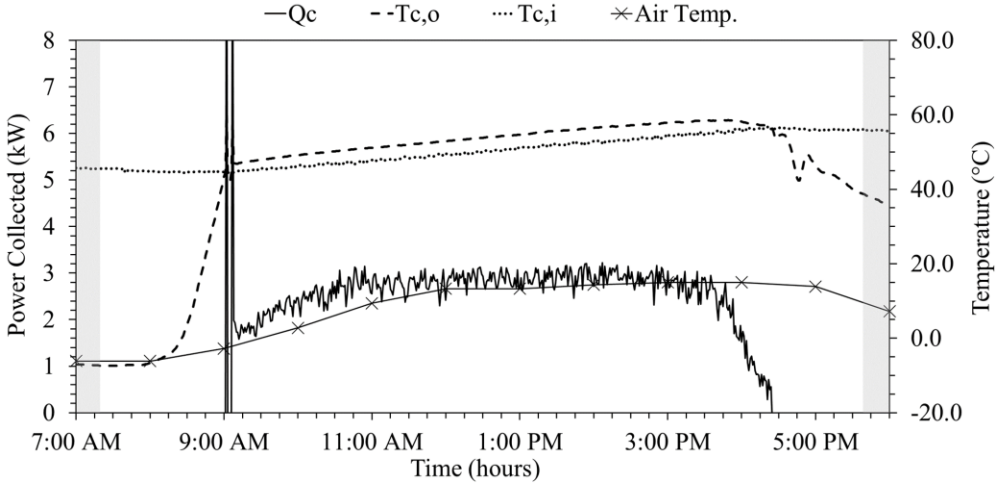

Figure 132: HP-ETC power curve during the January 28, 2018 tank-heating test cycle.

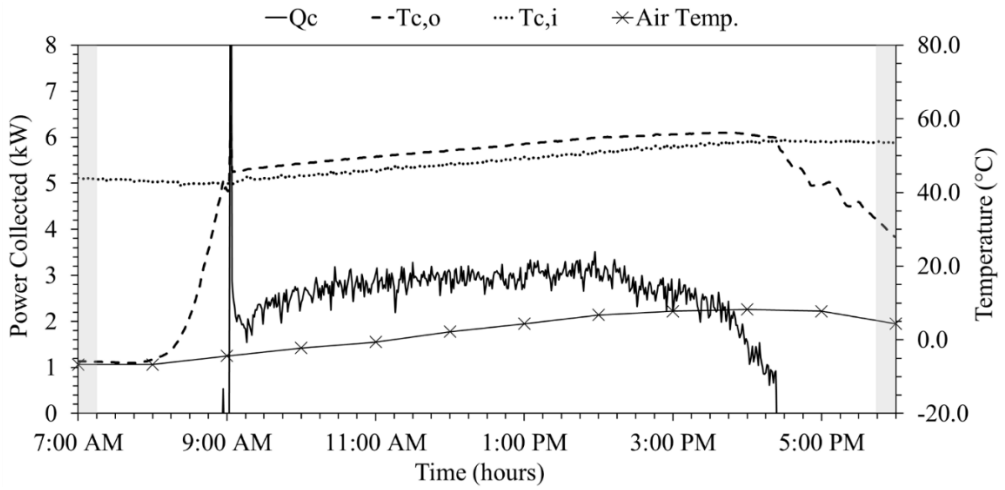

Figure 133: HP-ETC power curve during the February 2, 2018 tank-heating test cycle.

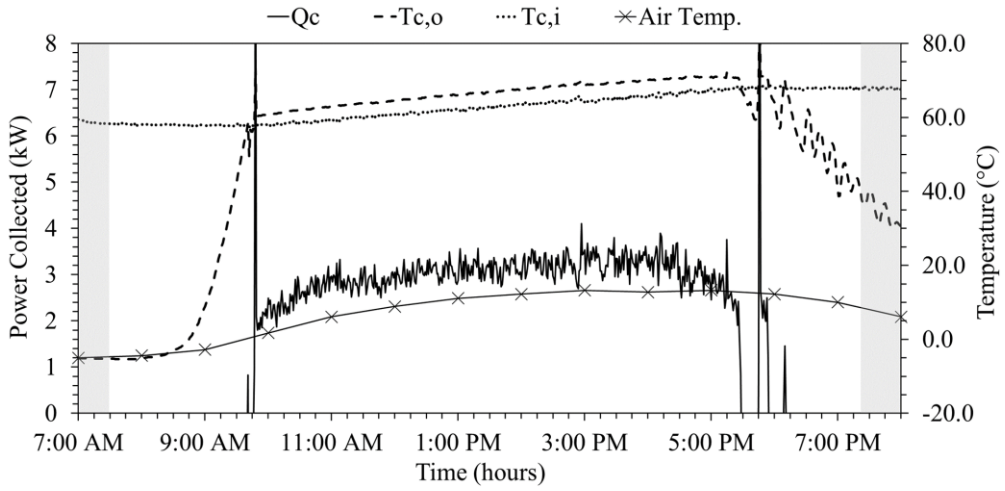

Figure 134: HP-ETC power curve during the March 13, 2018 tank-heating test cycle.

APPENDIX E

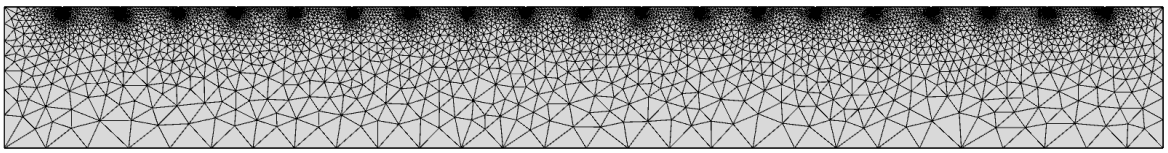

Figure 135: Solar-EHPS Slab 1 model cross-section.

DES MOINES INTERNATIONAL AIRPORT

Table 22: DSM Snowfall Statistics and Average Monthly Winter Weather Statistics

Selected Airport Code	DSM		
Snowfall Hours per Winter Season (hours)	105		
Snowfall Amount per Winter Season (cm)	71		
Winter Days with Snowfall (days)	21		
Snowfall Duration per Day (hours/day)	5		
Average Monthly Weather Statistics	November	December	February
Air Temperature (°C)	0	-2.22	-2.78
Dew Point (°C)	-4.44	-7.22	-8.33
Wind Speed (m/s)	4.92	4.47	4.47
Relative Humidity (%)	65	71	68

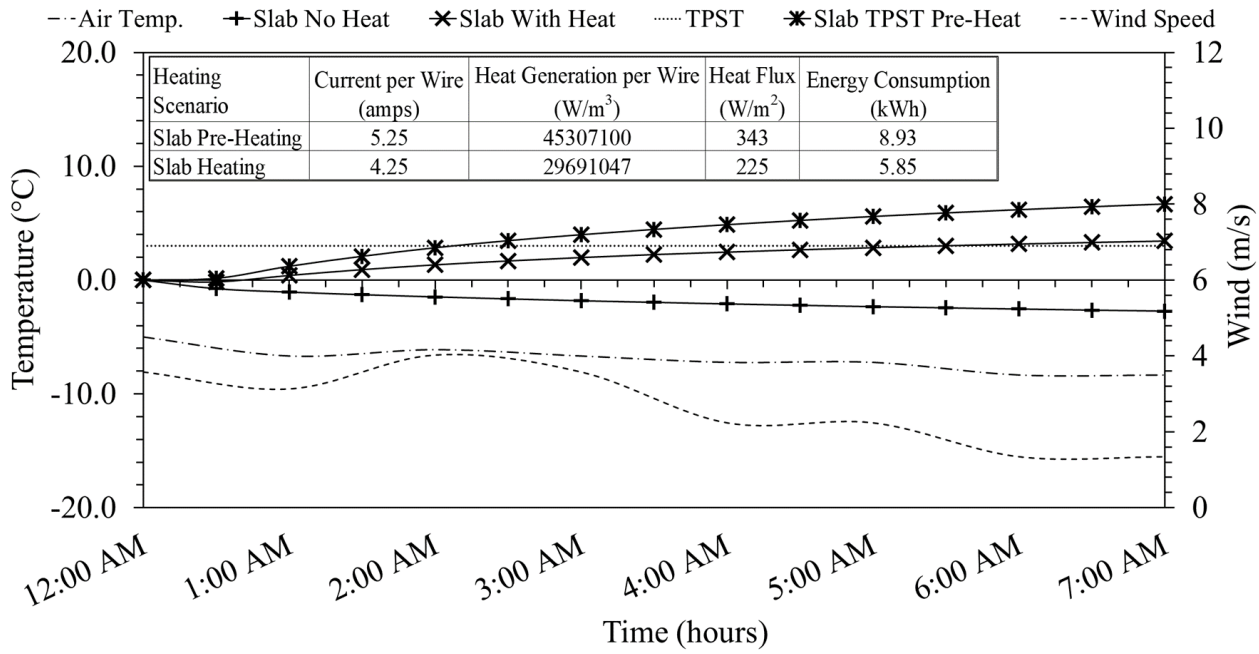

Figure 136: FEM heat testing simulation for DSM pavement on November 22, 2017.

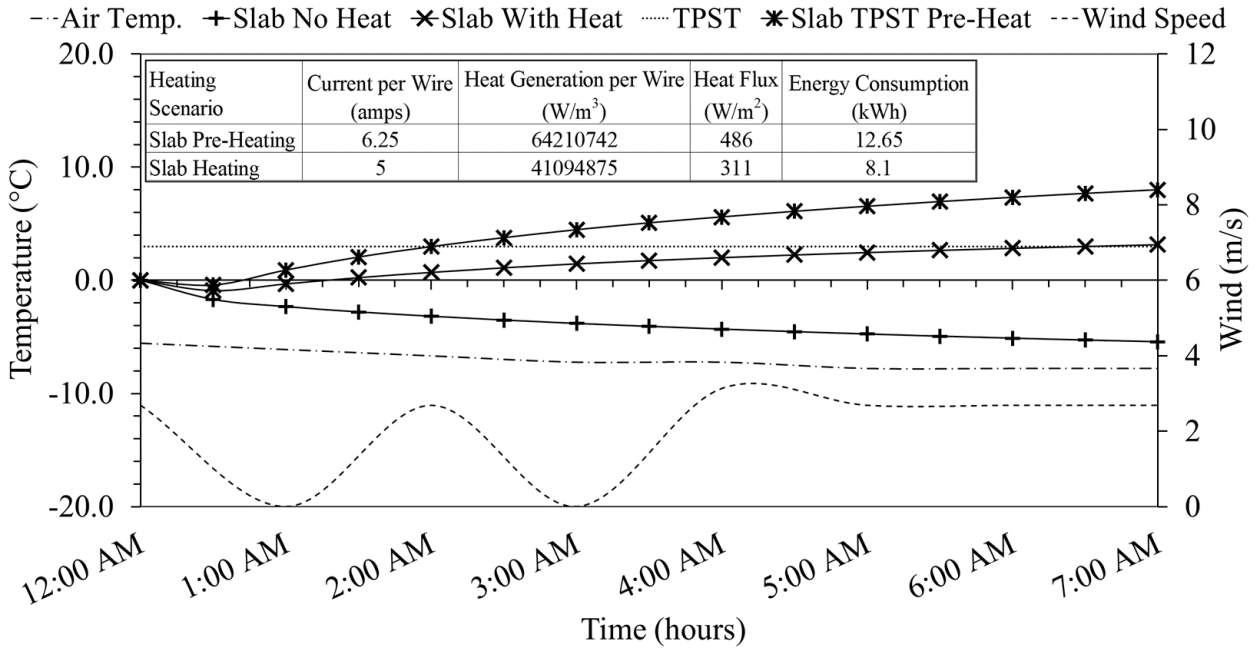

Heating Scenario	Current per Wire (amps)	Heat Generation per Wire (W/m^3)	Heat Flux (W/m^2)	Energy Consumption (kWh)
Slab Pre-Heating	6.25	64210742	486	12.65
Slab Heating	5	41094875	311	8.1

Figure 137: FEM heat testing simulation for DSM pavement on December 24, 2017.

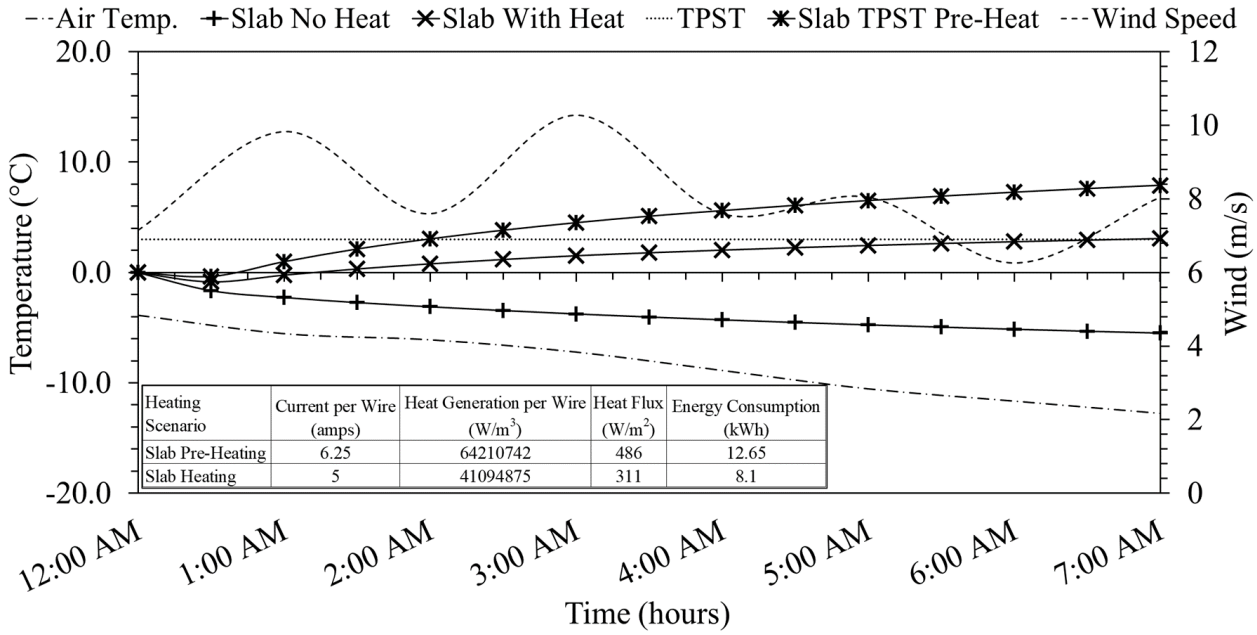

Heating Scenario	Current per Wire (amps)	Heat Generation per Wire (W/m^3)	Heat Flux (W/m^2)	Energy Consumption (kWh)
Slab Pre-Heating	6.25	64210742	486	12.65
Slab Heating	5	41094875	311	8.1

Figure 138: FEM heat testing simulation for DSM pavement on February 16, 2018.

CHICAGO'S O'HARE INTERNATIONAL AIRPORT

Table 23: ORD Snowfall Statistics and Average Monthly Winter Weather Statistics

Selected Airport Code	ORD		
Snowfall Hours per Winter Season (hours)	100.5		
Snowfall Amount per Winter Season (cm)	75		
Winter Days with Snowfall (days)	23.1		
Snowfall Duration per Day (hours/day)	4.35		
Average Monthly Weather Statistics	November	December	February
Air Temperature (°C)	0.56	-1.67	-2.78
Dew Point (°C)	-3.89	-5	-7.22
Wind Speed (m/s)	4.47	4.47	4.92
Relative Humidity (%)	69	75	70

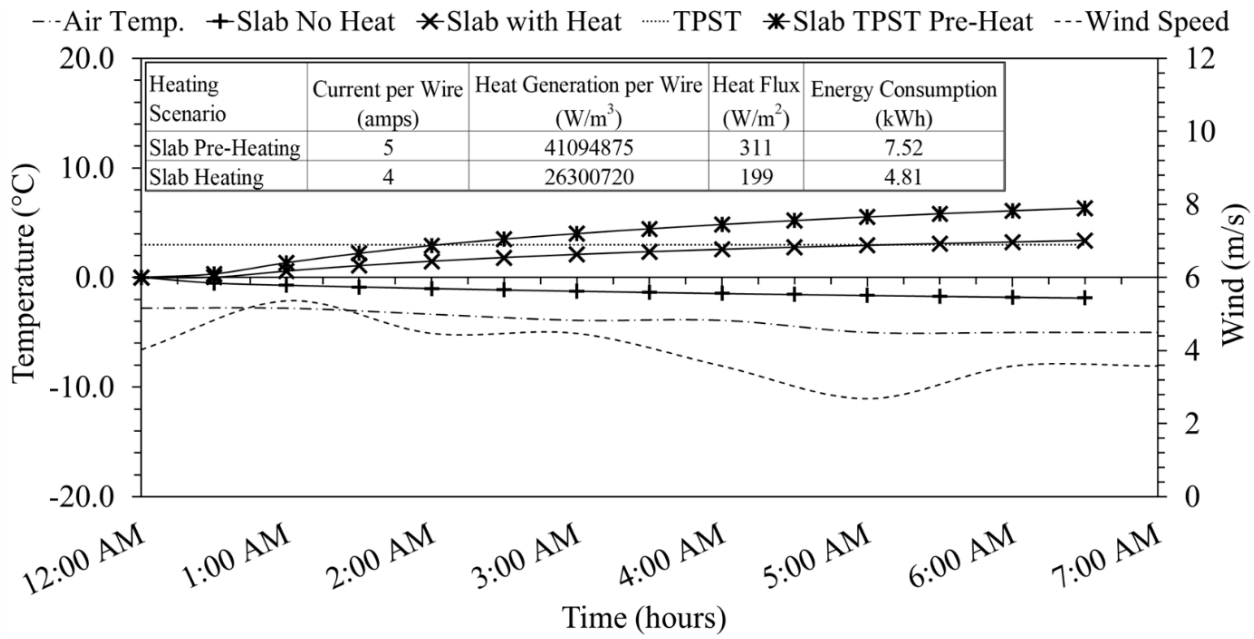

Figure 139: FEM heat testing simulation for DSM pavement on November 22, 2017.

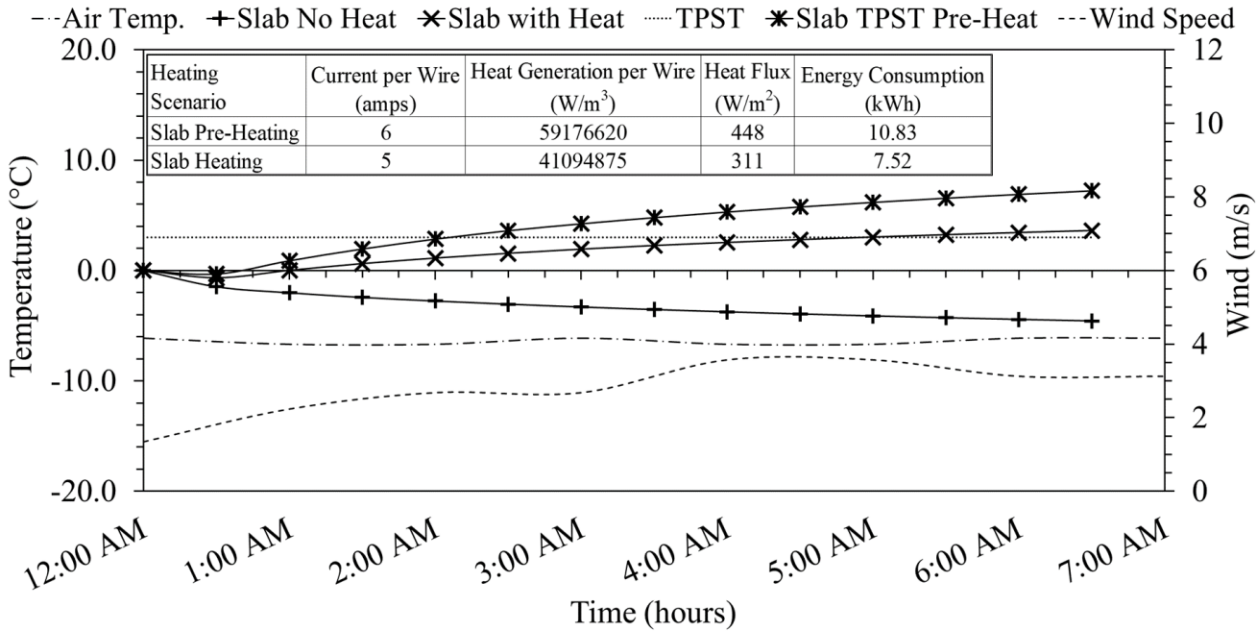

Heating Scenario	Current per Wire (amps)	Heat Generation per Wire (W/m^3)	Heat Flux (W/m^2)	Energy Consumption (kWh)
Slab Pre-Heating	6	59176620	448	10.83
Slab Heating	5	41094875	311	7.52

Figure 140: FEM heat testing simulation for DSM pavement on December 24, 2017.

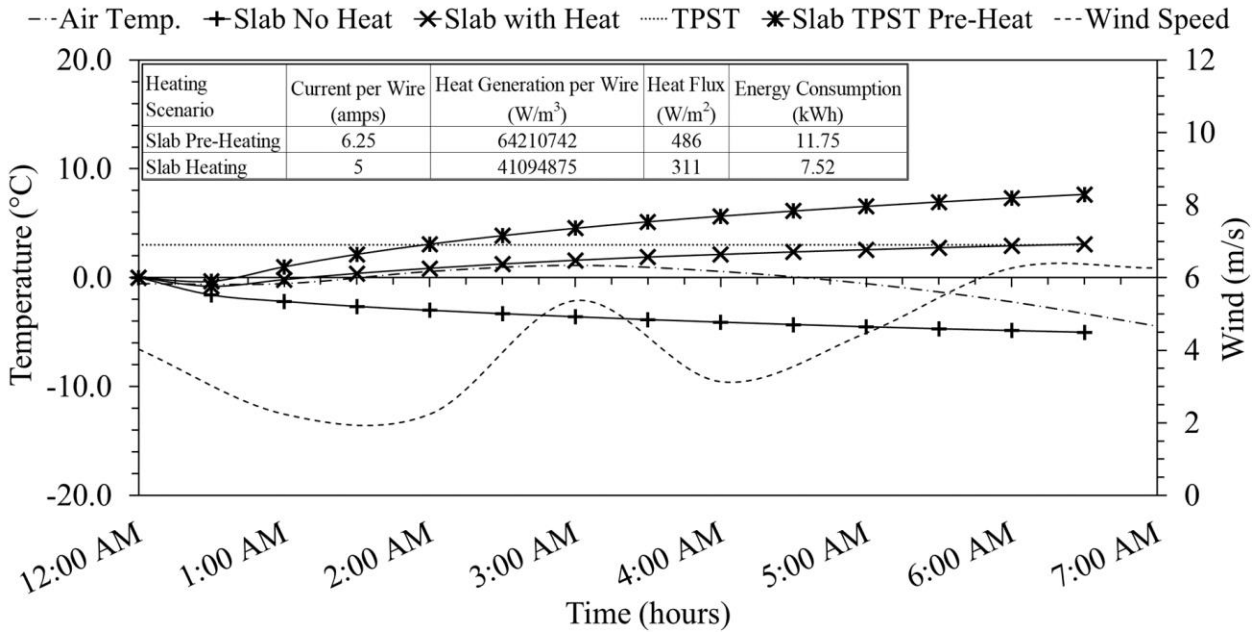

Heating Scenario	Current per Wire (amps)	Heat Generation per Wire (W/m^3)	Heat Flux (W/m^2)	Energy Consumption (kWh)
Slab Pre-Heating	6.25	64210742	486	11.75
Slab Heating	5	41094875	311	7.52

Figure 141: FEM heat testing simulation for DSM pavement on February 4, 2018.

LAGUARDIA AIRPORT

Table 24: LGA Snowfall Statistics and Average Monthly Winter Weather Statistics

Selected Airport Code	LGA	
Snowfall Hours per Winter Season (hours)	50.6	
Snowfall Amount per Winter Season (cm)	53	
Winter Days with Snowfall (days)	9.2	
Snowfall Duration per Day (hours/day)	5.5	
Average Monthly Weather Statistics	December	February
Air Temperature (°C)	1.67	-1.67
Dew Point (°C)	-6.11	-10
Wind Speed (m/s)	5.36	5.36
Relative Humidity (%)	48	41

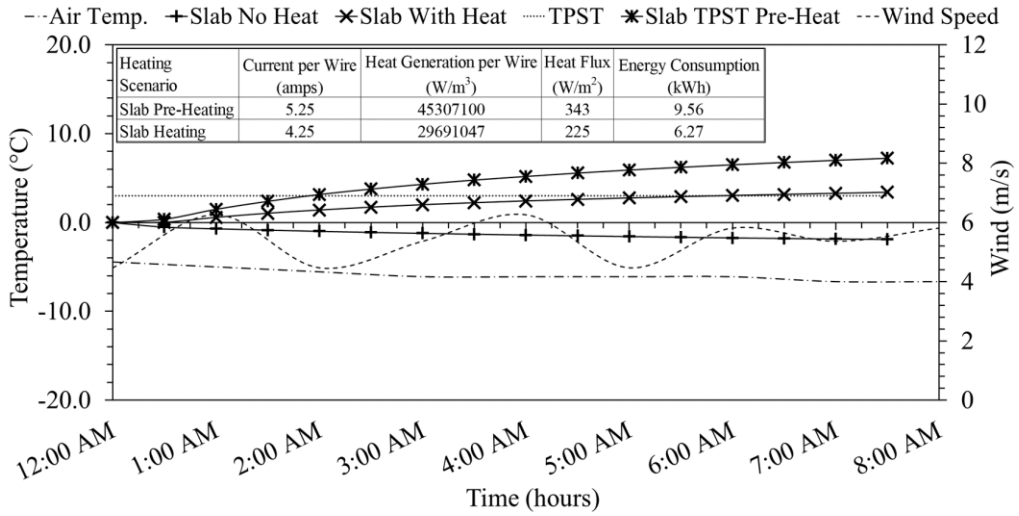

Figure 142: FEM heat testing simulation for DSM pavement on December 27, 2017.

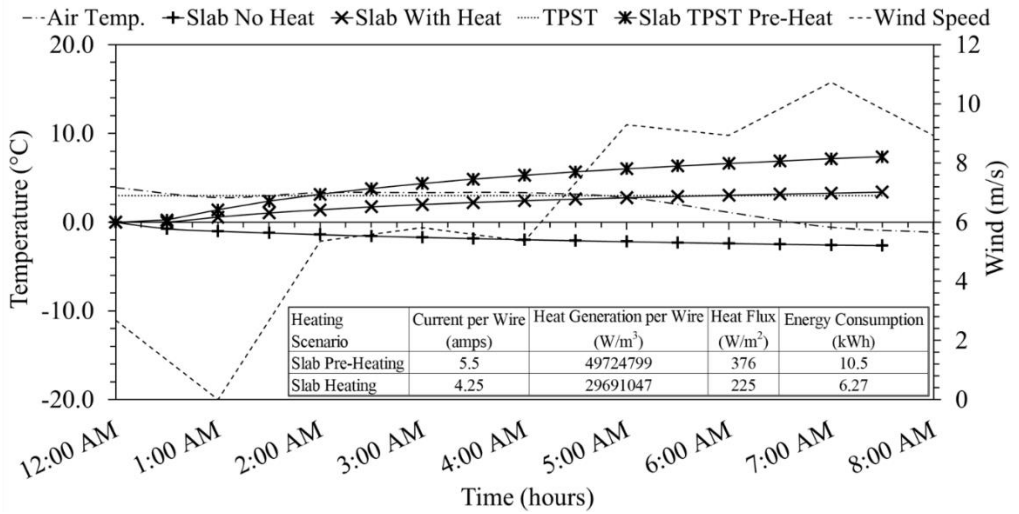

Figure 143: FEM heat testing simulation for DSM pavement on February 2, 2018.

APPENDIX F

XNA Snow Removal Operation Survey – Thane Seely, Airport Operations Manager

Snow and Ice Operation Routine:

Q: What is the XNA airfield snow and ice removal routine:

A: This completely depends on the snow storm, each storm is completely different. If there is snow, we will end up using all pieces of equipment that we have. We use the same equipment for every priority level depending on what precipitation the storm drops. If it is only an ice storm, we will only use the spreader trucks. Priority 1 surfaces are the runway, taxiway bravo, ARFF Road to the runway, and 2 connecting taxiways. Priority 2 surfaces are the existing cross taxiways. Priority 3 surfaces are the ramps. What typically happens on any event is we will take the equipment needed and start on priority 1 surfaces and work them until they are clear. Once they are clear we will move on priority 2, then 3. If the storm continues we will then start all over again at priority 1.

Q: What snow removal equipment is used for "Priority 1"; Runway 16/34, Taxiway B, F (apron/terminal access), ARFF? What is the clearance time?

A: The type of equipment will depend on the type of storm. Runway 16/34 is
where most of our time would be spent. Depending on the storm it could take 10 minutes to a couple of hours to clear the runway. Taxiways usually don't take as long usually, 30 minutes to an hour.

Q: What snow removal equipment is used for the apron area? What parts of the apron area is cleared by airport operations? What is the clearance time?

A: We are responsible for everything on the ramps except the immediate gate areas around the jet bridges. The airline is supposed to clear those areas.

Q: Chemical treatment procedure. Is it used for anti-icing or deicing? What chemical is used and what pavement area is it used on? What is the application rate?

A: We use deicing liquid and dry for both anti- ice and de-icing. We use New Deal granular Sodium Acetate/ Formate Blend and Cryotech LC-17 Liquid Potassium Acetate/ Glycol Blend. The application rates varies depending on the storm. Typically 4 super sacs is enough granular to pretreat all areas of the airfield and ramps. About 1600 gallons of liquid is enough to pre-treat the runway. The application rate will depend on the storm and precipitation type. Between December 2017 and March 2018, we have spent about $180,000.00 on snow removal.

Initial and Operation Cost:

Q: What is the cost per snow removal equipment and how much fuel is required?

A: Each piece of equipment will run for at least 12 hours per tank. We pay around $2.50 per gallon. With the new equipment we have not used it enough to know exactly how long they will run before needing refueled.

- Snow blower: Cost = , Fuel Capacity = 250 gallon capacity per unit
- MTE: Cost = , Fuel Capacity = 360 gallon capacity per unit
- Plow Truck: Cost = , Fuel Capacity = 140 gallon capacity per unit
- Total fuel capacity of all pieces: 1,500 gallons

Q: What is the snow removal labor cost?

A: The average wage rate for our personnel would be around $25 an hour.

Maintenance

Q: What is the snow removal equipment maintenance cost (percentage relative to purchase cost)?

A: Since we have brand new equipment, would do not have a cost on maintenance for them. However, even our old equipment had relatively low maintenance cost. The main cost would be oil changes once a year and the occasional break down.

Q: Is there any required pavement maintenance from damage when using snow removal equipment and deicing agents?

A: We really have not had any major pavement issues caused by snow equipment. The only issue we have is if someone runs over a light or hits a sign.

Safety

Q: Has there been any personnel injury in the gate area/aircraft parking area? If yes, are there any known cost associated?

A: None

Q: In the last 20 years, has there been any aircraft accidents/incidents during ground operation caused by snow, slush, or ice? If yes, are there any known cost associated?

A: None

Flight Delays

Q: Can you categorize any flight delays (during taxi or at gate) due to extreme weather?

A: Usually the delays are not caused by our airport. Usually the delays are from the origin airport. It is not very common for us to cause delays.

General Questions:

Q: What are the challenges faced during pavement deicing operation?

A: I think the biggest problem we have with deicing operations is having enough chemical on hand and knowing exactly when to put the chemical down (when to pre-treat). Also, aircraft traffic flow can create a timing issue and can delay our reactions times.

Q: Do you know the percentage difference between business travelers and non-business travelers?

A: 65% of our traffic flow is business travelers.

Q: Do you have a breakdown of the aircraft types that fly in and out of XNA?

A: Almost all of the aircraft we get are regional jets. The type of aircraft can change daily depending on number of passengers. We get 2 717s or MD 88s a day, these are the only mainline aircraft we get. Allegiant brings either a MD 88 or Airbus A319. The majority of aircraft we get are CJRs 700 and 900s, EJRs 145s and 175s.

Q: Do you know the cost (purchase and maintenance) of the older snow removal equipment? What was the operation data with the older equipment (i.e. clearance times)?

A: The old Equipment was purchased for $664,510.37. The old equipment's operation speed was around 5-10 MPH. The new equipment is capable of speeds up to 30 MPH The Runway would take at least an hour to clear the snow. The old spreader trucks and new spreader trucks operate at about the exact same speed.

Q: Are there plans to utilize the second runway in the future? What are the forecast projects for XNA on the airside that will affect capacity and increased demand?

A: The second runway could eventually be utilized but there is no time line for the runway to be used. We have added on two different sections of concrete to the terminal ramp with in the last 3 years. A 120' section to the east of the terminal and a 40' section to the north of the terminal. Otherwise, we do not have any other plans for added capacity on the airfield. We are currently adding two gates on to the terminal for increased capacity and new airlines that may want to begin new service. We are also planning on expanding the TSA check point area for added passenger screening capacity.

Q: Does the Regional Jet Center have their own snow clearing operation? If not, how does it affect your deicing operations?

A: They have a small plow truck and they will clean right in front of their hangar. What they do really does not affect us either way we clean the same amount around RJCs building.